Stability of Municipal Solid Waste Landfills

Dissertation
submitted to and approved by the
Faculty of Architecture, Civil Engineering and Environmental Sciences
University of Braunschweig - Institute of Technology

and the

Faculty of Engineering
University of Florence

in candidacy for the degree of a
Doktor-Ingenieur (Dr.-Ing.) /
Dottore di Ricerca in Risk Management on the Built Environment *)

by
Dipl.-Ing. Volker Krase
from Magdeburg

Submitted on	10 October 2007
Oral examination on	23 November 2007
Professorial advisors	Prof. Dr.-Ing. habil. Dieter Dinkler
	Prof. Dr.-Ing. Giovanni Vannucchi

Braunschweig 2008

*) Either the German or the the Italian form of the title may be used.

ISBN 978-3-926031-02-0

Herausgeber: Prof. Dr.-Ing. Dieter Dinkler

Kurzfassung

Die vorliegende Arbeit behandelt die Modellierung und Simulation des Deformationsverhaltens von Siedlungsabfall. Siedlungsabfall ist ein poröses Medium, wobei Deponiegas und Sickerwasser im Porenraum frei beweglich sind. Die *Theorie der Porösen Medien* bildet den kontinuumsmechanischen Rahmen für die Modellentwicklung. Die verwendeten kinematischen Beziehungen sind nichtlinear, da große Verschiebungen und Verformungen zu beschrieben sind. Der Feststoff Abfall besteht aus einer Grundmatrix mit Eigenschaften granularer Materialien, in der faserartige Bestandteile eingebettet sind. Stoffgesetze für die beiden Feststoffphasen umfassen sowohl spontan als auch zeitabhängig inelastisches Verhalten. Effekte aus der anisotropen Ausrichtung der Fasern sind berücksichtigt. Ein verallgemeinertes DARCY-Modell für Mehrphasentransport beschreibt die Bewegung der Porenfluide. Numerische Simulation von Laborversuchen validiert und verifiziert das entwickelte Modell. Strukturuntersuchungen unter Anwendung der Finiten-Elemente-Methode zeigen Risiken für die Standsicherheit von Deponiestrukturen auf. Die Transportgleichungen sind mit dem Box-Verfahren, einem Sonderfall der Finiten-Volumen-Methode, simultan gelöst.

Abstract

The present thesis deals with modelling and simulation of the deformation behaviour of municipal solid waste. Municipal solid waste is a porous medium, in which landfill gas and leachate can move freely in the pore space. The *Theory of Porous Media* is the continuum mechanical framework for the model development. The applied kinematics are nonlinear because large displacements and deformations have to be described. The solid material consists of a basic matrix with properties similar to granular materials, in which fibrous constituents are embedded. Constitutive relations for the two solid phases include spontaneous as well as time-dependent inelastic behaviour. Effects from the anisotropic orientation of the fibres are considered, too. A generalised DARCY model for multiphase transport describes the motion of the pore fluids. Numerical simulations of laboratory experiments validate and verify the model. Structural analyses using the finite element method identify risks concerning the stability of landfill structures. The transport equations are simultaneously solved by the box method, a special case of the finite volume method.

Acknowledgement

The present work is financially supported by the Deutsche Forschungsgemeinschaft within the international graduate research program »Risk Management of Natural and Civilisation Hazards on Buildings and Infrastructure«. Essential parts are developed in close cooperation with the collaborative research center 477 »Life Cycle Assessment of Structures via Innovative Monitoring«.

Contents

Notations

Mathematical symbols

d	differential
∂	partial derivative
Δ	increment
δ	virtual
$(\ )^T$	transposition of a second order tensor $\mathbf{A}^T = (\boldsymbol{a}_1 \otimes \boldsymbol{a}_2)^T = \boldsymbol{a}_2 \otimes \boldsymbol{a}_1$
$(\ )^{-1}$	inversion of a second order tensor
$(\ )^{-T}$	transposition and inversion of a second order tensor
$(\ )^{T_{ij}}$	transposition of basis i and j for higher order tensor $(\boldsymbol{a}_1 \otimes \boldsymbol{a}_2 \otimes \boldsymbol{a}_3 \otimes \boldsymbol{a}_4)^{T_{24}} = \boldsymbol{a}_1 \otimes \boldsymbol{a}_4 \otimes \boldsymbol{a}_3 \otimes \boldsymbol{a}_2$
$\dot{(\ )}$	material time derivative
$[\ ]'^{\alpha}$	time derivative concerning motion of component α
$\overset{\vartriangle}{(\ )}$	lower (covariant) OLDROYD derivative $\overset{\vartriangle}{\mathbf{A}} = \dot{\mathbf{A}} + \mathbf{A} \cdot \mathbf{L} + \mathbf{L}^T \cdot \mathbf{A}$
$\overset{\triangledown}{(\ )}$	upper (contravariant) OLDROYD derivative $\overset{\triangledown}{\mathbf{A}} = \dot{\mathbf{A}} - \mathbf{L} \cdot \mathbf{A} - \mathbf{A} \cdot \mathbf{L}^T$
$\mathrm{grad}\,(\ )$	gradient in current configuration
$\mathrm{Grad}\,(\ )$	gradient in reference configuration
$\mathrm{div}\,(\ )$	divergence in current configuration
$\mathrm{tr}\,(\ )$	trace of a second order tensor
$\det(\ )$	determinant of a second order tensor
$(\ ) \cdot (\ )$	dot product - single contraction $\mathbf{A} \cdot \mathbf{B} = (\boldsymbol{a}_1 \otimes \boldsymbol{a}_2) \cdot (\boldsymbol{b}_1 \otimes \boldsymbol{b}_2) = (\boldsymbol{a}_2 \cdot \boldsymbol{b}_1)\ (\boldsymbol{a}_1 \otimes \boldsymbol{b}_2)$
$(\ ) : (\ )$	double dot product - double contraction $\mathbf{A} : \mathbf{B} = (\boldsymbol{a}_1 \otimes \boldsymbol{a}_2) : (\boldsymbol{b}_1 \otimes \boldsymbol{b}_2) = (\boldsymbol{a}_1 \cdot \boldsymbol{b}_1)\,(\boldsymbol{a}_2 \cdot \boldsymbol{b}_2)$
$(\ ) \otimes (\ )$	dyadic product
$(\ ) \times (\ )$	outer product $\mathbf{A} \times \mathbf{B} = \overset{3}{\mathbf{E}} : (\mathbf{B} \cdot \mathbf{A}^T)$
exp	EULERIAN number
π	LUDOLF's number
ln	natural logarithm (base exp)
log	decadic logarithm (base 10)

Scalar variables

t	time
T	dimensionless time
Θ	temperature
b	gravitational constant
I_1	1st invariant of second order tensor
I_2	2nd invariant of second order tensor
I_3	3rd invariant of second order tensor
$J_{2,D}$	2nd invariant of deviator
$J_{3,D}$	3rd invariant of deviator
$s(t)$	settlement in time
σ	stress in experiments
ε	strain in experiments
ϕ'	angle of internal friction
c'	cohesion
ψ	angle of dilatancy
$\tilde{\rho}$	physical (intrinsic) density
ρ	partial density
a_v	volume strain
$a_{v,in}$	inelastic volume strain
W	potential
Ψ	HELMHOLTZ free energy
$\mathcal{D}_{int}$	internal dissipation
$f(\quad)$	Yield surface
$q_E(\quad)$	Plastic potential
$h()$	Hardening/softening function
$\dot{\gamma}_{pl}$	multiplier for flow rule in plasticity
$\dot{\gamma}_{cr}$	multiplier for creep
n^α	volume ratio of a component α
Φ	porosity
S^β	saturation of a fluid β
p	fluid pressure
p^c	matric suction (capillary pressure)
k_{rel}^α	relative permeability of component α
S_e	effective saturation
S_r	residual saturation
k_f	hydraulic conductivity
μ^α	dynamic viscosity of a fluid α

Vectors

$\mathbf{n}$	surface normal vector
$\boldsymbol{x}$	position vector in current configuration
$\boldsymbol{X}$	position vector in reference configuration
$\boldsymbol{u}$	displacement vector
$\boldsymbol{v}$	velocity vector
$\boldsymbol{w}$	seepage velocity
$\tilde{\boldsymbol{w}}$	diffusive velocity
$\hat{\boldsymbol{\pi}}$	momentum exchange
$\mathbf{b}$	gravitational vector
$\mathbf{t}_R$	surface traction current configuration
$\mathbf{t}_{R,0}$	surface traction reference configuration
$\mathbf{t}^{\alpha}$	mass flow of component α

2nd order tensors

$\mathbf{F}$	deformation gradient
$\mathbf{H}$	displacement gradient
$\mathbf{R}$	rotational tensor
$\mathbf{U}$	right stretch tensor
$\mathbf{V}$	left stretch tensor
$\mathbf{C}$	right CAUCHY-GREEN tensor
$\mathbf{B}$	left CAUCHY-GREEN tensor
$\mathbf{E}$	GREEN-strain tensor
$\mathbf{A}$	ALMANSI-strain tensor
$\dot{\mathbf{F}}$	material velocity gradient
$\mathbf{L}$	spatial velocity gradient
$\mathbf{D}$	strain rate (stretching) tensor
$\mathbf{W}$	spin (vorticity) tensor
$\mathbf{T}$	CAUCHY stress tensor
$\tilde{\mathbf{T}}$	KIRCHHOFF stress tensor
$\mathbf{S}$	2nd PIOLA-KIRCHHOFF stress tensor
$\mathbf{P}$	1st PIOLA-KIRCHHOFF stress tensor
$\hat{\mathbf{\Gamma}}$	strain tensor in intermediate configuration
$\hat{\mathbf{S}}$	2nd PIOLA-KIRCHHOFF stress tensor in intermediate configuration
$\hat{\mathbf{P}}$	MANDEL stress tensor in intermediate configuration
$\mathbf{K}_{abs}$	intrinsic permeability
$\mathbf{\Xi}$	inverse of permeability

Higher order tensors

$\mathbb{C}$	elasticity tensor
$\mathbb{F}$	flexibility tensor

Matrix-vector notation

$\underline{\underline{\mathbf{K}}}_{uu}$	submatrix - derivative balance of momentum with respect to displacements
$\underline{\underline{\mathbf{K}}}_{up}$	submatrix - derivative balance of momentum with respect to transport variables
$\underline{\underline{\mathbf{K}}}_{pu}$	submatrix - derivative transport equations with respect to displacements
$\underline{\underline{\mathbf{K}}}_{pp}$	submatrix - derivative transport equations with respect to transport variables
$\underline{\mathbf{r}}_u$	residual vector balance of momentum
$\underline{\mathbf{r}}_p$	residual vector transport equations

Indices

s	solid
l	liquid
g	gas
M	mixture
B	basic matrix
F	fibrous fraction
α, β	component
el	elastic
in	inelastic
pl	plastic
cr	creep
atm	atmospheric
tr	trial state
T	stress
A	inelastic strain
a_v	inelastic volume strain
f	yield condition

Other variables are defined in the context of their appearing.

1 Introduction

Municipal solid waste landfills are constructed to safely separate the disposed waste from the surrounding environment. Main component of such engineering constructions is the waste itself. The mechanical stability of landfills has to be guaranteed during the operation and in the aftercare stage. Further, the drainage system, gas wells or cover systems can be damaged or totally destroyed by the load impact of the landfilled waste. Slope failures are often connected with dramatic consequences. For instance, a 30 m high landfill slope collapsed after heavy monsoon rain in Manila, Philippines, in 2000 and the moving waste masses overwhelmed a residential area and its inhabitants. Thus, stability analyses of landfills are required in order to assess the risks concerning such accidents. In-situ measurements of settlements on top of the landfill body as well as of horizontal deformations together with experimental and theoretical investigations help to predict the future development during the operation and in the aftercare period. Numerical modelling of the deformation behaviour of the solid waste, of the transport of fluids and of the biochemical reactions occurring in landfills is a challenging task.
Advanced constitutive models describing the time-dependent stress-strain relations are vital for such analyses. In general, one distinguishes soil-like and non-soil-like wastes. Concepts developed in the field of classical soil mechanics can be adopted easily in static and dynamic analyses for wastes with properties similar to soils, e.g., excavated earths, sludges or ashes. In contrast, non-soil-like domestic, bulky and organic refuses and mixed deposits are much more inhomogeneous. Such wastes behave totally different from ordinary engineering materials. The high compressibility due to the large porosity and the degradation of organic matter cause large volume reductions over decades. Embedded fibrous constituents like textiles, cardboards, papers or foils act similar to a reinforcement and increase the strength of the material considerably. The emplacement of the waste in layers induces anisotropic conditions concerning the deformation behaviour as well as the transport processes because the fibrous particles orientate in a horizontal plane mainly. Although large strains are applied to waste samples in laboratory compressive and shear tests, no failure states are often reached. Due to the particle size and the compressibility carrying out of experiments is quite difficult. Variation of the particle size and spatial fluctuation of the properties complicates the modelling and the long-term prediction. Nevertheless, model equations are formulated in this thesis that include all major phenomena observed in-situ and in laboratory scale.

The influence of the liquids flowing through the pores requires special attention. Almost all large slope failures reported about in the literature are connected with changes in the pore water content. The water content inside a landfill is mainly influenced by climate conditions. Especially, heavy monsoon rain can besiege landfills in tropical areas. Thereby, some hundred millimetres of precipitation water infiltrate the landfill within few hours. Sometimes the deposition of very wet material is dangerous, too. Recirculation of leachate or an artificial irrigation are often part of modern operating strategies in order to accelerate the biodegradation of organic substances and the decay of long-term settlements.
Biodegradation of organic substances reduces the amount of the landfilled waste considerably and contributes to the large volume reduction and settlement observed in-situ. Thereby, microorganisms decompose carbohydrates, fats, proteins etc. in different stages mainly into methane and carbon hydroxide under anaerobic conditions. The chemical reactions are exothermic.

1.1 State of the art

Investigations concerning the mechanical behaviour and the transport and reaction processes inside a landfill are object of actual research. A comprehensive summary of engineering properties is provided by Dixon and Jones [27]. The section 'Umweltgeotechnik' (Environmental Geotechnics) of the 'Deutsche Gesellschaft für Geotechnik e.V. DGGT' (German Geotechnical Society) provides the GDA-recommendations for constructions of landfills and investigations of the behaviour of the dumped material.

Laboratory and in-situ observations Cowland et al. [16] report about a 6 m vertical trench cut in a six month old waste that did not fail during the whole investigation period. The landfilled material is classified as a mixture of construction waste and domestic refuses including sheet-like constituents. The surfaces of the cut-in are wetted in order to minimise matric suction effects of the pore water. A heavy rainfall of 240 mm rain does not influence the stability. Such observation of stable steep slopes over a long period are typical for municipal solid waste landfills. The stability of the slopes is explained by the activation of tensile forces carried by fibrous constituents allowing the characterisation of waste as a composite material comparable to reinforced earth structures.
Kockel [60] investigates the strength of waste in uniaxial and triaxial compressive tests and proves the influence of the fibrous particles experimentally. Thereby, the material is divided into a basic matrix including more grainy particles and into the fibrous fraction. Kölsch develops a test device in order to determine the strength of the fibrous fraction and the interaction with the surrounding basic matrix. BISHOP's slip circle method for

slope stability analysis is extended in order to capture the anisotropic reinforcement effect of the fibres.
A large number of one-dimensional approaches exists in order to predict the vertical settlement behaviour of landfills. A recent overview is provided by Liu et al. [71]. Thereby, a trend is recognisable to distinguish the dominating mechanisms - spontaneous deformation due to loading, time-depending settlements caused by mechanical creep as well as by biodegradation of organic matter following the municipal solid waste compression curve proposed by Grisolia and Napoleoni [42].
Pumping tests carried out in-situ provide a rough estimation of averaged hydraulic conductivity inside a landfill. Beaven [10] reports about more detailed investigations and proposes a dependency of the conductivity on the density of the solid material and on the vertical stresses, respectively. Münnich et al. [85] observe a similar behaviour in laboratory experiments and point out that the horizontal hydraulic conductivity is higher than the vertical by a factor of about ten. The anisotropy is caused by the orientation of the fibrous constituents in a horizontal plane hindering the vertical fluid flow.

Structural analysis Engineering methods for stability analysis and settlement prediction are useful tools for practical purposes, but a more detailed description concerning the deformation behaviour as well as the fluid transport and chemical reactions occurring in municipal solid waste landfills is object of international research. Aim of such complex approaches is to understand better the different processes and their interactions. Thereby, partial differential equations describe the mechanisms, which have to be solved under given initial and boundary conditions using numerical tools.
Ebers-Ernst [29] develops a constitutive model for municipal solid waste in the framework of large deformation theory assuming small elastic strains. The solid material is divided into the basic matrix and the fibres as proposed by Kockel [60]. An elasto-plastic model is applied in order to describe the shear failure mechanism for the basic matrix using the DRUCKER-PRAGER hypothesis. Time-dependent settlements are additionally included by an isotropic creep model. The fibrous constituents are described by a smeared approach applying an anisotropic elasticity model. It is assumed that the fibres carry tensile forces only and their strength is formulated in the framework of plasticity theory using a RANKINE criterion with hardening.
Lüke [73] also adopts Kockel's idea of splitting the material into two fractions. Thereby, an elasto-viscoplastic model is developed for the basic matrix within linear kinematics. Lüke applies HOOKE's law for the elastic branch, which is enclosed by a yield surface of cam-clay type with hardening. The flow rule is formulated on the basis of viscoplastic theory. A micromechanical based approach is used for the fibres modelling the behaviour of the single elements by elasto-viscoplasticity in order to limit their tensile and compressive strength. The interaction of the fibres with the surrounding basic matrix as well as the anisotropic orientation is included into the approach, too.

Machado et al. [75] propose an advanced constitutive model for municipal solid waste based on laboratory experiments. The authors consider waste as a mixture of fibrous elements consisting of plastics mainly and of a 'paste' composed by nonfibrous particles, e.g., rubber, organic matter etc. The behaviour of the fibres is modelled by ideal plasticity applying the von MISES yield criterion. The elastic strains are connected with the elastic strains of the 'paste' by an activation function. The stress-strain behaviour of the 'paste' is reproduced with a critical state line model using a cam-clay yield locus. YOUNG's modulus is formulated stress dependent. The total stresses of the mixture of the two components are equal to the sum of the partial stresses weighted by their volume ratios. A simple isotropic creep model is applied in order to describe time-dependent deformations applying a simple hyperbolic function with two parameters.
Wehnert et al. [104] report about investigations of the landfill Berg, Germany. Thereby, a finite element simulation predicts the further development of settlements of the existing landfill. The underlying constitutive model includes HOOKE's law for linear elasticity. The stresses of the material are limited by a multi-surface yield envelope formed by the MOHR-COULOMB criterion and a soft-soil creep model as cap. Modelling time-dependent settlements is included by viscoplastic flow for the cap. Only few model parameters are required due to the simplicity of the material model. Strength parameters are suggested to be constant and stiffness parameters are fitted on in-situ monitored deformations by back calculation.
McDougall et al. [80], [82] report about a coupled model for loading, creep, biodegradation and fluid transport in landfills. The model consists of three modules - one for the deformation behaviour, one for the unsaturated fluid flow and one for the biochemical processes. The modules interact in a sequential manner. The occurring deformations are divided into elastic and inelastic strains using linear kinematics. The inelastic strains are further decomposed into spontaneously plastic, viscoplastic and inelastic strains due to the degradation of organic matter. The stresses are connected with the elastic strains by a linear relation. A modified cam-clay model with hardening limits the shear stresses. Spontaneously plastic strains are produced if the stress state violates the yield condition. An isotropic creep law describes time-dependent deformation under constant load. Additionally, inelastic strains are produced by the decomposition of organic matter. The volume occupied by the degraded organics is added partially to the pore space and partially to the inelastic strains. The transport model describes the flow of landfill gas and leachate applying DARCY's law for unsaturated conditions using van GENUCHTEN relations in addition. Biodegradation is modelled in dependency on the moisture content.
A couple of models exist in order to describe the complex processes of biodegradation and fluid transport and their interactions inside landfills. For instance, White [106] develops a complex biochemical model further subdividing the organic matter into carbohydrates, fats and proteins. The partial differential equations of the transport

of fluids are numerically solved by the finite differences method. Kindlein et al. [59] report about a coupled model for transport and biodegradation using a reduced two reaction model applying a finite volume element based concept in the numerical treatment. Ricken and Ustohalova [91] couple fluid transport processes, biodegradation and deformation behaviour. They assume that the landfill gas can move free, whereas the water is immobile. The solid skeleton behaves elastically in their approach.

1.2 Goals of the thesis

Main goal of the thesis is to analyse the mechanical behaviour of landfills, which is considered as a porous medium. Liquid as well as gas flow through the voids of the solid waste. It is well-known from in-situ and laboratory observations that waste undergoes large irreversible deformations. Thus, the modelling approach requires the application of advanced kinematic relations in order to capture effects of geometrical nonlinearity. Further, the occurring of irreversible time-dependent deformations has to be included by physically nonlinear constitutive plasticity and creep models. An adequate framework for modelling the coupled processes is the *Theory of Porous Media*, which has to be discussed. The model equations for the fluid flow and the linear momentum of the mixture as well as appropriate initial and boundary conditions have to be provided.
Three-dimensional constitutive relations for municipal solid waste and for the fluids complete the model. Thus, the idea of considering solid waste as a composite material consisting of a granular basic matrix and a fibrous fraction, which is proven by Kockel [60] experimentally, is adopted in this thesis using the work of Ebers-Ernst [29] as basis. Such an approach enables the establishment of constitutive equations for the two solid fractions independently. The flow of the fluids through the pores has to describe unsaturated states including effects generated by the large compaction of the waste.
The coupled initial-boundary value problem has to be solved applying numerical algorithms. The displacement based finite element method is a standard tool for solid mechanical problems. In contrast, finite volume element based concepts are used for the fluid flow widely. Both methods have to be combined in this contribution solving the discrete problem simultaneously. The ordinary differential equations of the constitutive model must be integrated in time by a predictor-corrector algorithm for large strain plasticity.
Simulation of standard laboratory experiments shall verify the developed constitutive model for the solid waste. The identification of model parameters requires the usage of advanced techniques as genetic algorithms. Structural analyses show the applicability of the chosen approach investigating time-dependent settlements as well as discussing slope stability problems. Effects from interactions between solid deformation and fluid transport will be investigated for different model scenarios.

2 Geotechnical Description of Landfills

The essential properties of wastes are outlined, possible failure modes occurring in landfills are briefly sketched and common engineering methods for analysing landfill structures are summarised in the following section.

2.1 Classification Systems

The German GDA-recommendation E1-7 [25] provides an advanced system to identify and classify different types of waste in view of their geotechnical properties. Similar classification methods are used in international research, for instance, by Manassero et al. [77]. Important classification criteria are the origin, the composition, the kind of collection and transport as well as the structure and the arrangement of the particles. The first step in cataloguing on a landfill site is to record data about the state before emplacement concerning mass, volume, homogeneity and composition. Thus, the wastes are distinguished in following main groups

1. *Municipal solid waste:* domestic refuses from private households, bulky wastes, organic waste, waste from craft production and clearing sludges,
2. *Waste from building industry:* demolition rubble, wastes from construction sites, excavation residues and demolition debris of roads,
3. *Industrial waste:* waste from industrial production, e.g., sludges, ashes, slags, or other solid material, e.g., wood, paper, metal, plastic, rubber, textile,
4. *Mechanical-biological pretreated wastes.*

The assessment of the substantial composition is an important indicator for the mechanical behaviour of a waste and its biological stability. The classification of GDA-recommendation E1-7 orientates on technical and practical circumstances on a landfill site. The refuses are subdivided into four groups concerning the particle size. Sieving fractions with particle size of 40 - 120 mm, 8 - 40 mm and smaller than 8 mm are not quantified in detail. In contrast, particles larger than 120 mm are characterised in view of their substantial composition. Such analyses distinguish large particles composed of different components, paper and cardboard, soft and rigid plastic, metals, minerals, wood, organic matter and putrescible waste or sludges. A rougher classification is to

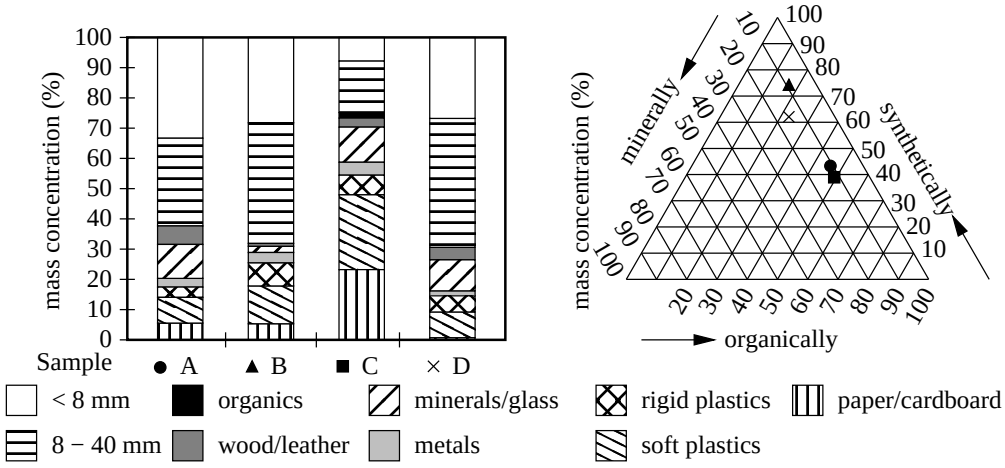

Figure 2.1: Substantial analysis of waste samples from [62]

divide into mineral, organic and synthetic substances only. Typical results of substantial analysis are shown in figure 2.1. The four year old waste A consists of domestic refuses and bulky particles, the waste B is composed by domestic refuses rotted for a period of eighteen month. The waste C consists on fresh domestic refuses from a residential area with separated collection of putrescibles. All three wastes are from Braunschweig, Germany. The waste D is domestic refuses from Freiburg, Germany, which is biologically pretreated under aerobic conditions. One can easily detect that the composition of the four waste samples varies in wide ranges. Untypically, they include only a small mass portion of degradable organic matter.
The description of the shape and size includes two criteria. The dimension of a single particle is identified by analysing its shape subdividing four groups

- Dim 0 - grain (no long side, diameter smaller than 8 mm),
- Dim 1 - fibre (one long and two short sides),
- Dim 2 - (two long and one short sides),
- Dim 3 - box (three long sides).

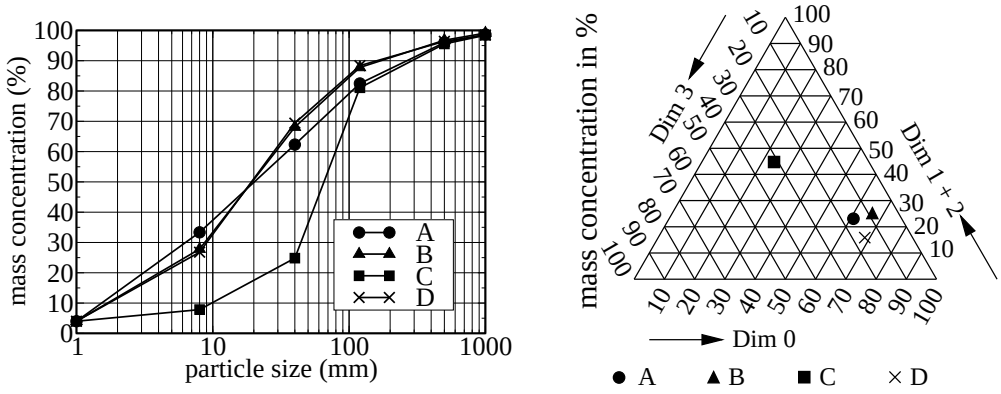

Figure 2.2: Particle size distribution and dimension analysis of waste samples from [62]

soil-like waste	non-soil-like waste
up to now deposed, untreated waste: - excavated earth - sludges - demolition debris of roads - residuals of combustion processes (slags, ashes, dusts) - demolition rubbles - clearing sludge	up to now deposed, untreated waste: - domestic refuses - bulky waste - biological refuses - industrial wastes - mixed waste from construction sites - other solids
waste under the requirements of the *TA Siedlungsabfall*: - residuals of combustion processes (slags, ashes, dusts)	waste under the requirements of the *TA Siedlungsabfall*: - mechanical-biologically pretreated waste

Table 2.1: Geotechnical classification of waste

The particles of group Dim 1 and Dim 2 can be merged into one group. The particle size distribution is determined using standard sieves with diameter of 8 mm, 40 mm, 120 mm for soil-like wastes. In addition, a visual distinction of particles larger than 500 mm and 1000 mm is necessary for non-soil-like material. The particle size analyses of the aforementioned described waste samples are plotted in figure 2.2. Sieve curves as well as the dimensional plot show considerable differences between the samples again. The GDA-recommendation E1-8 [25] allows a simple geotechnical classification in soil-like and non-soil-like wastes. Thus, the recommendation distinguishes untreated wastes and wastes, which fulfils the requirements of the *TA Siedlungsabfall* [53] concerning the biochemical stability. The different wastes are categorised in this scheme in table 2.1. Soil-like and non-soil-like wastes are landfilled together in most existing disposal sites. Analysing strategies and methods from soil mechanics can be adopted for soil-like wastes. In contrast, additional investigations are necessary for non-soil-like waste in order to describe the material correctly.

2.2 Mechanical properties of municipal solid waste

Acknowledgement about the deformation behaviour and about hydraulic properties is necessary in order to characterise the actual state and to forecast the future development of landfills. Investigations carried out in-situ and on laboratory scale are summarised in the following concerning the bulk density, the time-dependent settlements, the strength analysis as well as the influence of water and leachate.

2.2.1 Unit weights and densities

Waste density and bulk unit weight are key indicators to characterise the actual state inside a landfill. Since the waste composition differs considerably, the dry density of the solid material varies in wide ranges, too. Of course, the water content influences the density. The actual waste density depends on different factors. The transport and collection method as well as the kind of emplacement of the material influence the initial pore structure and the dry solid density. The influence of initial compaction during the emplacement is pointed out in table 2.2 for fresh waste investigated in the USA. Good compacted waste exhibits a higher density than poor compacted. Moderate and good compacted waste have higher mean values than samples from poor treated sites.

operation during emplacement	poor compaction	moderate compaction	good compaction
range (kN/m^3)	3.0 to 9.0	5.0 to 7.8	8.8 to 10.5
average (kN/m^3)	5.3	7.0	9.0
standard deviation (kN/m^3)	2.5	0.5	0.8
coefficient of variation (%)	48	8	8

Table 2.2: Statistical properties of bulk unit weight for fresh waste (Fassett et al. [33])

The density differs considerably for pretreated waste. Especially, the variation and inhomogeneities decrease by the treatment drastically. The waste density and bulk unit weight change in time after emplacement. For instance, the material is compacted and its dry density increases if an old waste layer is loaded by new fresh waste. On the other hand, the water content can decrease under such circumstances resulting in a lower wet density. Furthermore, biochemical reaction processes decompose organic substances into landfill gas and water, which run out of the landfill. Thereby, the volume occupied by the degraded particles is only partially compressed and new pore space can be created. The underlying biochemical processes and the interaction with the mechanical properties of waste are object of actual research work. The water content also changes in time due to transport and evaporation processes.
In general, it can be concluded that the values for bulk unit weight fluctuate considerably inside a landfill. Typically, the density is higher in deeper layers as illustrated by two presumed profiles shown in figure 2.3. Thereby, it is suggested that the density increases rapidly up to a depth of 50 m, and then a slight increasing is expected only. Measured bulk unit weights of international research are compared within table 2.3 pointing out that measured values vary from site to site.

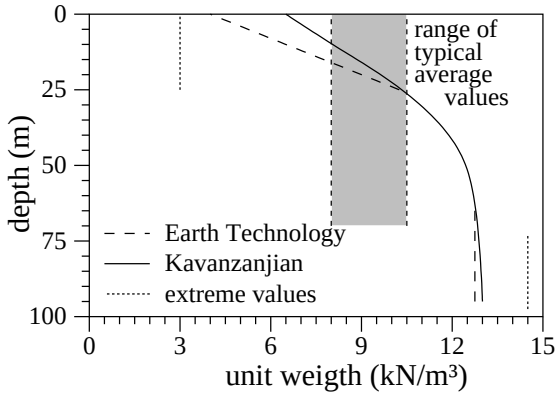

Figure 2.3: Typical density profile in landfills (redrawn after Manassero et al. [77])

country	measured bulk unit weights (kN/m^3)	references
UK	6 to 8	Watts and Charles [102]
Belgium	5 to 10	Manassero et al. [77]
France	7	Gourc et al. [40]
USA	6 to 7 (fresh) 14 to 20 (degraded / high % of soil-like)	Manassero et al. [77] Kavazanjian [56]
Canada	6.8 to 14	Landva et al. [66].
Germany	6.2 to 15.6 9.7 to 11.9 2 to 10 (untreated) 2 to 15 (pretreated)	Reuter et al. [90] Gertloff et al. [39] GDA-recom. E2-35 [37] GDA-recom. E2-35 [37]
Hong Cong	11.9 to 14.7	Cowland et al. [16]

Table 2.3: Comparison of bulk unit weights

2.2.2 Time-dependent deformation behaviour

Different mechanical processes as well as the biochemical degradation of organic matter result in time-dependent settlements, which can be observed and measured on top of a landfill only. According to Grisolia and Napoleoni [42], five different stages are distinguishable. Large reduction of macropores and rearrangement of deformable particles, which exhibit a micropore structure, cause initial deformations within few minutes after emplacement or loading. Creep and consolidation inside the deformable particles occur within few hours. Viscous behaviour of the solid skeleton as well as consolidation phenomenon in macropores proceed slowly and decay after months. Furthermore, the degradation of organic matter creates new voids, which collapse partially. A similar effect is generated by physico-chemical processes as solution, corrosion, oxidation or degradation of inorganic components. The developed theoretical municipal solid waste compressibility curve is plotted in figure 2.4.

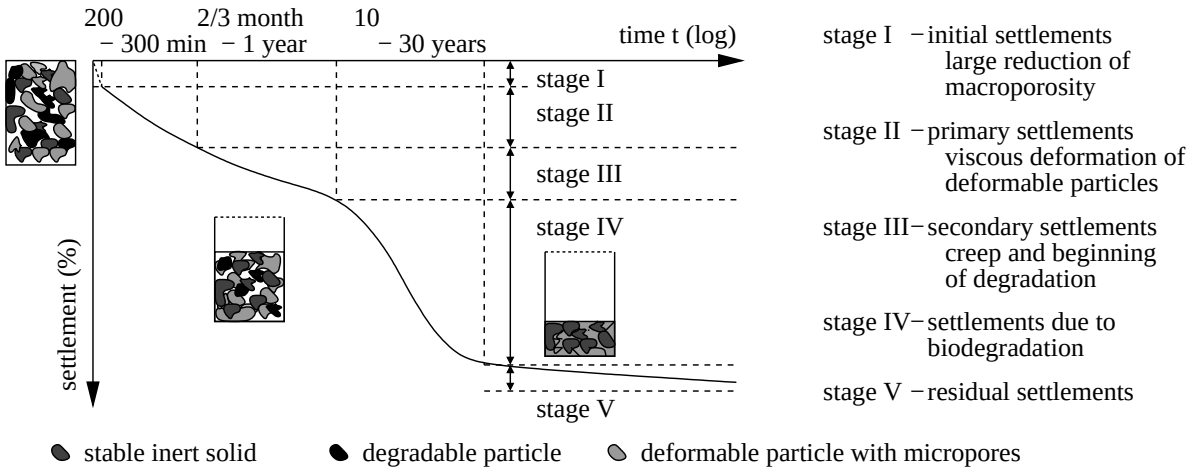

Figure 2.4: MSW compression curve redrawn from [42]

For practical assessments, GDA-recommendation E2-24 [25] provides a simple method distinguishing three settlement stages

$$
\begin{aligned}
s(t) &= s(\sigma) + s(c_{\alpha,k}) + s(c_{\alpha,l})\,, \qquad (2.1)\\
s(\sigma) &= p \int_0^{H_0} \frac{1}{E_c(\sigma(z))} dz\,, \qquad s(c_{\alpha,k}) = H_0\, c_{\alpha,k} \log\left(\frac{t_{i,k}}{t_{1,k}}\right)\,,\\
s(c_{\alpha,l}) &= H_0\, c_{\alpha,l} \log\left(\frac{t_{i,l}}{t_{1,l}}\right)\,.
\end{aligned}
$$

Load dependent settlements $s(t)$ occur in the first period of only ten days using a stress dependent constrained modulus E_c. Short-term creep settlements $s(c_{\alpha,k})$ are characterised by a small inclination in the half-logarithmic time-settlement curve using the compressive parameter $c_{\alpha,k}$. In contrast, accelerated deformations $s(c_{\alpha,l})$ are typically for long-term periods described by a second compressive parameter $c_{\alpha,l}$. The meaning of the different parameters is clarified in figure 2.5. The parameters are fitted on laboratory experiments as well as on in-situ measurements.

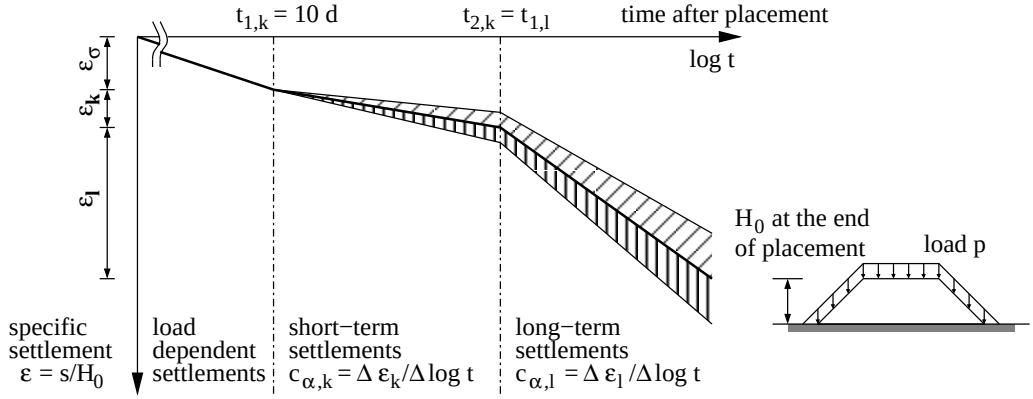

Figure 2.5: Idealised time-settlement curve of GDA recommendation E2-24 [25]

In a second approach of GDA-recommendation E2-24, the time dependent function is replaced by

$$s(t) = s_K \ \left(1 - c_K^t\right) + s_L \ \left(1 - c_L^t\right) \ . \tag{2.2}$$

The parameters s_K and s_L describe the final value of the short-term creep and the long-term creep period, respectively. The parameters c_K and c_L are additional model parameters.

A large number of one-dimensional approaches for prediction of settlements exist in the literature. The models differ mainly in the applied relations to describe the time-dependent part, e.g., power creep laws, bilinear, hyperbolic or logarithmic functions etc. Liu et al. [71] provide an overview of most important references. Nevertheless, a trend is noticeable to separate the different mechanisms - loading, mechanical creep and biodegradation. Among others, Marques et al. [78] present a rheological model describing the composite compressibility, which is shown in figure 2.6. The decomposition of deformation into initial compression, mechanical creep and biodegradation is expressed as

$$\frac{\Delta s_i(t)}{\Delta h_i} = C_c \ \ln\left(\frac{\sigma_0 + \Delta\sigma}{\sigma_0}\right) + \frac{\Delta\sigma}{b} \ \left(1 - \exp^{-c\,t_1}\right) + \frac{\Delta\sigma}{e} \ \left(1 - \exp^{-d\,t_2}\right). \tag{2.3}$$

The approach of equation (2.3) enables the subdivision of the landfill in several vertical layers having an initial height h_i, and therefore it captures the process of emplacement better. The parameter set can vary for each layer. Thereby, C_c describes the compressive ratio, σ_0 is the initial vertical stress and $\Delta\sigma$ the stress increment added at time t_1 in the layer under observation. The parameters b and c describe the mechanical creep using a Kelvin-Voigt element. The parameters d and e model the biodegradation beginning after emplacement of the investigated layer at time t_2 with a first order kinetic in the backround. The total settlement equals the sum of the contribution of all layers $\Delta s_i(t)$.

The aforementioned empirical approaches are simple in their structure and can be applied for practical purposes and prognoses very easily. But they have some fundamen-

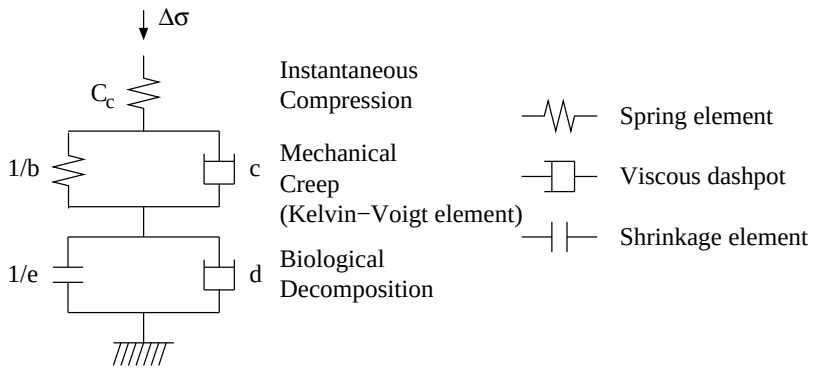

Figure 2.6: Rheological settlement model from Marques et al. [78]

tal disadvantages. First, simplified approaches work only one-dimensional. Thus, they cannot describe effects and displacements in horizontal direction. Furthermore, they use model parameter kept constant for any stage. Environmental factors as pH-value, temperature or water content influence the underlying biochemical processes during the degradation significantly. Thus, if the conditions change, e.g., after starting recirculation of leachate or construction of a final top cover, the biodegradation can increase, decrease or stop totally. Therefore, more sophisticated methods are required in order to describe better the governing mechanisms.

2.2.3 Strength analysis

The investigation of material strength is a key issue in the geotechnical description of waste. Laboratory experiments originally developed for granular materials as soils or concrete are applied and improved for the analysis. Compressive strength is obtained from uniaxial compressive tests. Shear resistance is measured in triaxial cell tests as well as in direct shear tests or direct simple shear tests. A large tensile test exists in order to characterise the behaviour under tension. The main difficulties for the investigators are caused by the particle size of waste and by the huge compressibility of the material. Thus, the test equipment has to be in an adequate ratio to the particle size distribution requiring test devices with larger dimensions as usually applied in soil mechanics. Further, the compressibility of the material often leads to such large deformations of the tested samples that a limit state is not reached although very large stretches are applied. As mentioned before, the composition of the samples varies in wide ranges and cause a wide spread of parameters. Thus, the reproducibility of experiments is given only for wastes having a similar substantial composition, particle size and particle dimension distribution. For the same reasons, carrying out in-situ tests is connected with heavy difficulties, too. Data published in the literature are only comparable among themselves with stringent carefullness because often not all required information about the tested waste as composition etc. is included into the report.

Compressive strength Kockel [60] carries out test series on untreated mixed municipal solid waste in order to investigate the compressive strength. The cylindrical samples exhibit an initial diameter of 540 mm and an initial height of about 1020 mm. The sample height is reduced by preconsolidation before starting the compressive test. The tests are load-controlled applying the vertical stress in different stages until failure or reaching a vertical stretch of 50 %. No limit state is reached for all three tests on untreated waste as shown in figure 2.7.
On the contrary, the vertical stresses on the actual sample cross sectional area increase considerably and the samples behave contractant. Thereby, the stiffness of the material

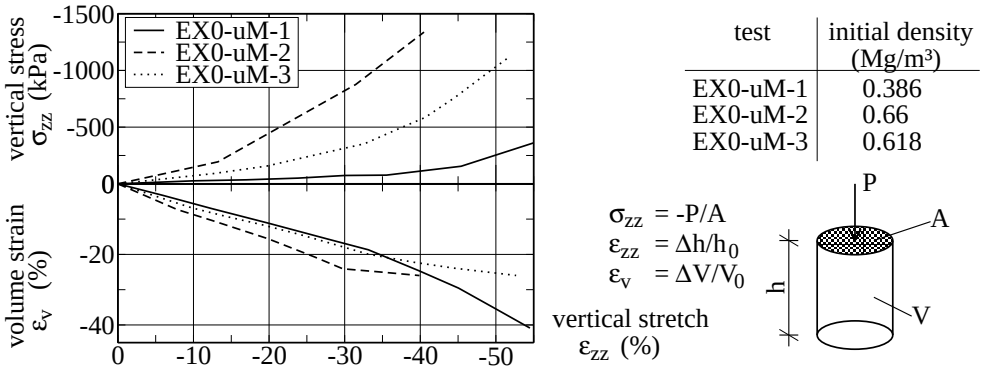

test	initial density (Mg/m³)
EX0-uM-1	0.386
EX0-uM-2	0.66
EX0-uM-3	0.618

Figure 2.7: Compressive tests on original municipal solid waste from Kockel [60]

increases, too. The sample with the highest initial density EX0-uM-2 achieves a stiffer path much earlier than the sample with the lowest initial density EX0-uM-1. Kockel recognises that the activation of reinforcement effects of larger particles contributes to this behaviour essentially. Therefore, the tests are repeated with a modified material after sieving out constituents larger than 120 mm consisting of plastics, textiles and wood mainly and possessing a sheet-like shape catalogued in Dim 1 + 2. Failure modes are reached for the modified material in four tests plotted in figure 2.8.

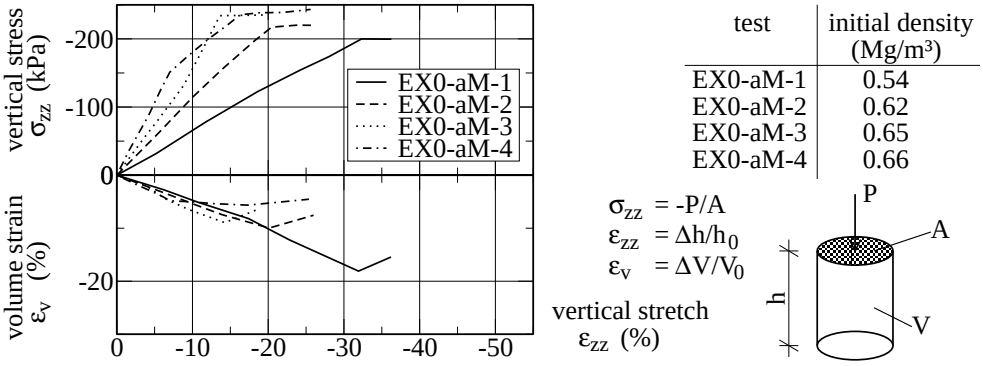

test	initial density (Mg/m³)
EX0-aM-1	0.54
EX0-aM-2	0.62
EX0-aM-3	0.65
EX0-aM-4	0.66

Figure 2.8: Compressive tests on modified municipal solid waste from Kockel [60]

Thereby, the maxima of applied vertical stresses are significantly lower than for the original material. The influence of the initial density is identical. Thus, the material fails by a lower vertical compression if the sample exhibits a higher initial density. The influence is not so apparently since only the density of samples EX0-aM-1 is marginally lower than the densities of the other three samples. Further, the material is compressed first, but behaves dilatant during the collapse. Thereby, cracks open at first, and then parts of the sample spall. Kockel assumes that plastic deformations in large shear bands develop at the beginning of the collapse.

Kockel contrives the model idea of a composite material for municipal solid waste in view of a geotechnical description. Thereby, the concept of reinforced earth is employed in order to explain the observed behaviour. In contrast to reinforced earth, in

which fibrous and sheet-like constituents with known mechanical properties are mixed in non-cohesive soils, the reinforcement elements cannot be separated out of the particle structure of municipal solid waste clearly. Kockel considers particles with one size larger than 120 mm as reinforcement elements only and subsumes all particles smaller than 120 mm into the basic matrix. The fibres are embedded into the basic matrix, see figure 2.9. But a significant portion of sheet-like particles exists also in the fraction with a particle size of 40 to 120 mm. They are able to carry tensile forces, too. Thus, Kockel interprets this tensile strength as cohesion of the basic matrix.

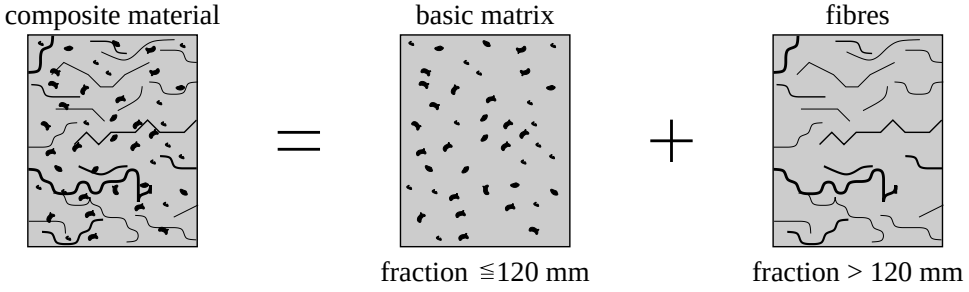

Figure 2.9: Composite model for municipal solid waste from Kockel [60]

Shear strength Shear resistance is analysed by Kockel [60] in triaxial tests using a test cell with a 300 mm diameter. A typical plot of the difference between averaged vertical and radial stresses versus the applied vertical stretch is shown in figure 2.10 on the left. Obviously, no limit state can be detected although the vertical stretch reaches the maximal value of 20 % for all four samples varying the radial pressure from 100 kPa up to 400 kPa. The material is densified only and no change in the stiffness occurs.

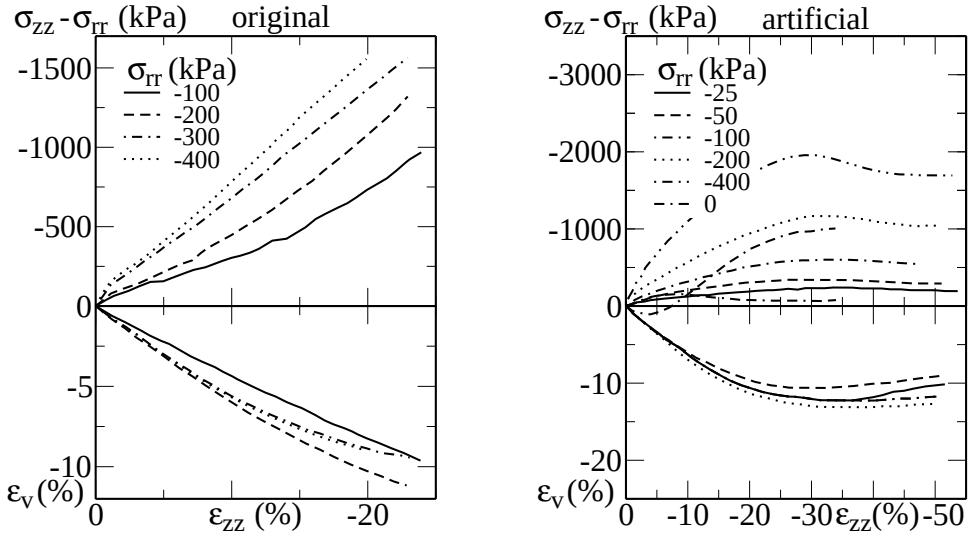

Figure 2.10: Triaxial compressive tests on original and artificial waste ([60])

Therefore, the test procedure is modified. The fibrous constituents are sieved out of the material. The remaining particles of the basic matrix are shredded to a particle size smaller than 15 mm. The fibrous constituents are hackled in such way that the dimensional ratio is conserved. Then, the samples can be investigated in a smaller triaxial cell with a diameter of 100 mm only allowing vertical stretches of about 50 % of the initial height of 200 mm. The test samples are isotropically loaded in a consolidation period of 16 hours. Afterwards, the samples are loaded under a constant vertical stretch rate of 0.2 %/min. Results of test samples consisting of the pure basic matrix are shown on the right of figure 2.10 varying the lateral compressive stresses from 0 to 400 kPa. Beside the uniaxial compressive test, the maximal deviatoric stress is reached at a vertical stretch of about 30 % for all other triaxial stress states. After reaching the maximum, the deviatoric stresses stay on a high level. The residual stresses are marginally smaller than the peak strength for lateral pressures of 200 and 400 kPa. The volume strains plotted in figure 2.10 in the lower part show that the material is not compressed after reaching the critical state. In contrast, the samples change to a dilatant behaviour indicating that the failure occurs. The maximum of deviatoric stress is reached for the uniaxial test by a vertical stretch of 8 % only. A distinct dilatant behaviour is observable due to the formation of cracks in the sample. Recapitulating the observations, Kockel draws the conclusion that the behaviour of the shredded basic matrix is comparable to a loose sand. Main difference is the high compressibility.

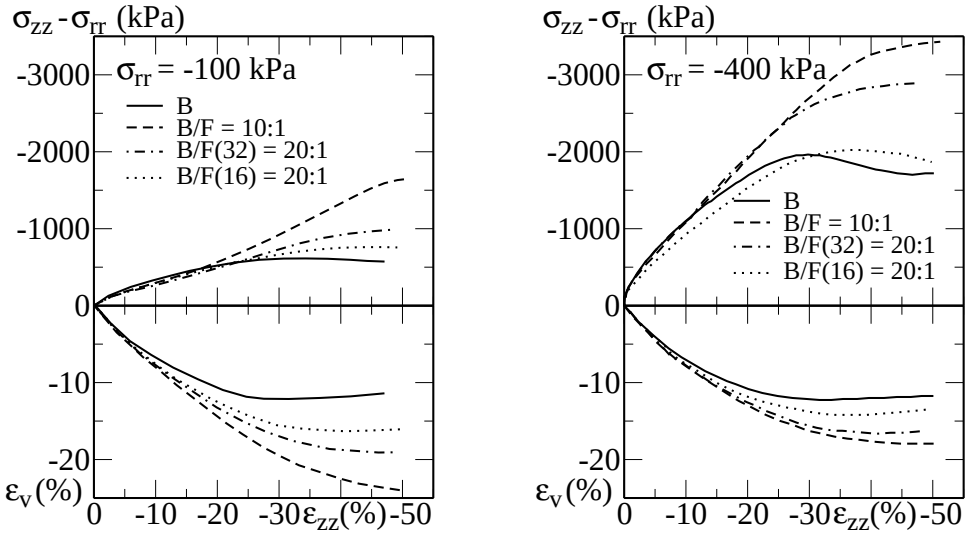

Figure 2.11: Triaxial compressive tests on artificial waste ([60])

The influence of the fibrous constituents is investigated in further tests series. Thereby, the mixture ratio between fibrous constituents and the basic matrix (mass ratio of 1:20 and 1:10) as well as the size of fibres (<32 mm and <16 mm) is varied. Plots of the obtained curves are shown in figure 2.11 for radial pressures of 100 and 400 kPa, respectively. Again, a critical limit state occurs for all test samples. The vertical stretch

at the maximum of deviatoric stress is higher if more fibres are mixed in. The volume change behaves in a similar manner compared with the tests of the pure basic matrix. Kockel derives shear parameters for the MOHR-COULOMB failure criterion from the triaxial shear tests, which depend on the vertical stretch. The outcome of his work supports the development of GDA-recommendation E2-23 [25], which emphasises the usage of different values for the shear parameters in different zones of the landfill for slope stability analysis with slip circle methods.
Grisolia and Napoleoni [43] also report about triaxial compressive tests on artificial reconstructed waste. The used triaxial cell has an initial height of 600 mm and a diameter of 250 mm. The material is emplaced in 10 layers and compacted to an initial unit weight of 6 to 7.4 kN/m^3. The tests are performed after a consolidation period of 24 hours varying the lateral pressure in the range of 50 to 300 kPa. Typical plots of vertical stress versus the vertical stretch are shown in figure 2.12. Similar to the tests of Kockel, no failure state could be reached. In contrast, the material is compressed at the beginning and with ongoing deformation the stiffness increases drastically. Grisolia and coworkers conclude that no plastic shear deformations occur in the tested waste material. But Kavazanjian [56] suggests that data from triaxial test should be handled with care because the test starts from an isotropic stress state. Thus, most of the occurring deformation is caused by the vertical compression before a state is reached, which coincides with in-situ conditions.

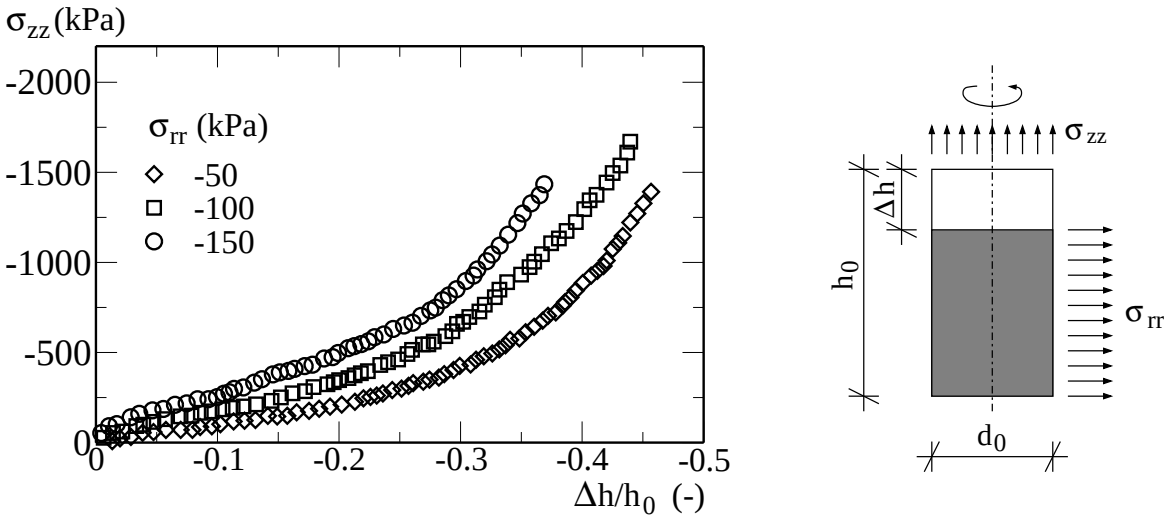

Figure 2.12: Triaxial compressive tests on reconstructed waste [43]

Kavazanjian et al. [57] report about direct shear tests and direct simple shear tests in a large test equipment with a diameter of 460 mm for a waste characterised in general as soil-like material. The samples are reconstituted removing particles larger than 100 mm. Thus, the material is similar concerning its size with the basic matrix of the

references	shear parameters		comment
	cohesion c' (kPa)	friction angle ϕ' (°)	
Kockel	7	38	reported by Gay
Kockel	10	15	back analysis by Spillmann
Kockel	10	17	back analysis by Spillmann
Jessberger	0	30	estimation from field observations
Jessberger	0	40	estimation from field observations
Kockel	7	42	simple shear, Gay, 9 month old waste
Kockel	28	26,5	simple shear, Gay, fresh waste
Fassett	10	23	suggestion by authors
Kölsch	15	15	suggestion by author
Kölsch	18	22	suggestion by author
Cowland	10	25	back analysis
Del Greco	15.7	21	direct shear, baled waste, lower density
Del Greco	23.5	22	direct shear, baled waste, higher density
Landva	19	42	direct shear, old refuse
Landva	16	38	direct shear, old refuse
Landva	16	33	direct shear, old refuse
Landva	23	24	direct shear, fresh, shredded refuse
Landva	10	33.6	direct shear, mixture wood and refuse
Kavazanjian [57]	0	30	direct simple shear, shear zone in layer interface
Kavazanjian [57]	16.3	33	direct simple shear, shear zone inside waste, lower bound
Thomas et al. [97]	22	28.2	direct shear

Table 2.4: Shear parameters taken from [27] with supplementation

test series of Kockel. The experimenters obtain an internal friction angle of 31° and a high cohesion of 43 kPa in direct shear tests. Further, they observe that samples with higher content of non-soil-like particles exhibit a higher strength. The tested material is subjected to monotonic as well as cyclic loading in direct simple shear tests in order to evaluate the large strain behaviour and the damping characteristics. Values for the shear parameters are derived from the tests in different kind. The authors calculate the friction angle to 30° under the assumption of failure in the interface between different layers and the friction angle to 33° and cohesion to 16.3 kPa as a lower bound for failure in the plane within the maximal principal stress ratio.

Del Greco and Oggeri [23] carry out large direct shear tests on baled municipal solid waste. Thereby, the shear band is predetermined by the interface between two vertical piled up bales. The shear parameters are assessed to 16 kPa for the cohesion and 21° for the friction angle for a waste with a density of 0.5 Mg/m^3. The shear parameters increase up to 24 kPa for the cohesion and to 22° for the friction angle for a density of

0.7 Mg/m^3. In addition, tests of waste bales on a HDPE-geomembrane and on gravel soil are performed. Furthermore, the equipment is used to determine the shear resistance between a clay layer and a HDPE -geomembrane.
Direct shear tests are also performed by Thomas et al. [97]. The material is emplaced in a large shear box with a basic area of 1000x1000 mm and a total volume of 0.7 to 2 m^3. Shear parameters are determined by an applied deformation of 100 mm to 18.2° for the friction angle and 22 kPa for the cohesion, respectively.
Table 2.4 summarises values for the shear parameters published in the literature that are determined by laboratory experiments as well as from back calculations of slope failures.

Tensile strength Kölsch [62] suggests that the idealisation of municipal solid waste to be a purely frictional material is not valid in general. The waste should be considered rather as a loose agglomeration of solid particles, in which fibrous and sheet-like constituents are embedded. The fibrous constituents are orientated in a horizontal layer predominantly observed also by Cowland [16] in-situ and Langer et. al. [67] in compressive tests. Kölsch separates the effects of the fibrous reinforcement from the frictional behaviour of the granular components of the basic matrix in the load bearing model of the composite material. The main mechanisms are illustrated in figure 2.13.

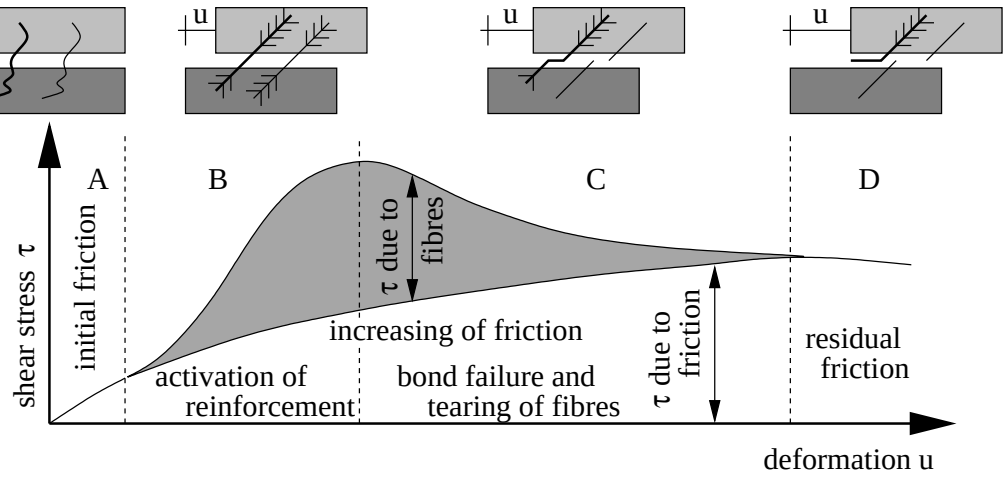

Figure 2.13: Idealised bearing model of Kölsch [62]

The fibrous constituents are still limp and only frictional effects are activated in a first stage A during shearing. Then, the tensile forces in the fibres are activated and lead to a considerable increase of the overall shear resistance in the second stage B. While the frictional bearing capacity reaches a maximum in the third stage C, the fibres exhibit a softening behaviour resulting in a significant decrease of overall shear strength. Two mechanisms exist, which are responsible for the decrease of tensile forces carried by the fibres. First, the fibres can be pulled out of the surrounding matrix material reduc-

ing the length of their anchorage and the transferred forces. Further, the strength of single fibres may be exceeded and the fibres tear themselves. Then, the residual shear resistance of the frictional components is still active in a final stage D only because all reinforcement effects are destroyed.
Kölsch develops the equipment for a large tensile test in order to quantify the tensile strength of municipal solid waste. The waste is emplaced in several layers up to a final height of 1500 mm in a test box with a base area of 1000 x 3000 mm in order to reproduce anisotropic in-situ conditions. At first, the material inside the box is loaded vertically. After decaying of time-dependent consolidation settlements, the box is split into two parts. Then, the tested material is subjected to tensile stresses by pulling one half of the box and increasing the horizontal deformation slowly until the applied tensile force reaches a maximum. After unloading, the next step commences by increasing the vertical load. A typical tensile force versus horizontally tensile displacement curve is shown in figure 2.14. The vertical pressure changes from -97 kPa in the first stage, to -199 kPa in the second stage and finally to -282 kPa in the last stage. The applied tensile force increases for all three stages slowly. The reinforcement effects are destroyed in the last test manifesting in ongoing of softening.

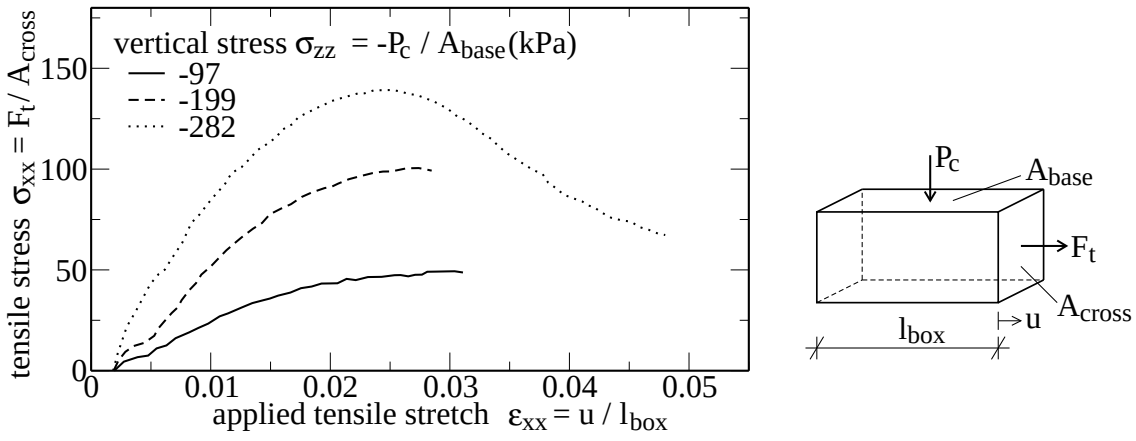

Figure 2.14: Tensile test on waste after Kölsch [62]

Kölsch introduces the concept of load-dependent tensile strength using the results of the tests. Thereby, it is assumed that the maximum of tensile forces is decomposed into a load independent and a load dependent part described by a linear relation between tensile force and vertical load as outlined in figure 2.15. The specific strength of the fibrous constituents is reached at a critical vertical load and further increasing of vertically compressive stresses does not increase the tensile strength anymore. For practical investigations, GDA-recommendation E2-29 [36] provides an extended method based on the results of Kölsch. Thereby, BISHOP's conventional slip circle method for slope stability analysis is enlarged by an additional term in order to include the effects of the fibrous reinforcement.

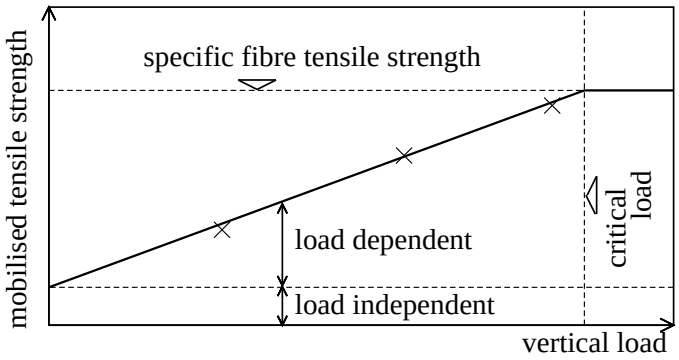

Figure 2.15: Tensile test on waste after Kölsch [62]

2.3 Hydraulic properties

The same difficulties as in the description of compressibility and strength exist for the investigation of hydraulic properties of municipal solid waste. The hydraulic conductivity is strongly connected with the amount of pores inside the solid waste skeleton. But waste consists of particles with a stable microstructure incorporating no or only a small quantity of voids and of particles with a particular microstructure. Voids, which are initially closed and do not interact with the flow of landfill gas and leachate, can be opened if the solid matter around crushes due to the loading or if particles degrade in biochemical or physiochemical processes. Young [107] describes the fluid flow through the waste skeleton by a double porosity model as illustrated in figure 2.16. Thus, the free water is defined to be in the larger interparticle crevices. In contrast, immobile bound water is mainly situated in the micropores inside of solid particles.

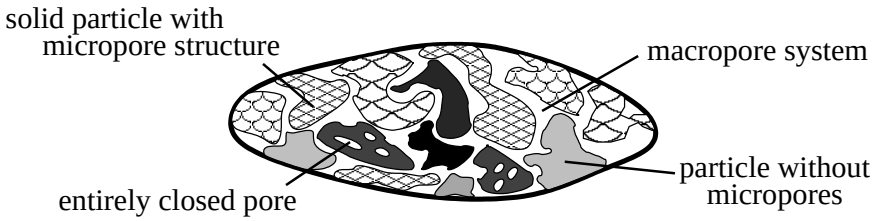

Figure 2.16: Microscopical view of pore system in waste

In the literature, few data are only published for porosity and for drainable porosity designated also as specific yield, which is the available pore space for the fluid flow. Münnich and Collins [84] determine pore volume fractions of 0.45 to 0.75. Scheelhaase et al. [93] list values in the range between 0.49 and 0.58 for pretreated waste. Hjelmar et. al [52] assume a low value of only 0.30 in a scenario investigation. Beaven [10] summarises values from the literature for the specific yield of 15 to 20 % for waste density of 0.9 Mg/m^3 and 40 % for density below 0.5 Mg/m^3. Obviously, porosity and unit weight are in strong dependency.

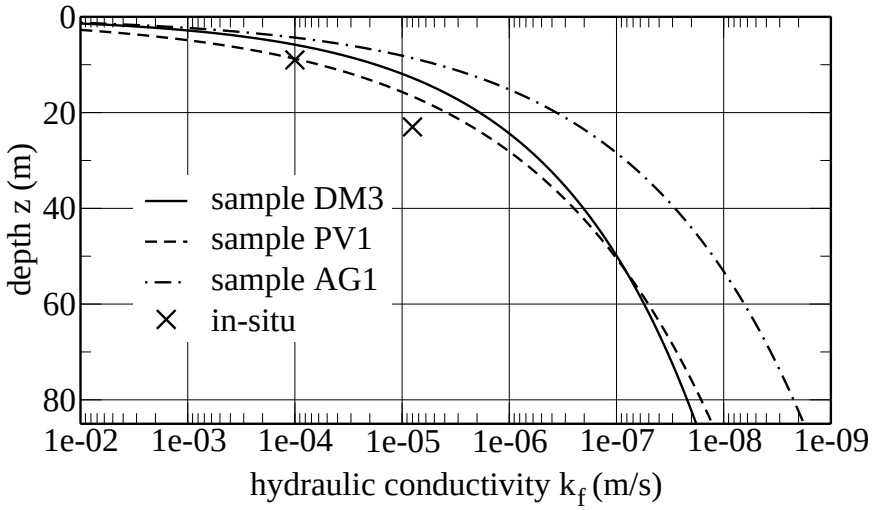

Figure 2.17: Relationship between hydraulic conductivity and landfill depth after Beaven [10]

In general, a specific part of the voids is filled with water described by the water content usually defined as the mass ratio between water and the dry mass of solid waste. Sometimes, the water content is alternatively defined as the mass of water related to the sum of mass of dry solid waste and water together. Furthermore, the water content can be introduced as volume fraction, too. The initial water content depends on the climate conditions during emplacement. After landfilling, the water content can increase due to absorption of free water by papers, cardboards, textiles and other particles or decrease due to evaporation. Beyond a certain limit of the content, the water can move free inside the solid skeleton due to gravity. A groundwater table may exist if the landfill basis is not drained or if a layer with low permeability inhibits the water flow. The field capacity is used to describe the absorptive capacity of waste analogous to the specific retention in hydrology as mass or volume ratio. Münnich and Collins [84] report about investigations in a landfill measuring water contents in borehole samples, which vary from 30 to 62 %. Further, they do not detect any relation between depth and water content. In contrast, the water content fluctuates without any regularity.
Variations in a wide range are also measured for the intrinsic or absolute permeability K_{abs}, the portion of hydraulic conductivity k_f that is representative for the properties of the porous medium. Conductivity and intrinsic permeability of the aquifer are related by the dynamic viscosity μ and the physical density $\tilde{\rho}$ of the fluid and the gravity b by means of

$$k_f = \frac{\tilde{\rho}\, b}{\mu} K_{abs}. \tag{2.4}$$

Usually values for the hydraulic conductivity k_f of water flow are reported in the literature. They are determined in-situ by pumping tests or under laboratory conditions in permeability tests. For instance, Landva and Clarke [66] measure coefficients k_f of

1 x 10^{-5} to 4 x 10^{-4} m/s. Beaven [10] reports about pumping tests in 9 m depth carried out in 1985 and obtains a hydraulic conductivity k_f of 1 x 10^{-4} m/s. The tests are repeated in 1994. The height of the landfill increases meanwhile so that the investigated layer is overburdened by 23 m waste and much more compacted. Thus, the hydraulic conductivity decreases to 8 x 10^{-6} m/s.
In an extensive laboratory program, Beaven [10] develops functional relations between hydraulic conductivity and effective vertical stress $\sigma_{e,v}$, which are related theoretically to the landfill depth z as well as to the density at field capacity ρ_F

$$\begin{aligned} k_f &= 2\,(-\sigma_{e,v})^{-2.71} \quad \text{with } \sigma_{e,v} \approx -(3.8\,z)^{1.19} \approx -(2.2\,\rho_F)^{6.4} \text{ for DM3,} \\ k_f &= 65\,(-\sigma_{e,v})^{-3.40} \quad \text{with } \sigma_{e,v} \approx -(3.4\,z)^{1.16} \approx -(2.6\,\rho_F)^{7.3} \text{ for PV1,} \\ k_f &= 36\,(-\sigma_{e,v})^{-3.34} \quad \text{with } \sigma_{e,v} \approx -(7.5\,z)^{1.10} \approx -(1.2\,\rho_F)^{11} \text{ for AG1.} \end{aligned} \tag{2.5}$$

The sample DM3 is composed as a typical fresh domestic refuse. The sample PV1 is a pulverised material passing a 150 mm filter removing heavy particles and putrescibles. Finally, the sample AG1 is an old in 1960's landfilled mixture of soil, crude and pulverised municipal solid waste. The suggested decrease of hydraulic conductivity with ongoing depth is found out in the experiments and plotted in figure 2.17. Thus, the experiments indicate a considerable change of the conductivity due to vertical loading and to densification. Furthermore, the degraded old waste of sample AG1 has a significant lower permeability compared to the fresh waste. The results confirm the aforementioned in-situ measurement of Beaven [10].

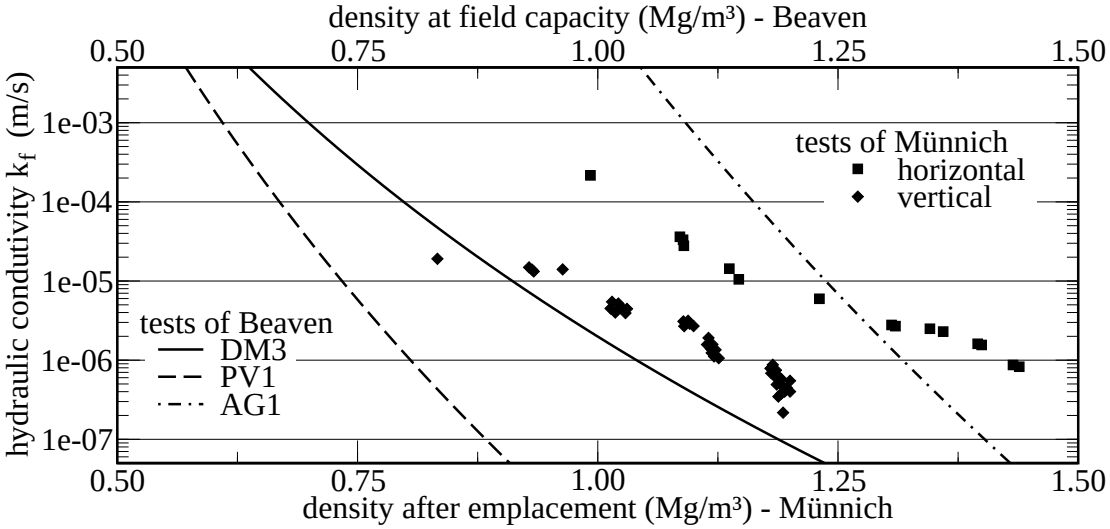

Figure 2.18: Experimental relation between hydraulic conductivity and density

A similar dependency is published by Münnich et al. [85] plotted in figure 2.18. Thereby, a considerable decrease of hydraulic conductivity is experimentally determined by ongoing densification of the solid waste, which corresponds well with the functional relations for the three test cells of Beaven. Furthermore, Münnich emphasises the difference of hydraulic conductivity in horizontal and vertical direction. The

conductivity in horizontal direction exceeds the vertical by a factor of about ten. The anisotropy depends on the texture of the solid skeleton generated by the emplacement in relatively small layers and by the vertical compaction. Thereby, sheet-like particles like papers or plastics orientate mainly horizontal and form a barrier for vertical flow. Beaven provides an overview of measured hydraulic conductivity published in the literature, which is supplemented in table 2.5. Perched leachate is often present above low permeable layers. Summarised, there are anisotropic conditions inside a landfill and it exists a strong correlation between waste density and hydraulic conductivity, which has to be taken into account for an advanced description of the landfill behaviour.

references	hydraulic conductivity k_f (m/s)	comment
Field tests		
Lloyd	4-5.5x10^{-5}	boreholes in landfill
EMCON	1-.5x10^{-4}	field permeameter in 10 year old waste
Colden	2x10^{-2}	-
Landva.	4x10^{-4} to 1x10^{-5}	-
Townsend	3-4x10^{-8}	-
Oweis	2.4x10^{-5} to 9.4x10^{-6}	density 0.68 Mg/m^3
Beaven	1x10^{-4} to 8x10^{-6}	pumping test, repeated after 9 years
Burrows	2.2x10^{-5} to 3.9x10^{-7}	pumping test, repeated after 9 years
Gawande [38]	2.5x10^{-5}	back calculation of field test
Laboratory tests		
Chen	1x10^{-4}	dry density 0.24 Mg/m^3
	1x10^{-7}	dry density 0.72 Mg/m^3
Fungaroli	1x10^{-4}	wet density 0.10 Mg/m^3
	1x10^{-6}	wet density 0.35 Mg/m^3
Korfiatis	1x10^{-4}	wet density 0.88 Mg/m^3
Landva	6.8x10^{-5}	vertical stress 20 kPa
	6x10^{-9}	vertical stress 400 kPa
Oweis	1.5x10^{-5}	wet density 0.57 Mg/m^3
	7x10^{-6}	wet density 1.14 Mg/m^3
Bleiker	1x10^{-5}	dry density 0.5 Mg/m^3
	5x10^{-9}	dry density 1.2 Mg/m^3
Chen	9.5x10^{-4}	wet density 0.16 Mg/m^3
	5x10^{-7}	dry density 0.48 Mg/m^3
Münnich [85]	9x10^{-3} to 2x10^{-6}	horizontal, dependent on density
	9x10^{-4} to 9x10^{-7}	vertical, dependent on density

Table 2.5: Hydraulic conductivity taken from Beaven [10] with supplementation

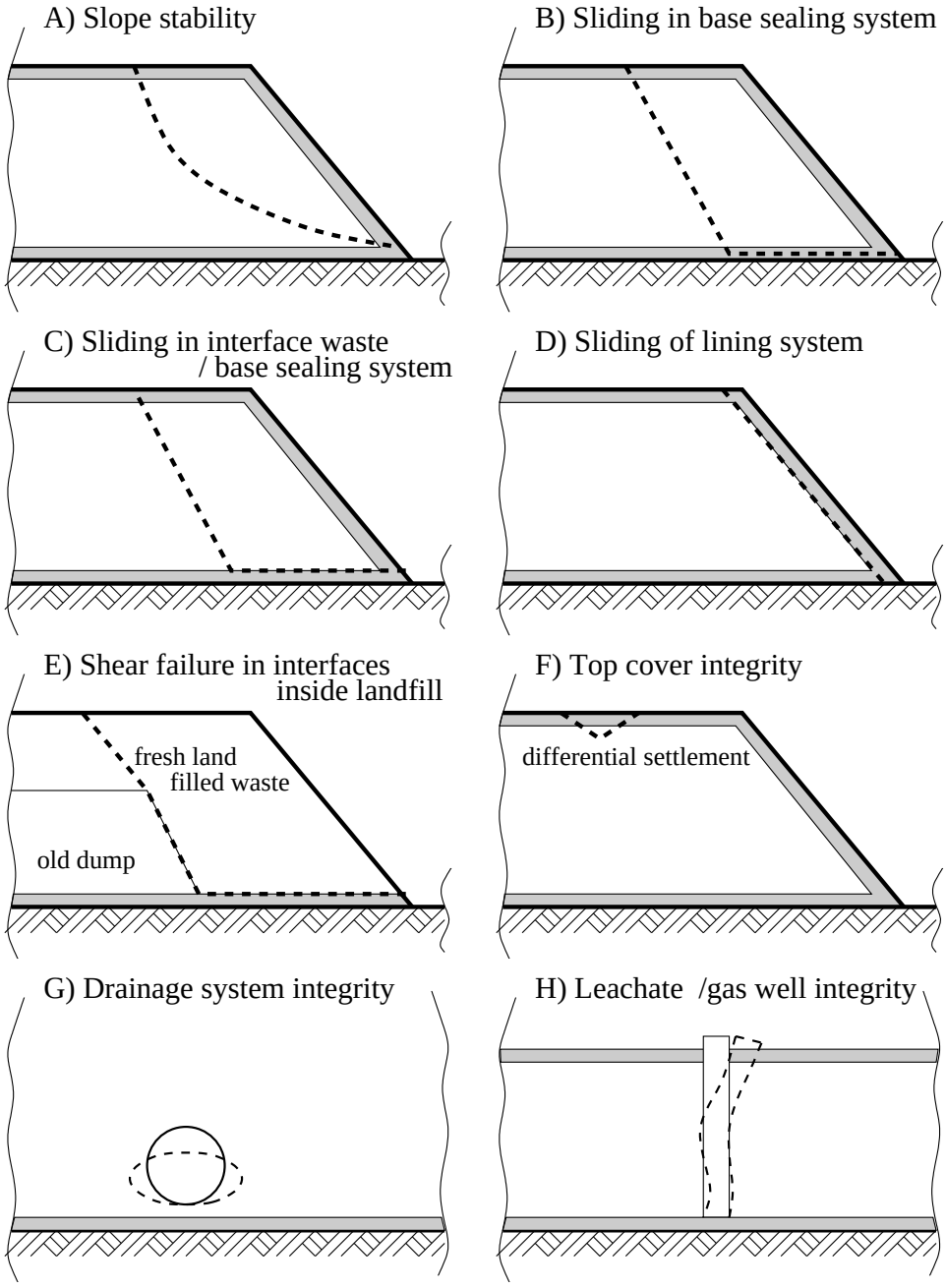

Figure 2.19: Typical failure modes

2.4 Failure modes

In general, the stability failure of landfills can be basically distinguished into two classes - failure mechanisms including only the dumped waste and failure mechanisms including the lining system in addition. Furthermore, the integrity of drainage system or of leachate and gas wells can be destroyed. Differential settlements can cause holes

in the top cover system and affect the serviceability limit state, too. Some typical potential failure modes are illustrated in figure 2.19. Both classical slope failure and block sliding can occur. Due to the technical construction of the landfill special attention has to be spent on avoiding sliding mechanisms, which includes the lining system. A soft geosynthetic membrane is integrated in a complex structure of drainage and barrier layers. The interfaces between the different materials inside the lining system and to the waste are often weak points. Finally, the waste is dumped at different times on a landfill site. Thus, old landfilled waste is covered by a thin layer consisting of soft clay to avoid infiltration of precipitation water. In some countries, it is common practice to build in a thin daily cover. If new fresh waste is deposited on this older material, the interface between both zones has often a lower shear resistances and forms a predetermined sliding joint.

2.4.1 Slope failure events

Large failures of landfills are not common, but they occur occasionally. Koerner and Soong [61] discuss ten landfill failures, which are summarised in table 2.6. The lining system is involved in half of the accidents. The authors suggest for an initially stable situation the geometry of the landfill as well as geotechnical parameters, e.g., density profiles, shear strengths of the dumped material by back calculation with conventional slip circle method etc. Then, the factor of safety is assessed by applying a supposed triggering mechanism using information from the failed site. Thereby, the factor of safety decreases usually below a value of 1.0 indicating a non-stable situation. The existing pore water plays a crucial role in most of the investigated failures. The increase of leachate head originates from different influences. Environmental conditions like heavy rainfall, problematic built-in of extremely wet waste, phreatic raise about low permeable clay layers or an aggressive leachate insection for clearing the water in a special case are announced. Usually, the amount of moved waste is huge and includes a multiple of 100,000 cubic metre.
Some special attention should be dedicated to landfill failures in developing countries. There, badly operated landfills are often situated inside residential areas. If a large failure happens, the moving waste masses overwhelm houses and bury their inhabitants. A deplorable example is the failure of the Payatas landfill in Quezon City, Philippines, in 2000. Thereby, the flowing waste killed at least 278 persons, while 80 to 350 people are missed. Causing mechanism for the slope instability including the subsoil is investigated by Kavazanjian and Merry [58]. In the two weeks prior the failure, two typhoons had besieged the metropolitan area of Manila. Thus, the investigators suppose a significant contribution of leachate flow, pore pressure of landfill gas as well as excess pore water pressure induced by the heavy precipitation. A similar accident occurred in Bandung, Indonesia, in 2005. Kölsch [63] reports about it in detail. Thereby, a debris

location	year	type of failure	involved quantity m^3	triggering mechanism
Excluding lining system				
N. America	1984	single rotational	110,000	3-day rain with phreatic raise from 0.0 m up to 3.2 m
N. America	1989	multiple rotational	500,000	120 mm rain in 10 days trench excavation near toe
Europe	1993	translational	470,000	leachate level build up
N. America	1996	translational	1,110,000	buildup of leachate head due to ice formation at exposed waste near toe
N. America	1997	single rotational	100,000	increasing leachate head on clay layer behind trench back-filled with clayey material
Including lining system				
N. America	1988	translational	490,000	excessive wetness of clay component of liner system
Europe	1994	translational	60,000	excessive wetness of clay component of liner system
N. America	1997	translational	100,000	progressively increasing wet of bentonite layer
Africa	1997	translational	300,000	placement of excessive liquid waste on old saturated waste
S. America	1997	translational	1,200,000	increase of leachate head due to aggressive leachate injection

Table 2.6: Summary of ten landfill failures [61]

flow consisting of 2.7 million cubic metre waste destroyed a small village and killed 147 inhabitants. The waste was originally disposed up to an height of approximately 60 to 70 m in a valley cut-in. The waste was poorly compacted and inside the landfill uncontrolled combustion processes took place. Before the landslide a three day tropic rainfall besieges the area. Kölsch presumes that the combustion of plastic and textiles reduces the tensile strength and the translational sliding mechanism was initiated by increase of pore water content and wetting of the underlying clayey subsoil.

3 Continuum Mechanical Framework

As already mentioned, municipal solid waste landfills are structures consisting of a porous skeleton, in which leachate and gas flow through the voids of the landfilled solid matter. The *Theory of Mixtures* and its special form the *Theory of Porous Media* described in detail by Bowen [15], de Boer and Ehlers [22] or Lewis and Schrefler [70] are an adequate mechanical framework to analyse processes occurring in such multi-component medium. The large displacements and the large irreversible deformations of the solid waste require the application of an advanced kinematic description, which is presented in the following together with the general mechanical balance laws and principles.

3.1 Theory of Mixtures and Theory of Porous Media

The constituents - phases or components - containing particles of the same physical state of aggregation are introduced in order to develop the mechanical model for municipal solid waste. The solid phase is indicated by the index 's', the pore liquid by the index 'l' and the landfill gas by the index 'g'. In contrast, the whole mixture of the three phases is designated by 'M'. The observations in a sufficient large volume, the representative elementary volume, in which all constituents are distributed representatively in a statistic sense, yield after averaging of all relevant physical quantities to the macroscopic model of superimposed continua. Thereby, it is assumed that each of the constituents exists on every material point at the same time. Hassanizadeh and Gray [46], [47], [48] describe in detail the averaging process for multicomponent systems. The process of homogenisation is illustrated in figure 3.1.
A constituent occupies in a microscopic consideration a certain part of the representative elementary volume described by the scalar field

$$n^\alpha = \frac{\mathrm{d}v^\alpha}{\mathrm{d}v} \qquad \text{for} \quad \alpha \in \{s, l, g\}\,. \tag{3.1}$$

The ratio n^α in equation (3.1) is the volume fraction. The saturation condition is a natural restriction due to the fact that all three constituents have to fill out the whole

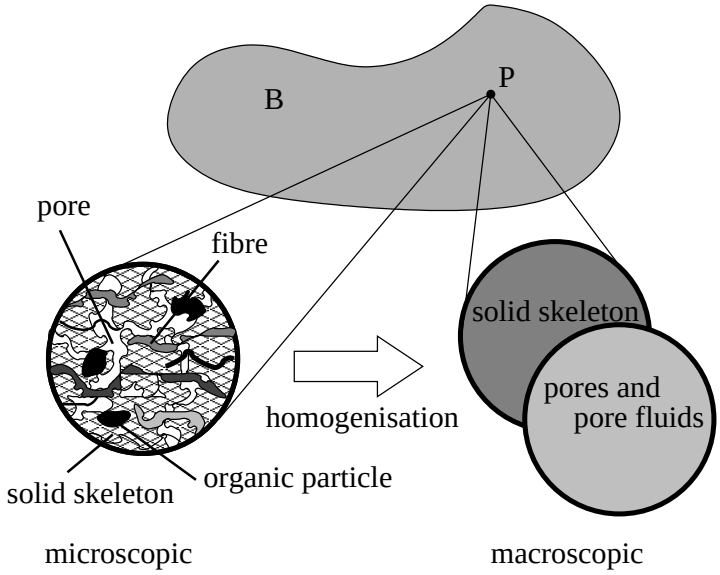

Figure 3.1: Homogenisation and macroscopic model

space of the representative elementary volume

$$\sum_{\alpha} n^{\alpha} = n^{s} + n^{l} + n^{g} = 1\,. \tag{3.2}$$

The sum of the volume occupied by the two fluids, landfill gas and leachate, coincides with the pore space Φ

$$\Phi = n^{f} = n^{l} + n^{g} = 1 - n^{s}\,. \tag{3.3}$$

Saturation functions S^{β} describe the filling of the pores with the two fluids

$$S^{\beta} = \frac{\mathrm{d}v^{\beta}}{\mathrm{d}v^{l} + \mathrm{d}v^{g}} = \frac{n^{\beta}}{n^{f}} \qquad \text{for} \quad \beta \in \{l, g\}\,. \tag{3.4}$$

Again, it is easily to detect that for all points a second saturation condition holds true

$$\sum_{\beta} S^{\beta} = S^{l} + S^{g} = 1\,. \tag{3.5}$$

In classical soil mechanics the term 'fully saturated' medium is used if all pores are filled out by only one liquid ($S^{l} = 1$), e.g., water or oil.

3.2 Kinematic description

Essential kinematic relations are briefly summarised for finite deformation analysis in this section. Textbooks about continuum mechanics, e.g., from Haupt [49], or Greve [41] contain a more detailed description and include proofs of most statements and conclusions used in the following. The tensorial notation follows widely the textbook of de Boer [19].

3.2.1 Motion

The particles of the three constituents identified by the number triple $x^{\alpha,1}, x^{\alpha,2}, x^{\alpha,3}$ form the material body under consideration. In a multicomponent medium each of the constituents possesses its own LAGRANGIAN function of motion

$$\chi_t^\alpha = \chi_t^\alpha(x^{\alpha,1}, x^{\alpha,2}, x^{\alpha,3}) \tag{3.6}$$

describing the placement of the particles in time t. Each arrangement of all material points is a configuration. The reference configuration may be chosen arbitrarily, but the mapping $\chi_{t_0}^\alpha$ at beginning of the observation at time t_0 is usually selected for this purpose. The time-dependent mapping χ_t^α is the current configuration. At time t every particle of the constituent α is identified by the position vector $\boldsymbol{x}^\alpha$

$$\boldsymbol{x}^\alpha = \chi_t^\alpha(\boldsymbol{X}^\alpha, t) = \boldsymbol{x}^\alpha(\boldsymbol{X}^\alpha, t)\,. \tag{3.7}$$

At time t_0 the position vector $\boldsymbol{X}^\alpha$ is connected with the reference configuration. The invertibility of the motion function

$$\boldsymbol{X}^\alpha = (\chi_t^\alpha)^{-1}(\boldsymbol{x}^\alpha, t) \tag{3.8}$$

ensures that a particle of the component α cannot occupy two spatial positions and that two different particles of the same component cannot occupy the same spatial position at time t. The displacement vector quantifies the difference between the current position and the position in the reference configuration of a particle

$$\boldsymbol{u}^\alpha = \boldsymbol{x}^\alpha - \boldsymbol{X}^\alpha\,. \tag{3.9}$$

Figure 3.2 visualises the relations for two components. At time t particles of the components a and b occupy the material point indicated by the position vector $\boldsymbol{x}^a = \boldsymbol{x}^b$.

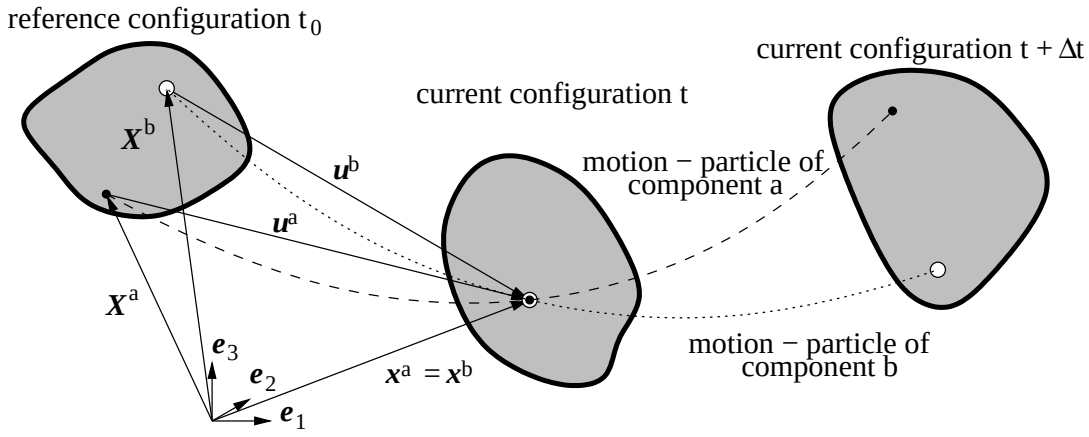

Figure 3.2: Motion and coordinates

The particle of the component a has the position $\boldsymbol{X}^a$ in the reference configuration at time t_0, whereas the particle of the component b moves from the point $\boldsymbol{X}^b$. Thus, two different displacement vectors $\boldsymbol{u}$ exist and the particles occupy different places at time $t + \Delta t$ due to the different motion functions.
The spatial or EULERIAN and the material or LAGRANGIAN representation of any physical quantity are expressed by means of the functions

$$\omega = \omega(\boldsymbol{x}^\alpha, t)\,, \quad \bar{\omega} = \bar{\omega}(\boldsymbol{X}^\alpha, t)\,. \tag{3.10}$$

Both functions describe the same quantity, but the spatial representation is defined on the current configuration, whereas the material representation acts on the reference configuration. The material time derivative of a physical quantity in its spatial representation with respect to the motion of the constituent α consists of a local partial time derivative and a convective part obtained by the GATEAUX derivative in the direction of the component velocity $\boldsymbol{v}^\alpha$

$$[\omega]'^\alpha = \frac{\mathrm{d}^\alpha \omega}{\mathrm{d}t} = \frac{\partial \omega}{\partial t} + \mathrm{grad}\omega \cdot \boldsymbol{v}^\alpha\,. \tag{3.11}$$

In contrast, the material time derivative of a physical quantity coincides with its partial time derivative

$$\dot{\bar{\omega}} = \frac{\mathrm{d}\bar{\omega}}{\mathrm{d}t} = \frac{\partial \bar{\omega}}{\partial t}\,. \tag{3.12}$$

The time derivative of the position vector $\boldsymbol{x}^\alpha$ is the spatial representation of the velocity field $\boldsymbol{v}^\alpha$ of the component α

$$\boldsymbol{v}^\alpha = \frac{\mathrm{d}^\alpha \boldsymbol{x}^\alpha}{\mathrm{d}t}\,. \tag{3.13}$$

The seepage velocity $\boldsymbol{w}^\beta$ is the difference between the velocity of a fluid $\boldsymbol{v}^\beta$ and the velocity of the solid waste $\boldsymbol{v}^s$

$$\boldsymbol{w}^\beta = \boldsymbol{v}^\beta - \boldsymbol{v}^s\,. \tag{3.14}$$

3.2.2 Deformation gradient and strain measures

Series expansion of the motion function (3.7) and truncation after the linear term results in

$$\mathrm{d}\boldsymbol{x}^\alpha = \frac{\partial \boldsymbol{x}^\alpha}{\partial \boldsymbol{X}^\alpha} \cdot \mathrm{d}\boldsymbol{X}^\alpha = \mathrm{Grad}^\alpha \boldsymbol{x}^\alpha \cdot \mathrm{d}\boldsymbol{X}^\alpha\,. \tag{3.15}$$

Therein, the deformation gradient $\mathbf{F}^\alpha$ arises, which is connected to the material displacement gradient $\mathbf{H}^\alpha = \mathrm{Grad}^\alpha \boldsymbol{u}^\alpha$

$$\mathbf{F}^\alpha = \frac{\partial \boldsymbol{x}^\alpha}{\partial \boldsymbol{X}^\alpha} = \mathrm{Grad}^\alpha \boldsymbol{x}^\alpha = \mathbf{1} + \mathrm{Grad}^\alpha \boldsymbol{u}^\alpha\,. \tag{3.16}$$

The deformation gradient describes the deformation behaviour in the surrounding of a material point and maps material line elements from the reference configuration to the current configuration. Furthermore, it also describes the transformation behaviour of material area elements and material volume elements

$$\mathrm{d}\mathbf{a}^\alpha = \det\mathbf{F}^\alpha \; (\mathbf{F}^\alpha)^{-T} \cdot \mathrm{d}\mathbf{A}_0^\alpha \,, \quad \mathrm{d}v^\alpha = \det\mathbf{F}^\alpha \, \mathrm{d}V_0^\alpha \,. \tag{3.17}$$

The polar decomposition of the deformation gradient introduces the orthogonal rotational tensor $\mathbf{R}^\alpha$ and the right and left stretch tensors $\mathbf{U}^\alpha$ and $\mathbf{V}^\alpha$, which are symmetric and positive definite and own the same eigenvalues,

$$\mathbf{F}^\alpha = \mathbf{R}^\alpha \cdot \mathbf{U}^\alpha = \mathbf{V}^\alpha \cdot \mathbf{R}^\alpha \,. \tag{3.18}$$

The right CAUCHY-GREEN tensor $\mathbf{C}^\alpha$ and the left CAUCHY-GREEN tensor $\mathbf{B}^\alpha$ are free from any rotational parts

$$\mathbf{C}^\alpha = (\mathbf{U}^\alpha)^2 = (\mathbf{F}^\alpha)^T \cdot \mathbf{F}^\alpha \,, \quad \mathbf{B}^\alpha = (\mathbf{V}^\alpha)^2 = \mathbf{F}^\alpha \cdot (\mathbf{F}^\alpha)^T \,. \tag{3.19}$$

The important GREEN-strain tensor $\mathbf{E}^\alpha$ and ALMANSI-strain tensor $\mathbf{A}^\alpha$ are defined by

$$\mathbf{E}^\alpha = \frac{1}{2}\left(\mathbf{C}^\alpha - \mathbf{1}\right) \,, \quad \mathbf{A}^\alpha = \frac{1}{2}\left(\mathbf{1} - (\mathbf{B}^\alpha)^{-1}\right) \,. \tag{3.20}$$

GREEN and ALMANSI strain tensors describe the difference of squares of material line elements during the process of motion. They own a contravariant vector basis and are connected by a covariant Push-Forward and Pull-back, respectively,

$$\mathbf{A}^\alpha = (\mathbf{F}^\alpha)^{-T} \cdot \mathbf{E}^\alpha \cdot (\mathbf{F}^\alpha)^{-1} \,, \quad \mathbf{E}^\alpha = (\mathbf{F}^\alpha)^T \cdot \mathbf{A}^\alpha \cdot \mathbf{F}^\alpha \,. \tag{3.21}$$

Furthermore, time derivatives of the deformation and strain tensor introduced so far are required in the introduction of mechanical balance and in constitutive modelling. The material velocity gradient $\dot{\mathbf{F}}^\alpha$ is defined as

$$\dot{\mathbf{F}}^\alpha = \frac{\partial}{\partial t}\left(\frac{\partial \boldsymbol{x}^\alpha(\boldsymbol{X}^\alpha, t)}{\partial \boldsymbol{X}^\alpha}\right) = \mathrm{Grad}^\alpha\left(\frac{\partial \boldsymbol{x}^\alpha(\boldsymbol{X}^\alpha, t)}{\partial t}\right) \,. \tag{3.22}$$

Transformation of equation (3.22) to the current configuration delivers the spatial velocity gradient $\mathbf{L}^\alpha$, which is additively decomposable into its symmetric stretching or strain rate tensor $\mathbf{D}^\alpha$ and its skew-symmetric spin or vorticity tensor $\mathbf{W}^\alpha$,

$$\mathbf{L}^\alpha = \dot{\mathbf{F}}^\alpha \cdot (\mathbf{F}^\alpha)^{-1} \,, \;\; \mathbf{D}^\alpha = \frac{1}{2}\left(\mathbf{L}^\alpha + (\mathbf{L}^\alpha)^T\right) \,, \;\; \mathbf{W}^\alpha = \frac{1}{2}\left(\mathbf{L}^\alpha - (\mathbf{L}^\alpha)^T\right) \,. \tag{3.23}$$

The material time derivative of the GREEN strain tensor is obtained as

$$\dot{\mathbf{E}}^\alpha = \frac{1}{2}\left((\dot{\mathbf{F}}^\alpha)^T \cdot \mathbf{F}^\alpha + (\mathbf{F}^\alpha)^T \cdot \dot{\mathbf{F}}^\alpha\right) \,. \tag{3.24}$$

Using the covariant transformation (3.21), the spatial stretching tensor $\mathbf{D}^\alpha$ arises

$$\mathbf{D}^\alpha = (\mathbf{F}^\alpha)^{-T} \cdot \dot{\mathbf{E}}^\alpha \cdot (\mathbf{F}^\alpha)^{-1} = \overset{\triangle}{\mathbf{A}}{}^\alpha = \left[\mathbf{A}^\alpha\right]'^\alpha + \mathbf{A}^\alpha \cdot \mathbf{L}^\alpha + (\mathbf{L}^\alpha)^T \cdot \mathbf{A}^\alpha \,, \tag{3.25}$$

which equals the covariant or lower OLDROYD derivative of the ALMANSI strain tensor $\overset{\vartriangle}{\mathbf{A}}{}^{\alpha}$. The covariant OLDROYD derivative is an objective tensor rate. Objective quantities are invariant under EUCLIDEAN transformations. The principle of objectivity in continuum mechanics requires the aforementioned property for constitutive equations and all relevant quantities to describe the physical behaviour of a system. Wegener [103] discusses the basic principles of continuum mechanics in profundity and provides a large number of objective time derivatives.

3.3 Balance laws and thermodynamic principles for mixtures

The continuum mechanical founded *Theory of Mixtures* follows three metaphysical principles formulated by Truesdell [98]:

1. *All properties of the mixture must be mathematical consequences of properties of the constituents*
2. *So as to describe the motion of a constituent, we may in imagination isolate it from the rest of the mixture, provided we allow properly for the actions of the other constituents upon it.*
3. *The motion of the mixture is governed by the same equations as is a single body.*

Thus, the axiomatically introduced balance laws of mechanics for conservation of mass, linear momentum and moment of momentum and the thermodynamic principles of conservations of energy and non-negative entropy production are valid for the constituents as well as for the mixture. The essential difference between the partial balances of the constituents and the balance of the mixture consists in additional production terms describing the interactions between the different constituents. From a thermodynamical viewpoint the mixture is a closed system composed by several open partial systems. The derivation of the general statements and their mathematical formulations are discussed in detail in the literature, e.g., Bowen [15] or de Boer and Ehlers [22].

3.3.1 Balance law of mass

Two spatial densities are distinguishable from the concept of volume fractions. They are scalar fields attached at each material point. The intrinsic or real physical density of a constituent is the outcome of the averaging process of its mass related to the real occupied volume

$$\tilde{\rho}^{\alpha} = \frac{\mathrm{d}(\text{mass of constituent } \alpha)}{\mathrm{d}(\text{volume of constituent } \alpha)} = \frac{\mathrm{d}m^{\alpha}}{\mathrm{d}v^{\alpha}} \,. \tag{3.26}$$

In contrast, the partial density of a constituent is the ratio between its mass and the total volume

$$\rho^\alpha = \frac{\mathrm{d}(\text{mass of constituent } \alpha)}{\mathrm{d}(\text{volume of mixture})} = \frac{\mathrm{d}m^\alpha}{\mathrm{d}v} \,. \tag{3.27}$$

The mass concentration factor ω^α relates the mass of a component to the total mass of the mixture expressed by its physical density $\tilde{\rho}^M$

$$\omega^\alpha = \frac{\mathrm{d}(\text{mass of constituent } \alpha)}{\mathrm{d}(\text{mass of mixture})} = \frac{\rho^\alpha}{\tilde{\rho}^M} = \frac{\rho^\alpha}{\sum_{\beta=1}^{n} \rho^\beta} \,. \tag{3.28}$$

The partial density (3.27) occurs in the axiom of balance of mass, which states for each constituent

$$\left[\rho^\alpha\right]'^\alpha + \rho^\alpha \operatorname{div}(\boldsymbol{v}^\alpha) = \frac{\partial \rho^\alpha}{\partial t} + \operatorname{div}(\rho^\alpha \, \boldsymbol{v}^\alpha) = \hat{\rho}^\alpha \,. \tag{3.29}$$

The mass supply term $\hat{\rho}^\alpha$ describes mass exchange processes between the different constituents of the mixture. For landfills exchange processes originate from biodegradation of organic solid particles, from water evaporation or condensation and from solution of gases into the leachate mainly. The sum of mass production terms has to vanish in order to fulfil the mass conservation requirement for the mixture

$$\sum_\alpha \hat{\rho}^\alpha = 0 \,. \tag{3.30}$$

3.3.2 Balance law of linear momentum

The axiom of balance of linear momentum states for each constituent in its local form

$$\rho^\alpha \, \left[\boldsymbol{v}^\alpha\right]'^\alpha = \rho^\alpha \, \mathbf{b}^\alpha + \operatorname{div}(\mathbf{T}^\alpha) + \hat{\boldsymbol{\pi}}^\alpha - \hat{\rho}^\alpha \, \boldsymbol{v}^\alpha \,. \tag{3.31}$$

Momentum supply terms emanate from volume forces caused by the gravity $\mathbf{b}^\alpha$ and from surface traction $\mathbf{t}_R^\alpha$, which introduces the partial CAUCHY stress tensor of a component $\mathbf{T}^\alpha$ in a common way

$$\int_a (\mathbf{t}_R^\alpha) \, \mathrm{d}a = \int_a \mathbf{T}^\alpha \cdot \mathbf{n} \, \mathrm{d}a = \int_v \operatorname{div}(\mathbf{T}^\alpha) \, \mathrm{d}v \,. \tag{3.32}$$

The total CAUCHY stress tensor of the whole mixture is obtained with the diffusive velocity $\tilde{\boldsymbol{w}}^\alpha = \boldsymbol{v}^\alpha - \boldsymbol{v}^M$ as

$$\mathbf{T} = \sum_\alpha T^\alpha - \sum_\alpha \left(\rho^\alpha \, \tilde{\boldsymbol{w}}^\alpha \otimes \tilde{\boldsymbol{w}}^\alpha\right) \,. \tag{3.33}$$

Linear momentum exchange terms $\hat{\boldsymbol{\pi}}^\alpha$ and interaction terms caused by mass exchange describe the local interaction between the different components inside the mixture. The sum of linear momentum transfer vanishes

$$\sum_\alpha \hat{\boldsymbol{\pi}}^\alpha = 0 \,. \tag{3.34}$$

The 1st PIOLA-KIRCHHOFF stress tensor $\mathbf{P}^\alpha$ emerges from the transformation of the surface traction to the reference configuration combining the equations (3.32) and (3.17)

$$\mathbf{P}^\alpha = \det\mathbf{F}^\alpha \, \mathbf{T}^\alpha \cdot (\mathbf{F}^\alpha)^{-T} \, . \tag{3.35}$$

The 2nd PIOLA-KIRCHHOFF stress tensor originates from the Pull-back of the first basis of the 1st PIOLA-KIRCHHOFF stress tensor from the current configuration

$$\mathbf{S}^\alpha = (\mathbf{F}^\alpha)^{-1} \cdot \mathbf{P}^\alpha = \det\mathbf{F}^\alpha \, (\mathbf{F}^\alpha)^{-1} \cdot \mathbf{T}^\alpha \cdot (\mathbf{F}^\alpha)^{-T} \, . \tag{3.36}$$

The spatial KIRCHHOFF stress tensor, which is also known as *weighted* CAUCHY stress tensor, is important for constitutive modelling

$$\tilde{\mathbf{T}}^\alpha = \mathbf{F}^\alpha \cdot \mathbf{S}^\alpha \cdot (\mathbf{T}^\alpha)^T = \det\mathbf{F}^\alpha \, \cdot \mathbf{T}^\alpha \, . \tag{3.37}$$

All stress tensors defined so far have contravariant components. The transformation of contravariant second order tensors between the reference and the current configuration ia carried out with the contravariant Push-forward and the contravariant Pull-back operators

$$\tilde{\mathbf{T}}^\alpha = \mathbf{F}^\alpha \cdot \mathbf{S}^\alpha \cdot (\mathbf{F}^\alpha)^T \, , \quad \mathbf{S}^\alpha = (\mathbf{F}^\alpha)^{-1} \cdot \tilde{\mathbf{T}}^\alpha \cdot (\mathbf{F}^\alpha)^{-T} \, . \tag{3.38}$$

The material time derivative of the 2nd PIOLA-KIRCHHOFF stress tensor equals its partial time derivative

$$\dot{\mathbf{S}}^\alpha = \frac{\partial \mathbf{S}^\alpha}{\partial t} \, . \tag{3.39}$$

The transformation of the time derivative of the 2nd PIOLA-KIRCHHOFF (3.39) results in the objective contravariant or upper Oldroyd rate of the Kirchhoff stress tensor

$$\overset{\triangledown\alpha}{\tilde{\mathbf{T}}}{}^\alpha = \mathbf{F}^\alpha \cdot \dot{\mathbf{S}}^\alpha \cdot (\mathbf{F}^\alpha)^T = \left[\tilde{\mathbf{T}}^\alpha\right]'^\alpha - \mathbf{L}^\alpha \cdot \tilde{\mathbf{T}}^\alpha - \tilde{\mathbf{T}}^\alpha \cdot (\mathbf{L}^\alpha)^T \, . \tag{3.40}$$

3.3.3 Balance law of moment of momentum

In a nonpolar Boltzmann-continuum the axiom of balance of moment of momentum with respect to an arbitrarily chosen material point $\boldsymbol{x}^\alpha - \boldsymbol{c}$ states in its local form for a component

$$\mathbf{1} \times \mathbf{T}^\alpha + \hat{\boldsymbol{\mu}}^\alpha - (\boldsymbol{x}^\alpha - \boldsymbol{c}) \times \hat{\boldsymbol{\pi}}^\alpha = \mathbf{0} \, . \tag{3.41}$$

Thereby, equation (3.41) includes a momentum exchange term $\hat{\boldsymbol{\mu}}^\alpha$ and a second part arising from the exchange of linear momentum. Summing up the partial balances allows the conclusion that the total CAUCHY stress tensor of the mixture $\mathbf{T}$ is symmetric

$$\mathbf{1} \times \mathbf{T} = \mathbf{0} \quad \Longrightarrow \quad \mathbf{T} = \mathbf{T}^T \, . \tag{3.42}$$

Furthermore, the sum of the exchange terms of angular momentum must vanish

$$\sum_{\alpha} \hat{\boldsymbol{\mu}}^{\alpha} = 0\,. \tag{3.43}$$

Although the CAUCHY stress tensor of the whole mixture $\mathbf{T}$ is symmetric, no statements about the structure of the partial CAUCHY stress tensors can be drawn from equation (3.41) so far because only the sum of all partial stress tensors has to be symmetric. Therefore, it is usually assumed that for each constituent the exchange term of angular momentum equals the term connected with interactions of linear momentum

$$\hat{\boldsymbol{\mu}}^{\alpha} = (\boldsymbol{x}^{\alpha} - \boldsymbol{c}) \times \hat{\boldsymbol{\pi}}^{\alpha}\,. \tag{3.44}$$

This assumption fulfils the requirement of equation (3.43) due to condition (3.34) and leads to the desired symmetric partial stress tensors

$$\mathbf{1} \times \mathbf{T}^{\alpha} = \mathbf{0} \quad \rightarrow \quad \mathbf{T}^{\alpha} = (\mathbf{T}^{\alpha})^{T}\,. \tag{3.45}$$

Especially in view of constitutive modelling, non-symmetric stress tensors of the pore fluids in landfills are meaningless in a physical interpretation.

3.3.4 Balance law of energy

The partial balance of energy quantifies the changes of internal and kinetic energy during the process of motion for each component and states after incorporation of balance axioms of mass and linear momentum

$$\begin{aligned} \rho^{\alpha}\ [u^{\alpha}]'^{\alpha} = \mathbf{T}^{\alpha} : \mathbf{L}^{\alpha} + \rho^{\alpha}\, r^{\alpha} - \operatorname{div}(\mathbf{q}^{\alpha}) \\ + \hat{\xi}^{\alpha} + \boldsymbol{v}^{\alpha}\,(\hat{\boldsymbol{\pi}}^{\alpha} - \rho^{\alpha}\,\boldsymbol{v}^{\alpha}) - \hat{\rho}^{\alpha}\left(u^{\alpha} + \frac{\boldsymbol{v}^{\alpha}\cdot\boldsymbol{v}^{\alpha}}{2}\right)\,. \end{aligned} \tag{3.46}$$

Thereby, the internal energy u^{α} equals the stress power term $\mathbf{T}^{\alpha} : \mathbf{L}^{\alpha}$ and the heat supply due to heat flow expressed by the CAUCHY heat flux vector $\mathbf{q}^{\alpha}$ and the volume distributed heat radiation r^{α}. Interaction terms originate from the partial mass balance (3.29) as well as from the balance of linear momentum (3.31). Additionally, a direct exchange term $\hat{\xi}^{\alpha}$ occurs compared to a single component medium. The sum of the energy transfer terms vanishes

$$\sum_{\alpha} \hat{\xi}^{\alpha} = 0\,. \tag{3.47}$$

The internal energy is often replaced by the Helmholtz free energy Ψ^{α} or the potential $W^{\alpha} = \rho_0^{\alpha}\,\Psi^{\alpha}$ and the specific entropy s^{α} introducing the temperature Θ^{α} of each constituent as a state variable into the investigation

$$u^{\alpha} = \Psi^{\alpha} - \Theta^{\alpha}\, s^{\alpha} = \frac{1}{\rho_0^{\alpha}} W - \Theta^{\alpha}\, s^{\alpha}\,. \tag{3.48}$$

The potential function W^{α} has a significant role in formulating stress-strain relation for solids materials.

3.3.5 2nd law of thermodynamics

The net entropy production γ^α exists for each constituent

$$\rho^\alpha \, \gamma^\alpha = \rho^\alpha \, [s^\alpha]'^\alpha - \frac{1}{\Theta^\alpha} \rho^\alpha \, r^\alpha + \operatorname{div}(\frac{1}{\Theta^\alpha} \, \mathbf{q}^\alpha) - (\hat{\zeta}^\alpha - \hat{\rho}^\alpha \, s^\alpha) \, . \tag{3.49}$$

After summing (3.49) over all constituents, the entropy production of the mixture is obtained, which has to be non-negative,

$$\mathcal{D}_{int} = \tilde{\rho} \, \gamma = \sum_\alpha \rho^\alpha \, \gamma^\alpha \geq 0 \, . \tag{3.50}$$

Additionally, the sum of entropy exchange terms vanishes

$$\sum_\alpha \hat{\zeta}^\alpha = 0 \, . \tag{3.51}$$

During the development of the theoretical framework of the mixture theory it was controversially discussed for a long time if only the entropy production of the mixture (3.50) has to be non-negative or if the entropy production of each of the constituents (3.49) has to satisfy this restriction, too. In recent literature the first statement prevails, e.g., Ehlers [31], Bluhm [11]. The 2nd law of thermodynamics restricts the constitutive modelling. Diebels [26], Ehlers [31], Bluhm [11], [12] investigate the case of a biphasic mixture consisting of a solid skeleton filled with liquid or gas. The solid is described by different micropolar, nonpolar elastic and elasto-plastic formulations. The pore fluids are modelled incompressible as well as compressible. Thermodynamic investigations of single component materials are common practise in development of material models. Moreover, de Boer and Bluhm [20] also derive a thermodynamic consistent model including three phases, which consists of a solid skeleton with gases and liquids acting in the pore space. In addition, they incorporate mass exchange processes, but they do not establish any constitutive relations. More recent, de Boer and Didwania [21] formulate a model based on a thermodynamic approach in order to explain the capillarity phenomenon and to describe multiphase flow through a rigid solid skeleton.

3.4 Modelling of governing equations

Different models for the investigation of processes inside a landfill are derived in the following using the outlined framework of the *Theory of Porous Media*. At first, the governing equations for a biphasic model consisting of a solid skeleton filled by one fluid are presented, which helps to clarify the meaning of interaction terms in the balance laws of linear momentum. The obtained results are transferred to a three component model, where the pores are filled by two fluids. Finally, some remarks on model extension and simplifications are pointed out.

Biphasic models

At first, some theoretical investigations of Bluhm [12] for a two component model consisting of a fully saturated solid skeleton are enlarged by mass exchange terms. In this case the material time derivative with respect to the solid motion of the saturation condition (3.2) is obtained as

$$\begin{aligned}[n^s + n^l - 1]'^s &= [n^s]'^s + [n^l]'^l - \operatorname{grad} n^l \cdot \boldsymbol{w}^l \\ &= n^s\, \mathbf{L}^s : \mathbf{1} + \frac{n^s}{\tilde{\rho}^s}\,[\tilde{\rho}^s]'^s + n^f\, \mathbf{L}^l : \mathbf{1} + \frac{n^l}{\tilde{\rho}^l}\,[\tilde{\rho}^l]'^l - \frac{\hat{\rho}^s}{\tilde{\rho}^s} - \frac{\hat{\rho}^l}{\tilde{\rho}^l} = 0\,. \end{aligned} \tag{3.52}$$

Now, the entropy inequality (3.50) may be extended by (3.52) using a LAGRANGIAN multiplier p. Assuming incompressible solid particles as well as an incompressible fluid, the partial stress tensors of the solid and the fluid component are composed by

$$\mathbf{T}^s = \mathbf{T}^s_e - p\, n^s\, \mathbf{1}\,, \tag{3.53a}$$

$$\mathbf{T}^l = \mathbf{T}^l_e - p\, n^l\, \mathbf{1}\,. \tag{b}$$

The terms indicated by 'e' are the *extra* stresses and can be interpreted as the *effective* stresses of classical soil mechanics as discussed by Bluhm and de Boer [13]. Revoking the assumption of incompressibility of solid and fluid does not change the general statement. The multiplier p is the real pore pressure of the fluid. Furthermore, the exchange term in the balance of linear momentum of the fluid can be substituted by

$$\hat{\boldsymbol{\pi}}^l - \hat{\rho}^l\, \mathbf{v}^l = -\boldsymbol{\Xi} \cdot \boldsymbol{w}^l + p \operatorname{grad} n^l\,. \tag{3.54}$$

Neglecting inertia terms in a quasi-static analysis and neglecting the *extra* term of the partial fluid stress tensor, which is justified for almost inviscid fluids, the partial balance of linear momentum of the fluid reads

$$\rho^l\, \mathbf{b}^l + \operatorname{div}(-p\, n^l\, \mathbf{1}) - \boldsymbol{\Xi} \cdot \boldsymbol{w}^l + p \operatorname{grad} n^l = 0\,.$$

It is rapidly transformed into the well-known DARCY model

$$n^l\, \boldsymbol{w}^l = (n^l)^2\, \boldsymbol{\Xi}^{-1} \cdot \left[-\operatorname{grad} p \; + \tilde{\rho}^l\, \mathbf{b}^l\right] \tag{3.55}$$

clarifying the physical meaning of the positive definite second order tensor $\boldsymbol{\Xi}$, which is related to the permeability tensor $\mathbf{K}_{abs}$ of the porous medium by

$$\boldsymbol{\Xi} = (n^l)^2\, \mu^l\, (\mathbf{K}_{abs})^{-1}\,. \tag{3.56}$$

The dynamic viscosity μ^l characterises the fluid. Summing up the partial balances (3.29) combined with the decomposition of the stress tensors (3.53), the seepage velocity (3.14) and the requirement (3.34), the balance of linear momentum of the two component mixture is derived as

$$\operatorname{div}(\mathbf{T}^s_e - p\, \mathbf{1}) + (\rho^s + \rho^l)\, \mathbf{b} - \hat{\rho}^l\, \boldsymbol{w}^l = \mathbf{0}\,. \tag{3.57}$$

The last equation ensures equilibrium. The summand connected with the mass exchange can be skipped in most practical cases if the exchange process proceeds slowly and the seepage velocity is in ordinary range. For instance, a mass exchange of $1\,\mathrm{kg\,m^{-3}\,s^{-1}}$ and a seepage velocity of $1\,\mathrm{m\,s^{-1}}$ result in an additional volume force of only $1\,\mathrm{N\,m^{-3}}$.
The total CAUCHY stresses of the mixture $\mathbf{T}$ are decomposed in the *extra* stresses of the solid skeleton $\mathbf{T}_e^s$ and in the pore pressure p

$$\mathbf{T} = \mathbf{T}_e^s - p\,\mathbf{1}\,. \tag{3.58}$$

Equation (3.58) coincides with von TERZAGHI's effective stress concept. The partial balance of mass of the fluid is transformed into

$$[\rho^l]'^l + \rho^l \operatorname{div}(\boldsymbol{v}^l) = \frac{\partial \rho^l}{\partial t} + \operatorname{div}(\rho^l\,\boldsymbol{v}^s) + \operatorname{div}(n^l\,\tilde{\rho}^l\,\boldsymbol{w}^l) = \hat{\rho}^l \tag{3.59}$$

and the mass balance of the solid states

$$[\rho^l]'^s + \rho^s \operatorname{div}(\boldsymbol{v}^s) = \frac{\partial \rho^s}{\partial t} + \operatorname{div}(\rho^s\,\boldsymbol{v}^s) = -\hat{\rho}^l\,. \tag{3.60}$$

Considerations on a control volume $\mathrm{d}v_B$, which moves with the solid velocity, may clarify the physical meaning of the different terms of equation (3.59)

$$\begin{aligned} 0 &= \int_{\mathrm{d}v} \left\{ \frac{\partial \rho^l}{\partial t} + \operatorname{div}(\rho^l\,\boldsymbol{v}^s) + \operatorname{div}(n^l\,\tilde{\rho}^l\,\boldsymbol{w}^l) - \hat{\rho}^l \right\} \mathrm{d}v_B \\ &= \int_{\mathrm{d}v_B} (\rho^l \mathrm{d}v_B)^{\cdot} + \int_{\mathrm{d}a_B} \rho^l\,\boldsymbol{w}^l \cdot \mathbf{n}\,\mathrm{d}a_B - \int_{\mathrm{d}v_B} \hat{\rho}^l\,\mathrm{d}v_B\,. \end{aligned}$$

The term $\frac{\partial \rho^l}{\partial t}$ describes the changes of partial density of the fluid in the control volume that moves with the solid velocity. The term $\operatorname{div}(\rho^l\,\boldsymbol{v}^s)$ captures changes of the size of the control volume as well as of the volume ratios. The term $\operatorname{div}(n^l\,\tilde{\rho}^l\,\boldsymbol{w}^l)$ includes the in- and outcoming mass fluxes and the term $\hat{\rho}^l$ covers all mass exchanges with the solid phase. The different processes are illustrated in figure 3.3.

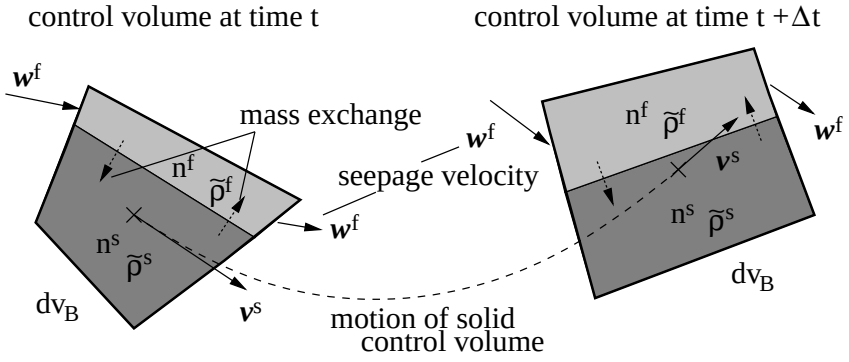

Figure 3.3: Physical meaning of terms in partial mass balance of fluids

The equations (3.57), (3.59), and (3.60) are the governing equations of the biphasic model for a fully saturated porous medium under isothermal condition. Thereby, the 1st law of thermodynamics is fulfilled automatically and all terms connected with heat and temperature are skipped. The model is completed by constitutive relations for the *extra* stresses of the solid skeleton depending on the deformation expressed by the displacement function $\boldsymbol{u}^s$ and by constitutive relations for the mass exchange processes. Appropriate initial and boundary conditions have to be defined in order to solve the initial-boundary value problem uniquely. Surface forces and fluid fluxes are prescribed on the von NEUMANN boundary. The displacements and the pore pressures are known on DIRICHLET boundary as thermodynamic state variables. Mixed ROBIN or CAUCHY boundary conditions connect the applied surface forces with the displacements of the boundary and the fluid fluxes with the fluid pressure, respectively. Such boundaries are interpretable as springs for the solid motion. In contrast, the CAUCHY boundary for the transport is modelled by a jump between the fluid pressure inside p_i^l and outside the domain p_a^l and has a structure similar to the DARCY law

$$\mathbf{t}^l = \left(n^l\,\tilde{\rho}^l\,\boldsymbol{w}^l\cdot\mathbf{n}\right)\,\mathbf{n} = \left\{-\frac{\tilde{\rho}^l}{\mu^l}\mathbf{K}_{abs}\left[\left(p_a^l - p_i^l\right)\mathbf{n} - \tilde{\rho}^l\mathbf{b}\right]\cdot\mathbf{n}\right\}\,\mathbf{n}\,. \tag{3.61}$$

Initial values at time t_0 have to be defined for the volume fractions and the state variables as well as for internal variables of the constitutive model. The aforementioned facts are illustrated in figure 3.4.

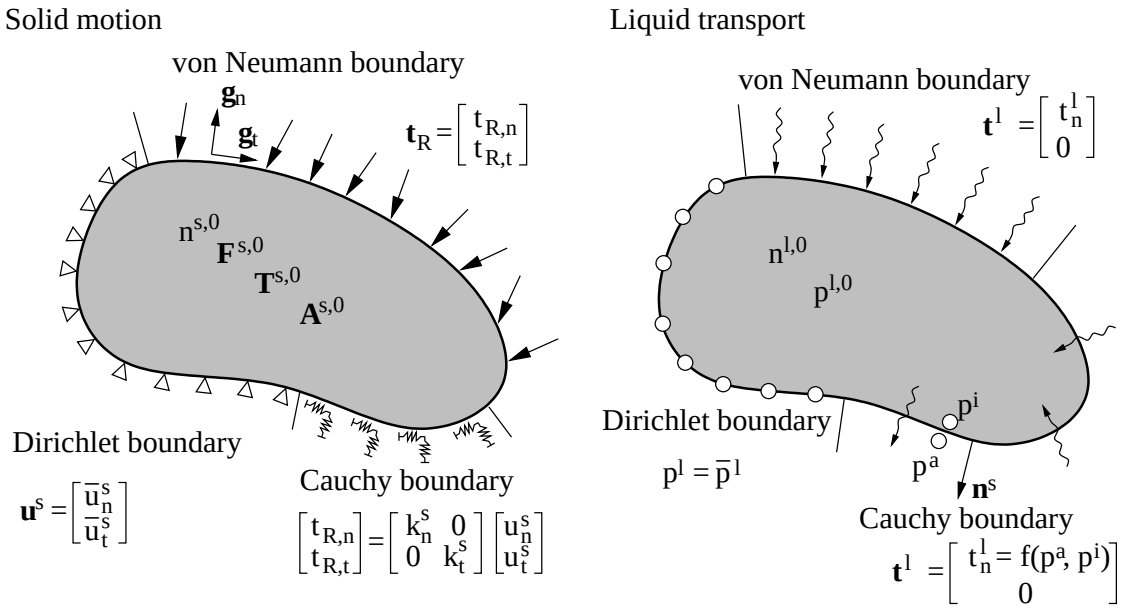

Figure 3.4: Initial and boundary conditions

Triphasic models

The extension of the biphasic model to a triphasic model is straightforward and results in the decomposition of the stresses for all components

$$\mathbf{T}^s = \mathbf{T}^s_e - p\, n^s\, \mathbf{1}\,, \tag{3.62a}$$
$$\mathbf{T}^l = \mathbf{T}^l_e - p^l\, n^l\, \mathbf{1}\,, \tag{b}$$
$$\mathbf{T}^g = \mathbf{T}^g_e - p^g\, n^g\, \mathbf{1}\,. \tag{c}$$

Once again, the *extra* stresses of the gas and the liquid phase are small. Therefore, they are neglected in the modelling approach as well as inertia terms. The interaction terms in linear momentum are obtained as

$$\hat{\boldsymbol{\pi}}^l - \hat{\rho}^l\, \boldsymbol{v}^l = -\boldsymbol{\Xi}^l \cdot \boldsymbol{w}^l + p^l\, \mathrm{grad}\, n^l\,, \tag{3.63a}$$
$$\hat{\boldsymbol{\pi}}^g - \hat{\rho}^g\, \boldsymbol{v}^g = -\boldsymbol{\Xi}^g \cdot \boldsymbol{w}^g + p^g\, \mathrm{grad}\, n^g\,. \tag{b}$$

Moreover, DARCY relations for a two fluid flow model arise

$$n^l\, \boldsymbol{w}^l = \frac{k^l_{rel}}{\mu^l}\, \mathbf{K}_{abs} \cdot \left[-\mathrm{grad}\, p^l \;+ \tilde{\rho}^l\, \mathbf{b}^l\right] \tag{3.64a}$$
$$n^g\, \boldsymbol{w}^g = \frac{k^g_{rel}}{\mu^g}\, \mathbf{K}_{abs} \cdot [-\mathrm{grad}\, p^g \;+ \tilde{\rho}^g\, \mathbf{b}^g] \tag{b}$$

The parameters k^β_{rel} describe the deviation in the flow behaviour for the fluid components β between partially saturated and fully saturated situations. The overall balance of linear momentum is obtained after summing up the three partial balances

$$\mathrm{div}\,(\mathbf{T}^s_e - p\,\mathbf{1}) + (\rho^s + \rho^l + \rho^g)\,\mathbf{b} - \hat{\rho}^l\, \boldsymbol{w}^l - \hat{\rho}^g\, \boldsymbol{w}^g = \mathbf{0}\,. \tag{3.65}$$

Therein, the pore pressure is defined by

$$p = p^g + \chi\, \left(p^l - p^g\right)\,, \tag{3.66}$$

leading to a decomposition of the total stress tensor by BISHOP's effective stress concept for partial saturated porous media

$$\mathbf{T} = \mathbf{T}^s_e - p\,\mathbf{1} = \mathbf{T}^s_e - p^g\,\mathbf{1} + \chi\, \left(p^l - p^g\right)\, \mathbf{1}\,. \tag{3.67}$$

The factor χ depends on the state of saturation. The overall linear momentum balance (3.65) form together with the mass balances of all three constituents as well as sufficient initial and boundary conditions the governing differential equation system for a triphasic model

$$[\rho^s]'^s + \rho^s\, \mathrm{div}(\boldsymbol{v}^s) = \frac{\partial \rho^s}{\partial t} + \mathrm{div}(\rho^s\, \boldsymbol{v}^s) = -\hat{\rho}^s\,, \tag{3.68a}$$
$$[\rho^l]'^l + \rho^l\, \mathrm{div}(\boldsymbol{v}^l) = \frac{\partial \rho^l}{\partial t} + \mathrm{div}(\rho^l\, \boldsymbol{v}^s) + \mathrm{div}(n^l\, \tilde{\rho}^l\, \boldsymbol{w}^l) = \hat{\rho}^l\,, \tag{b}$$
$$[\rho^g]'^g + \rho^g\, \mathrm{div}(\boldsymbol{v}^g) = \frac{\partial \rho^g}{\partial t} + \mathrm{div}(\rho^g\, \boldsymbol{v}^s) + \mathrm{div}(n^g\, \tilde{\rho}^g\, \boldsymbol{w}^g) = \hat{\rho}^g\,. \tag{c}$$

Simplified and advanced models

The aforementioned set of equations is too complex for many analyses. The model is simplified by the absence of the liquid constituent assuming a 'dry' solid skeleton. Thus, all influences of the pore gas are neglected totally, which presupposes that excess pore pressures in the gas phase disappear immediately. Then, the only governing equation is the balance law of linear momentum of the solid skeleton

$$\operatorname{div}\left(\mathbf{T}^s\right) + \left(\rho^s\right)\mathbf{b} = \mathbf{0}\,. \tag{3.69}$$

The distinction between total stress tensor, partial stress tensor and *extra* stress tensor is not necessary in this special case anymore. Initial and boundary conditions have to be defined only for displacements and surface tractions.
A two component fluid transport model arises by assuming an immobile solid skeleton. Thereby, the two mass balances of the fluids (3.68) are the governing model equations, which simplify to

$$\frac{\partial \rho^l}{\partial t} + \operatorname{div}(n^l\,\tilde{\rho}^l\,\boldsymbol{w}^l) = \hat{\rho}^l\,, \tag{3.70a}$$

$$\frac{\partial \rho^g}{\partial t} + \operatorname{div}(n^g\,\tilde{\rho}^g\,\boldsymbol{w}^g) = \hat{\rho}^g\,. \tag{b}$$

Obviously, the equations (3.70) are reduced to a single mass balance in case of a fully saturated medium describing the flow of only one fluid through the pores.
Extension of the models described so far is possible for non-isothermal conditions. Then, the balance of energy has a crucial role and the temperature arises as thermodynamic state variable. Furthermore, it is possible to split the gas or the liquid component in different chemical substrates, e.g., the landfill gas into methane, carbon dioxide, water vapour etc. or the liquid in water, aceton, alcohols etc. Adding mass balances for each chemical substrate to the set of governing equations is necessary in order to describe the transport phenomena in this case. Hanel [44] develops coupled models for biodegradation and fluid transport in landfills assuming an immobile solid phase and using about 20 chemical substrates for the description of degradation of organics as cellulose, fats, etc.

4 Constitutive Model

The model equations for an empty, saturated or partially saturated porous medium derived in section 3.4 together with the kinematic relations of section 3.2 are not sufficient in order to describe the investigated process of motion. In fact, appropriate constitutive relations have to be incorporated into the considerations in order to connect dynamic with kinematic variables and to characterise the specific material behaviour of the body under observation. In general, one distinguishes reversible and irreversible processes that may also depend on time.
Haupt [49] motivates the use of energetic conjugated dynamic and kinematic variables in constitutive modelling. The concept bases on the assumption that, when stress and stain tensors are applied that do not operate on the reference configuration, the physically significant scalar products between the 2nd PIOLA-KIRCHHOFF stress tensor $\mathbf{S}$ and the GREEN strain tensor $\mathbf{E}$ and its time-derivatives remain invariant. According to the concept of dual variables, following relations between variables of the reference and the current configuration hold true

$$\mathbf{S} : \mathbf{E} = \tilde{\mathbf{T}} : \mathbf{A}\,, \quad \dot{\mathbf{S}} : \mathbf{E} = \overset{\triangledown}{\tilde{\mathbf{T}}} : \mathbf{A}\,, \quad \mathbf{S} : \dot{\mathbf{E}} = \tilde{\mathbf{T}} : \overset{\triangle}{\mathbf{A}}\,, \quad \dot{\mathbf{S}} : \dot{\mathbf{E}} = \overset{\triangledown}{\tilde{\mathbf{T}}} : \overset{\triangle}{\mathbf{A}}\,. \tag{4.1}$$

Thereby, the KIRCHHOFF stress tensor $\tilde{\mathbf{T}}$ and its contravariant OLDROYD rate $\overset{\triangledown}{\tilde{\mathbf{T}}}$ and the ALMANSI strain tensor $\mathbf{A}$ and its covariant OLDROYD rate $\overset{\triangle}{\mathbf{A}}$ appear. A wide class of material models for granular soils, e.g., hypoplastic models described by von Wolffersdorff [101], employ the Jaumann-Zaremba rate of the stress tensor, which is the simplest of all objective rates operating on the current configuration. The application of this rate is not excluded by thermodynamic restriction, but Haupt [49] proves that the utilisation of this rate can lead to unphysical oscillations in simple material models. Constitutive relations have to be developed for the solid skeleton of municipal solid waste as well as for the pore fluids. Before the constitutive model is presented in detail, some general remarks on kinematics for inelastic deformation behaviour are provided.

4.1 Kinematics in large strain inelasticity

It is well known from field observations and laboratory experiments that municipal solid waste undergoes large irreversible deformations. Thus, the small strain assumption

usually applied in the constitutive description of most engineering materials and soils is not valid anymore. Furthermore, the typical additive decomposition of linearised GREEN strain tensor $\boldsymbol{\varepsilon}$ into elastic and inelastic part

$$\boldsymbol{\varepsilon} = \frac{1}{2}(\mathrm{grad}\mathbf{u} + \mathrm{grad}^T\mathbf{u}) = \boldsymbol{\varepsilon}_{el} + \boldsymbol{\varepsilon}_{in} \tag{4.2}$$

could not be applied. The treatment of large inelastic deformations is still object of research and not all questions are finally answered. The index 's' designating the solid material is omitted for simplification in the following.

4.1.1 Multiplicative split of the deformation gradient

In continuum mechanical research, e.g., Haupt [49] or Wegener [103], the multiplicative split of the deformation gradient dominates during the last decades

$$\mathbf{F} = \hat{\mathbf{F}}_{el} \cdot \mathbf{F}_{in} \,. \tag{4.3}$$

Most cited source of equation (4.3) are the articles of Lee [69], [68]. An alternative way to introduce a plastic metric proposed by Miehe [83] and Apel [5] is not pursued within this thesis.
The inelastic part $\mathbf{F}_{in}$ summarises following deformation processes, see Wegener [103].

1. Time dependent processes $\mathbf{F}_v$, e.g., visco-plastic and visco-elastic deformations.
2. Deformation path dependent processes $\mathbf{F}_p$, e.g., irreversible processes in the sense that the initial value is not reached in a closed stress cycle (mainly all spontaneous plastic deformations).
3. Stress-independent deformations $\mathbf{F}_\Theta$, e.g., thermally induced deformations.

Thus, the inelastic deformation gradient expands into

$$\mathbf{F}_{in} = \mathbf{F}_\Theta \cdot \mathbf{F}_v \cdot \mathbf{F}_{pl} \,. \tag{4.4}$$

The split of the deformation gradient (4.3) is interpretable as a series of mappings. The inelastic part $\mathbf{F}_{in}$ transforms material line elements from the reference configuration to an arising intermediate configuration, which is itself a reference configuration for the elastic deformation described by the mapping using the elastic deformation gradient $\mathbf{F}_{el}$ as shown in figure 4.1. The intermediate configuration is not a state, which the material body can occupy in reality. Thus, neither elastic nor inelastic deformation gradient are determinable from any displacement field. Moreover, neighbouring particles are incompatible in the intermediate configuration. The elastic part of the deformation process reconstitutes the compatibility. Obviously, the aforementioned reflections prove

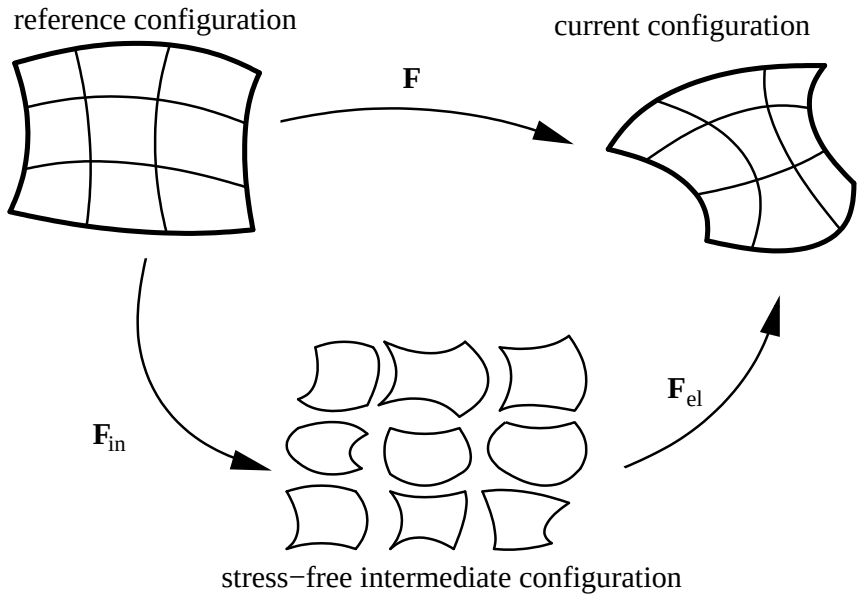

Figure 4.1: Intermediate Configuration

that the intermediate configuration has to be stress-free because only elastic strains are able to generate stresses.
The polar decomposition into stretch $\mathbf{V}, \mathbf{U}$ and rotational parts $\mathbf{R}$ show that the split (4.3) is not unique

$$\begin{aligned}\mathbf{F} &= \hat{\mathbf{F}}_{el} \cdot \mathbf{F}_{in} = \hat{\mathbf{V}}_{el} \cdot \hat{\mathbf{R}}_{el} \cdot \mathbf{R}_{in} \cdot \mathbf{U}_{in} \\ &= \hat{\mathbf{V}}_{el} \cdot \hat{\mathbf{R}}_{el} \cdot \mathbf{Q} \cdot \mathbf{Q}^T \cdot \mathbf{R}_{in} \cdot \mathbf{U}_{in} = \hat{\mathbf{V}}_{el} \cdot \hat{\mathbf{R}}^*_{el} \cdot \mathbf{R}^*_{in} \cdot \mathbf{U}_{in} = \mathbf{F}^*_{el} \cdot \mathbf{F}^*_{in} \,. \end{aligned} \tag{4.5}$$

Thereby, the orthogonal tensor $\mathbf{Q}$ rotates the intermediate configuration.
After inserting of (4.3) into the definition of GREEN and ALMANSI strain tensor (3.20), it is clear that both strain tensors cannot be decomposed in purely elastic and purely inelastic parts. Covariant Push-forward of the GREEN strains by the inelastic deformation gradient or covariant Pull-back of the ALMANSI strains by the elastic deformation gradient introduces a strain tensor $\hat{\mathbf{\Gamma}}$ acting in the intermediate configuration, which is decomposed additively into elastic and inelastic parts

$$\hat{\mathbf{\Gamma}} = \mathbf{F}^T_{in} \cdot \mathbf{E} \cdot \mathbf{F}_{in} = \hat{\mathbf{F}}^{-T}_{el} \cdot \mathbf{A} \cdot \hat{\mathbf{F}}^{-1}_{el} = \hat{\mathbf{\Gamma}}_{el} + \hat{\mathbf{\Gamma}}_{in} \,, \tag{4.6a}$$

$$\hat{\mathbf{\Gamma}}_{el} = \frac{1}{2}\left(\hat{\mathbf{F}}^T_{el} \cdot \hat{\mathbf{F}}_{el} - \mathbf{1}\right) = \frac{1}{2}\left(\hat{\mathbf{C}}_{el} - \mathbf{1}\right) \,, \tag{b}$$

$$\hat{\mathbf{\Gamma}}_{in} = \frac{1}{2}\left(\mathbf{1} - \mathbf{F}^{-T}_{in} \cdot \mathbf{F}^{-1}_{in}\right) = \frac{1}{2}\left(\mathbf{1} - \mathbf{B}^{-1}_{in}\right) \,. \tag{c}$$

The transformation of the material time derivative of the GREEN strains or the covariant OLDROYD rate of the ALMANSI strains delivers the covariant OLDROYD rate with respect to the intermediate configuration of the strain measure (4.6), which is also ad-

ditively decomposable

$$\overset{\vartriangle_{in}}{\hat{\boldsymbol{\Gamma}}} = \overset{\vartriangle_{in}}{\hat{\boldsymbol{\Gamma}}}_{el} + \overset{\vartriangle_{in}}{\hat{\boldsymbol{\Gamma}}}_{in} = \dot{\hat{\boldsymbol{\Gamma}}} + \hat{\mathbf{L}}_{in}^{T} \cdot \hat{\boldsymbol{\Gamma}} + \hat{\boldsymbol{\Gamma}} \cdot \hat{\mathbf{L}}_{in} \,, \tag{4.7a}$$

$$\overset{\vartriangle_{in}}{\hat{\boldsymbol{\Gamma}}}_{in} = \hat{\mathbf{D}}_{in} = \frac{1}{2}(\hat{\mathbf{L}}_{in} + \hat{\mathbf{L}}_{in}^{T}) = \dot{\hat{\boldsymbol{\Gamma}}}_{in} + \hat{\mathbf{L}}_{in}^{T} \cdot \hat{\boldsymbol{\Gamma}}_{in} + \hat{\boldsymbol{\Gamma}}_{in} \cdot \hat{\mathbf{L}}_{in} \,, \tag{b}$$

$$\overset{\vartriangle_{in}}{\hat{\boldsymbol{\Gamma}}}_{el} = \dot{\hat{\boldsymbol{\Gamma}}}_{el} + \hat{\mathbf{L}}_{in}^{T} \cdot \hat{\boldsymbol{\Gamma}}_{el} + \hat{\boldsymbol{\Gamma}}_{el} \cdot \hat{\mathbf{L}}_{in} \,. \tag{c}$$

Thereby, the inelastic velocity rate $\hat{\mathbf{L}}_{in}$ is defined as

$$\hat{\mathbf{L}}_{in} = \dot{\mathbf{F}}_{in} \cdot \mathbf{F}_{in}^{-1} \,. \tag{4.8}$$

Transformation of the KIRCHHOFF stress tensor or the 2nd PIOLA-KIRCHHOFF stress tensor of the reference configuration and their time derivatives in the same way defines the symmetric 2nd PIOLA-KIRCHHOFF stress tensor of the intermediate configuration

$$\hat{\mathbf{S}} = \mathbf{F}_{in} \cdot \mathbf{S} \cdot \mathbf{F}_{in}^{T} = \hat{\mathbf{F}}_{el}^{-1} \cdot \tilde{\mathbf{T}} \cdot \hat{\mathbf{F}}_{el}^{-T} \,. \tag{4.9}$$

and its objective contravariant OLDROYD rate

$$\overset{\triangledown_{in}}{\hat{\mathbf{S}}} = \dot{\hat{\mathbf{S}}} - \hat{\mathbf{L}}_{in} \cdot \hat{\mathbf{S}} - \hat{\mathbf{S}} \cdot \hat{\mathbf{L}}_{in}^{T} \,. \tag{4.10}$$

Finally, some considerations are presented for spontaneously ideal-plastic processes in order to derive the flow rule. The dissipation inequality for a single component medium under isothermal conditions taking into account the symmetry of the stress tensor reads

$$\mathcal{D}_{int} = \tilde{\mathbf{T}} : \mathbf{L} - \dot{W} = \hat{\mathbf{S}} : \overset{\vartriangle_{in}}{\hat{\boldsymbol{\Gamma}}} - \dot{W} = \hat{\mathbf{S}} : \overset{\vartriangle_{in}}{\hat{\boldsymbol{\Gamma}}}_{el} + \hat{\mathbf{S}} : \overset{\vartriangle_{in}}{\hat{\boldsymbol{\Gamma}}}_{in} - \dot{W} \geq 0 \,.$$

Using further the definition (4.7) and formulating the potential as function of the elastic strains $\hat{\boldsymbol{\Gamma}}_{el}$, the dissipation inequality is modified after some steps to

$$\begin{aligned} \mathcal{D}_{int} &= \hat{\mathbf{S}} : \left(\dot{\hat{\boldsymbol{\Gamma}}}_{el} + \hat{\mathbf{L}}_{in}^{T} \cdot \hat{\boldsymbol{\Gamma}}_{el} + \hat{\boldsymbol{\Gamma}}_{el} \cdot \hat{\mathbf{L}}_{in} \right) + \hat{\mathbf{S}} : \left(\frac{1}{2} \left(\hat{\mathbf{L}}_{in} + \hat{\mathbf{L}}_{in}^{T} \right) \right) - \frac{\partial W}{\partial \hat{\boldsymbol{\Gamma}}_{el}} : \dot{\hat{\boldsymbol{\Gamma}}}_{el} \\ &= \left[\hat{\mathbf{S}} - \frac{\partial W}{\partial \hat{\boldsymbol{\Gamma}}_{el}} \right] : \dot{\hat{\boldsymbol{\Gamma}}}_{el} + \left[\left(\mathbf{1} + 2\hat{\boldsymbol{\Gamma}}_{el} \right) \cdot \hat{\mathbf{S}} \right] : \hat{\mathbf{L}}_{in} \geq 0 \,. \end{aligned} \tag{4.11}$$

Standard argumentation for purely elastic behaviour allows the conclusion that the 2nd PIOLA-KIRCHHOFF stresses of the intermediate configuration are derived from the potential in a hyperelastic formulation

$$\hat{\mathbf{S}} - \frac{\partial W}{\partial \hat{\boldsymbol{\Gamma}}_{el}} = \mathbf{0} \quad \longrightarrow \quad \hat{\mathbf{S}} = \frac{\partial W}{\partial \hat{\boldsymbol{\Gamma}}_{el}} \,. \tag{4.12}$$

The MANDEL stress tensor $\hat{\mathbf{P}}$ occurs in the remaining part of the dissipation inequality, which is related to the 2nd PIOLA-KIRCHHOFF stresses of the intermediate configuration and the KIRCHHOFF stresses of the current configuration by

$$\hat{\mathbf{P}} = \left(\mathbf{1} + 2\hat{\boldsymbol{\Gamma}}_{el} \right) \cdot \hat{\mathbf{S}} = \hat{\mathbf{C}}_{el} \cdot \hat{\mathbf{S}} = \hat{\mathbf{F}}_{el}^{T} \cdot \tilde{\mathbf{T}} \cdot \hat{\mathbf{F}}_{el}^{-T} \,. \tag{4.13}$$

Adding a yield condition f using the LAGRANGIAN multiplier $\dot{\gamma}$ and applying the principle of maximum dissipation, the flow rule is finally obtained as

$$\hat{\mathbf{L}}_{in} = \dot{\gamma}\,\frac{\partial f}{\partial \hat{\mathbf{P}}} = \dot{\gamma}\,\hat{\mathbf{C}}_{el}^{-1}\cdot\frac{\partial f}{\partial \hat{\mathbf{S}}}\,. \tag{4.14}$$

The MANDEL stress tensor is symmetric for isotropic potential functions, and therefore the plastic flow rule is expressed by the inelastic stretch tensor $\hat{\mathbf{D}}_{in}$ only because all skew-symmetric parts vanish. Against it, additional structural tensors have to be included into the kinematic investigations for anisotropic material behaviour, see Haupt and Kersten [50]. The constitutive model is usually transformed to the reference or the current configuration.

4.1.2 Small elastic strains - finite plastic strains

The section 4.1.1 points out the theoretical framework for finite elastic and finite inelastic behaviour. Otherwise, the reversible part of the deformation is comparably small for municipal solid waste. Thus, the investigations are considerably simplified taking into account this fact. The elastic strains are small, too,

$$\|\hat{\mathbf{\Gamma}}_{el}\| \ll \mathbf{1}\,. \tag{4.15}$$

Then, the elastic stretch tensor coincides nearly with the second order identity

$$\hat{\mathbf{\Gamma}}_{el} = \frac{1}{2}\left(\hat{\mathbf{U}}_{el}^2 - \mathbf{1}\right) \quad \Longrightarrow \quad \hat{\mathbf{U}}_{el} = \sqrt{\mathbf{1} + 2\hat{\mathbf{\Gamma}}_{el}} \approx \mathbf{1}\,. \tag{4.16}$$

and the elastic deformation gradient equals approximately the elastic rotational tensor

$$\hat{\mathbf{F}}_{el} \approx \hat{\mathbf{R}}_{el}\,. \tag{4.17}$$

Moreover, the split of the deformation gradient coincides with its polar decomposition

$$\mathbf{F} = \hat{\mathbf{R}}_{el}\cdot\hat{\mathbf{U}}_{el}\cdot\mathbf{R}_{in}\cdot\mathbf{U}_{in} \approx \hat{\mathbf{R}}_{el}\cdot\mathbf{R}_{in}\cdot\mathbf{U}_{in} = \hat{\mathbf{R}}_{el}\cdot\mathbf{F}_{in}\,. \tag{4.18}$$

From the above definitions it is clear that intermediate and current configuration differ by a purely rotational motion. Thus, the orthogonal tensor $\hat{\mathbf{R}}_{el}$ appears in the co- and contravariant Push-forward and Pull-back operations only. The transformations of the strain tensor are approximately

$$\hat{\mathbf{\Gamma}} = \hat{\mathbf{F}}_{el}^T\cdot\mathbf{A}\cdot\hat{\mathbf{F}}_{el} \approx \hat{\mathbf{R}}_{el}^T\cdot\mathbf{A}\cdot\hat{\mathbf{R}}_{el}\,, \tag{4.19a}$$

$$\hat{\mathbf{\Gamma}}_{el} = \hat{\mathbf{F}}_{el}^T\cdot\mathbf{A}_{el}\cdot\hat{\mathbf{F}}_{el} \approx \hat{\mathbf{R}}_{el}^T\cdot\mathbf{A}_{el}\cdot\hat{\mathbf{R}}_{el}\,, \tag{b}$$

$$\hat{\mathbf{\Gamma}}_{in} = \hat{\mathbf{F}}_{el}^T\cdot\mathbf{A}_{in}\cdot\hat{\mathbf{F}}_{el} \approx \hat{\mathbf{R}}_{el}^T\cdot\mathbf{A}_{in}\cdot\hat{\mathbf{R}}_{el}\,. \tag{c}$$

2nd PIOLA-KIRCHHOFF and MANDEL stresses are connected with KIRCHHOFF stresses by

$$\hat{\mathbf{S}} = \hat{\mathbf{F}}_{el}^{-1} \cdot \tilde{\mathbf{T}} \cdot \hat{\mathbf{F}}_{el}^{-T} \approx \hat{\mathbf{R}}_{el}^{T} \cdot \tilde{\mathbf{T}} \cdot \hat{\mathbf{R}}_{el} \,, \tag{4.20a}$$

$$\hat{\mathbf{P}} = \hat{\mathbf{F}}_{el}^{T} \cdot \tilde{\mathbf{T}} \cdot \hat{\mathbf{F}}_{el}^{-T} \approx \hat{\mathbf{R}}_{el}^{T} \cdot \tilde{\mathbf{T}} \cdot \hat{\mathbf{R}}_{el} \,. \tag{b}$$

Since 2nd PIOLA-KIRCHHOFF and MANDEL stress are not distinguishable anymore, the skew-symmetric part in the inelastic velocity rate $\hat{\mathbf{L}}_{in}$ disappears and the flow rule states for the inelastic stretch tensor

$$\hat{\mathbf{L}}_{in} \approx \hat{\mathbf{D}}_{in} \approx \dot{\gamma} \frac{\partial f}{\partial \hat{\mathbf{S}}} \approx \hat{\mathbf{R}}_{el}^{T} \cdot \mathring{\hat{\mathbf{A}}}_{in} \cdot \hat{\mathbf{R}}_{el} \,. \tag{4.21}$$

It equals the pull-back of the inelastic strain rate tensor $\mathring{\hat{\mathbf{A}}}_{in}$ from the current configuration. In constitutive modelling, the small strain assumption plays a significant role. The reflections in section 4.1.1 show that the constitutive relations act in the intermediate configuration. Thus, stresses and other measures of the current configuration are obtained after transformation using the elastic deformation gradient. Since this transformation is almost a purely rotational motion for small elastic strains and taking into account the principle of objectivity, see Haupt [49], the constitutive relations established in the intermediate configuration can be transformed to the current configuration without changing their structure. Thereby, appropriate stress and strain measures acting in the current configuration have to be applied instead of variables defined in the intermediate configuration.

4.2 Constitutive model for municipal solid waste

As a result of the investigations of Kockel [60], municipal solid waste can be considered as a composite material consisting of a granular solid skeleton, in which fibrous particles are embedded. Ebers-Ernst [29] adopts Kockel's idea of describing municipal solid waste in the same way as the material 'reinforced earth'. The constitutive model of Ebers-Ernst is the basis for establishment of stress-strain relations here.
The assumption of complete bond is persisted for coupling the basic matrix indicated by the index 'B' and the fibres marked by 'F'. Therefore, both solid fractions undergo the same displacement fields

$$\boldsymbol{u}^{s}(\boldsymbol{X}, t) = \boldsymbol{u}^{B}(\boldsymbol{X}, t) = \boldsymbol{u}^{F}(\boldsymbol{X}, t) \,. \tag{4.22}$$

Kinematic variables describing the deformation, for instance the deformation gradient or GREEN and ALMANSI strains coincide for the two solid fractions

$$\mathbf{F}^{s}(\boldsymbol{X}, t) = \mathbf{F}^{B}(\boldsymbol{X}, t) = \mathbf{F}^{F}(\boldsymbol{X}, t) \,,\; \mathbf{E}^{s} = \mathbf{E}^{B} = \mathbf{E}^{F} \,,\; \mathbf{A}^{s} = \mathbf{A}^{B} = \mathbf{A}^{F} \,. \tag{4.23}$$

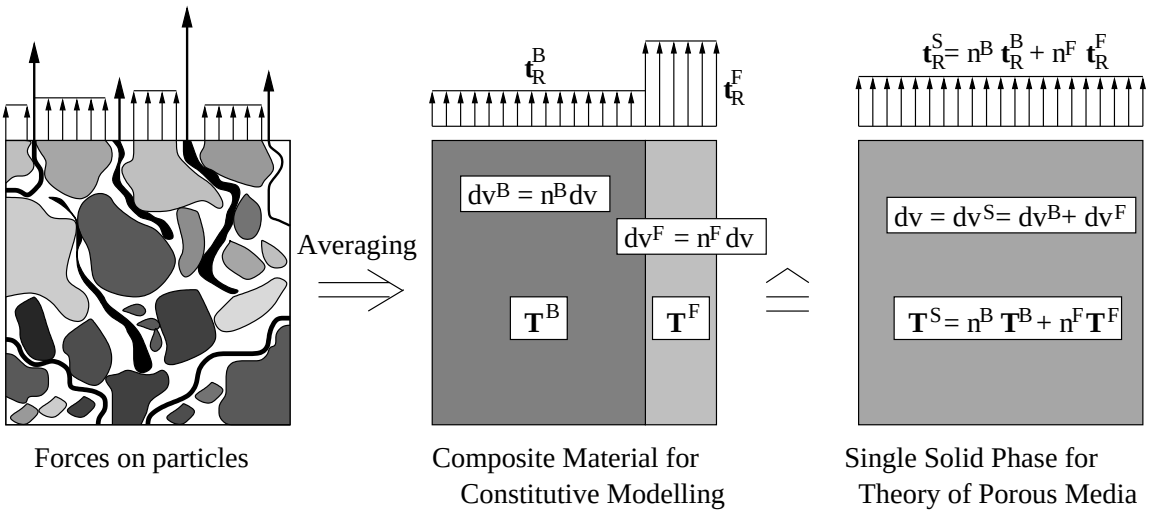

Figure 4.2: Surface traction

As a consequence of the assumption (4.22), the volume ratios of the basic matrix and the fibrous fraction cannot change during the process of motion as long as no mass exchange with other phases occurs

$$n^\alpha = \frac{dv^\alpha}{dv^B + dv^F} = \frac{\det\mathbf{F}^\alpha \, dV^\alpha}{\det\mathbf{F}^B \, dV^B + \det\mathbf{F}^F \, dV^F} = \frac{dV^\alpha}{dV^B + dV^F} = \text{const.} \qquad \text{for} \quad \alpha \in \{B, F\}\,. \tag{4.24}$$

The stress tensors of the basic matrix and the fibres are defined here in such manner that they act within the occupied volume including the pore space, which is clarified in figure 4.2. Thus, the volume filled with the basic matrix coincides with the volume of the granular particles and the macro- and micropores enclosed by them. The volume of the fibrous fraction is naturally the difference of the total volume and the volume of the basic matrix. The total surface traction $\mathbf{t}_R^s$ and the total stress $\mathbf{T}_e^s$ of the solid phase equals the sum of surface tractions $\mathbf{t}_R^\alpha$ and the partial stress tensors $\mathbf{T}^\alpha$ of the two solid fractions weighted by their volume ratios likewise a VOIGT approximation of parallel spring elements

$$\mathbf{t}_R^s = n^B \, \mathbf{t}_R^B + n^F \, \mathbf{t}_R^F\,, \qquad \mathbf{T}_e^s = n^B \, \mathbf{T}^B + n^F \, \mathbf{T}^F\,. \tag{4.25}$$

The two equations (4.25) are valid because the volume ratio coincides with the ratio of the areas of the surrounding surface. Furthermore, it is unnecessary to establish interaction terms in the partial balance laws of mechanics for the two solid fractions due to the coupling of the displacement fields. In contrast, the composite material can be viewed as a single phase in the *Theory of Porous Media* composing the extra stress tensor by the two partial stress tensors. Thus, constitutive relations are developed

independently for the two solid components in the following using a phenomenological approach in the framework of continuum mechanics. Thereby, the assumption of small elastic strains is applied allowing the formulation of the constitutive equations in the current configuration as already discussed in section 4.1.2.

4.3 Basic matrix

The basic matrix of municipal solid waste behaves similar to frictional materials. Compressive loads compact the waste by decreasing the macro- and micropore space and increase the density of the solid phase. The compaction is time-dependent as mentioned in section 2.2.2. Furthermore, biodegradation of organic matter results in additional settlements, but is not the scope of this thesis. Due to the similarity of the mechanical deformation behaviour with classical soil materials, models developed in this field are adopted here in order to describe the stress-strain behaviour. It is presumed that the total ALMANSI strain tensor $\mathbf{A}^B$ is decomposed into elastic and inelastic parts, which is admissible under the assumption of small elastic strains

$$\mathbf{A}^B = \mathbf{A}^B_{el} + \mathbf{A}^B_{in} \,. \tag{4.26}$$

Both spontaneously plastic and creep processes are irreversible and produce inelastic strains. Thus, the inelastic strain rate $\mathbf{D}^B_{in}$ that coincides with the lower OLDROYD rate of inelastic ALMANSI strain tensor is additively decomposed into

$$\mathbf{D}^B_{in} = \mathring{\mathbf{A}}^B_{in} = \mathbf{D}^B_{pl} + \mathbf{D}^B_{cr} \,. \tag{4.27}$$

Thereby. $\mathbf{D}^B_{pl}$ denotes the plastic and $\mathbf{D}^B_{cr}$ the creep induced rate.

4.3.1 Elastic regime

A fully reversible and closed deformation process is non-dissipative independently from the followed path. Thus, a potential W has to exist as a measure of the stored energy. The potential is defined by a strain energy function and such material behaviour is known as GREEN elasticity or hyperelasticity. It is a special case of CAUCHY elastic materials, in which the stress power depends on the deformation path. The strain energy function is formulated by invariants of kinematic variables, e.g., the elastic deformation gradient $\hat{\mathbf{F}}^B_{el}$, its inverse $(\hat{\mathbf{F}}^B_{el})^{-1}$ or other elastic strain measures, respectively. The elastic potential has to be polyconvex. That means, it has to be convex in all its arguments discussed in profundity by Reese [89]. The condition of coerciveness ensures that a sufficient large tangent exists in the strain energy function in terms of a norm of its arguments and that an infinite amount of energy is required to compress and extend the

material fully. A compressible NEO-HOOKEAN material taken from Bonet and Wood [14] is chosen to describe the reversible deformation behaviour of the basic matrix. The potential is formulated using the first and the third invariant of the elastic right CAUCHY-GREEN tensor $\hat{\mathbf{C}}_{el}^{B}$ as

$$W^B = \frac{\mu}{2}\left(I_{1,\hat{\mathbf{C}}_{el}^{B}} - 3\right) - \mu \ln\sqrt{I_{3,\hat{\mathbf{C}}_{el}^{B}}} + \frac{\lambda}{2}\left(\ln\sqrt{I_{3,\hat{\mathbf{C}}_{el}^{B}}}\right)^2 , \tag{4.28}$$

in which μ and λ are LAME's constants and the invariants are related to the elastic deformation gradient by

$$I_{1,\hat{\mathbf{C}}_{el}^{B}} = \mathrm{tr}(\hat{\mathbf{C}}_{el}^{B}) = (\hat{\mathbf{F}}_{el}^{B})^T \cdot \hat{\mathbf{F}}_{el}^{B} : \mathbf{1} , \qquad \sqrt{I_{3,\hat{\mathbf{C}}_{el}^{B}}} = \sqrt{\det(\hat{\mathbf{C}}_{el}^{B})} = \det(\hat{\mathbf{F}}_{el}^{B}) .$$

The 2nd PIOLA-KIRCHHOFF stresses of the intermediate configuration is obtained by applying equation (4.12)

$$\hat{\mathbf{S}}^B = \frac{\partial W^B}{\partial \hat{\mathbf{\Gamma}}_{el}} = 2\,\frac{\partial W^B}{\partial \hat{\mathbf{C}}_{el}^{B}} = \mu\left(\mathbf{1} - (\hat{\mathbf{C}}_{el}^{B})^{-1}\right) + \lambda \ln\left(\sqrt{I_{3,\hat{\mathbf{C}}_{el}^{B}}}\right)\,(\hat{\mathbf{C}}_{el}^{B})^{-1} . \tag{4.29}$$

The KIRCHHOFF stress tensor $\tilde{\mathbf{T}}^B$ of the current configuration is obtained by the covariant Push-forward of the 2nd PIOLA-KIRCHHOFF stresses of the intermediate configuration by the elastic deformation gradient

$$\begin{aligned}\tilde{\mathbf{T}}^B = \hat{\mathbf{F}}_{el}^{B} \cdot \hat{\mathbf{S}}^B \cdot (\hat{\mathbf{F}}_{el}^{B})^T &= \mu\left(\mathbf{B}_{el}^{B} - \mathbf{1}\right) + \lambda \ln(\sqrt{I_{3,\mathbf{B}_{el}^{B}}})\,\mathbf{1} \\ &= \mu\left(\hat{\mathbf{F}}_{el}^{B} \cdot (\hat{\mathbf{F}}_{el}^{B})^T - \mathbf{1}\right) + \lambda \ln(\det\hat{\mathbf{F}}_{el}^{B})\,\mathbf{1} .\end{aligned} \tag{4.30}$$

The elastic left CAUCHY-GREEN tensor is determined by equation (4.26)

$$\mathbf{B}_{el}^{B} = \left(\mathbf{1} - 2\,\mathbf{A}_{el}^{B}\right)^{-1} = \left[\mathbf{1} - 2\,\left(\mathbf{A}^B - \mathbf{A}_{in}^{B}\right)\right]^{-1} \tag{4.31}$$

Since the small elastic strain assumption is valid, a linearised elastic stress-strain relation may be employed instead of equation (4.30)

$$\tilde{\mathbf{T}}^B = 2\,\mu\,\mathbf{A}_{el}^{B} + \lambda\,\mathrm{tr}\mathbf{A}_{el}^{B}\,\mathbf{1} . \tag{4.32}$$

4.3.2 Yield surface for spontaneously inelastic behaviour

The elastic region of the stress space is limited by a yield envelope. The MOHR-COULOMB criterion is the most important failure hypothesis for frictional materials and soils. It is expressed by invariants of the stress tensor in three-dimensional version as

$$f_{MC} = \sqrt{J_{2D,\tilde{\mathbf{T}}^B}}\left(\cos(\theta) + \frac{\sin\phi'}{\sqrt{3}}\sin(\theta)\right) + I_{1,\tilde{\mathbf{T}}^B}\frac{\sin\phi'}{3} - c'\,\cos\phi' \le 0 . \tag{4.33}$$

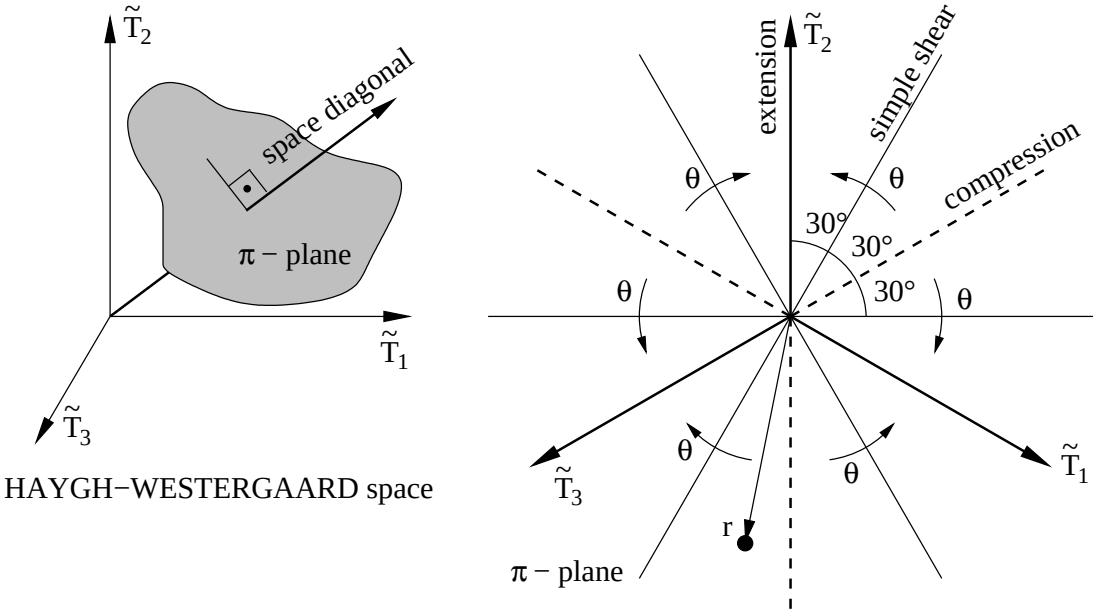

Figure 4.3: Definitions in π-plane

Thereby, the shear parameters angle of internal friction ϕ' and cohesion c' characterise the specific material. The invariants of the stress tensor are defined as followed

$$I_{1,\tilde{\mathbf{T}}^B} = \mathrm{tr}\tilde{\mathbf{T}}^B = \tilde{\mathbf{T}}^B : \mathbf{1},\;\; I_{2,\tilde{\mathbf{T}}^B} = \frac{1}{2}\left((\tilde{\mathbf{T}}^B)^T : \tilde{\mathbf{T}}^B - \mathrm{tr}(\tilde{\mathbf{T}}^B)^2\right),\;\; I_{3,\tilde{\mathbf{T}}^B} = \det\tilde{\mathbf{T}}^B\,.$$

The deviator of the stress tensor is computed by

$$\tilde{\mathbf{T}}^B_D = \mathrm{dev}\tilde{\mathbf{T}}^B = \tilde{\mathbf{T}}^B - \frac{1}{3}\tilde{\mathbf{T}}^B : \mathbf{1}\,.$$

and its invariants are denoted by J instead of I here. It is helpful to reformulate yield envelopes in REUSS-coordinates in order to illustrate their shapes. The three coordinates are defined as

$$\xi = \frac{I_{1,\tilde{\mathbf{T}}^B}}{3}\,,\quad r = \sqrt{2\,J_{2D,\tilde{\mathbf{T}}^B}}\,,\quad \theta = \frac{1}{3}\arcsin\left(\frac{\sqrt{27}}{2}\frac{J_{2D,\tilde{\mathbf{T}}^B}}{J^{3/2}_{3D,\tilde{\mathbf{T}}^B}}\right)\,. \tag{4.34}$$

The coordinate axis ξ coincides with the space diagonal of the HAYGH-WESTERGAARD space and represents the hydrostatic part of the stresses illustrated in figure 4.3. The coordinate r corresponds with the distance of a stress state in the deviatoric π-plane to the space diagonal and the coordinate θ is the LODE-angle characterising the position with respect to the images of the CARTESIAN axes in the π-plane having in mind that its domain is limited by $-30° < \theta \leq 30°$.

Transforming of equation (4.33) results in

$$r_{MC} = \sqrt{2}\;(c'\,\cos\phi' - \xi\,\sin\phi')\;\;\frac{1}{\cos(\theta) + \frac{\sin\phi'}{\sqrt{3}}\sin(\theta)} \leq 0\,. \tag{4.35}$$

	Lode-angle	Parameter	
	θ	α_f	κ_f
compression cone	$-\frac{\pi}{6}$	$\frac{2\,\sin\phi'}{\sqrt{3}(3-\sin\phi')}$	$\frac{6\,c'\,\cos\phi'}{\sqrt{3}(3-\sin\phi')}$
extension cone	$\frac{\pi}{6}$	$\frac{2\,\sin\phi'}{\sqrt{3}(3+\sin\phi')}$	$\frac{6\,c'\,\cos\phi'}{\sqrt{3}(3+\sin\phi')}$
simple shear	0	$\frac{\sin\phi'}{3}$	$c'\,\cos\phi'$
plane strain		$\frac{\tan\phi'}{9+12\,\tan^2\phi'}$	$\frac{3\,c'}{9+12\,\tan^2\phi'}$

Table 4.1: Parameters for DRUCKER-PRAGER yield criterion

The first part is a function of the coordinate ξ only and the second part describes the shape of the yield envelope in the π-plane. Since one easily detects that the deviatoric part defines a straight line, the MOHR-COULOMB envelope (4.33) is a pyramid with a hexagonal base area. Thus, the edges of the pyramid can cause considerably additional effort in numerical implementations. A couple of single yield surfaces is developed to overcome and avoid such extra treatments. The DRUCKER-PRAGER criterion [28] is the oldest and simplest approach

$$f_{DP} = \sqrt{J_{2D,\tilde{\mathbf{T}}^B}} + \alpha_f\, I_{1,\tilde{\mathbf{T}}^B} - \kappa_f \leq 0\,, \tag{4.36}$$

$$r_{DP} = \sqrt{2}\,\left(\kappa_f - 3\,\alpha_f\,\xi\,\right)\;\; 1 \leq 0 \tag{4.37}$$

Its shape function in the π-plane is a circle. The parameters α_f and κ_f are fitted on the MOHR-COULOMB criterion (4.35) for a chosen value of θ. The most important parameter sets are summarised in table 4.1. A comparison of the yield surfaces in the π-plane is shown in figure 4.4. Obviously, the DRUCKER-PRAGER criterion is not able to reproduce the different behaviour of granular materials under compression and extension in a satisfying way. The compressive cone encloses all stress points taken from cubically triaxial tests on sand of Lade and Duncan [65], but it overestimates the strength considerably. In contrast, the extensional cone fits better the values under extension, but it underestimates the strength under compressive load paths. Therefore, the DRUCKER-PRAGER yield criterion is improper for modelling granular materials and is not used in this thesis. More sophisticated yield criteria are developed in the past in order to reproduce better the behaviour of frictional materials. Davis and Selvadurai [18] discuss in detail the criterion of Matsuoka and Nakai and of Lade and Duncan.
A simplified version of a single yield surface originally proposed by Ehlers [30] for sand is employed in this thesis

$$f_E = \sqrt{J_{2D,\tilde{\mathbf{T}}^B}\left(1+\gamma\frac{J_{3D,\tilde{\mathbf{T}}^B}}{J^{3/2}_{2D,\tilde{\mathbf{T}}^B}}\right)^m + \frac{1}{2}\delta_f\, I^2_{1,\tilde{\mathbf{T}}^B}} + \alpha_f\, I_{1,\tilde{\mathbf{T}}^B} - \kappa_f \leq 0\,, \tag{4.38}$$

$$r_E = \sqrt{2}\,\left[\left(\kappa - 3\,\alpha_f\,\xi\,\right)^2 - \frac{9}{2}\delta_f\,\xi^2\right]^{1/2}\;\left[1+\gamma\frac{2}{\sqrt{27}}\sin(3\theta)\right]^{-m/2} \leq 0\,. \tag{4.39}$$

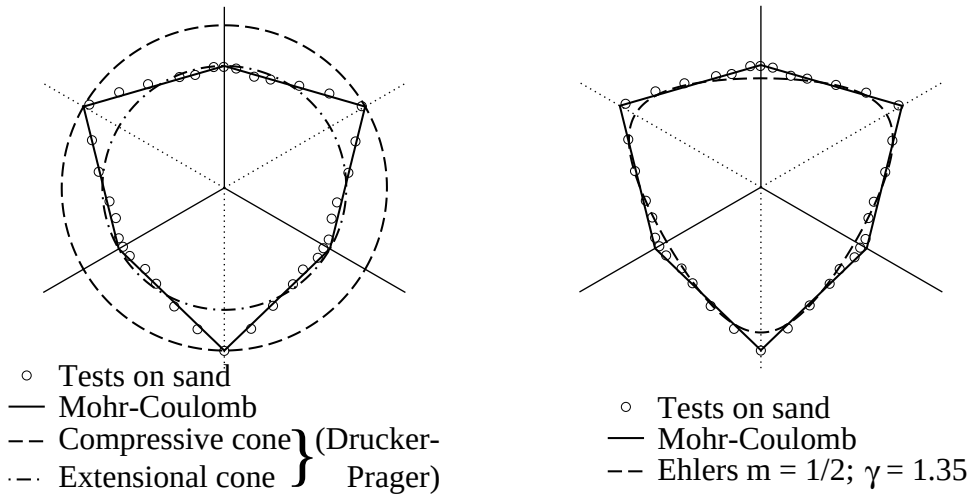

Figure 4.4: Yield surfaces in π-plane

The model parameters m and γ determine the shape of the yield surface in the π-plane. But not all possible combinations of the two parameters are admissible without violating the convexity requirement of plasticity theory. Own investigations expose that setting the parameter $m = 1/2$ enables an accurate representation of MOHR-COULOMB criterion and experimental data for friction angles up to 45°. The parameter γ is fitted on the ratio between the minor and the major vertex of the MOHR-COULOMB criterion for a given angle of internal friction

$$\frac{r_{min}}{r_{maj}} = \frac{3-\sin\phi'}{3+\sin\phi'} = \left(\frac{1+\gamma\frac{2}{\sqrt{27}}}{1-\gamma\frac{2}{\sqrt{27}}}\right)^{-m/2} \quad \rightarrow \quad \gamma = \frac{\sqrt{27}}{2}\,\frac{1-\left(\frac{3-\sin\phi'}{3+\sin\phi'}\right)^{2/m}}{1+\left(\frac{3-\sin\phi'}{3+\sin\phi'}\right)^{2/m}}.$$

For instance, a friction angle of 30°leads to $\gamma = 1.52$, which is used in the computations later. The parameters α and κ are fitted on the hydrostatic part of MOHR-COULOMB envelope for simple shear $\theta = 0$. Thus, they are related to the classical shear parameters by

$$\alpha = \frac{\sin\phi'}{3}\,, \qquad\qquad \kappa = c'\,\cos\phi'\,. \tag{4.40}$$

The parameter δ_f is defined in the tensile regime $\xi > 0$ only in order to round the tip of the yield cone. The special form of Ehlers' model allows such a procedure without introducing any discontinuity. A cap can be modelled in the pressure regime by the yield envelope, too. The effects of different values for δ_f are shown in figure 4.5.
In section 4.1 the flow rule is derived under the assumption of maximal dissipation. Thereby, the plastic strain rate is proportional to the gradient of the yield condition. Such an associated flow rule is in a good agreement with experimental observations for metals. In contrast, an associated flow rule often leads to unrealistic dilatant behaviour

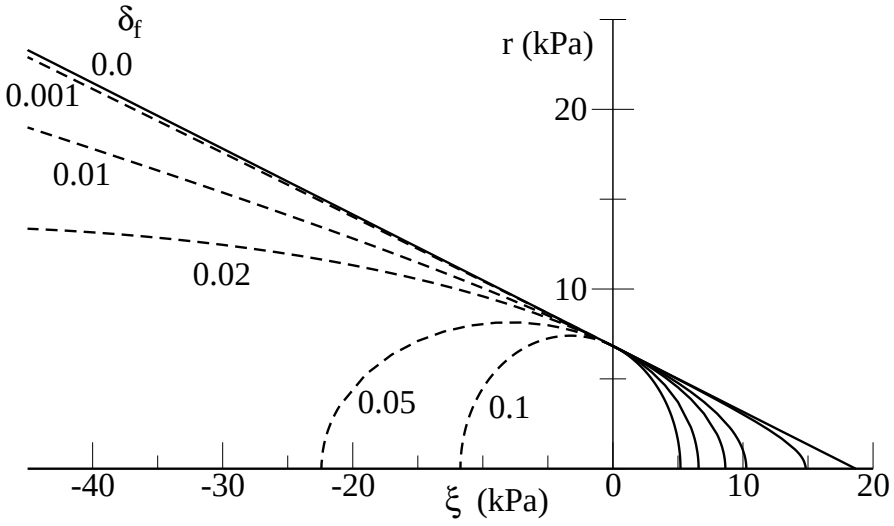

Figure 4.5: Yield envelope in dependency of parameter δ_f ($\phi' = 15°$, $c' = 5$ kPa ,$\theta = 0°$)

for granular materials. Thus, a plastic potential is introduced here

$$q_E = \sqrt{J_{2D,\tilde{\mathbf{T}}^B} + \frac{1}{2}\delta_q \, I^2_{1,\tilde{\mathbf{T}}^B}} + \alpha_q \, I_{1,\tilde{\mathbf{T}}^B} \, . \tag{4.41}$$

and the plastic strain rate is obtained with an LAGRANGIAN multiplier $\dot{\gamma}^B_{pl}$ as

$$\mathbf{D}^B_{pl} = \dot{\gamma}^B_{pl} \frac{\partial \, q_E}{\partial \, \tilde{\mathbf{T}}^B} \, . \tag{4.42}$$

Since the guarantee of non-negative dissipation is not maintained automatically, such an approach has to be applied with care and the compliance with the 2nd law of thermodynamics must be checked. The parameter α_q, which is related to the angle of dilatancy ψ in a similar manner as the parameter α_f to the angle of internal friction ϕ', appears compared to the yield condition (4.38)

$$\alpha_q = \frac{\sin \psi}{3} \, . \tag{4.43}$$

In addition, the complex shape in the deviatoric plane is eliminated and the parameter δ_q is used in the tensile regime to avoid numerical trouble due to the singularity on the top of the cone. In general, it is possible to model a cap also in the compressive regime of the plastic potential. Then, more complex strain histories can be reproduced changing from contractant to dilatant behaviour. But within the model for municipal solid waste presented here, all inelastic decreasing of volume is attributed to the creep processes described later on.
Obviously, the shear parameters cannot be constants for municipal solid waste. Moreover, the shear resistance of the highly deformable skeleton depends on the porosity and dry density of the material as mentioned before in section 2.2.3. Two limits exist in general. If the material achieves its highest density, the shear strength reaches a maximum

caused by interlocking effects and an increased contact area between different particles. On the contrary, the shear resistance is lost rapidly if the dry density decreases drastically and the porosity grows. Thereby, the contact between neighbouring particles may be lost.

4.3.3 Volumetric strains

It is necessary to introduce some volume definitions in order to describe the volume changes during the deformation process. The volume for the loosest bulk density is denoted by dv_l, the volume in the densest state by dv_d. After emplacement the material occupies the volume dv_0, at the current time the volume dv_t and after decaying of creep processes under a given load the volume dv_∞. Figure 4.6 clarifies the meaning of different volume definitions. The inelastic volume strain of the basic matrix is an internal kinematic variable, which characterises the state of densification. At first, the current total volume strain is defined by

$$a_v^B = \frac{dv_t^B - dv_l^B}{dv_t^B} = 1 - \frac{dv_0^B}{\det\mathbf{F}^B\, dv_0^B} + \frac{dv_0^B - dv_l^B}{\det\mathbf{F}^B\, dv_0^B}$$
$$= 1 - \frac{1}{\det\mathbf{F}^B} + \frac{a_{v,0}^B}{\det\mathbf{F}^B} = 1 - \frac{1 - a_{v,0}^B}{\det\mathbf{F}^B}\,. \tag{4.44}$$

The initial value $a_{v,0}^B$ describes the difference between the loosest possible bulk density and the density after emplacement at beginning of the observation. The maximal reachable inelastic volume strain $a_{v,max}^B$ expresses the differences between the density after emplacement and the highest possible bulk density

$$a_{v,0}^B = \frac{dv_0^B - dv_l^B}{dv_0^B}\,, \qquad a_{v,max}^B = \frac{dv_d^B - dv_0^B}{dv_0^B}\,.$$

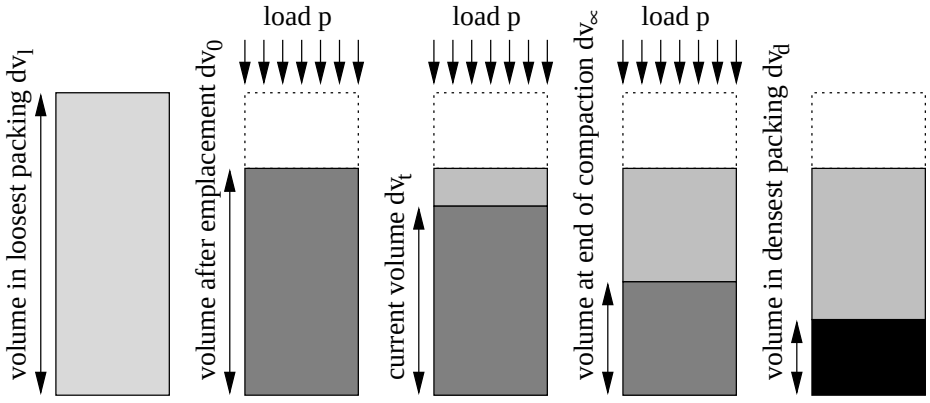

Figure 4.6: Meaning of differential volumes during process of deformation

Since most of the occurring deformation is irreversible, the elastic part of the deformation is negligible ($\det\mathbf{F}^B_{el} \approx 1$). For this reason, the total volume strain equals the inelastic volume strain approximately

$$\begin{aligned} a^B_v \approx a^B_{v,in} &= 1 - \frac{1 - a^B_{v,0}}{\det\mathbf{F}^B_{in}} \\ &= 1 - (1 - a^B_{v,0}) \sqrt{1 - 2\, I_{1,\mathbf{A}^B_{in}} + 4\, I_{2,\mathbf{A}^B_{in}} - 8\, I_{3,\mathbf{A}^B_{in}}} \end{aligned} \tag{4.45}$$

replacing the determinant of the inelastic deformation gradient by the invariants of the inelastic Almansi strains using standard tensor calculus.
Hyperbolic functions are applied to capture the mentioned limits and to ensure that non-negative values for the angle of internal friction, the cohesion and the angle of dilatancy occur

$$\phi' = a_{\phi'} \left(\frac{1 - \tanh(b_{\phi'}\, a^B_{v,in})}{2} \right)^{c_{\phi'}} f^{\phi'}_w \,, \tag{4.46a}$$

$$c' = a_{c'} \left(\frac{1 - \tanh(b_{c'}\, a^B_{v,in})}{2} \right)^{c_{c'}} f^{c'}_w \,, \tag{b}$$

$$\psi = a_{\psi} \left(\frac{1 - \tanh(b_{\psi}\, a^B_{v,in})}{2} \right)^{c_{\psi}} f^{\psi}_w \,. \tag{c}$$

The parameter $a_{\phi'}$ is the angle of internal friction in the densest packing ($a^B_{v,in} \to -\infty$). Furthermore, the parameter $c_{\phi'}$ describes the ratio of the frictional angle between the highest and the lowest bulk density

$$c_{\phi'} = \log_2 \left(\frac{\phi'_{a^B_{v,in} \to -\infty}}{\phi'_{a_{v,in}=0}} \right) .$$

The parameter $b_{\phi'}$ controls the development during densification or loosening. Similar considerations are valid for the functions for the cohesion and the angle of dilatancy.
The factors $f^{\phi'}_w$, $f^{c'}_w$ and f^{ψ}_w describe the influence of the liquid content on the shear resistance of the solid material. The effects are not fully understood in detail until now. Experimental results of Kockel [60] and Münnich et al. [85] indicate that the shear strength is reduced if a higher water content is present. The experimental determination is quite difficult because effects from changing of the porosity and from matric suction or excess pore water are superposed. In general, it is assumed that water situated in the joints between different solid particles can reduce the frictional effects. Thus, the factors are predefined here by

$$\begin{aligned} f^{\phi'}_w &= \frac{1}{2} - \frac{1}{\pi} \arctan\left(a^{\phi'}_w (\omega^l_s - b^{\phi'}_w) \right) , \quad f^{c}_w = \frac{1}{2} - \frac{1}{\pi} \arctan\left(a^{c}_w (\omega^l_s - b^{c}_w) \right) , \\ f^{\psi}_w &= \frac{1}{2} - \frac{1}{\pi} \arctan\left(a^{c}_w (\omega^l_s - b^{\psi}_w) \right) . \end{aligned} \tag{4.47}$$

The liquid or water content ω_s^l is defined as mass concentration factor of the mass of the pore liquid related to the mass of the dry solid waste

$$\omega_s^l = \frac{m^l}{m^s} = \frac{\rho^l}{\rho^s} = \frac{\tilde{\rho}^l \, \Phi \, S^l}{\rho^s} \approx \frac{\tilde{\rho}^l \, \Phi \, (1 - S^g)}{\tilde{\rho}^s \, (1 - \Phi)} \, . \tag{4.48}$$

The parameters $b_w^{\phi'}$ is the water content, where the shear angle ϕ' is half of the shear angle of the dry material $\omega_s^l = 0$. The parameter $a_w^{\phi'}$ controls the reduction of ϕ' from the dry to the wet regime. Since no experimental data are available to quantify the influence is skipped and the parameters $f_w^{\phi'}$, $f_w^{c'}$ and f_w^{ψ} are set to 1.0 for all computations later on. The problem of constitutive modelling of granular materials under partially saturated conditions is object of actual research. A lot of open questions are still existing concerning the influence of pore pressure as well as water content for constitutive modelling. Some general remarks on this topic are provided by Jommi [54].

4.3.4 Time-dependent compaction

As discussed in section 2.2.2 time-dependent deformations are produced by mechanical processes as well as by decomposition of organic matter. In this thesis short-time creep processes are modelled for the 3rd stage of the characteristic time-settlement curve of municipal solid waste only. Thereby, the solid particles go into a denser packing. The macro- and micropore space is reduced and solid particles crush partially. The creep rate depends on the actual stress level, the actual density and porosity and a final value of the process of compaction in a phenomenological description.
The material is asymptotically compacted to the highest bulk density if the compressive load tends to infinity. No compaction occurs under tensile stresses. The rate converges to zero for a constant pressure if the final value of compaction is reached. Furthermore, the compaction occurs mainly in the direction of the load. Therefore, the inelastic rate is the sum of the dyads formed by the eigenvectors of the KIRCHHOFF stresses multiplied by a LAGRANGIAN factor

$$\mathbf{D}_{cr}^B = \sum_{\alpha=1}^{3} \dot{\gamma}_{cr,\alpha} \left(\mathbf{n}_{\tilde{\mathbf{T}}^B,\alpha} \otimes \mathbf{n}_{\tilde{\mathbf{T}}^B,\alpha} \right) \, . \tag{4.49}$$

The multiplier $\dot{\gamma}_{cr,\alpha}$ is the rate in every principal direction of the stresses $\boldsymbol{n}_{\tilde{\mathbf{T}}^B,\alpha}$ and is formulated as a function of the stress level and the state of densification using the inelastic volume strain as internal variable

$$\dot{\gamma}_{cr,\alpha} = f_1(\tilde{\mathbf{T}}^B) \, f_2(a_{v,in}^B) \tag{4.50}$$

The stress dependency is expressed by a NORTON creep law using the eigenvalue of the stress tensor $\tilde{T}^B_{\alpha\alpha}$ in the investigated direction

$$f_1(\tilde{\mathbf{T}}^B) = -A \left(\frac{\left\langle -\tilde{T}^B_{\alpha\alpha} \right\rangle}{\sigma_0} \right)^n . \tag{4.51}$$

The ramp function <...> ensures that only negative principal stresses create compaction. The parameter $\sigma_0 = 1.0$ kPa normalises the stress inside the brackets, whereas A and n are model parameters controlling the stress dependency. The dependency on the actual density is expressed applying the inelastic volume strain again. Thereby, the function

$$f_2(a^B_{v,in}) = \left[\ln \left(\frac{a^B_{v,\infty}}{a^B_{v,\infty} - a^B_{v,in}} \right) \right]^{-p} \tag{4.52}$$

ensures that the rate decreases drastically if the densest possible packing under a certain stress level is reached. The final inelastic volume strain under a specific stress level $a^B_{v,\infty}$ is modelled as a function of the stresses, too,

$$a^B_{v,\infty} = \frac{dv_\infty - dv_l}{dv_t} = \det\mathbf{F}^B_{in} \; \frac{b_{cr}\, c_{v,0} + \left| \sum_{\alpha=1}^{3} \left\langle -\tilde{T}^B_{\alpha\alpha} \right\rangle \right|^{a_{cr}} c_{v,max}}{b_{cr} + \left| \sum_{\alpha=1}^{3} \left\langle -\tilde{T}^B_{\alpha\alpha} \right\rangle \right|^{a_{cr}}} . \tag{4.53}$$

Therein, $c_{v,0}$ and $c_{v,max}$ are correlated to the initial density and the density in highest possible compaction, respectively. In the computations later on the parameter $c_{v,0}$ coincides with the initial inelastic volume strain $a^B_{v,0}$. The parameters p, a_{cr} and b_{cr} have no physical meaning and are determined using identification procedures on laboratory tests, e.g. oedometric tests. The function (4.52) tends to infinity for values nearby the lowest bulk density $a^B_{v,in} \approx 0$. Thus, the function is regularised in a crude matter and limited by a value of 10^8. Function f_2 is set to zero if the actual volume strain is lower than the final value $a^B_{v,\infty}$ for a given load level. Such situations may occur if a layer is vertically loaded first and than partially unloaded.

The compaction model couples the shear strength parameters with the development of the inelastic volume strain as internal variable. Since municipal solid waste is usually loaded vertically by the dead loads of overburden layers, the material is mainly compacted in vertical direction due to the anisotropic strain rate for creeping in the modelling approach. The densification results in an increase of the shear strength expressed by the functional dependency of the angle of internal friction and the cohesion on the inelastic volume strain.

A further dependency on the water content and the pore water flow of the compaction can be supposed. In-situ observations [85] show an increase of settlements after heavy rain, but laboratory tests are contradictorily and partially inconsistent with the in-situ observations. Thus, including the contribution of pore water content on the mechanical creep is still outstanding.

4.4 Fibrous constituents

The fibrous constituents are orientated in a horizontal plane mainly, which is caused by the emplacement and the compaction due to the compression by overburden layers. Thus, they behave anisotropically in the proposed smeared approach. The fibrous fraction is characterised by a small initial elastic branch and undergoes irreversible deformation exhibiting hardening as well as softening behaviour as displayed in figure 2.14. The time-independent behaviour is modelled by an elasto-plastic approach. Therefore, the total Almansi-strains are decomposed into elastic and inelastic parts by

$$\mathbf{A}^F = \mathbf{A}^F_{el} + \mathbf{A}^F_{in}\,. \tag{4.54}$$

The hardening and softening is modelled using internal variables. The anisotropy is contributed to the elastic regime.

4.4.1 Elastic regime

Since the fibres act in a horizontal plane, a transversal-isotropic elastic relation is an appropriate instrument to capture this kind of anisotropy. Lürding [74] proposes a strain energy function for the elastic response of similar materials

$$\begin{aligned} W^F = {} & a_{\shortparallel}\,(I_{\shortparallel} - 1) + a_{\perp}\,(I_{\perp} - 2) + b_{\perp}\,(II_{\perp} - 1) + b_{\shortparallel}\,(II_{\shortparallel} - 2) + c\,(III - 1) \\ & - \frac{1}{2}a^*_{\shortparallel}\ln(I_{\shortparallel}) - \frac{1}{2}b^*_{\perp}\ln(II_{\perp}) - \frac{1}{2}c^*_{\perp}\ln(III) \end{aligned} \tag{4.55}$$

using different invariants of the elastic right CAUCHY-GREEN tensor in CARTESIAN coordinates. The transversal axis indicating by '$\shortparallel$' coincides with the 3rd basis and stands orthogonal on the fibrous plane denoted by '$\perp$'. The 1st and 2nd basis vector span the fibrous plane. The definitions of the invariants are given in the original literature and the 2nd PIOLA-KIRCHHOFF stresses in the intermediate configuration equal the derivation of the potential with respect to the elastic strains. Since the small elastic strain assumption is also valid for the fibrous constituents, the linearised version of the local stress-strain relation is implemented later on

$$\hat{\mathbf{\Gamma}}^F_{el,loc} = \mathbb{F}^{lin}_{loc} : \hat{\mathbf{S}}^F_{loc}\,. \tag{4.56}$$

The flexibility tensor is defined in VOIGT notation, published by Altenbach [4],

$$\underline{\underline{\mathbb{F}}}^{lin}_{loc} = \begin{bmatrix} \frac{1}{E_{\perp}} & \frac{-\nu_{\perp}}{E_{\perp}} & \frac{-\nu_{\shortparallel}}{E_{\shortparallel}} & 0 & 0 & 0 \\ \frac{-\nu_{\perp}}{E_{\perp}} & \frac{1}{E_{\perp}} & \frac{-\nu_{\shortparallel}}{E_{\shortparallel}} & 0 & 0 & 0 \\ \frac{-\nu_{\shortparallel}}{E_{\shortparallel}} & \frac{-\nu_{\shortparallel}}{E_{\shortparallel}} & \frac{1}{E_{\shortparallel}} & 0 & 0 & 0 \\ 0 & 0 & 0 & \frac{2\,(1+\nu_{\perp})}{E_{\perp}} & 0 & 0 \\ 0 & 0 & 0 & 0 & \frac{1}{2\,G_{\shortparallel}} & 0 \\ 0 & 0 & 0 & 0 & 0 & \frac{1}{2\,G_{\shortparallel}} \end{bmatrix}.$$

YOUNG's modulus $E_{\shortparallel}$ and POISSON's ratio $\nu_{\shortparallel}$ describe the deformation behaviour parallel to the transversal axis. The shear modulus $G_{\shortparallel}$ characterises the stress-strain relation including the transversal axis and one axis of the fibrous plane. Both parameters $E_{\perp}$ and $\nu_{\perp}$ describe the elastic stiffness in the fibrous plane. After carrying out the transformation of equation (4.56) into the current configuration, the elastic relation between the KIRCHHOFF-stress tensor and the elastic ALMANSI strains is obtained as

$$\tilde{\mathbf{T}}^F = \left[(\mathbf{R}^F)^T \otimes (\mathbf{R}^F)^T\right]^{T_{23}} : \mathbb{C}_{loc}^{lin} : \left[\mathbf{R}^F \otimes \mathbf{R}^F\right]^{T_{23}} : \mathbf{A}_{el}^F \,. \tag{4.57}$$

The rotational tensor $\mathbf{R}^F$ describes the current position of the fibrous plane in global coordinates. It is formed by three vectors

$$\mathbf{R}^F = \begin{bmatrix} \boldsymbol{n}_1^T \\ \boldsymbol{n}_2^T \\ \boldsymbol{n}_3^T \end{bmatrix} \tag{4.58}$$

$$\text{with } \boldsymbol{n}_1 = \frac{(\mathbf{F}^s \cdot \boldsymbol{N}_1)}{|(\mathbf{F}^s \cdot \boldsymbol{N}_1)|}\,, \quad \boldsymbol{n}_3 = \frac{(\mathbf{F}^s \cdot \boldsymbol{N}_1) \times (\mathbf{F}^s \cdot \boldsymbol{N}_2)}{|(\mathbf{F}^s \cdot \boldsymbol{N}_1) \times (\mathbf{F}^s \cdot \boldsymbol{N}_2)|}\,, \quad \boldsymbol{n}_2 = \boldsymbol{n}_3 \times \boldsymbol{n}_1 \,.$$

The two vectors $\boldsymbol{N}_1$ and $\boldsymbol{N}_2$ span the plane in the reference configuration. They are mapped by the deformation gradient $\mathbf{F}^s$ into the current configuration and their images are used to construct the new local basis $\boldsymbol{n}_i$. The mechanism is pointed out graphically in figure 4.7. The dyadic products constructed by the rotational tensor $\mathbf{R}^F$ and its transpose are fourth order tensors to rotate strains and stresses. At first, the strains are transformed into the local coordinates. Then, the locally defined stresses are computed, which have to be rotated back into the global framework.

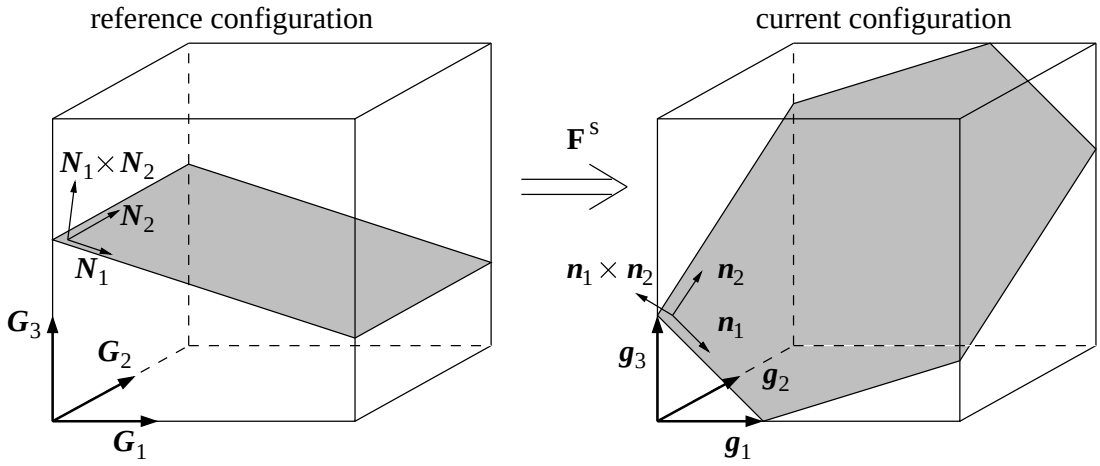

Figure 4.7: Rotation of fibrous plane during deformation

4.4.2 Inelastic behaviour

As discussed before in section 2.2.3, two mechanisms exist that limit the bearing capacity of the fibres. The fibres are pulled out of the surrounding basic matrix during bonding failure. Against it, the fibres rupture themselves if their specific strength is exceeded. The bonding mechanism bases mainly on frictional effects in the contact zone between a single fibre and the granular particles around. The friction depends on the surface structure of the particles and on the pressure orthogonal to the contact plane. Due to the bonding mechanism a difference in the local displacements between the two solid fraction occurs, but it is not considered here. A micromechanical approach is necessary in order to incorporate such effects. The specific tensile strength of a single fibre depends on its substantial composition. Thus, fibres and sheets of papers or cardboards behave completely different compared to particles consisting of metal, wood or rubber. Some weaker particles may be teared, whereas others are marginally loaded only. It can be assumed that the fibres are not able to carry any compressive stresses due to the fact that they consist mainly of thin elements, e.g., papers and foils, which buckle under low tangential pressure.
A RANKINE criterion is applied here in order to model the listed failure mechanisms. Thus, each of the three principal stresses $\tilde{T}^F_{\alpha\alpha}$ of the fibrous fraction has to fulfil the yield criterion in the compressive zone

$$f_{c,\alpha} = -\tilde{T}^F_{\alpha\alpha} - \tilde{T}_{c,\alpha} \leq 0 \tag{4.59}$$

and in the tensile zone

$$f_{t,\alpha} = \tilde{T}^F_{\alpha\alpha} - \left[\tilde{T}_{t,0} + \tilde{T}_{h,\alpha}(\tilde{\mathbf{T}}^B, \mathbf{A}^F_{in}) + \tilde{T}_{s,\alpha}(\tilde{\mathbf{T}}^B, \mathbf{A}^F_i n)\right] \leq 0\,. \tag{4.60}$$

Since the fibres fail under low compressive stresses, the constant compressive strength value $\tilde{T}_{c,\alpha}$ is set to a small value lower than 1 kPa, which is slightly modified for each direction in order to avoid numerical trouble. The tensile strength is decomposed into three parts. The first part $\tilde{T}_{t,0}$ is the initial tensile strength, which is independent of the state of loading. The second part models the bonding mechanism in dependency on the stresses of the basic matrix as well as on the state of hardening by a multiplicative approach

$$\tilde{T}_{h,\alpha}(\tilde{\mathbf{T}}^B, \mathbf{A}^F_{in}) = \tilde{T}_{m,\alpha}(\tilde{\mathbf{T}}^B)\;\; h_{1,\alpha}(\mathbf{A}^F_{in})\,. \tag{4.61}$$

The bond is modelled following Kölsch's idea of a load-depending tensile strength of the fibres by a trilinear function applying indirectly a linear friction law

$$\tilde{T}_{m,\alpha}(\tilde{\mathbf{T}}^B) = \begin{cases} \tilde{T}_{min} & \text{for} \quad \tilde{T}^B_{V,\alpha} > 0\,, \\ \tilde{T}_{min} + \frac{\tilde{T}_{max} - \tilde{T}_{min}}{\tilde{T}^B_{crit}} \tilde{T}^B_{V,\alpha} & \text{for} \quad 0 \geq \tilde{T}^B_{V,\alpha} > \tilde{T}^B_{crit}\,, \\ \tilde{T}_{max} & \text{for} \quad \tilde{T}B_{crit} > \tilde{T}^B_{V,\alpha}\,. \end{cases} \tag{4.62}$$

$\tilde{T}^B_{V,\alpha}$ are the major KIRCHHOFF stresses of the basic matrix acting in the plane orthogonal to the investigated principal stress axis $\boldsymbol{n}_\alpha$ of the fibrous fraction. Furthermore, $\tilde{T}_{min}$ characterises the load-independent part and $\tilde{T}_{max}$ the maximal part that can be mobilised during hardening. Tensile stresses of the basic matrix $\tilde{T}^B_{V,\alpha}$ are not able to increase the fibrous strength. If $\tilde{T}^B_{V,\alpha}$ falls below the critical value $\tilde{T}_{crit}$, the fibres start to rupture predominantly. Thus, an increase of the bonding does not result in higher strength. The hardening is modelled by an exponential function. The component of the inelastic ALMANSI strains $A^F_{in,\alpha\alpha}$ in direction of the investigated principal stress axis $\boldsymbol{n}_\alpha$ controls the development

$$h_{1,\alpha}(\mathbf{A}^F_{in}) = 1 - a^{(-b\,A^F_{in,\alpha\alpha})}\,. \tag{4.63}$$

Two model parameter a and b are required to describe the hardening process. The discussed idea is displayed in figure 4.8.

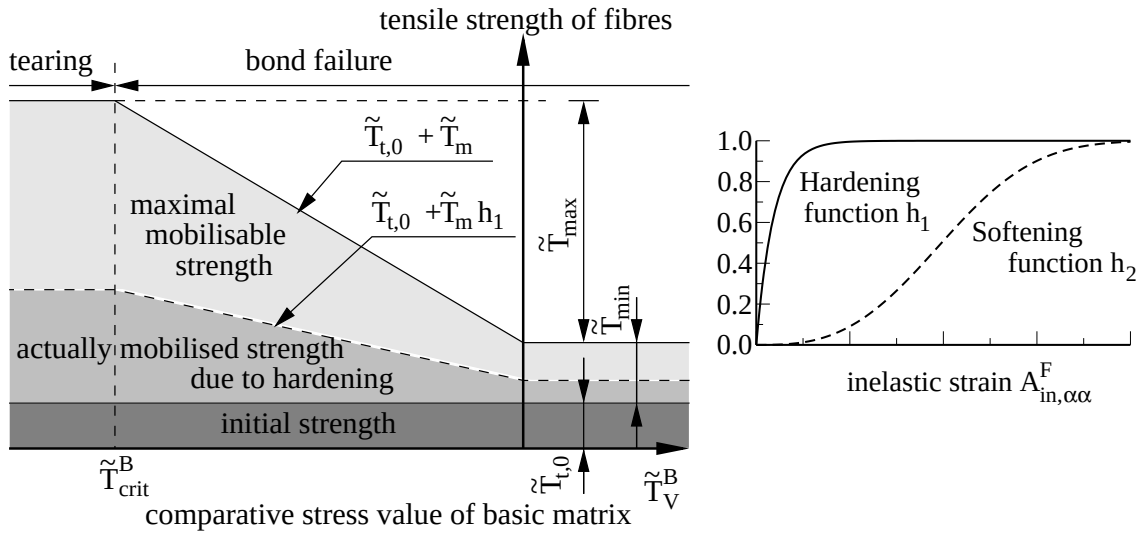

Figure 4.8: Development of fibrous strength depending on stresses of basic matrix and on inelastic strains

The tensile strength is reduced by ongoing extraction of the material due to the occurring bonding failure and the fibre rupture. Thus, a softening term is added formulating in such manner that the strength can be lost completely. Since weak fibres fail at a very early stage, the softening begins immediately with the loading and is formulated as a product

$$\tilde{T}_{s,\alpha} = -(\tilde{T}_{t,0} + \tilde{T}_{m,\alpha})\;\; h_{2,\alpha}(\mathbf{A}^F_{in}) \tag{4.64}$$

using an exponential function for describing the ongoing softening with the parameters c, d and e

$$h_{2,\alpha}(\mathbf{A}^F_{in}) = 1 - c^{\left[-d\,(A^F_{in,\alpha\alpha})^e\right]}\,. \tag{4.65}$$

The flow rule is formulated associatively. Thereby, six LAGRANGIAN multipliers $\dot{\gamma}^F_{pl,\alpha}$ are required for the six yield conditions

$$\mathbf{D}^F_{in} = \sum_{\alpha=1}^{3} \dot{\gamma}^F_{pl,\alpha} \frac{\partial f_{t,\alpha}}{\partial \tilde{\mathbf{T}}^F} + \sum_{\alpha=1}^{3} \dot{\gamma}^F_{pl,\alpha+3} \frac{\partial f_{c,\alpha}}{\partial \tilde{\mathbf{T}}^F} \,. \tag{4.66}$$

The LAGRANGIAN multipliers are unequal to zero if a stress state hits the related yield condition by preserving the KUHN-TUCKER conditions. The model constitutes a cuboid as elastic range in the HAYGH-WESTERGAARD space. The three surfaces under compression are hold fix and the three surfaces in the tensile regime expand the volume first due to hardening. Then, the softening leads to a shrinkage of the elastic range.
Similar to the basic matrix the water content may influence the behaviour of the fibrous fraction. It is expected that the strength is reduced if the water content rises. Again, carrying out of experiments is difficult and quantitative statements do not exist until now. Thus, incorporation of the pore water action and a further improvement of the model are tasks for future research.

4.5 Pore fluids and hydraulic properties of waste

The convective flow of fluids in porous media is often modelled by a relation of DARCY-type connecting the discharge velocity v_D with the hydraulic gradient i by the hydraulic conductivity k_f as proportional factor that reads in one-dimensional form

$$v_D = k_f \;\; i \; = \frac{k_{abs}\, \tilde{\rho}\, b}{\mu} \;\; i \,. \tag{4.67}$$

DARCY's relation is derived from experimental observations, but it is thermodynamically consistent as discussed in section 3.4. For the two approaches the same restrictions concerning inertia effects, viscosity of the fluid and the fluid-solid interaction are required, see Bear [9] or Ehlers [31]. DARCY's law is valid for laminar flow, which is assumed to occur in landfills only. It is generalised for three-dimensional analysis and multicomponent flow of landfill gas and leachate to

$$\boldsymbol{v}^\alpha_D = S^\alpha \, \Phi \, \boldsymbol{w}^\alpha = -\frac{k^\alpha_{rel}}{\mu^\alpha} \mathbf{K}_{abs} \cdot (\operatorname{grad} p^\alpha - \tilde{\rho}^\alpha \, \boldsymbol{b}) \;, \tag{4.68}$$

in which the discharge velocity vector $\boldsymbol{v}^\alpha_D$ of a phase α is related by the saturation S^α and the porosity Φ to its seepage velocity $\boldsymbol{w}^\alpha$. Further, the discharge velocity depends on the dynamic viscosity μ^α, a characteristic value of the fluid, and on the intrinsic permeability tensor $\mathbf{K}_{abs}$ describing the porous waste. The relative permeability k^α_{rel} is a scaling factor between zero and one that depends on the state of saturation of the present phase α. The fluid flow is driven by spatial pressure differences that diverge from static equilibrium.

4.5.1 Matric suction

The physical pressures in the non-wetting phase landfill gas and in the wetting phase water are not independent from each other. The difference between the two pressures is the matric suction or capillary pressure

$$p^c = p^g - p^l \,. \tag{4.69}$$

The underlying physical phenomena are described in detail for soils by Lu and Likos [72] or Helmig [51], who provide modelling approaches, too. The matric suction usually undergoes hysteretic behaviour during drying-wetting cycles as shown in the soil-water characteristic curves in figure 4.9 on the left. Two characteristic points of the curve are the air-entry or bubbling pressure p_{bub}, the suction where gas first starts to enter the largest pores and the desaturation commences, and the residual liquid saturation S_r^l where the pore water remains as isolated menisci and extremely large suctions are required to remove additional water. Some typical soil-water characteristic curves for different materials are plotted in figure 4.9 on the right. In general, finer graded material exhibits a higher air-entry pressure and is characterised by a rapid increase of suction during drying contributed to the smaller dimensions of the pores existing in it. A single function is usually applied for simplicity in constitutive modelling of the characteristic curve in dependency on the effective saturation S_e defined by

$$S_e = \frac{S^l - S_r^l}{1 - S_r^l - S_r^g} = \frac{n^l - n_r^l}{\Phi - n_r^l - n_r^g} \quad \text{or} \quad S_e = \frac{S^l - S_r^l}{1 - S_r^l} = \frac{n^l - n_r^l}{\Phi - n_r^l} \,. \tag{4.70}$$

The saturation S^l describes the real filling state of the pores with leachate. The residual water content S_r^l and the residual gas content S_r^g are connected with situations, in which one of the fluids is almost immobile. The residual gas content S_r^g is often set to zero and the two relations coincide. The dependency on the effective saturation can be expressed equivalently using volume fractions n^l, n_r^l, n_r^g and the porosity Φ. Finsterle [34] discusses the parametric character of residual saturations and the underlying concept of effective saturation in profundity.

The BROOKS-COREY model is a simple formulation to connect p^c with the effective saturation S_e using the air-entry pressure p_{bub} and one additional model parameter λ_{BC}

$$p^c = \begin{cases} \frac{p_{bub}}{(S_e)^{\frac{1}{\lambda_{BC}}}} & \text{for} \quad S_e < 1 \\ 0 & \text{for} \quad S_e = 1 \end{cases} \,. \tag{4.71}$$

The relative permeabilities are formulated for the BROOKS-COREY model in conjunction with the BURDINE theorem for the leachate as well as for the landfill gas by

$$k_{rel}^l = (S_e)^{\left(\frac{2+3\lambda_{BC}}{\lambda_{BC}}\right)} \,, \tag{4.72a}$$

$$k_{rel}^g = (1 - S_e)^2 \left[1 - (S_e)^{\frac{2+\lambda_{BC}}{\lambda_{BC}}}\right] \,. \tag{b}$$

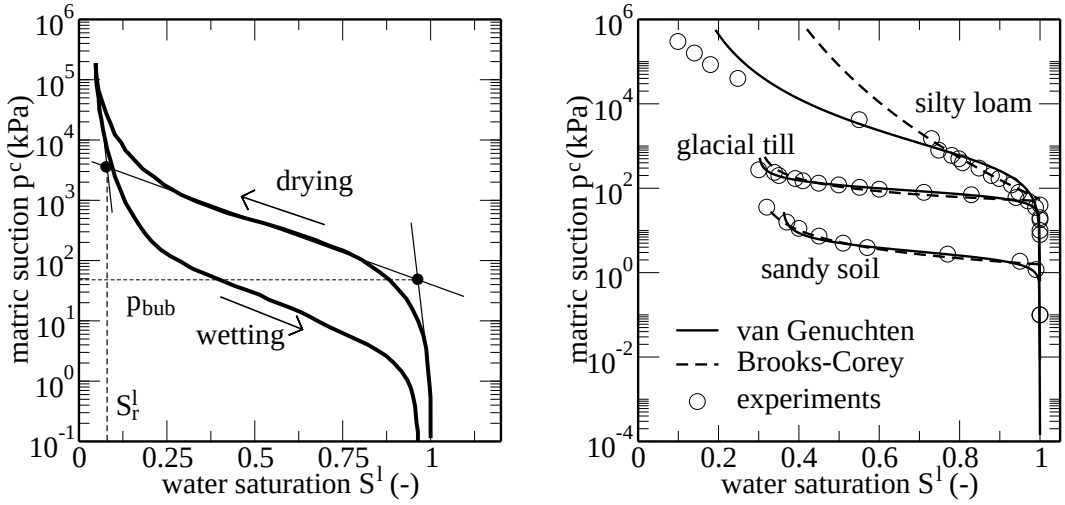

Figure 4.9: Hysteresis in soil-water characteristic curve and models for soils ([72])

The BROOKS-COREY model behaves well for coarse-grained soils with a low and narrow range of suction. It loses its applicability nearby the residual water content and has a sharp discontinuity at liquid saturation point, which requires special attention in numerical implementation. Further, the matric suction is overestimated close to this point resulting in a wrong assessment of the pore pressure defined in equation (3.66), too. In contrast, the VAN GENUCHTEN model is smooth and closed-formed, but it requires three parameters α_{VG}, m_{VG} and n_{VG} for the matric suction versus effective saturation curve

$$p^c = \frac{1}{\alpha_{VG}} \left[(S_e)^{-1/m_{VG}} - 1 \right]^{1/n_{VG}} . \tag{4.73}$$

Therein, $m_{VG} = 1 - 1/n_{VG}$ or $m_{VG} = 1 - 1/(2\,n_{VG})$ is often set a-priori to reduce the number of independent parameters. The parameter α_{VG} models the air-entry pressure. A lower value represents a higher air-entry pressure. Both m_{VG} and n_{VG} control the changeover from saturation state to the residual water content. The MUALEM approach constitutes the relative permeabilities

$$k^l_{rel} = (S_e)^{\epsilon_{VG}} \left[1 - \left(1 - (S_e)^{\frac{1}{m_{VG}}} \right)^{m_{VG}} \right]^2 , \tag{4.74a}$$

$$k^g_{rel} = (1 - S_e)^{\gamma_{VG}} \left[1 - (S_e)^{\frac{1}{m_{VG}}} \right]^{2m_{VG}} . \tag{b}$$

Thus, additional parameters ϵ_{VG} and γ_{VG} arise that are fitted on experimental data or often set to 1/2 and 1/3, respectively. Figure 4.10 displays the influences of the parameter λ_{BC} for the BROOKS-COREY model and of the parameter m_{VG} for the VAN GENUCHTEN model on the relative permeabilities. A small value for λ_{BC} results in a faster decrease of the conductivity of the liquid phase. In contrast, the relative permeability of the gas phase is almost independent of λ_{BC}. The parameter m_{VG} influences the relative permeability of the gas as well as of the liquid phase. A small value

m_{VG} = 0.1 stops the liquid transport almost totally, whereas the gas transport remains mobile for large effective saturations. Increase of m_{VG} results in an increase of the mobility of the liquid phase and a decrease of the mobility of the gas phase.

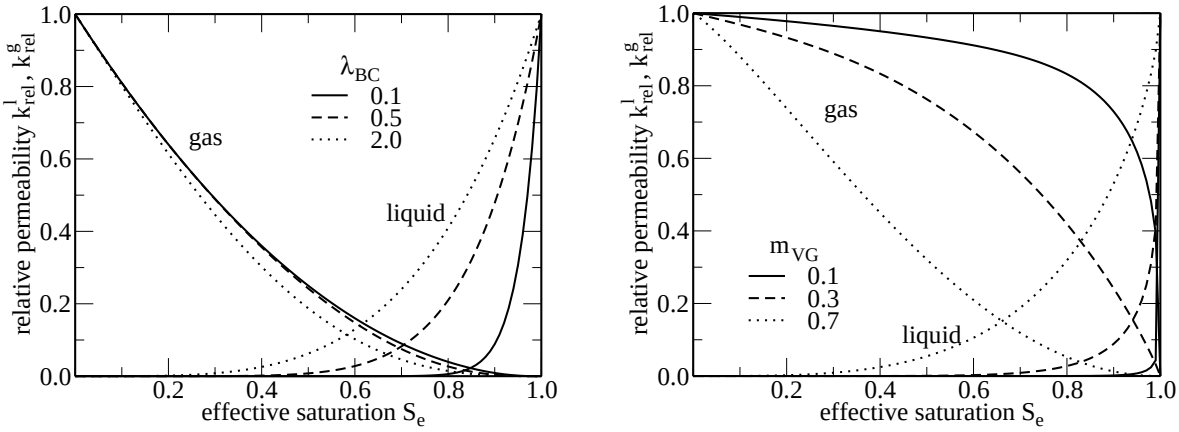

Figure 4.10: Relative permeability in dependency of model parameters

The effective stress parameter χ arising in equation (3.66) is a function of the liquid saturation S^l. Ehlers [31] proposes a linear relation adopted in this thesis

$$\chi = \chi(S^l) = S^l \,. \tag{4.75}$$

Experiments on soils [72] show that the real behaviour diverges from the simplified assumption (4.75).
Obviously, it is debatable if the ideas of ground water modelling can be adopted for the fluid flow in municipal solid waste. Fundamental investigation on suction-saturation curves are rarely published in the literature. Laboratory experiments cannot be carried out easily due to the complexity of the composition of municipal solid waste and the size of the particles. The fluids flow through likewise large macropores in fresh domestic refuses. Thus, no or only small suction is expected to occur. In contrast, the waste is compressed by overburden layers and mineralised by biodegradation and crushing of larger particles after emplacement. Thereby, the material achieves a finer graded state and the hydraulic properties are modified during the process, too. Although the composition strongly influences the hydraulic conductivity, drawing conclusions from macroscopic values as porosity, density or particle size distribution on the nature of the suction-saturation curve does not work well. A similar hydraulic conductivity can occur in loose packing with large pores if a high content of foils and sheet-like material is present and hinders the fluid flow as well as in dense packing with dominant mineral texture and smaller pores.

gas component	CO_2	CH_4	H_2O
B $(10^8 Pa\,s\,K^{-1/2})$	165.5	108.2	182.3
C (K)	274	198	673

Table 4.2: SUTHERLAND's constants for viscosity of landfill gas components

4.5.2 Viscosity

It is well known that the dynamic viscosity of fluids μ depends on the temperature Θ. The viscosity decreases for most liquids and increases for most gases if temperature raises up. The functional relation of POISEUILLE for water is assumed to be valid for the leachate

$$\mu^l = \frac{1.78\ 10^{-3}}{1 + 0.0337(\Theta - 273.15) + 0.000221(\Theta - 273.15)^2}\,. \tag{4.76}$$

SUTHERLAND's law [17] is an excellent approximation for gases using two constants B^α and C^α summarised in table 4.2 for typical landfill gas components

$$\mu^\alpha = B^\alpha \frac{\sqrt{\Theta}}{1 + \frac{C^\alpha}{\Theta}}\,. \tag{4.77}$$

Under anaerobic conditions the landfill gas is a mixture of methane CH_4, carbon dioxide CO_2 and water vapour H_2O mainly. Thus, the viscosity of gas mixtures consisting of n components can be assessed applying complex models from kinetic gas theory, see Baerns et al. [79],

$$\mu^g = \sum_{\alpha=1}^{N} \frac{\xi^\alpha\,\mu^\alpha}{\sum_{\beta=1} \xi^\beta\,\psi^{\alpha\beta}}\,. \tag{4.78}$$

Therein, ξ^α is the molar concentration of the gas component α and the value $\psi^{\alpha\beta}$ depends on the temperature of the gas mixture, on the temperature and the molar volume at the critical point as well as on the molar masses of the gas components. Nevertheless, an accurate description is not required for modelling processes in landfills because a coarse assessment of the composition exists only. Thus, an engineering approach published in [51] seems to be sufficient

$$\mu^g = \sum_{\alpha=1}^{N} \omega_g^\alpha\,\mu^\alpha\,. \tag{4.79}$$

The viscosity of the gas mixture is the sum of the viscosities of the components α weighted by their mass concentration in the gas phase ω_g^α. The viscosity versus temperature curves are plotted in figure 4.11 for water and the gas components.

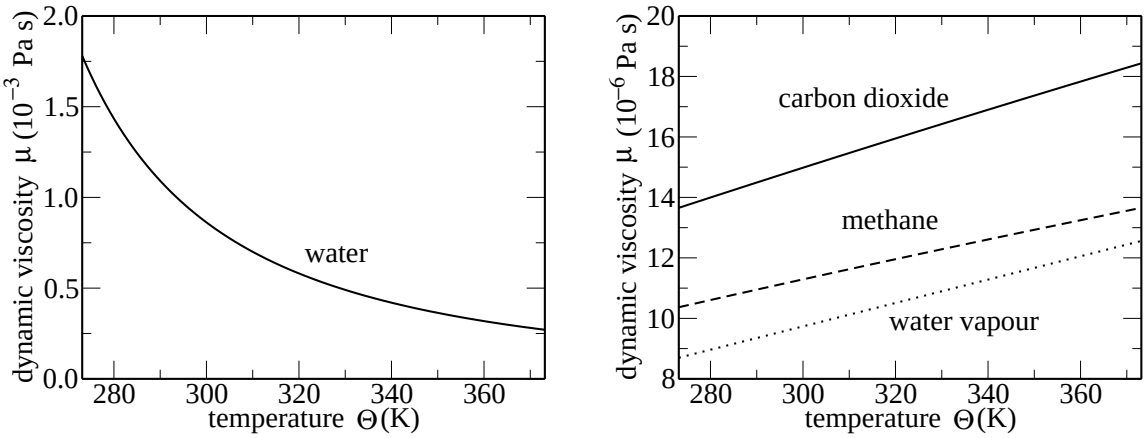

Figure 4.11: Viscosity

4.5.3 Compressibility

Since the pore water and the leachate are almost incompressible, a constant physical density $\tilde{\rho}^l$ is assumed during the whole process of motion

$$\tilde{\rho}^l = const. = 1.0 \frac{Mg}{m^3} \,. \tag{4.80}$$

The ideal gas law is applied for each gas component. The partial gas pressure p_g^α of the component α depends on its partial density ρ_g^α with respect to the whole gas phase n^g, the universal gas constant R, its molar mass M_α and the temperature Θ. It can be expressed by the mass concentration ω_g^α and the real gas density $\tilde{\rho}^g$ equivalently

$$p_g^\alpha = \rho_g^\alpha \frac{R}{M_\alpha} \Theta = \omega_g^\alpha \tilde{\rho}^g \frac{R}{M_\alpha} \Theta \,. \tag{4.81}$$

Using DALTON's law, the total gas pressure p^g is the sum of the gas pressures of its components

$$p^g = p_g^{CO_2} + p_g^{CH_4} + p_g^{H_2O} \,. \tag{4.82}$$

The constitutive equation for the landfill mixture is obtained by combination of equation (4.81) and (4.82)

$$p^g = \tilde{\rho}^g \left(\frac{\omega_g^{CH_4}}{M_{CH_4}} + \frac{\omega_g^{CO_2}}{M_{CO_2}} + \frac{\omega_g^{H_2O}}{M_{H_2O}} \right) R \, \Theta = \tilde{\rho}^g \frac{R}{M_g} \Theta \,. \tag{4.83}$$

The averaged molar mass of the landfill gas M_g can be determined only if the mass concentrations ω_g^α are known. Since biochemical processes, water evaporation as well as dissolution of gases in the leachate are not modelled in this thesis, an accurate development of mass fractions cannot be determined by the modelling approach. Thus, realistic compositions have to be postulated for computations carried out later on. Setting $\omega_g^{CH_4}$ = 0.50 and $\omega_g^{CO_2}$ = 0.50 neglecting the water vapour seems to be a realistic

scenario in a crude assessment because methane and carbon dioxide is produced in the same mass ratio by biodegradation. Thus, the dynamic viscosity is about 1.3 10^{-5} Pa s for a temperature of 293 K.

4.5.4 Intrinsic permeability

The intrinsic permeability is a property of the aquifer only. It depends on the actual density of the material as discussed in section 2.3. The permeability of the porous waste is much lower in denser states compared to situations with a poor compaction of the solid material. In addition, the orientation of the fibres causes anisotropic behaviour. Horizontal and vertical conductivity distinguish by a factor of ten.
Eipper [32] already describes deformation-depending permeability of a porous medium under isotropic initial conditions. The intrinsic permeability is isotropically reduced by the compaction of the material in a first approach. In a second proposal an anisotropic modification is modelled influencing the permeability orthogonal to the direction of the deformation only. Thus, the horizontal flow can be totally inhibited in the limit case of a purely vertical compaction, whereas the vertical flow is unhindered. For that reason, the first proposal of Eipper is applied here, which is enlarged for anisotropic initial conditions. Then, the second order intrinsic permeability tensor is defined as

$$\mathbf{K}_{abs} = \left(\frac{\Phi}{\Phi^0}\right)^{n_\Phi} \mathbf{R}^F \cdot \mathbf{K}_{abs}^{loc,0} \cdot (\mathbf{R}^F)^T \,. \tag{4.84}$$

The tensor $\mathbf{K}_{abs}^{loc,0}$ includes the initial state in local coordinates, in which the first and second local basis vector span the fibrous plane. The rotational tensor $\mathbf{R}^F$ pushes the local defined tensor to the global frame. The procedure is equivalent to the transformation of the local fourth order elasticity tensor discussed in section 4.4. The dependency on the density is modelled by a power function using the porosity as state variable. Assuming an incompressible solid material, which means that all observable volume reductions are caused by the compression of macro- and micropores, the current porosity Φ can be determinded by the determinant of deformation gradient $\mathbf{F}^s$ from the initial porosity Φ^0 by

$$\Phi = 1 - \frac{1 - \Phi^0}{\det \mathbf{F}^s} \,. \tag{4.85}$$

The model parameter n_Φ controls the reduction of the permeability with ongoing compaction and is determined using the laboratory experiments of Beaven or Münnich described already in section 2.3.

5 Solving the initial-boundary value problem

The model equations discussed in section 3.4 form together with the constitutive relations of chapter 4 a partial differential equation system. Appropriate boundary and initial conditions are necessary in order to obtain a unique solution. A closed analytic solution exists only in a very rare number of special cases due to the geometrical and physical nonlinearities attributed to the coupled problem of mechanical deformation of the solid waste and the transport of pore fluids. In general, the initial-boundary value problem has to be solved numerically. Two methods are applied in this thesis. Standard displacement based finite element method is used in order to discretise the weak form of the balance of linear momentum of the mixture (3.65). In contrast, the box-method developed by Helmig [51] is a robust and reliable numerical algorithm for the two mass balances describing the transport of the fluids leachate and gas (3.68). The mass balance of the solid waste is not a model equation because mass exchange processes are neglected. The set of constitutive equations of the solid waste represents an initial value problem for the internal variables and is integrated by a predictor-corrector schema here. The solving algorithm is sketched in figure 5.5 at the end of the chapter.

5.1 Weak form of model equations

The *Principle of Virtual Work* is equivalent to the balance of linear momentum. Thereby, the strong form of balance of linear momentum for the mixture, equation (3.65), is transformed in standard way as discussed by Haupt [49]. The differential equation is multiplied by a scalar field, the virtual displacement $\delta \boldsymbol{u}^s$, and integrated over the domain. The weak form in its EULERIAN representation is obtained after shifting of spatial derivations and using GREEN-GAUSS integral theorem. The weak form of the forces equilibrium in its material representation is obtained by th pull-back of the integro-differential equation to the reference configuration

$$\begin{aligned} \mathbf{r}_u = \int_{V_0^s} \delta \mathbf{E}^s : \left(\mathbf{S}_e^s - \det\mathbf{F}^s \, (p - p_{atm}) \left((\mathbf{F}^s)^T \cdot \mathbf{F}^s \right)^{-1} \right) \mathrm{d}V_0^s \\ - \int_{V_0^s} \delta \boldsymbol{u}^s \cdot (\rho_0^s + \rho_0^l + \rho_0^g) \, \mathbf{b} \, \mathrm{d}V_0^s - \int_{A_0^s} \delta \boldsymbol{u}^s \cdot \mathbf{t}_{R,0} \, \mathrm{d}A_0^s = \mathbf{0} \,. \end{aligned} \quad (5.1)$$

Therein, the virtual GREEN strain tensor $\delta\mathbf{E}^s$ is defined by

$$\delta\mathbf{E}^s = \frac{1}{2}\left((\mathbf{F}^s)^T \cdot \mathrm{Grad}\delta\boldsymbol{u}^s + \mathrm{Grad}^T\delta\boldsymbol{u}^s \cdot \mathbf{F}^s\right) . \tag{5.2}$$

It produces virtual work on the effective 2nd PIOLA-KICHHOFF stresses of the solid waste $\mathbf{S}_e^s$ and on the total pore pressure p reduced by the atmospheric pressure p_{atm}. The deformation gradient $\mathbf{F}^s$ arises in connection with the pore pressure due to the transformation from the current to the reference configuration. The atmospheric pressure is subtracted from the total pore pressure p directly because it is present on the whole surface of the landfill body. Otherwise, the atmospheric pressure has to be treated as additional surface traction $\mathbf{t}_{R,0}$. While the partial density of the solid fraction ρ_0^s is constant as long as no mass exchange is included into the model, the material representation of the partial densities of the leachate ρ_0^l and the gas ρ_0^g vary throughout the deformation process. Equation (5.1) has to be fulfilled at every time, but in the numerical analysis the force equilibrium is investigated to discrete time points only. The actual time point is indicated by t^{n+1} and variables at this time by the index '$n+1$' here. In contrast, the time point analysed before that provides initial values for the constitutive model is marked by t^n and the variables by the index 'n'. The time step size is the time difference $\Delta t = t^{n+1} - t^n$. Such an approach allows the applying of external loads on the surface or the addition of fluid mass due to rain or recirculation in small increments in order to maintain the convergence of the applied numerical methods. The procedure is shown in figure 5.1, where a solid particle indicated by $\boldsymbol{x}^{s,n}$ changes its position between the two time steps and is situated in $\boldsymbol{x}^{s,n+1}$ at time t^{n+1}. The surface load $\mathbf{t}_R$ on the top of the landfill defined in the current configuration also changes between the two time points. The leachate flow causes a positional change of a wetter zone. In addition, the volume distributed forces alter in time. Thus, the stresses of the solid phase are changing and the creep behaviour is influenced by the ongoing fluid flow.

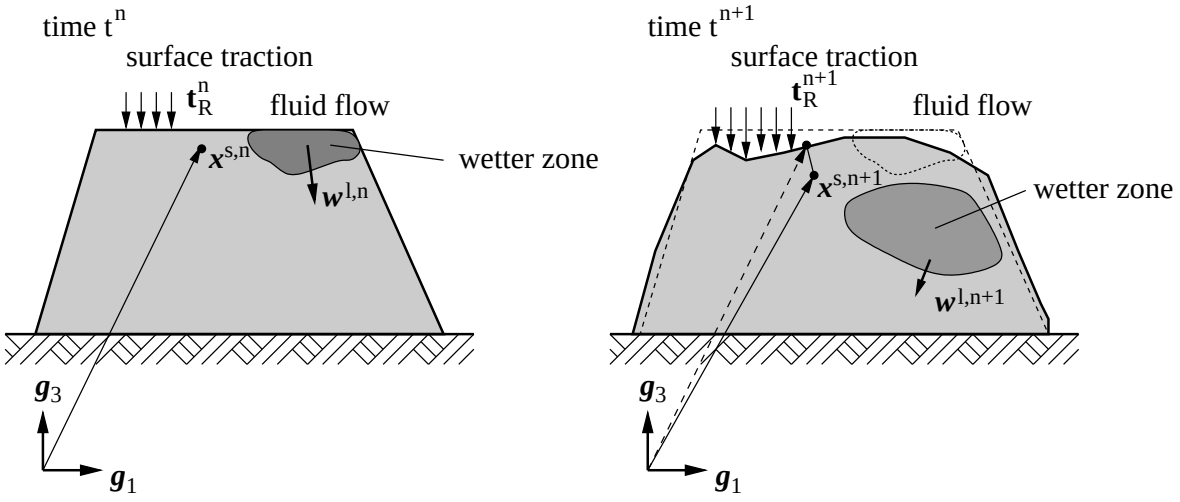

Figure 5.1: Incremental analysis of structures

The mass balances of the fluids, equation (3.68), are transformed by the method of weighted residuals into their integral formulations. The scalar weighting function δp^β is multiplied to each term. Then, the equation is integrated over the solid domain. Applying GREEN-GAUSS integral theorem to the term $\delta p^\beta \operatorname{div}(n^\beta \tilde{\rho}^\beta \boldsymbol{w}^\beta)$ result in the weak form of the model equation

$$r_p^\beta = \int_{v^s} \delta p^\beta \left(\frac{\partial \rho^\beta}{\partial t} + \operatorname{div}(\rho^\beta \boldsymbol{v}^s) \right) dv^s + \int_{v^s} \operatorname{grad}\delta p^\beta \cdot (n^\beta \tilde{\rho}^\beta \boldsymbol{w}^\beta)\, dv^s - \int_{a^s} \delta p^\beta (n^\beta \tilde{\rho}^\beta \boldsymbol{w}^\beta) \cdot \mathbf{n}^s da^s - \int_{v^s} \delta p^\beta \hat{\rho}^\beta \, dv^s = 0\,, \quad \beta \in (l, g)\,, \tag{5.3}$$

in which $\boldsymbol{n}^s$ is the outward directed surface normal vector. Both equation (5.1) and (5.3) are nonlinear and have to be linearised with respect to the state variables. The displacement field $\boldsymbol{u}^s$ of the solid waste is naturally chosen as state variable for the balance of linear momentum. The pressure of the liquid phase p^l and the gas saturation of the pore space S^g are selected as state variables for the transport model in a partially saturated medium summarised in the vector $\boldsymbol{p}^T = (p^l,\, S^g)$. An alternative pressure-pressure or saturation-saturation formulation is not investigated in this thesis. Linearisation of the weak form of the model equations $\mathbf{r}_i$ reads in dependency on the set of state variables $\boldsymbol{z}^T = (\boldsymbol{u}^s, \boldsymbol{p})$

$$\mathbf{r}_i(\boldsymbol{z})|_{\boldsymbol{z}=\boldsymbol{z}^{n+1}} + \left.\frac{\partial\, \mathbf{r}_i(\boldsymbol{z})}{\partial\, \boldsymbol{u}^s}\right|_{\boldsymbol{z}=\boldsymbol{z}^{n+1}} \mathrm{d}\boldsymbol{u}^s + \left.\frac{\partial\, \mathbf{r}_i(\boldsymbol{z})}{\partial\, \boldsymbol{p}}\right|_{\boldsymbol{z}=\boldsymbol{z}^{n+1}} \mathrm{d}\boldsymbol{p} = 0\,, \tag{5.4}$$

in which $\boldsymbol{z}^{n+1}$ is the vector of actual values of variables. The linearised forms are written in a matrix-vector scheme for the set of model equations

$$\begin{bmatrix} \underline{\underline{\mathbf{K}}}_{uu} & \underline{\underline{\mathbf{K}}}_{up} \\ \underline{\underline{\mathbf{K}}}_{pu} & \underline{\underline{\mathbf{K}}}_{pp} \end{bmatrix} \begin{bmatrix} \mathrm{d}\underline{\boldsymbol{u}}^s \\ \mathrm{d}\underline{\boldsymbol{p}} \end{bmatrix} + \begin{bmatrix} \underline{\mathbf{r}}_u \\ \underline{\mathbf{r}}_p \end{bmatrix} = \begin{bmatrix} \underline{\mathbf{0}} \\ \underline{\mathbf{0}} \end{bmatrix}, \tag{5.5}$$

introducing by $\underline{\underline{\mathbf{K}}}_{ij}$ the partial derivation of the model equation $\mathbf{r}_i$ with respect to the state variable $\boldsymbol{z}_j$. The vectors $\underline{\mathbf{r}}_i$ represent the actual residuals

$$\underline{\underline{\mathbf{K}}}_{ij} = \left.\frac{\partial\, \underline{\mathbf{r}}_i(\boldsymbol{z})}{\partial\, \boldsymbol{z}_j}\right|_{\boldsymbol{z}=\boldsymbol{z}^{n+1}}, \quad \underline{\mathbf{r}}_i = \underline{\mathbf{r}}_i(\boldsymbol{z})|_{\boldsymbol{z}=\boldsymbol{z}^{n+1}}\,, \qquad i,\, j \in \{\boldsymbol{u}^s, \boldsymbol{p}\}\,. \tag{5.6}$$

The equation system (5.5) is the iteration rule for the NEWTON-RAPHSON method in order to solve the initial-boundary value problem after its spatial and temporal discretisation. The special cases of an empty solid skeleton or the transport of fluids in an immobile porous solid medium are obtained neglecting all influences of the non-present state variables. The matrix-vector form reads for the deformation problem of the solid phase

$$\underline{\underline{\mathbf{K}}}_{uu}\, \mathrm{d}\underline{\boldsymbol{u}}^s + \underline{\mathbf{r}}_u = \underline{\mathbf{0}} \tag{5.7}$$

and for the pure transport of the fluids, respectively,

$$\underline{\underline{\mathbf{K}}}_{pp}\, \mathrm{d}\underline{\boldsymbol{p}} + \underline{\mathbf{r}}_p = \underline{\mathbf{0}}\,. \tag{5.8}$$

5.2 Discrete formulation

Aim of the discretisation is to express the fields of the state variables by a limited number of values on certain interpolation points approximating the exact curves by simple functions. The numerical methods differ only in the chosen interpolation functions for the state variables and for the weighting term.

5.2.1 Discretisation of weak form of balance of linear momentum

The balance of linear momentum of the mixture in its total LAGRANGIAN form is discretised by standard BUBNOV-GALERKIN finite element method in this thesis. Textbooks of Ahrens and Dinkler [2] or Bathe [7] describe the method in detail. A quadratic function for the ansatz is used in order to discretise the displacement field

$$u_i^s = \sum_{k=1}^{m} \Omega_k^2(\boldsymbol{\xi})\, \check{u}_i^{s,k}\,, \qquad\qquad i \in (1,2,3)\,, \tag{5.9}$$

Thereby, the shape functions $\Omega_k^2(\boldsymbol{\xi})$ formulated in local defined coordinates $\boldsymbol{\xi}$ depend on the applied element type and the spatial dimensionality of the investigated problem. The node values $\check{u}_i^{s,k}$ are the unknown displacements of the solid phase. The virtual displacement field is constructed using the same shape functions

$$\delta u_i^s = \sum_{k=1}^{m} \Omega_k^2(\boldsymbol{\xi})\, \delta\check{u}_i^{s,k}\,, \qquad\qquad i \in (1,2,3)\,. \tag{5.10}$$

The liquid pressure and the gas saturation are disctretised by a linear ansatz

$$p^l = \sum_{k=1}^{n} \Omega_k^1(\boldsymbol{\xi})\, \check{p}^{l,k} \quad \text{and} \quad S^g = \sum_{k=1}^{n} \Omega_k^1(\boldsymbol{\xi})\, \check{S}^{g,k}\,, \tag{5.11}$$

using only the values $\check{p}^{l,k}$, $\check{S}^{g,k}$ on the n corner nodes as unknowns. The definitions of the global variables are pictured in figure 5.2 on the left.
Due to the structure of the finite element method the global matrices $\underline{\underline{\mathbf{K}}}_{uj}$ and the vector $\underline{\mathbf{r}}_u$ are assembled by submatrices $\underline{\underline{\mathbf{K}}}_{uj}^e$ and subvectors $\underline{\mathbf{r}}_u^e$ defined on element level. Thereby, the matrix $\underline{\underline{\mathbf{K}}}_{uu}^e$ summarises all dependencies on the displacements of elemental nodes

$$\underline{\underline{\mathbf{K}}}_{uu}^e = \int_{V_0^{s,e}} \underline{\underline{\mathbf{B}}}^T\, \underline{\underline{\mathbf{S}}}_{,F}\, \underline{\underline{\mathbf{H}}}\, dV_0^{s,e} + \int_{V_0^{s,e}} \underline{\underline{\mathbf{B}}}_{nl}^T\, \underline{\underline{\mathbf{S}}}\, \underline{\underline{\mathbf{B}}}_{nl}\, dV_0^{s,e} - \int_{V_0^{s,e}} (\underline{\underline{\boldsymbol{\Omega}}}^2)^T\, \underline{\underline{\boldsymbol{\rho}}}_{,F}\, \underline{\underline{\mathbf{H}}}\, dV_0^{s,e}\,.$$

The matrix $\underline{\underline{\boldsymbol{\Omega}}}^2$ includes the shape functions. The matrix $\underline{\underline{\mathbf{S}}}$ is formed by the actual total 2nd PIOLA-KIRCHHOFF stresses. The strain-displacement matrix $\underline{\underline{\mathbf{B}}}$ emerges from the virtual GREEN strain tensor $\delta\mathbf{E}^s$. The matrix $\underline{\underline{\mathbf{B}}}_{nl}$ is generated by the derivation

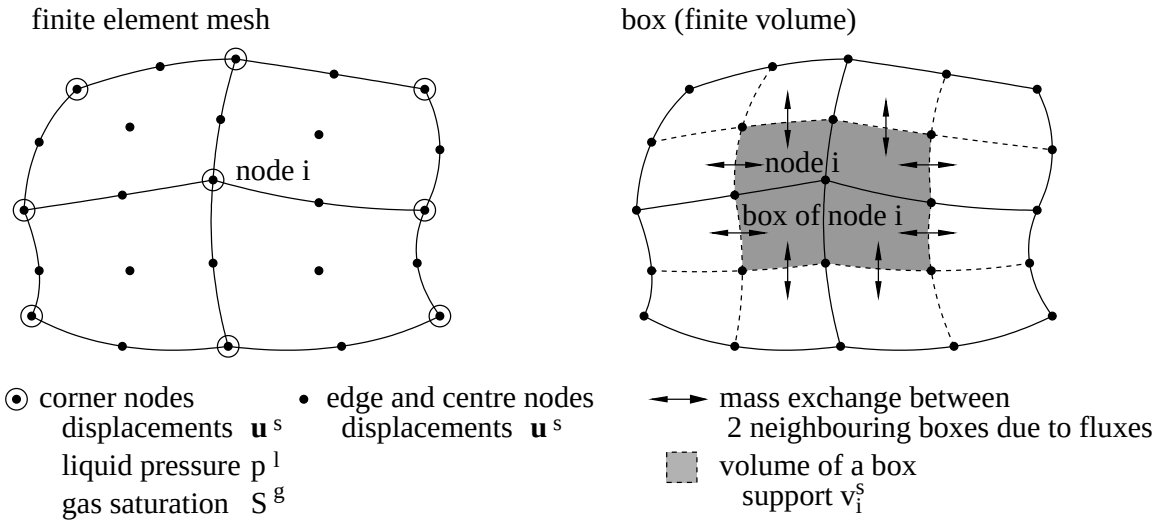

Figure 5.2: Global unknowns on finite element and definition of a box

of the virtual strains with respect to the solid displacements $\boldsymbol{u}^s$. They are discussed in profundity by Bathe [7]. The matrix $\underline{\underline{\mathbf{S}}}_{,F}$ considers the derivation of the total 2nd PIOLA-KIRCHHOFF stresses with respect to the deformation gradient of the solid displacement field $\mathbf{F}^s$ having in mind that the constitutive models for the solid phase as well as for the pore pressure work on the current configuration. The fourth order tensor required for the matrix is derived as

$$\begin{aligned}\frac{\partial \mathbf{S}}{\partial \mathbf{F}^s} =& \frac{\partial \left((\mathbf{F}^s)^{-1} \cdot \left[\tilde{\mathbf{T}}^s_e - \det\mathbf{F}^s \, (p - p_{atm}) \, \mathbf{1} \right] \cdot (\mathbf{F}^s)^{-T} \right)}{\partial \mathbf{F}^s} \\ =& \left[(\mathbf{F}^s)^{-1} \otimes (\mathbf{F}^s)^{-1} \right]^{T_{23}} : \left[\tilde{\mathbf{T}}^s_{e,\mathbf{F}^s} + (p - p_{atm}) \det\mathbf{F}^s \, \left(\mathbf{1} \otimes (\mathbf{F}^s)^{-T} \right) \right] \\ & - \left[\mathbf{S} \otimes (\mathbf{F}^s)^{-T} \right]^{T_{14}} - \left[(\mathbf{F}^s)^{-T} \otimes \mathbf{S}^T \right]^{T_{13}} .\end{aligned}$$

The derivation of the material operator $\tilde{\mathbf{T}}^s_{,\mathbf{F}^s}$ is closely related to the stress computation. All other terms of prior equation are the outcome of the linearisation of the transformation of the stresses from the current to the reference configuration. The matrix $\underline{\underline{\mathbf{H}}}$ summarises the linearisation of the deformation gradient $\mathbf{F}^s$ in direction of the displacement $\boldsymbol{u}^s$, which is determined by its GATEAUX derivative

$$\frac{\partial \mathbf{F}^s}{\partial \boldsymbol{u}^s} \cdot \mathrm{d}\boldsymbol{u}^s = \left. \frac{\mathrm{d} \left(\mathbf{1} + \mathrm{Grad}(\boldsymbol{u}^s + \lambda \, \mathrm{d}\boldsymbol{u}^s) \right)}{\mathrm{d}\,\lambda} \right|_{\lambda=0} = \mathrm{Grad}\, \mathrm{d}\boldsymbol{u}^s \, . \tag{5.12}$$

Combining the definitions of partial densities (3.27), real densities (3.26), volume fractions (3.1), pore space (3.3) and fluid saturations (3.4) and taking into account the transformation of densities between the reference and the current configuration $\rho^\beta_0 = \det\mathbf{F}^s \; \rho^\beta$, the partial fluid densities defined on the reference configuration are

equivalently expressed by

$$\rho_0^\beta = \det\mathbf{F}^s \;\; \Phi \, S^\beta \, \tilde{\rho}^\beta \,, \qquad\qquad \beta \in \{l,\, g\} \,.$$

Replacing Φ by equation (4.85), the derivation of the densities ρ_0^β with respect to the deformation gradient is finally obtained as

$$\frac{\partial \rho_0^\beta}{\partial \mathbf{F}^s} = \det\mathbf{F}^s \, S^\beta \, \tilde{\rho}^\beta \, (\mathbf{F}^s)^{-T} \,, \tag{5.13}$$

which is inserted into the matrix $\underline{\underline{\boldsymbol{\rho}}}_{,F}$.
The matrix $\underline{\underline{\mathbf{K}}}^e_{up}$ includes all dependencies on the transport variables

$$\underline{\underline{\mathbf{K}}}^e_{up} = \int_{V_0^{s,e}} \underline{\underline{\mathbf{B}}}^T \; \underline{\underline{\mathbf{S}}}_{,p} \; \underline{\underline{\boldsymbol{\Omega}}}^1 \, dV_0^{s,e} - \int_{V_0^{s,e}} (\underline{\underline{\boldsymbol{\Omega}}}^2)^T \; \underline{\underline{\boldsymbol{\rho}}}_{,p} \; \underline{\underline{\boldsymbol{\Omega}}}^1 \, dV_0^{s,e} \,.$$

The linear shape functions are ordered into the matrix $\underline{\underline{\boldsymbol{\Omega}}}^1$. The matrix $\underline{\underline{\mathbf{S}}}_{,p}$ is formed by the derivation of the total 2nd PIOLA-KIRCHHOFF stresses with respect to the state variables of the transport model

$$\begin{aligned} \frac{\partial \mathbf{S}}{\partial \boldsymbol{p}} =& \frac{\partial \left((\mathbf{F}^s)^{-1} \cdot \left[\tilde{\mathbf{T}}^s_e - \det\mathbf{F}^s \, (p - p_{atm}) \mathbf{1} \right] \cdot (\mathbf{F}^s)^{-T} \right)}{\partial \boldsymbol{p}} \\ =& \left[(\mathbf{F}^s)^{-1} \otimes (\mathbf{F}^s)^{-1} \right]^{T_{23}} : \left[\tilde{\mathbf{T}}^s_{e,\boldsymbol{p}} + \det\mathbf{F}^s \, \mathbf{1} \, p_{,\boldsymbol{p}} \right] \,. \end{aligned}$$

The derivation of the effective KIRCHHOFF stresses $\tilde{\mathbf{T}}^s_{e,\mathbf{p}}$ is caused by the dependency of the strength of the basic matrix as well as of the strength of the fibrous fraction on the water content. The dependency of the pore pressure on the liquid pressure and the gas saturation is apparently and the derivation is expressed by the term $p_{,\boldsymbol{p}}$. The matrix $\underline{\underline{\boldsymbol{\rho}}}_{,p}$ considers the dependencies of the fluid densities on the state variables liquid pressure p^l and gas saturation S^g, which are obtained by the partial derivatives

$$\frac{\partial \left(\rho_0^l + \rho_0^g \right) \mathbf{b}}{\partial \, p_i} = \frac{\partial \left(\det\mathbf{F}^s \, \Phi \, S^l \, \tilde{\rho}^l + \det\mathbf{F}^s \, \Phi \, S^g \, \tilde{\rho}^g \right) \mathbf{b}}{\partial \, p_i} \,, \qquad\qquad p_i \in \{p^l,\, S_g\} \,.$$

Finally, the residual vector $\underline{\mathbf{r}}^e_u$ is computed by

$$\underline{\mathbf{r}}^e_u = \int_{V_0^{s,e}} \underline{\underline{\mathbf{B}}}^T \; \underline{\mathbf{S}} \, dV_0^{s,e} - \int_{V_0^{s,e}} (\underline{\underline{\boldsymbol{\Omega}}}^2)^T \; \underline{\boldsymbol{\rho}} \, dV_0^{s,e} - \int_{A_0^{s,e}} (\underline{\underline{\boldsymbol{\Omega}}}^2)^T \; \underline{\mathbf{t}}_{R,0} \, dV_0^{s,e} \,.$$

The vector $\underline{\mathbf{S}}$ summarises the actual total 2nd PIOLA-KIRCHHOFF stresses, the vector $\underline{\boldsymbol{\rho}}$ the volume forces and the vector $\underline{\mathbf{t}}_{R,0}$ the surface traction without the atmospheric pressure.

5.2.2 Discretisation of weak form of mass balances

The discretisation of the transport equations is carried out with the box-method introduced by Helmig [51], which is extended for the case of a moving solid skeleton here.

Before the spatial discretisation of the weak forms of the mass balance is discussed in detail, the storage term is reformulated as

$$\left(\frac{\partial \rho^\beta}{\partial t} + \operatorname{div}(\rho^\beta \, \boldsymbol{v}^s) \right) \, dv^s = \frac{\mathrm{d}^{'s} \left(\rho^\beta \, dv^s \right)}{\mathrm{d}\, t} \, .$$

The time dependency is modelled by a linear ansatz $x(t^{n+1}) = x(t^n) + \dot{x}(t^n + \xi \, \Delta \, t)$. The EULER-backward method is obtained for $\xi = 1$

$$\begin{aligned} \int_{v^s} \delta p^\beta \, \frac{\mathrm{d}^{'s} \left(\rho^\beta \, dv^s \right)}{\mathrm{d}\, t} \bigg|_{t^{n+1}} &= \frac{\int_{v^s} \delta p^\beta \; \rho^\beta \, dv^s \big|_{t^{n+1}} - \int_{v^s} \delta p^\beta \; \rho^\beta \, dv^s \big|_{t^n}}{t^{n+1} - t^n} \\ &= \int_{v^s} \delta p^\beta \, \hat{\rho}^\beta \, dv^s \bigg|_{t^{n+1}} + \int_{a^s} \delta p^\beta \, (n^\beta \, \tilde{\rho}^\beta \, \boldsymbol{w}^\beta) \cdot \mathbf{n}^s da^s \bigg|_{t^{n+1}} \\ &\quad - \int_{v^s} \operatorname{grad} \delta p^\beta \; \cdot (n^\beta \, \tilde{\rho}^\beta \, \boldsymbol{w}^\beta) \, dv^s \bigg|_{t^{n+1}} \, . \end{aligned}$$

The state variables are discretised with the linear shape functions (5.11) again. A different test function δp^β is introduced, which is one in its support v_i^s and zero otherwise

$$\delta p^\beta(\boldsymbol{x}) = \begin{cases} 1 & \text{for} \quad \boldsymbol{x} \in v_i^s \\ 0 & \text{for} \quad \boldsymbol{x} \notin v_i^s \end{cases} \, . \tag{5.14}$$

If the domain is subdived into finite elements, the support belonging to an element corner node comprises only a part of the element close to it. The whole support forms a box similar to a finite volume element, which is displayed in figure 5.2 on the right. It follows immediately from the definition of δp^β that the flux term $\operatorname{grad} \delta p^\beta$ disappears. Using a lumped strategy, the mass balance of each box reduces to

$$(\rho^\beta \, v_i^s) \Big|_{t^{n+1}} - (\rho^\beta \, v_i^s) \Big|_{t^n} = \Delta t \left(\int_{a_i^s} (n^\beta \, \tilde{\rho}^\beta \, \boldsymbol{w}^\beta) \cdot \mathbf{n}^s da_i^s + \hat{\rho}^\beta \, v_i^s \right) \bigg|_{t^{n+1}} \, . \tag{5.15}$$

Equation (5.15) states that the difference of mass of a fluid component β between the time points t_n and t_{n+1} stored inside a box v_i^s equals the mass transported over the box surface da_i^s by the Darcy-flow $n^\beta \, \tilde{\rho}^\beta \, \boldsymbol{w}^\beta$ and the applied mass by exchange and source terms $\hat{\rho}^\beta$. The volume of the box and its porosity change in time due to the motion of the solid phase. The box-method is conservative because no mass losses can occur by the numerical procedure. State variables p^l and S^g as well as internal variables, e.g., the partial densities ρ^β or real densities $\tilde{\rho}^\beta$, matric suction p^c etc., are constant inside each box and are computed on the nodes only. The volumes of the boxes as well as their surfaces are numerically integrated element by element for each iteration in all time steps.

Special attention has to be dedicated to the flux term, which reads after inserting of DARCY's relation (4.68) for the interface between two neighbouring boxes i and j

$$(n^\beta \, \tilde{\rho}^\beta \, \boldsymbol{w}^\beta) \cdot \mathbf{n}^s a_{ij}^s = -\tilde{\rho}^\beta \frac{k_{rel}^\beta}{\mu^\beta} \left(\mathbf{K}_{abs} \cdot \left(\operatorname{grad} p^\beta - \tilde{\rho}^\beta \, \mathbf{b} \right) \right) \cdot \mathbf{n}^s a_{ij}^s \, . \tag{5.16}$$

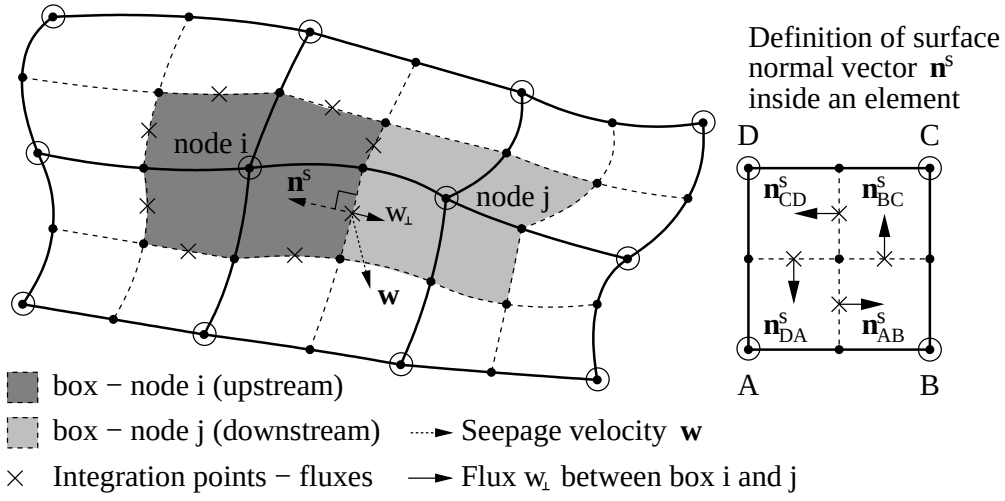

Figure 5.3: Integration and fully-upwinding stabilisation in box-method

The flux is integrated using only one GAUSSIAN-point between two neighbouring boxes on element level. The GAUSSIAN-points and the surface normal vectors inside an element are illustrated in figure 5.3. Since only convective flows are present in the transport equations of the fluids (3.68), the PECLET-number describing the ratio between convective and diffusive flows goes to ∞. The underlying differential equations are hyperbolic. Applying standard numerical techniques developed for the solution of elliptic and parabolic partial differential equations results in unphysical oscillations of the state variables that often cause divergence in the numerical procedure. A fully-upwinding scheme is employed here in order to avoid such failure of the numerical method. Thereby, it is checked, which of the two neighbouring boxes lays in the upstream marked by UP and which in the downstream

$$\begin{aligned} w_\perp &= -\left(\mathbf{K}_{abs} \cdot \left(\operatorname{grad} p^\beta - \tilde{\rho}\,\mathbf{b}\right)\right) \cdot \mathbf{n}^s_{ij} \;\geq\; 0 \quad \rightarrow \quad UP = i \\ w_\perp &= -\left(\mathbf{K}_{abs} \cdot \left(\operatorname{grad} p^\beta - \tilde{\rho}\,\mathbf{b}\right)\right) \cdot \mathbf{n}^s_{ij} \;<\; 0 \quad \rightarrow \quad UP = j \end{aligned} \;. \tag{5.17}$$

While densities and pressures are interpolated from the corner nodes of the element, the tensor of absolute permeability $\mathbf{K}_{abs}$ is constructed on the one GAUSSIAN-point for the numerical integration of the flux by equation (4.84). Then, the flux is described as

$$(n^\beta\, \tilde{\rho}^\beta\, \boldsymbol{w}^\beta) \cdot \mathbf{n}^s_{ij} a^s_{ij} = \left(\frac{\tilde{\rho}^\beta\, k^\beta_{rel}}{\mu^\beta}\right)^{UP} w_\perp\, a^s_{ij}\,. \tag{5.18}$$

Thereby, the information about real density and relative permeability is taken from the box laying on the upwind side. The fully-upwinding stabilisation leads to monotone numerical solutions, but it increases the unphysical numerical diffusion. Sharp fronts tend to be smeared out and the numerical solution is sensitive to the grid orientation. Advanced techniques, see Helmig [51] or Bastian [6], are available in order to minimise the errors induced by the numerical method, but a detailed investigation of such

approaches is out of the scope of this thesis.
The residuum formulation, equation (5.15), is the starting point for the linearisation of the transport model. Due to the fact that each finite element includes parts of the boxes of its corner nodes, the assembling of the global matrices $\underline{\underline{\mathbf{K}}}_{pu}$ and $\underline{\underline{\mathbf{K}}}_{pp}$ as well as the vector $\underline{\mathbf{r}}_p$ from local matrices and vectors defined on element level is very efficient for the numerical implementation. Thus, the matrix

$$\underline{\underline{\mathbf{K}}}^e_{pu} = \frac{\partial \underline{\mathbf{r}}_p}{\partial \check{u}^{s,k}} \tag{5.19}$$

includes the derivatives of the residuum $\underline{\mathbf{r}}_p$ with respect to the node values $\check{u}^{s,k}$ of the displacement field of the element e. Similarly, the matrix

$$\underline{\underline{\mathbf{K}}}^e_{pp} = \frac{\partial \underline{\mathbf{r}}_p}{\partial \check{p}^{k}} \tag{5.20}$$

comprehends the derivation with respect to the values of the transport model on the corner nodes of the finite elements $\check{p}^k \in \{\check{p}^{l,k}, \check{S}^{g,k}\}$. Both matrices $\underline{\underline{\mathbf{K}}}^e_{pu}$ and $\underline{\underline{\mathbf{K}}}^e_{pp}$ are constructed numerically applying finite differences method in order to compute the derivations.

5.3 Computation of stresses of the solid phase

In contrast to the fluid components, the internal variables of the constitutive model of the solid fraction cannot be determined from the global unknowns directly. Furthermore, the constitutive model is a first order initial-value problem, which is integrated by a predictor-corrector method originally developed as operator-split-method by Ortiz et al. [86], Simo and Ortiz [94] and which is employed for many different applications successfully. For instance, Hartmann [45] discusses the special case of small elastic strains for metal plasticity. The stress computation of the two solid fractions is separately performed on the GAUSSIAN-points of the finite elements, beginning with the basic matrix because no dependencies of the internal variables of the basic matrix on the internal variables of the fibrous fraction exist.
A new displacement field at time t^{n+1} is obtained from the global iteration of the actual time step indicating the actual deformation gradient by $\mathbf{F}^{s,n+1}$. Initial values are elastic and inelastic strains of the last converged time step at time t^n defined on the appropriate current configuration characterised by the deformation gradient $\mathbf{F}^{s,n}$. The time increment is split into an elastic and an inelastic part

$$\Delta t = t^{n+1} - t^n = \Delta t^{in} + \Delta t^{el} \,. \tag{5.21}$$

During the elastic predictor, which proceeds almost spontaneously $\Delta t^{el} \approx 0$, it is assumed that no additional inelastic deformations are generated by plastic flow or creep.

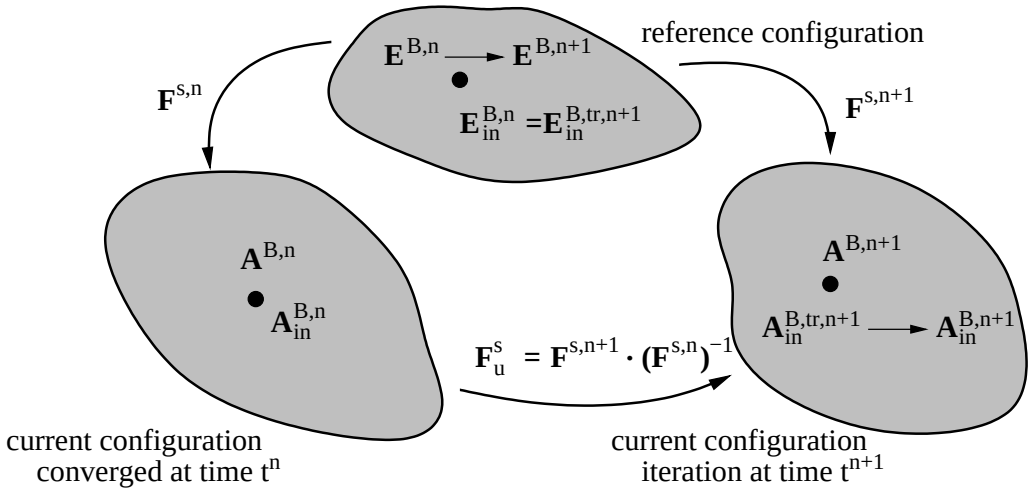

Figure 5.4: Incremental deformation - stress algorithm

Thus, equation (4.27) states

$$\mathring{\mathbf{A}}^{B}_{in} = \dot{\mathbf{A}}^{B}_{in} + (\mathbf{L}^{s})^{T} \cdot \mathbf{A}^{B}_{in} + \mathbf{A}^{B}_{in} \cdot \mathbf{L}^{s} = \mathbf{0}\,. \tag{5.22}$$

Pull-back of (5.22) to the reference configuration with (3.21) results in

$$\dot{\mathbf{E}}^{B}_{in} = \mathbf{0} \quad \rightarrow \quad \mathbf{E}^{B,n+1}_{in} = \int_{\Delta t^{el}} \dot{\mathbf{E}}^{B}_{in}\, dt = \mathbf{E}^{B,n}_{in} = (\mathbf{F}^{s,n})^{T} \cdot \mathbf{A}^{B,n}_{in} \cdot (\mathbf{F}^{s,n})\,,$$

which is integrated exactly. After Pushing-forward the result to the new current configuration, the initial inelastic or trial ALMANSI strains are obtained as

$$\mathbf{A}^{B,tr,n+1}_{in} = (\mathbf{F}^{s,n+1})^{-T} \cdot (\mathbf{F}^{s,n})^{T} \cdot \mathbf{A}^{B,n}_{in} \cdot (\mathbf{F}^{s,n}) \cdot (\mathbf{F}^{s,n+1})^{-1}\,. \tag{5.23}$$

It is clear that (5.23) coincides with the mapping of the inelastic strains from the current configuration at time t_n to the new configuration at time t_{n+1} by the incremental deformation gradient $\mathbf{F}^{s}_{u}$ that equals the tensorial product

$$\mathbf{F}^{s}_{u} = \mathbf{F}^{s,n+1} \cdot (\mathbf{F}^{s,n})^{-1}\,. \tag{5.24}$$

The transformation is pictured in figure 5.4. Trial KIRCHHOFF-stresses $\tilde{\mathbf{T}}^{B,tr,n+1}$ are determined combining the equations (3.19), (3.20), (4.31) and (4.30)

$$\begin{aligned}\tilde{\mathbf{T}}^{B,tr,n+1} = \mu \left(\left[\mathbf{1} - 2 \left(\mathbf{A}^{s,n+1} - \mathbf{A}^{B,tr,n+1}_{in} \right) \right]^{-1} - \mathbf{1} \right) \\ + \lambda \ln(\sqrt{\det \left[\mathbf{1} - 2 \left(\mathbf{A}^{s,n+1} - \mathbf{A}^{B,tr,n+1}_{in} \right) \right]^{-1}})\, \mathbf{1}\,,\end{aligned} \tag{5.25}$$

where $\mathbf{A}^{s,n+1}$ indicates the actual ALMANSI strains of the solid waste. If the trial stresses $\tilde{\mathbf{T}}^{B,tr,n+1}$ do not violate the yield condition (4.38) and do not generate additional inelastic creep (4.49), then the trial state coincides with the actual state and the computation is finished. Otherwise, the constitutive equations have to be integrated in

time with the trial variables as initial conditions. Since the time integration is performed on a fixed current configuration, the spatial velocity gradient $\mathbf{L}^s$ is zero during the whole inelastic corrector step. The OLDROYD-rate of inelastic strains (4.27) degenerates to a material time derivative

$$\mathring{\mathbf{A}}^B_{in} = \dot{\mathbf{A}}^B_{in} + (\mathbf{L}^s)^T \cdot \mathbf{A}^B_{in} + \mathbf{A}^B_{in} \cdot \mathbf{L}^s = \dot{\mathbf{A}}^B_{in} \,. \tag{5.26}$$

Using the EULER-backward integration method again, a nonlinear equation system arises for the initial value problem combining the equations (4.30), (4.31), (5.26), (4.42), (4.49), (4.45), and (4.38)

$$\begin{aligned}
\mathbf{r}^B_T &= \tilde{\mathbf{T}}^{B,n+1} - \mu \left(\left[\mathbf{1} - 2 \left(\mathbf{A}^{s,n+1} - \mathbf{A}^{B,n+1}_{in} \right) \right]^{-1} - \mathbf{1} \right) \\
&\qquad + \lambda \ln(\sqrt{\det \left[\mathbf{1} - 2 \left(\mathbf{A}^{s,n+1} - \mathbf{A}^{B}_{in,1} \right) \right]^{-1}}) \, \mathbf{1} = \mathbf{0} \,, \qquad \text{(5.27a)} \\
\mathbf{r}^B_A &= \mathbf{A}^{B,n+1}_{in} - \mathbf{A}^{B,tr,n+1}_{in} - \Delta\gamma^{B,n+1}_{pl} \frac{\partial \, q_E}{\partial \, \tilde{\mathbf{T}}^{B,n+1}} \\
&\qquad - \sum_{\alpha=1}^{3} \Delta\gamma^{n+1}_{cr,\alpha} \left(\boldsymbol{n}_{\tilde{\mathbf{T}}^{B,n+1},\alpha} \otimes \boldsymbol{n}_{\tilde{\mathbf{T}}^{B,n+1},\alpha} \right) = \mathbf{0} \,, \qquad \text{(b)} \\
r^B_{a_v} &= a^{B,n+1}_{v,in} - 1 \\
&\qquad + (1 - a^B_{v,0}) \sqrt{1 - 2\, I_{1,\mathbf{A}^{B,n+1}_{in}} + 4\, I_{2,\mathbf{A}^{B,n+1}_{in}} - 8\, I_{3,\mathbf{A}^{B,n+1}_{in}}} = 0 \,, \qquad \text{(c)} \\
r^B_f &= -\sqrt{ J_{2D,\tilde{\mathbf{T}}^{B,n+1}_1} \left(1 + \gamma \frac{J_{3D,\tilde{\mathbf{T}}^{B,n+1}}}{J^{3/2}_{2D,\tilde{\mathbf{T}}^{B,n+1}}} \right)^m + \frac{1}{2} \delta_f \, I^2_{1,\tilde{\mathbf{T}}^{B,n+1}} } \\
&\qquad - \alpha_f \, I_{1,\tilde{\mathbf{T}}^{B,n+1}} + \kappa_f = 0 \,. \qquad \text{(d)}
\end{aligned}$$

The nonlinear equation system (5.27) is solved by the NEWTON-RAPHSON method that requires a consistent linearisation with respect to the internal state variables of the basic matrix - KIRCHHOFF-stresses $\tilde{\mathbf{T}}^{B,n+1}$, inelastic ALMANSI-strains $\mathbf{A}^{B,n+1}_{in}$, inelastic volume strains $a^{B,n+1}_{v,in}$ and the LAGRANGIAN-multiplier connected to the yield condition multiplied with time increment $\Delta\gamma^{B,n+1}_{pl} = \Delta t \, \dot{\gamma}^{B,n+1}_{pl}$

$$\begin{bmatrix}
\frac{\partial \mathbf{r}^B_T}{\partial \tilde{\mathbf{T}}^{B,n+1}} & \frac{\partial \mathbf{r}^B_T}{\partial \mathbf{A}^{B,n+1}_{in}} & \mathbf{0} & \mathbf{0} \\
\frac{\partial \mathbf{r}^B_A}{\partial \tilde{\mathbf{T}}^{B,n+1}} & \frac{\partial \mathbf{r}^B_A}{\partial \mathbf{A}^{B,n+1}_{in}} & \frac{\partial \mathbf{r}^B_A}{\partial \Delta\gamma^{B,n+1}_{pl}} & \frac{\partial \mathbf{r}^B_A}{\partial \, a^{B,n+1}_{v,in}} \\
\mathbf{0} & \frac{\partial \, r^B_{a_v}}{\partial \mathbf{A}^{B,n+1}_{in}} & 0 & \frac{\partial \, r^B_{a_v}}{\partial \, a^{B,n+1}_{v,in}} \\
\frac{\partial \, r^B_f}{\partial \tilde{\mathbf{T}}^{B,n+1}} & \mathbf{0} & 0 & \frac{\partial \, r^B_f}{\partial \, a^{B,n+1}_{v,in}}
\end{bmatrix}
\begin{bmatrix}
\mathrm{d}\tilde{\mathbf{T}}^{B,n+1} \\
\mathrm{d}\mathbf{A}^{B,n+1}_{in} \\
\mathrm{d}\Delta\gamma^{B,n+1}_{pl} \\
\mathrm{d}a^{B,n+1}_{v,in}
\end{bmatrix}
=
\begin{bmatrix}
-\mathbf{r}^B_T \\
-\mathbf{r}^B_A \\
-r^B_{a_v} \\
-r^B_f
\end{bmatrix} . \tag{5.28}$$

The LAGRANGIAN-multiplier for the mechanical creep $\Delta\gamma^{n+1}_{cr,\alpha} = \Delta t \, \dot{\gamma}^{n+1}_{cr,\alpha}$ are in functional dependency on the other internal variables by equation (4.50) and do not appear

in addition. The main task is to compute the tensorial derivatives of the residuals r_i^B correctly in order to maintain the quadratic convergence of the NEWTON-RAHSON method. After converting of (5.28) into standard VOIGT-notation, the equation system is condensed and the increments of the internal variables are determined. The procedure is repeated until a norm formed by the residuals r_i^B falls below a predefined tolerance. Slight modifications of the matrices and vectors are necessary if only additional spontaneous inelastic strains ($\dot{\gamma}_{pl,\alpha}^{B,n+1} = 0$) or only additional time-dependent inelastic strains ($\dot{\gamma}_{cr}^{n+1} = 0$) are produced.
The stress computation of the fibrous fraction is carried out in the same way. After transforming of the inelastic strains from the current configuration of the last converged global time step to the actual current configuration, the trial KIRCHHOFF-stresses are determined by equation (4.57)

$$\tilde{\mathbf{T}}^{F,tr,n+1} = \left[(\mathbf{R}^{F,n+1})^T \otimes (\mathbf{R}^{F,n+1})^T\right]^{T_{23}} : \mathbb{C}_{loc}^{lin} : \left[\mathbf{R}^{F,n+1} \otimes \mathbf{R}^{F,n+1}\right]^{T_{23}} : \left(\mathbf{A}^{s,n+1} - \mathbf{A}_{in}^{F,tr,n+1}\right) , \tag{5.29}$$

$$\mathbf{A}_{in}^{F,tr,n+1} = (\mathbf{F}^{s,n+1})^{-T} \cdot (\mathbf{F}^{s,n})^T \cdot \mathbf{A}_{in}^{F,n} \cdot (\mathbf{F}^{s,n}) \cdot (\mathbf{F}^{s,n+1})^{-1} . \tag{5.30}$$

If the trial stresses $\tilde{\mathbf{T}}^{F,tr,n+1}$ violate one of the six yield conditions, the nonlinear equation system formed by the stress-strain relation (4.57), by the kinematic relation after integrating of the inelastic flow (4.66) and by the yield conditions (4.59) and (4.60) has to be fulfilled

$$\mathbf{r}_T^F = \tilde{\mathbf{T}}^{F,n+1} - \left[(\mathbf{R}^{F,n+1})^T \otimes (\mathbf{R}^{F,n+1})^T\right]^{T_{23}} : \mathbb{C}_{loc}^{lin} : \left[\mathbf{R}^{F,n+1} \otimes \mathbf{R}^{F,n+1}\right]^{T_{23}} : \left(\mathbf{A}^{n+1} - \mathbf{A}_{in}^{F,n+1}\right) = \mathbf{0} , \tag{5.31a}$$

$$\mathbf{r}_A^F = \mathbf{A}_{in}^{F,n+1} - \mathbf{A}_{in}^{F,tr,n+1} - \sum_{\alpha=1}^{3} \Delta\gamma_{pl,\alpha}^{F,n+1} \frac{\partial f_{t,\alpha}}{\partial \tilde{\mathbf{T}}^{F,n+1}} - \sum_{\alpha=1}^{3} \Delta\gamma_{pl,\alpha+3}^{F,n+1} \frac{\partial f_{c,\alpha}}{\partial \tilde{\mathbf{T}}^{F,n+1}} = \mathbf{0} , \tag{b}$$

$$\mathbf{r}_f^F = -(f_{c,\alpha},\, f_{t,\alpha})^T = \mathbf{0} . \tag{c}$$

Then, the equation system (5.31) is linearised with respect to the internal variables of the fibrous fraction - KIRCHHOFF-stresses $\tilde{\mathbf{T}}^{F,n+1}$, inelastic ALMANSI-strains $\mathbf{A}_{in}^{F,n+1}$, and the six LAGRANGIAN multipliers $\Delta\gamma_\alpha^{F,n+1} = \Delta t\, \dot{\gamma}_\alpha^{F,n+1}$ taking into account that not all of them are active in the same time increment

$$\begin{bmatrix} \frac{\partial \mathbf{r}_T^F}{\partial \tilde{\mathbf{T}}^{F,n+1}} & \frac{\partial \mathbf{r}_T^F}{\partial \mathbf{A}_{in}^{F,n+1}} & \mathbf{0} \\ \frac{\partial \mathbf{r}_A^F}{\partial \tilde{\mathbf{T}}^{F,n+1}} & \frac{\partial \mathbf{r}_A^F}{\partial \mathbf{A}_{in}^{F,n+1}} & \frac{\partial \mathbf{r}_A^F}{\partial \Delta\boldsymbol{\gamma}_{pl}^{F,n+1}} \\ \frac{\partial \mathbf{r}_f^F}{\partial \tilde{\mathbf{T}}_1^{F,n+1}} & \frac{\partial \mathbf{r}_f^F}{\partial \tilde{\mathbf{A}}_{in}^{F,n+1}} & \mathbf{0} \end{bmatrix} \begin{bmatrix} \mathrm{d}\tilde{\mathbf{T}}^{F,n+1} \\ \mathrm{d}\mathbf{A}_{in}^{F,n+1} \\ \mathrm{d}\Delta\boldsymbol{\gamma}_{pl}^{F,n+1} \end{bmatrix} = \begin{bmatrix} -\mathbf{r}_T^F \\ -\mathbf{r}_A^F \\ -\mathbf{r}_f^F \end{bmatrix} . \tag{5.32}$$

The LAGRANGIAN-multipliers are summarised into the vector $\Delta\boldsymbol{\gamma}_{pl}^{F,n+1}$, whose size can vary and depends on the number of active yield conditions. The nonlinear equation system (5.32) is implemented in its VOIGT form and solved by the NEWTON-RAPHSON procedure until a norm of the residuals r_i^F falls below a defined tolerance.
After solving the initial value problem of the basic matrix and of the fibrous fraction iteratively, the internal state variables on the actual current configuration are known and are used in order to check the global residuals .

5.4 Consistent material operator

A crucial point in reaching global convergence is the correct determination of the consistent material operators $\tilde{\mathbf{T}}^s_{,\mathbf{F}^s}$ and $\tilde{\mathbf{T}}^s_{,p}$. Both include the dependencies of the effective solid stress on the displacements and the state variables of the transport process, respectively. The tangential operator $\tilde{\mathbf{T}}^s_{,\mathbf{F}^s} = \frac{\partial \tilde{\mathbf{T}}_E^{s,n+1}}{\partial \mathbf{F}^{s,n+1}}$ is obtained by forming the total differential of the KIRCHHOFF stresses of the solid phase with respect to the deformation gradient of the solid phase $\mathbf{F}^{s,n+1}$

$$\frac{\partial \tilde{\mathbf{T}}_e^{s,n+1}}{\partial \mathbf{F}^{s,n+1}} : \mathrm{d}\mathbf{F}^{s,n+1} = n^B \frac{\tilde{\mathbf{T}}^{B,n+1}}{\partial \mathbf{F}^{s,n+1}} : \mathrm{d}\mathbf{F}^{s,n+1} + n^F \frac{\tilde{\mathbf{T}}^{F,n+1}}{\partial \mathbf{F}^{s,n+1}} : \mathrm{d}\mathbf{F}^{s,n+1} . \tag{5.33}$$

Thus, the total differential of equation system (5.27) reads

$$\underline{\underline{\mathbf{A}}}^B \begin{bmatrix} \frac{\partial \tilde{\mathbf{T}}^{B,n+1}}{\partial \mathbf{F}^{s,n+1}} : \mathrm{d}\mathbf{F}^{s,n+1} \\ \frac{\partial \mathbf{A}_{in}^{B,n+1}}{\partial \mathbf{F}^{s,n+1}} : \mathrm{d}\mathbf{F}^{s,n+1} \\ \frac{\partial \gamma_{pl}^{B,n+1}}{\partial \mathbf{F}^{s,n+1}} : \mathrm{d}\mathbf{F}^{s,n+1} \\ \frac{\partial a_{v,in}^{B,n+1}}{\partial \mathbf{F}^{s,n+1}} : \mathrm{d}\mathbf{F}^{s,n+1} \end{bmatrix} = \begin{bmatrix} \mathbf{0} \\ -\mathbf{r}_A^B \\ 0 \\ 0 \end{bmatrix} - \begin{bmatrix} \frac{\partial \mathbf{r}_T^B}{\partial \mathbf{F}^{s,n+1}} : \mathrm{d}\mathbf{F}^{s,n+1} \\ \frac{\partial \mathbf{r}_A^B}{\partial \mathbf{F}^{s,n+1}} : \mathrm{d}\mathbf{F}^{s,n+1} \\ \mathbf{0} \\ \frac{\partial r_f^B}{\partial \mathbf{F}^{s,n+1}} : \mathrm{d}\mathbf{F}^{s,n+1} \end{bmatrix} . \tag{5.34}$$

The matrix $\underline{\underline{\mathbf{A}}}^B$ includes the partial derivatives of the residuals $\mathbf{r}_i^B$ and coincides with the matrix used for the stress computations in the linearised equation system (5.28). The residuals are non-balanced in the first global iteration of a new time increment caused by mechanical creep. Thus, the non-equilibrium $\mathbf{r}_A^B$ exists in the residuum of the inelastic strains. Solving of the equation system for this term provides an additional portion for the global non-equilibrium force vector. This non-equilibrium is zero in all other iterations of a time step because the stress computation leads to balanced internal variables. The second vector on the right side of (5.34) includes the derivatives with respect to the deformation gradient $\mathbf{F}^{s,n+1}$ of the ALMANSI-strains $\mathbf{A}^{s,n+1}$ in the term $\frac{\partial \mathbf{r}_T^B}{\partial \mathbf{F}^{s,n+1}}$ as well as of the incremental deformation gradient in the term $\frac{\partial \mathbf{r}_A^B}{\partial \mathbf{F}^{s,n+1}}$. The latter dependency follows directly from the small elastic strain assumption discussed in section 4.1.2 and precludes a consistent material operator formed by the ALMANSI-strains as it is common in small strain plasticity. The influence of the water content

and the porosity on the shear parameters and on the angle of dilatancy includes further dependencies added to the terms $\frac{\partial r_f^B}{\partial \mathbf{F}^{s,n+1}}$ and $\frac{\partial \mathbf{r}_A^B}{\partial \mathbf{F}^{s,n+1}}$. Solving the equation system for the second vector provides the requested material operator for the basic matrix $\frac{\partial \tilde{\mathbf{T}}^{B,n+1}}{\partial \mathbf{F}^{s,n+1}}$. The material operator for the fibrous fraction $\frac{\tilde{\mathbf{T}}^{F,n+1}}{\partial \mathbf{F}^{s,n+1}}$ is obtained in the same way. Establishing the total differential of equation system (5.31) using the matrix $\underline{\underline{\mathbf{A}}}^F$ from equation system (5.32) leads to

$$\underline{\underline{\mathbf{A}}}^F \begin{bmatrix} \frac{\partial \tilde{\mathbf{T}}^{F,n+1}}{\partial \mathbf{F}^{s,n+1}} : \mathrm{d}\mathbf{F}^{s,n+1} \\ \frac{\partial \mathbf{A}_{in}^{F,n+1}}{\partial \mathbf{F}^{s,n+1}} : \mathrm{d}\mathbf{F}^{s,n+1} \\ \frac{\partial \Delta \boldsymbol{\gamma}_{pl}^{F,n+1}}{\partial \mathbf{F}^{s,n+1}} : \mathrm{d}\mathbf{F}^{s,n+1} \end{bmatrix} = - \begin{bmatrix} \frac{\partial \mathbf{r}_T^F}{\partial \mathbf{F}^{s,n+1}} : \mathrm{d}\mathbf{F}^{s,n+1} \\ \frac{\partial \mathbf{r}_A^F}{\partial \mathbf{F}^{s,n+1}} : \mathrm{d}\mathbf{F}^{s,n+1} \\ \frac{\partial \mathbf{r}_f^F}{\partial \mathbf{F}^{s,n+1}} : \mathrm{d}\mathbf{F}^{s,n+1} \end{bmatrix}, \tag{5.35}$$

from which the operator $\frac{\partial \tilde{\mathbf{T}}^{F,n+1}}{\partial \mathbf{F}^{s,n+1}}$ is received. Since no time-dependent phenomena are connected with the fibrous fraction, no additional non-equilibrium forces exist in the first new global iteration. The dependency of the strength of the fibres on the stresses of the basic matrix describing the bond failure has to be considered additionally

$$\frac{\partial \mathbf{r}_f^F}{\partial \mathbf{F}^{s,n+1}} : \mathrm{d}\mathbf{F}^{s,n+1} = \left(\frac{\partial \mathbf{r}_f^f}{\partial \tilde{\mathbf{T}}^{B,n+1}} : \frac{\tilde{\mathbf{T}}^{B,n+1}}{\partial \mathbf{F}^{s,n+1}} \right) : \mathrm{d}\mathbf{F}^{s,n+1}$$

The operator $\tilde{\mathbf{T}}_{e,p}^s = \frac{\partial \tilde{\mathbf{T}}_e^s}{\partial S^g}$ is computed in a similar way formulating the total differential of the KIRCHHOFF stresses with respect to the gas saturation S^g only because no dependencies on the liquid pressure p^l exist

$$\frac{\partial \tilde{\mathbf{T}}_e^s}{\partial S^g} \mathrm{d}S^g = n^B \frac{\tilde{\mathbf{T}}^B}{\partial S^g} \mathrm{d}S^g + n^F \frac{\tilde{\mathbf{T}}^F}{\partial S^g} \mathrm{d}S^g . \tag{5.36}$$

Thereby, the equation systems

$$\underline{\underline{\mathbf{A}}}^B \begin{bmatrix} \frac{\partial \tilde{\mathbf{T}}^{B,n+1}}{\partial S^{g,n+1}} \mathrm{d}S^{g,n+1} \\ \frac{\partial \mathbf{A}_{in}^{B,n+1}}{\partial S^{g,n+1}} \mathrm{d}S^{g,n+1} \\ \frac{\partial \gamma_{pl}^{B,n+1}}{\partial S^{g,n+1}} \mathrm{d}S^{g,n+1} \\ \frac{\partial a_{v,in}^{B,n+1}}{\partial S^{g,n+1}} \mathrm{d}S^{g,n+1} \end{bmatrix} = - \begin{bmatrix} \mathbf{0} \\ \frac{\partial \mathbf{r}_A^B}{\partial S^{g,n+1}} \mathrm{d}S^{g,n+1} \\ 0 \\ \frac{\partial r_f^B}{\partial S^{g,n+1}} \mathrm{d}S^{g,n+1} \end{bmatrix} \tag{5.37}$$

and

$$\underline{\underline{\mathbf{A}}}^F \begin{bmatrix} \frac{\partial \tilde{\mathbf{T}}^{F,n+1}}{\partial S^{g,n+1}} \mathrm{d}S^{g,n+1} \\ \frac{\partial \mathbf{A}_{in}^{F,n+1}}{\partial S^{g,n+1}} \mathrm{d}S^{g,n+1} \\ \frac{\partial \Delta \boldsymbol{\gamma}_{pl}^{F,n+1}}{\partial S^{g,n+1}} \mathrm{d}S^{g,n+1} \end{bmatrix} = - \begin{bmatrix} \mathbf{0} \\ \mathbf{0} \\ \frac{\partial \mathbf{r}_f^F}{\partial S^g} \mathrm{d}S^{g,n+1} \end{bmatrix} \tag{5.38}$$

have to be solved in order to get the derivatives $\frac{\partial \tilde{\mathbf{T}}^{B,n+1}}{\partial S^{g,n+1}}$ and $\frac{\partial \tilde{\mathbf{T}}^{F,n+1}}{\partial S^{g,n+1}}$. If the strength of the solid does not depend on the water content, the computation of the last operators is not necessary anymore.

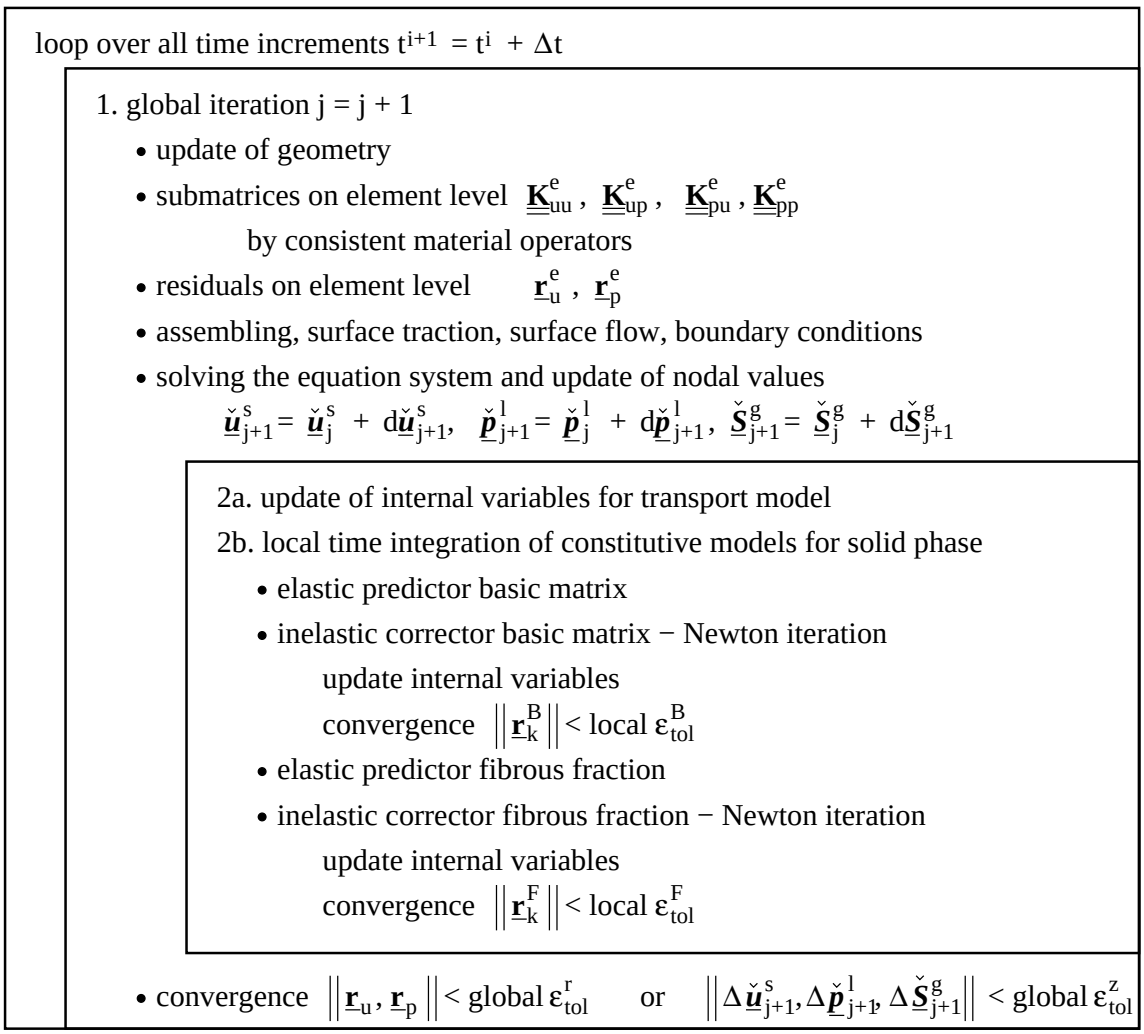

Figure 5.5: Scheme of solving algorithm

6 Parameter Identification and Model Verification

The development of powerful constitutive models includes different steps described by Ahrens et al. [3] for metals or Desai and Siriwardane [24] for soils. After recognising the physically relevant processes, mathematical equations are established in order to describe the observed phenomena. Thereby, essential parameters are identified, which have to be determined using laboratory experiments and in-situ measurements. Numerical simulations of experiments with different load paths validate the quality of the model formulation. Finally, the model is applied to reproduce in-situ test cases including a critical comparison between the model predictions and the real behaviour, in which model limitations become apparent.

In this chapter laboratory experiments are numerically reproduced with the developed constitutive model. Some difficulties are connected with the simulation of tests for municipal solid waste. First of all, the quantity of measured data is incomplete for many experiments reported about in the literature. Some information is missing, whereas other values could not be recorded due to the capacity and arrangement of the test device. Secondly, it is assumed that homogeneous conditions are present in some test samples only. Thus, experiments exhibiting points undergoing different load paths are reproduced inaccurately. Due to the complexity of the proposed constitutive model for municipal solid waste not all required parameters can be determined from the tests directly. In contrast, the application of nonlinear kinematics as well as a stress tensor differing from real CAUCHY-stresses complicates the parameter identification procedure.

Different approaches exist for the determination of the model parameters. The task of parameter identification is usually formulated as minimisation problem and all tools developed in this field are available. Aim of each optimisation strategy is to minimise the differences between the simulated and the experimental curves. The existing approaches are distinguished into stochastic and deterministic algorithms. Monte-Carlo simulation is the simplest stochastic method. In contrast, genetic algorithms use the information of foregoing steps in order to find a better parameter set. Deterministic algorithms, for instance Gradient-, Newton-, BFGS-, CG- or Simplex-methods, search the minimum of the objective function around a predefined starting point, and therefore they often find a local minimum only. Hybrid strategies combine stochastic and deterministic methods in order to ensure that the global minimum is detected. Thereby,

the stochastic method is used to find a good starting point for the deterministic search. Streilein [96] provides a comprehensive overview of the aforementioned approaches. An objective function compares the results of numerical simulations with the given experimental data. Kowalsky [64] proposes as target function for the evaluation of a parameter set

$$f = \sum_{i=1}^{n} \frac{\int w_i \mid Y_{sim,i} - Y_{exp,i} \mid \mathrm{d}t}{Y_{exp,,i}^{max}\, t_i^{dur}}\,, \tag{6.1}$$

in which $\mid Y_{sim,i} - Y_{exp,i} \mid$ is the absolute value of the difference of stresses, forces, displacement etc. between numerical simulation and laboratory test i. The difference is weighted by a factor w_i and integrated over the test duration. The derivation is scaled by the maximum value $Y_{exp,i}^{max}$ and the test duration t_i^{dur}.

6.1 Genetic algorithms

Genetic algorithms or evolutionary strategies that mimic the metaphor of natural biological evolution are probably the best and most efficient numerical tool for parameter determination. The most important steps are displayed in figure 6.1 and discussed in profundity by Pohlheim [88].

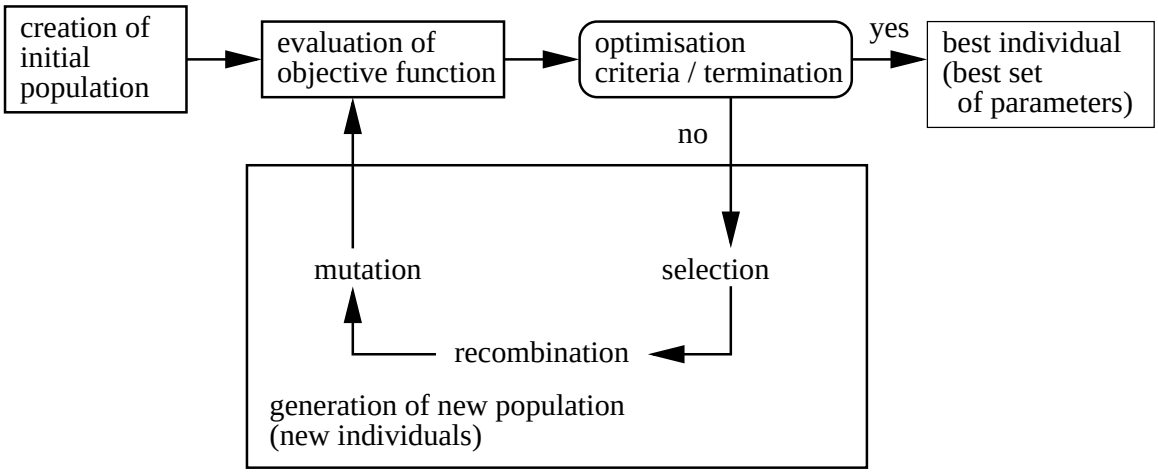

Figure 6.1: Scheme of genetic algorithms

At first, the initial population consisting of N_{ind} individuals is created randomly or by presetting. Each individual of a generation is evaluated by the objective function.
Then, the individuals are ordered in such a way that the best parameter set is the fittest individual indicated by $ind = 1$. A linear scheme associates the fitness value fit_{ind} to each individual

$$fit_{ind} = 2 - SP + 2\,(SP - 1)\frac{N_{ind} - ind}{N_{ind} - 1}\,, \qquad 1 \leq SP \leq 2\,, \tag{6.2}$$

in which SP is the selective pressure that governs the differences of selection between the fittest and the unfittest individual of the population. For $SP = 1$ each individual has the same chance for reproducing, whereas for $SP = 2$ the fittest individual hands down its properties much better than the unfittest. The selection probability $p_{s,ind}$ is attributed to each individual over its fitness value

$$p_{s,ind} = \frac{fit_{ind}}{N_{ind}} \,. \tag{6.3}$$

Thus, for stochastic sampling an interval of probability is defined by

$$\Delta p_{s,ind} = \left(\sum_{i=1}^{ind-1} p_{s,i}; \sum_{i=1}^{ind} p_{s,i} \right) \,. \tag{6.4}$$

An individual is selected if a generated uniform random number $\Omega \in [0; 1]$ lies within the interval $\Delta p_{s,ind}$.
Recombination produces new individuals using information from usually two parents of the mating generation. After selecting the two parents P_1 and P_2, the parameters PAR_i of the new individual are obtained applying following rule

$$PAR_i = a_i \, PAR_i^{P_1} + (1 - a_i) \, PAR_i^{P_2} \,, \qquad a_i \in [-0.25; 1.25] \;\; \text{uniform at random} \,. \tag{6.5}$$

Equation (6.5) is a linear interpolation of the properties of the two parents by a factor a_i chosen in the quoted interval randomly.
Mutation of the new individual helps to avoid persisting in a local minimum. Thus, one or more randomly picked parameters are slightly altered after creation

$$PAR_i^{Mut} = PAR_i + s_i \, r_i \, v_i \,. \tag{6.6}$$

Thereby, s_i defines the sign of the modification that is randomly picked

$$s_i \in \{-1; +1\} \;\; \text{uniform at random} \,.$$

The value r_i describes the range of mutation formed with lower and upper restriction PAR_i^{min} and PAR_i^{max} of the mutated parameter and a chosen value for r

$$r_i = \left(PAR_i^{max} - PAR_i^{min} \right) \, r \,, \qquad r \in \left[10^{-6}; 10^{-1} \right] \;\; \text{chosen} \,.$$

Finally, v_i controls the mutation step size

$$v_i = 2^{-k\,u} \,, \quad u \in \left[10^{-6}; 10^{-1} \right] \;\; \text{uniform at random} \,, \;\; k \in \{4; 5; ...; 20\} \;\; \text{chosen} \,.$$

The parameters u and k ensure that most mutated parameters PAR_i^{Mut} are near the original parameter PAR_i.
All new individuals of an offspring generation, usually much more than the number of individuals of the parent generation, are evaluated by the objective function. The best

of them form the new mating generation. Sometimes, it is auxiliary to reinsert some of the best individuals of the former generation into the new one. The procedure is repeated until a convergence criterion is met or the maximal number of repeating steps is exceeded.

6.2 Simulation of laboratory experiments

Laboratory tests described in section 2.2 are used for the determination of the model parameters as well as for the validation of the constitutive model. The simulation of lateral confined compressive tests, of uniaxial and triaxial tests as well as a tensile test indicates how the model can reproduce the observed phenomena. Finally, some comments for assessment of the hydraulic properties are provided.

6.2.1 Oedometric tests

The mechanical creep occurring in the third stage of the municipal solid waste compressive curve is modelled by the formulation for time-depending compaction including the influence of both actual stress state and actual state of density. Laterally confined compressive tests are carried out by Ziehmann [108] at the Leichtweiß-Institute, TU Braunschweig, Germany. Two samples consisting of mechanical-biologically pretreated waste taken from the landfill Meisenheim, Germany, are tested in a large oedometer possessing a diameter of 600 mm and an initial height of 500 mm. The first sample is sieved and the material passes a 60 mm filter and exhibits a dry density of 950 kg/m^3. In contrast, the material of the second sample passes a 300 mm filter and has a dry density of 810 kg/m^3. The two samples are filled in the oedometric cell. They are loaded vertically by a compressive stress p of 90 kPa, 220 kPa and 330 kPa, respectively. Since the material is pretreated, it is presumed that the portion of fibrous constituents is very low. Therefore, the influence of the fibres is neglected totally. Furthermore, the shear parameters of the basic matrix are kept constant during the simulation setting the friction angle to ϕ'=30°and the cohesion to 5 kPa. The simulation is carried out under volume-preserving spontaneously inelastic behaviour and the angle of dilatancy ψ' is zero. The ratio between the elastic parameters of equation (4.30) is predefined to λ/μ=1.5 tantamount to a value for POISSON's ratio ν=0.3 in HOOKE's law of small strain elasticity.
The parameters of the compaction model are determined applying the genetic algorithm. Since more or less homogeneous conditions exist in the sample carrying out the simulation in only one GAUSSION point is justified. Thereby, the deformation gradient is obtained from the displacements and the initial geometry, height and radius. The

elasticity		λ = 3,570 kPa; μ = 2,385 kPa
compaction		A = 1.625·10^{-15} $\frac{1}{s}$; n = 2.39; p = 13.48; a_{cr} = 0.67; b_{cr} = 44.69 kPa
density	test 1	$c_{v,0}$ = -0.207; $c_{v,max}$ = -1.82
	test 2	$c_{v,0}$ = -0.243; $c_{v,max}$ = -1.76

Table 6.1: Parameter set oedometric test for basic matrix

radial displacements are zero due to the lateral confinement and only vertical displacements are created by the applied vertical load. The problem is solved by the stress algorithm described in section 6.1 with the boundary conditions u=0, v=0, T_{zz}=-p. All shear components of stress and strain measures vanish leading to an acceleration in the computation. Here, the first sample is only used for the fitting process and the second test is simulated with the obtained parameter set after slightly changing the parameters $c_{v,0}$ and $c_{v,max}$ that describe the initial and the highest reachable density. The best parameter set is presented in table 6.1.
Figure 6.2 compares the results of simulation and test. Obviously, the numerical model fits the experimental data very well. Differences appear in the second load stage of the first test and in the first stage of the second test only. For the long duration of the third stage the two curves are reproduced very well. Especially, the final value of compaction is reached in a satisfying way. In contrast, some discrepancies exist in the unloading behaviour. Since the elastic parameters are fitted on the first curve, the final displacement after total unloading is hit quite well. But the unloading of the second test produces a displacement increment, which is too small in the simulation compared with the laboratory test.

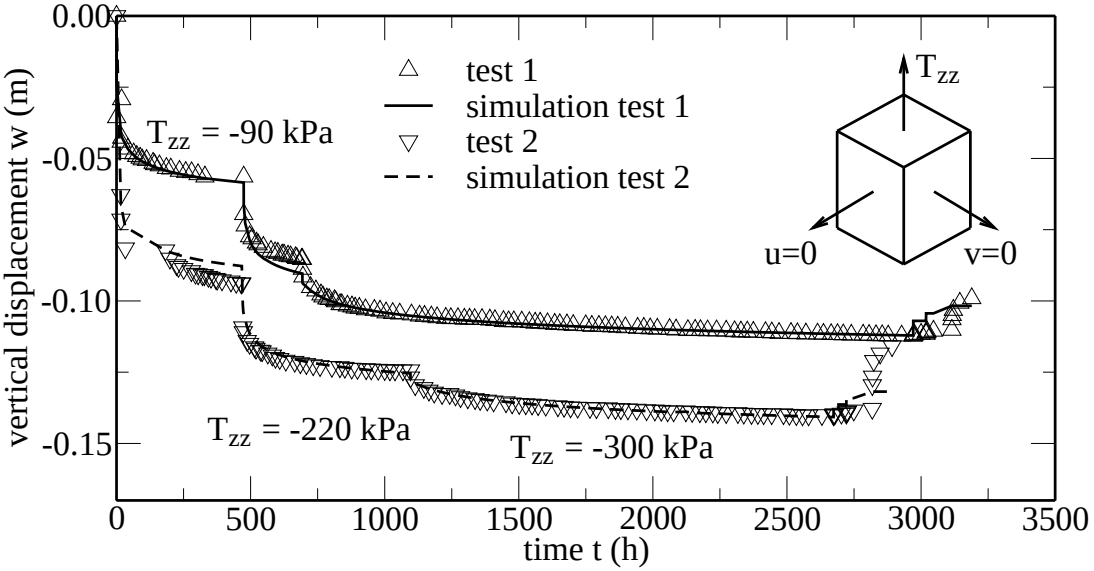

Figure 6.2: Fitting parameter on oedometric tests

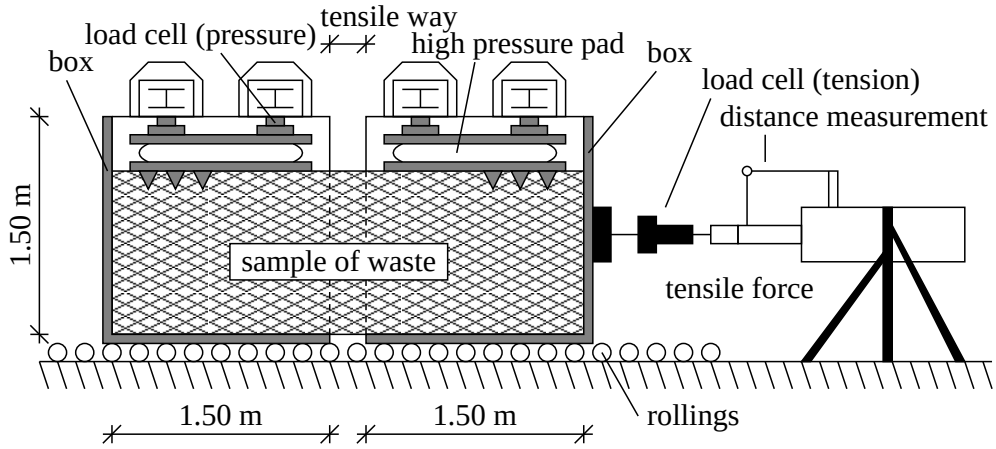

Figure 6.3: Sketch of large tensile test

6.2.2 Tensile tests

Tensile tests provided by the Leichweiß-Institute, TU Braunschweig, are used in order to calibrate the model of the fibrous constituents. The equipment for the large tensile test is developed by Kölsch [62] and sketched in figure 6.3. The waste of the sample originates from the landfill Göttingen, Germany. The sample material is excavated there and directly transported inside the tensile box to the laboratory. Concerning its dry mass, it consist of 28.5 % mixed material passing a 8 mm filter and 43.7 % mixed material passing a 40 mm filter. The particles with diameters larger than 40 mm are decomposed by 4.4 % textile, 2.4 % mineral matter, 9.9 % wood and leather, 0.8 % metals, 3.3 % hard plastics, 4.7 % soft plastics and 2.3 % paper and cardboard. Easily degradable organic matter is not present. The volume fraction of the fibrous particles is assumed to $n^F \approx 0.20$ for the simulation. The test consists of four different levels of vertical loading - 100 kPa, 200 kPa, 300 kPa and 400 kPa - under laterally confined displacements. Time-dependent settlements occur due to the compressive load. Therefore, the test is used in order to validate the creep model, too. After decaying of the creep, the displacement controlled tensile test is carried out. Thereby, the box having a base area of 3.00 m x 1.00 m with the waste sample inside is split into two parts and one of them is pulled away in horizontal direction until a maximum of the applied tensile force is reached. Then, the moved part of the box is rolled back and the next stage commences by increasing the vertical load. The last tensile test under a load level of 400 kPa is repeated and the applied displacement is increased until the softening of the material becomes apparent.
The simulation is carried out using only one GAUSSIAN point. Thus, all strains and stresses are smeared over the dimensions of the box. For some simulation steps not all desired data are available due to the complexity and the difficulties in carrying out the test. For instance, no information exists about horizontal stresses during the creep

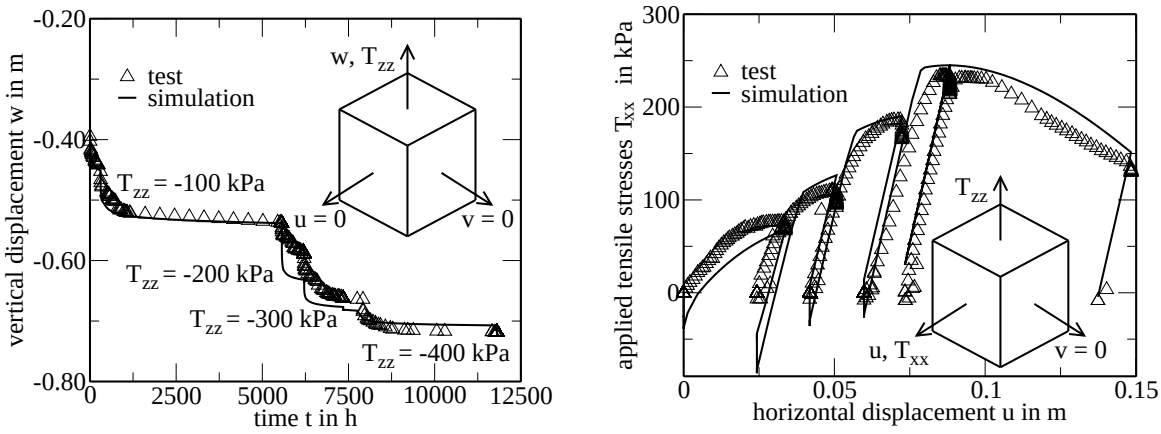

Figure 6.4: Fitting parameter on tensile tests

periods. Nevertheless, the complex stress-strain history is simulated completely and the curves of the laboratory experiment and the numerical analysis are compared to each other in figure 6.4. The settlement behaviour is reproduced quite well. Only the final value is overestimated by the model for the second creep period under a vertical load of 200 kPa. In contrast, the curves differ marginally for the first and last stage as shown in figure 6.4 on the left. The main goal of reproducing the tensile behaviour succeeds in a satisfying way. The hardening as well as the softening of the fibres is modelled in such a way that the behaviour of the waste sample is simulated correctly. Some variations are still present, but they are in a negligible range as displayed in the curves on the right of figure 6.4. Negative horizontal stresses, which are created by the vertical loading due to the lateral confined displacements in the creep periods, are not recorded in the test. Thus, simulation and test differ on the beginning of each tensile loading. A critical point is the assumption of homogeneous stress and strain distributions inside the sample. A proof that the dimensions of the box are sufficiently large enough to test municipal solid waste is still outstanding. It is concluded that the developed model can reproduce the overall smeared behaviour under vertical and tensile load correctly.

basic matrix	
elasticity	λ = 2,885 kPa; μ = 1,923 kPa
compaction	A = 3.2·10$^{-20}\frac{1}{\mathrm{s}}$; n = 7.14; p = 14.47; a_{cr} = 1.1; b_{cr} = 200.0 kPa
density	$c_{v,0}$ = -0.10; $c_{v,max}$ = -2.80
fibrous constituents	
elasticity	$E_{\perp}$ = 82,745 kPa; $E_{\shortparallel}$ = 1 kPa; $\nu_{\perp}$ = 0.33; $\nu_{\shortparallel}$ = 0.0; $G_{\shortparallel}$ = 0.5 kPa
strength	$\tilde{T}_{t,0}$ = 40 kPa; $\tilde{T}_{min}$ = 40 kPa; $\tilde{T}_{max}$ = 1500 kPa; $\tilde{T}^{B}_{crit}$ = 400 kPa
hardening	a = 2.887; b = 178.6
softening	c = 1.49; d = 7364; e = 2.75

Table 6.2: Parameter set of tensile test for basic matrix and fibrous constituents

The parameters for the compaction of the basic matrix and the tensile strength of the fibrous constituents are listed in table 6.2. The ratio between LAME's constants is predefined to $\lambda/\mu = 1.5$. The shear parameters are hold constant with ϕ'=30°and c'=5 kPa. The angel of dilatancy is set to zero. Due to the fact that fibres are orientated in a plane, YOUNG's modulus $E_{\shortparallel}$, POISSON' ratio $\nu_{\shortparallel}$ and the shear modulus $G_{\shortparallel}$ are zero. But, small values have to be set for $E_{\shortparallel}$ and $G_{\shortparallel}$ to avoid computational trouble.

6.2.3 Uniaxial compressive tests

Kockel [60] carries out uniaxial compressive tests on original and modified municipal solid waste from the central landfill of Hanover, Germany. The waste samples are disturbed by the excavation process and by the transport. A classification of the material provides following decomposition concerning its dry mass - wood 3 %, metals 3.6 %, plastic 14.1 %, textiles 2.4 %, papers/cardboards 24.1 %. The residual mass of 52.8 % cannot be classified and is described as dark mixture consisting of smaller grainy and fibrous particles. The water content is 40.4 %. The modified material is constituted by sieving out all particles larger than 120 mm. The samples are constructed by filling the material into cylindrical casings in several layers. After applying a vertical load and consolidation of the material, the samples exhibit different initial densities. The load controlled compressive test is carried out after removal of the casings. The experimental stress-strain curves are displayed in section 2.2.3 in figure 2.7 for the original waste composition and in figure 2.8 for the modified material.
Since no data for the consolidation stage are available, the test is simulated starting from an unloaded virgin state here. Thus, the parameter $c_{v,0}$ characterising the initial density is varied in the simulations. The initial sample height is set to 1.08 m and the initial radius to 0.27 m according to the values published by Kockel. 12 x 8 finite elements are used, in which the rotational symmetry of the cylindrical test equipment is exploited. The symmetry in the vertical direction z is not used. In contrast to the laboratory test, the simulation is performed displacement controlled moving all points on top of the cell with a constant vertical velocity of 3.33 mm/min. The finite element mesh and the boundary conditions are illustrated in figure 6.5. The parameters are taken from the tensile test, table 6.2, because no further information exists. The shear parameters angle of internal friction, and the cohesion as well as the angle of dilatancy are described with the parameter set of table 6.3. The volume ratio of the fibrous fraction is reduced

angle of internal friction	$a_{\phi'}$ = 45.0°; $b_{\phi'}$ = 2.05; $c_{\phi'}$ = 3.17
cohesion	$a_{c'}$ = 5.0 kPa; $b_{c'}$ = 2.05; $c_{c'}$ = 3.17
angle of dilatancy	a_{ψ} = 20.0°; b_{ψ} = 2.05; c_{ψ} = 3.17

Table 6.3: Parameter set of tensile test for basic matrix and fibrous constituents

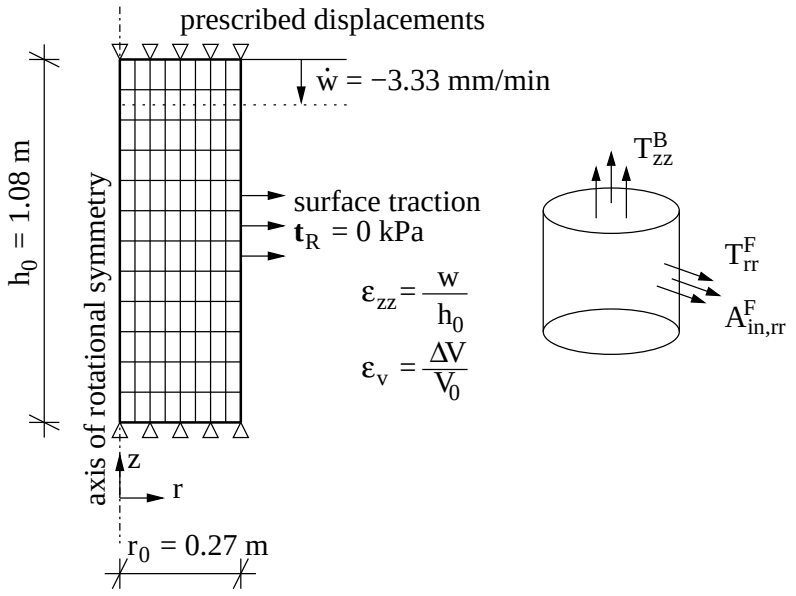

Figure 6.5: Discretisation and boundary conditions of uniaxial compressive test

to $n^F = 0.06$ for the modified waste in order to consider the removal of all particles larger then 120 mm.

The vertical stretch ε_{zz} versus vertical stress T_{zz} curves obtained by simulating the original material are shown in figure 6.6 on the left. Similar to the behaviour of the original material during the test, the sample undergoes large vertical displacements on a low vertical load level first. The material is compressed more or less inelastically because the material is very loose at the beginning. Although the vertical stresses are low, the compaction rate is high. The material densifies more and more with ongoing compaction and the creep rate decreases. Thus, more stresses have to be applied in order to hold the displacement rate constant. Thereby, the stiffness increases drastically and the stress-strain curves exhibit a much steeper tangent. Such a behaviour occurs for all three tests with different initial conditions. The sample indicated by $c_{v,0} = 0.05$ has the lowest initial density and represents test EX0-uM-1 of figure 2.7. In contrast, the state with the highest initial density is modelled by setting $c_{v,0} = 1.0$. A horizontal spalling is avoided due to the high portion of fibrous particles $n^F = 0.20$ inside the material. During the high vertical compaction the initially randomless distributed fibrous particles orientate horizontally in the real test. This effect cannot be captured by the proposed model because the orientation in a horizontal plane of the fibres is predefined. Thus, the extension of the sample in radial direction is underestimated by the simulations, which can be seen in the vertical strain ε_{zz} versus volumetric strain ε_v curve in the upper part of figure 6.6 on the left. The curves have an inclination of 1:1 approximately indicating that only vertical displacements are obtained during the simulation.

A vertical stress of about -200 kPa to -250 kPa is required to reach failure for the modified material in uniaxial compressive tests. Thus, the volumetric fraction of the fibres

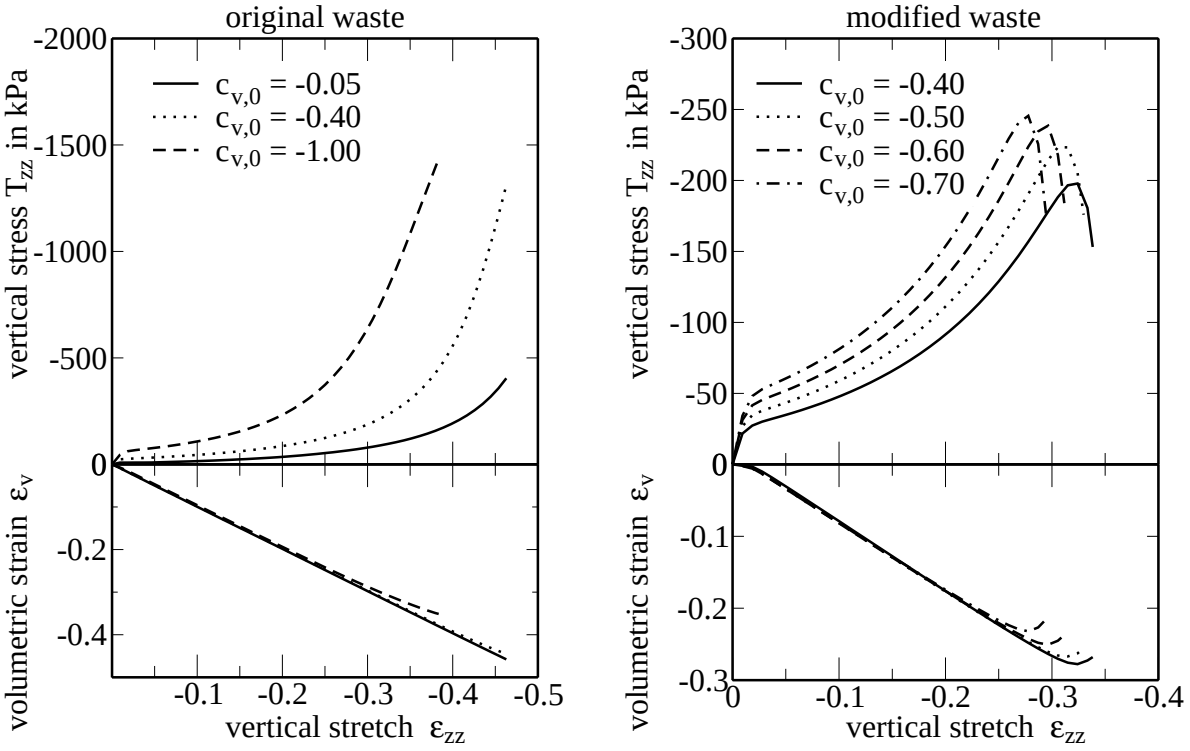

Figure 6.6: Simulations of uniaxial compressive tests

n^f is reduced to 0.06 in order to obtain the limit state on the aforementioned load level in the simulations. The initial densities of four tests carried out by Kockel, figure 2.8, distinguish slightly from 0.54 Mg/m^3 to 0.66 Mg/m^3. Thus, the value $c_{v,0}$ is varied from 0.4 to 0.7 in the simulations. The resulting vertical stretch versus vertical stress curves are plotted in figure 6.6 on the right. Failure is reached by a vertical stretch ε_{zz} of about 0.32 for the simulation with the loosest density $c_{v,0} = 0.4$ and by ε_{zz} of about 0.26 for $c_{v,0} = 0.7$. Thus, the model predicts correctly that samples having a higher initial density fail under a higher load on lower vertical stretch. The state of densification has different influences. At first, the shear resistance increases with ongoing densification. Further, the vertical stiffness is higher due to the reduced capability of compaction that is considered in the formulation of the creep rate. Therefore, the vertical stresses T_{zz} are lower on the same vertical displacement level if the the sample exhibits a higher initial density. Due to the bonding and anchorage effects, the stresses in the radial direction carried by the fibrous particles depend on the vertical stresses of the basic matrix, which are correlated to the total vertical stresses of the solid waste. Thus, the sample material tends to move in radial direction if the vertical load increases, but it is hold back by the activation of fibrous reinforcement. Compressive stresses are induced in radial direction for the basic matrix because force equilibrium with the fibres has to be fulfilled. Thus, the first invariant of the stresses of the basic matrix decreases and the frictional part of the shear resistance increases. On a certain point, the complex interactions between the

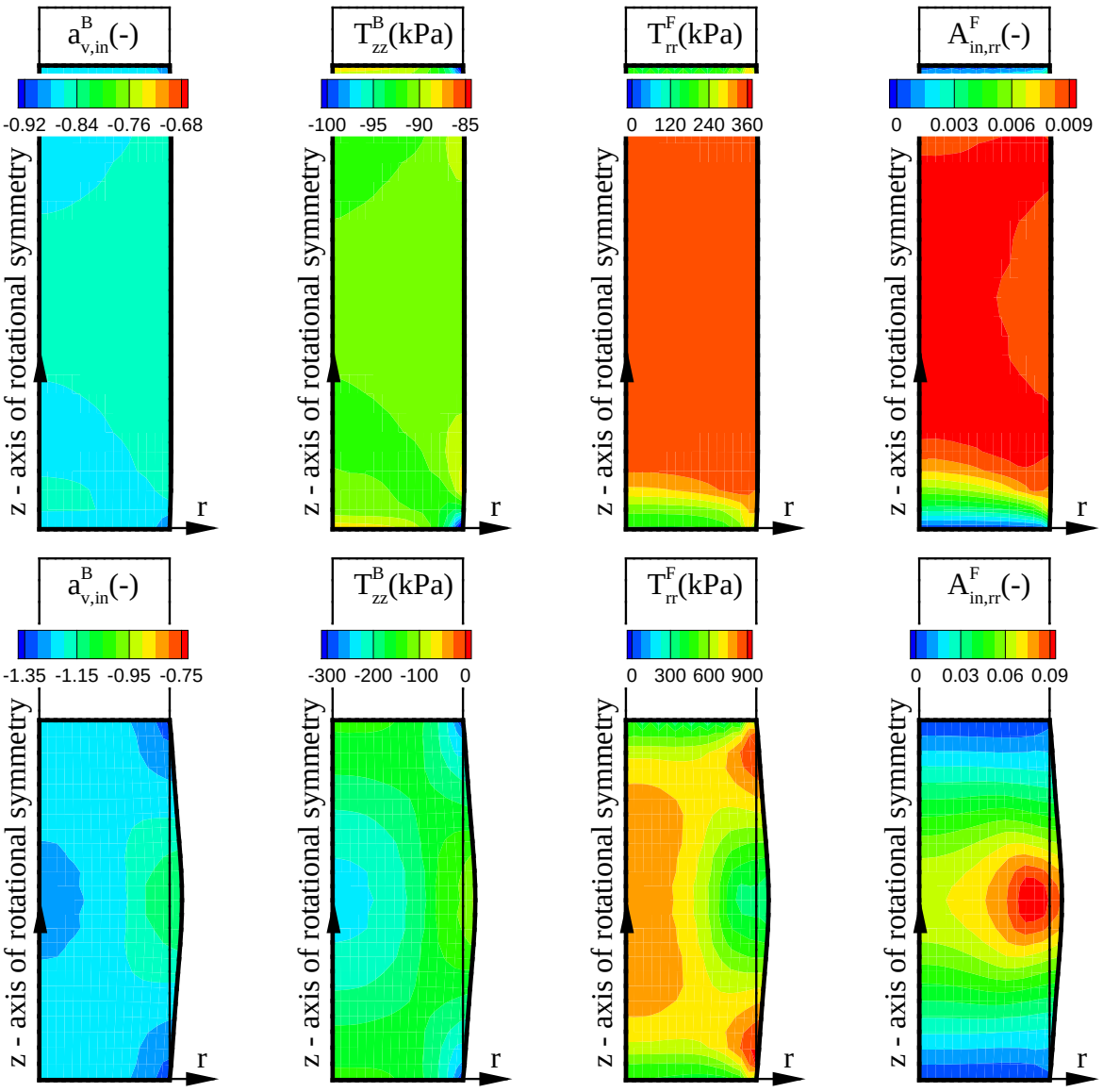

Figure 6.7: Failure in uniaxial compressive test

two partial stress tensors and the change of geometry of the sample allow no further increase of the the load and the sample fails. Thereby, the vertical load decreases and the anchorage mechanism leads to a reduced fibrous strength that accelerates the failure. Further, the ongoing of radial movement leads to an increase of inelastic ALMANSI strains of the fibrous fraction and to a softening. Figure 6.7 shows the changes of internal variables during the simulation for the test with an initial value $c_{v,0} = 0.7$. At an early stage by a vertical stretch of 11 % displayed in the upper figures inhomogeneities are mainly caused by the displacement boundary conditions on the top and on the bottom of the sample. Thus, the inelastic volume strain $a^B_{v,in}$ and the vertical stress of the basic matrix T^B_{zz} are almost constant in the whole sample. The radial stresses T^F_{rr} and the inelastic ALMANSI strains of the fibres change very fast in z-direction starting from

the boundary. Against it, if the sample exceeds the failure load, the situation changes considerably as illustrated in figure 6.7 in the lower row by a vertical stretch of 31 %. A zone, which has a lower density indicated by a higher value for $a^b_{v,in}$, is created on half the height nearby the surface. Thus, the vertical stresses of the basic matrix T^B_{zz} are only -125 kPa in this part compared to -250 kPa in the centre at $r = 0$. The internal variables of the fibrous fraction behave in a similar way. The stresses in radial direction T^F_{rr} are reduced drastically by the ongoing deformation and the inelastic strains A^F_{in} concentrate in this zone. The described phenomenon corresponds with a spalling of the sample as observed by Kockel in the experiments. It is concluded that the proposed model approach is able to reproduce the vertical stretch-stress behaviour correctly. A more quantitative analysis is possible if the same material is investigated in different laboratory tests. A main aspect is the correct assessment of the fibrous reinforcement. As shown in this section the high compressive strength has to be attributed to the action of the fibres mainly.

6.2.4 Triaxial compressive tests

As already described in section section 2.2.3, Kockel [60] also reports about triaxial compressive tests on waste samples reconstituted from the material used for the uniaxial compressive tests. Thereby, the basic matrix is milled and pulverised allowing the utilisation of a smaller triaxial test cell with a diameter of 100 mm and an initial height of 200 mm. The fibrous particles are shredded in such a manner that the geometric relations are conserved for the two solid fractions. Unfortunately, no data are available besides the stress-strain curves plotted in figure 2.11. Therefore, the simulations of the triaxial compressive tests allow only qualitative statements and a quantification of model parameters is impossible here. The test is reproduced using 12 x 8 finite elements exploiting the rotational symmetry. The boundary on the bottom is fixed in radial and vertical direction. The boundary on top of the sample is moved with a constant velocity of -0.4 mm/min in vertical direction preventing a radial movement. The applied lateral pressure is modelled as a constant surface traction normal to the surface of the solid waste. Thus, the originally radial pressure at the beginning of a test changes its direction if the waste sample is deformed. A sketch of the geometry and of the boundary conditions is shown in figure 6.8.
The material is consolidated uniaxially for a period of 16 hours and isotropically for a period of 1 hour before the triaxial compressive test is performed. The simulation carried out here includes only the triaxial test stage. Thus, the material is in an unloaded virgin state at the beginning of the computation. The parameters of the tensile test summarised in table 6.2 are used for the creep of the basic matrix and for the fibrous fraction compensating the consolidation by setting an initial value $c_{v,0} = -1.5$. The hardening of the fibres is decelerated setting the parameter $b = 17.86$ and the softening

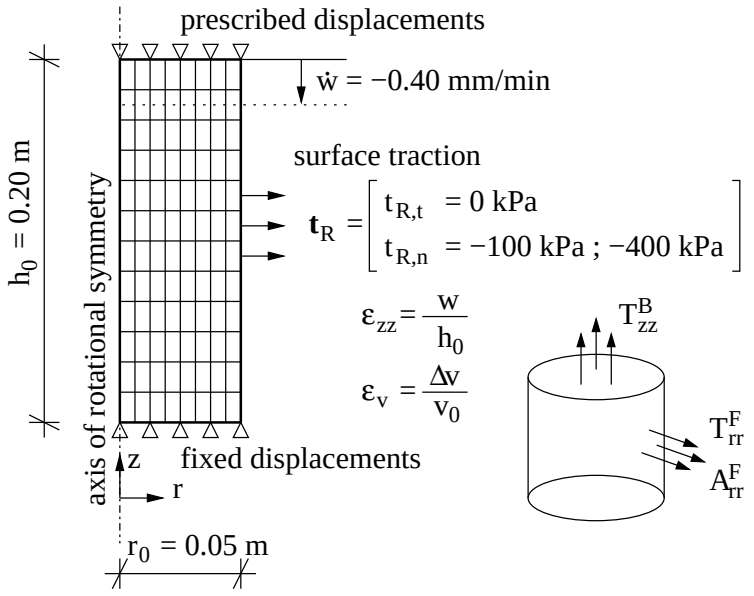

Figure 6.8: Discretisation and boundary conditions of triaxial compressive test

is eliminated by $d = 0.0$. Further, the shear strength of the basic matrix is modelled by the parameter set of table 6.3 reducing the parameters $b_{\phi'}$, $b_{c'}$ and b_{ψ} from 2.05 to 1.0. The volumetric content of fibres n^F is varied for the triaxial tests from 0.0 to 0.20.
The results of the simulations are displayed in figure 6.9 plotting the stress difference between the averaged vertical stress and the normal pressure in the cross section on half the height of the sample against the vertical stretch. Compared with the real tests, the failure load of the pure basic matrix obtained in the simulation is underestimated drastically although a high frictional angle ϕ' is activated. Thus, the basic matrix in Kockel's tests is able to carry much higher tensile forces as expected. There are different possibilities to explain this fact. At first, the cohesion is much higher, but this explanation contradicts the assumption that the basic matrix is a more granular material. The second possibility is to assume that the basic matrix after the definition of Kockel includes fibrous particles, too. Since Kockel includes all particles passing a 120 mm filter to the basic matrix, this assumption seems to be realistic. Thus, many smaller sticks and sheets can be inside the basic matrix used in the test, which is obtained by sieving. They act similar to small tensile elements in fibrous reinforced concrete. The shredding and milling does not change the general behaviour. Nevertheless, the increase of the overall strength of the composite material is contributed to the fibrous fraction mainly. Increasing the volumetric frather of fibrous particles results in a considerable increase of the strength of the material. The failure load reaches similar values in the simulation compared with the real test. Again a main problem is to reproduce the real radial displacements correctly. Similar to the uniaxial compressive tests, the simulation overestimates the volumetric changes, and therefore it underestimates the radial deformation. The influence of the chosen boundary conditions on top and bottom of the

sample has to be clarified in future. Probably, the prevention of the radial movement on top and bottom is to strict and a slip condition reproduces better the real behaviour.

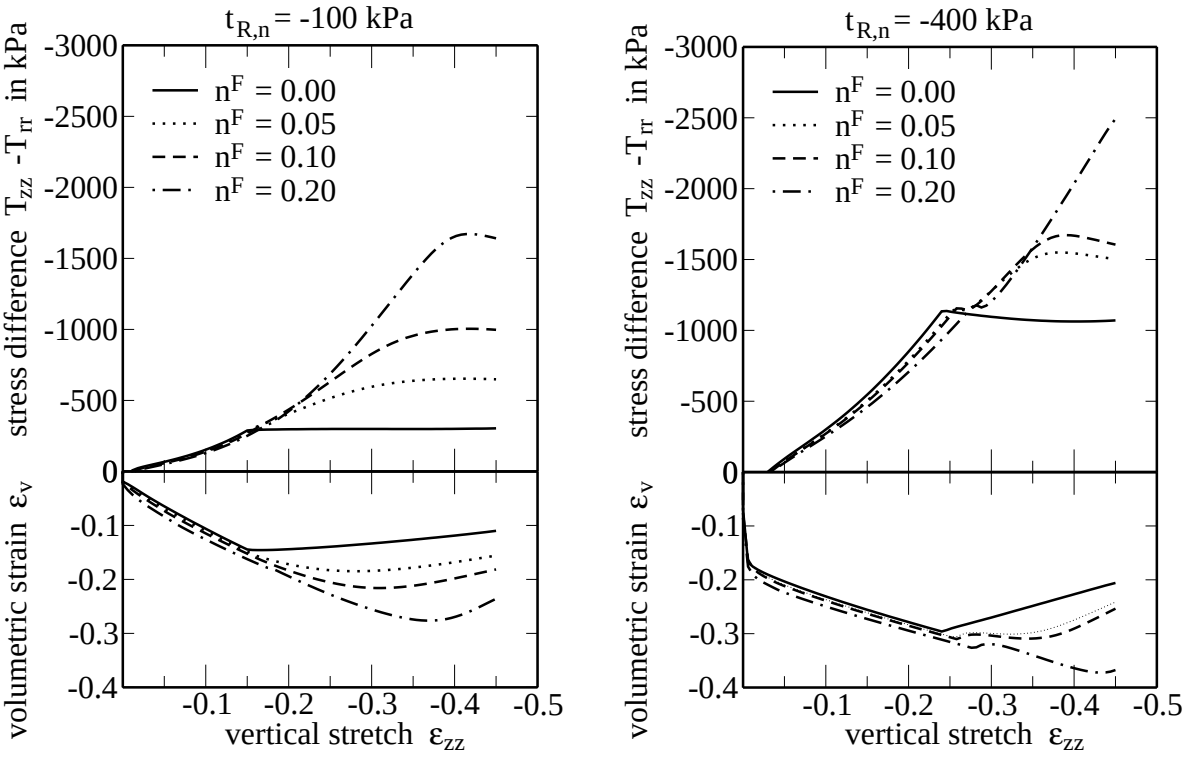

Figure 6.9: Simulations of triaxial compressive tests

6.2.5 Hydraulic tests

McDougall et al. [81] report about laboratory experiments, in which an artificial material composed by partially humified peat and cocoa shells should replicate the permeability and compressibility of municipal solid waste. The obtained curve for the composite material is translated to a presumed moisture content range for waste as shown in figure 6.10 on the left. The fitting of BROOKS-COREY model and the VAN GENUCHTEN model succeeds applying the genetic algorithm. Shifting the curve to other ranges of volumetric moisture content is connected with huge arbitrariness. Obviously, warrantable doubts remain existent concerning the comparability of waste and the tested artificial material. Thus, the results of McDougall are handled with care.
Stoltz and and Gourc [95] report about investigations on hydraulics of municipal solid waste. The one year old non-treated waste is taken from a drilled borehole on a french landfill site. The drilling operation shreds the waste in such way that the fraction passing a 50 mm sieve is larger than 70 mass-%. The waste consists of 20 % organic material including paper and cardboards, 16 % of plastics, 8 % of glass, 3 % of textiles, 7 % of metals, 29 % of dusts and 17 % non-identified material. Waste samples

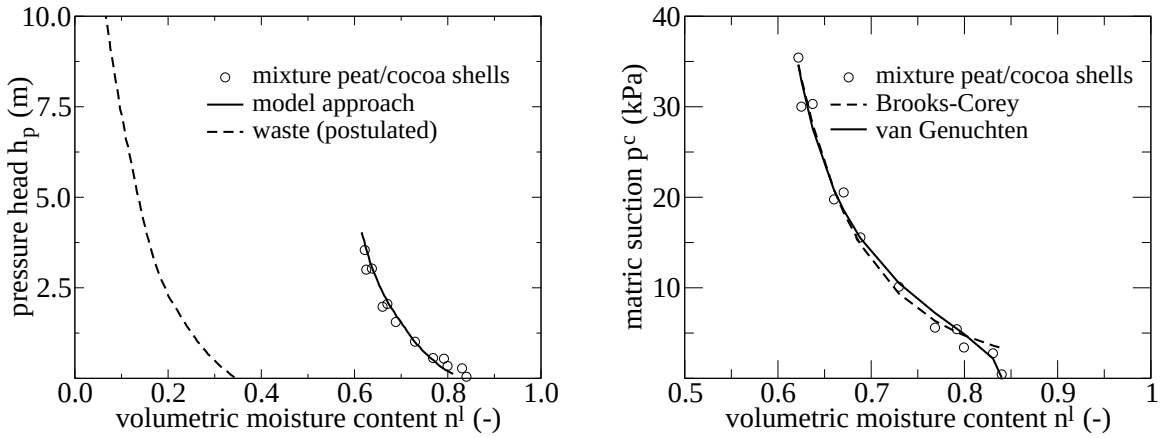

Figure 6.10: Experimental approach of McDougall et al. [81]

of 270 mm diameter and 290 mm initial height are tested in oedometric cells. Water retention curves are obtained for dry densities of 0.54 Mg/m^3 and 0.77 Mg/m^3 that are displayed in figure 6.11 together with theoretical graphs of BROOKS-COREY model and VAN GENUCHTEN model, respectively. The volumetic water content in saturated situation reduces from initially 0.63 down to 0.45 by the compaction of the waste. Furthermore, the reduction of pore space can be attributed to the closing of larger interparticle voids because the water retention curve is only present in a very small range of volumetric moisture content for the sample with a higher density. The residual water content increases by the densification indicating that the remaining water is less mobile and persists in smaller pores. Adopting the test results to the landfill scale is not so easy because the tested waste sample is considerably disturbed during the removal by drilling and shredding. It can be assumed that the solid-water characteristic curve of the in-situ dumped waste is below the curve with a dry density of 0.54 Mg/m^3 because larger particles construct larger interparticles pores and crevices, which reduce the suc-

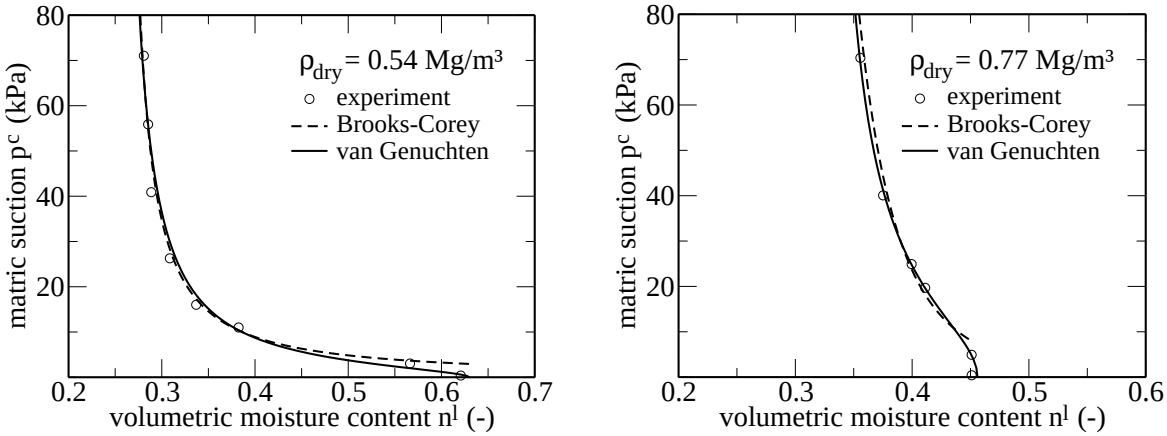

Figure 6.11: Fitting the experimental retention curves provided by Stoltz

	BROOKS-COREY	VAN GENUCHTEN
peat/cocoa shells	λ_{BC} = 0.227 ; p_{bub} = 1.92 kPa; n_l^r = 0.31; Φ = 0.84	α_{VG} = 0.13 kPa^{-1} ; m_{VG} = 0.45; n_{VG} = 2.07; n_l^r = 0.55; Φ = 0.84
waste ρ_{dry} = 0.54 Mg/m^3	λ_{BC} = 0.86 ; p_{bub} = 2.95 kPa; n_l^r = 0.26; Φ = 0.63	α_{VG} = 0.34 kPa^{-1} ; m_{VG} = 0.44; n_{VG} = 1.79; n_l^r = 0.25; Φ = 0.63
waste ρ_{dry} = 0.77 Mg/m^3	λ_{BC} = 0.21 ; p_{bub} = 7.98 kPa; n_l^r = 0.19; Φ = 0.46	α_{VG} = 0.05 kPa^{-1} ; m_{VG} = 0.49; n_{VG} = 1.96; n_l^r = 0.32; Φ = 0.46

Table 6.4: Parameter set for soil-water characteristic curves

tion. For the tests carried out by Stoltz and McDougall, respectively, the parameters for the BROOKS-COREY model and the VAN GENUCHTEN approach are summarised in table 6.4.
The parameter n_Φ in equation (4.84) controls the change of the intrinsic permeability $\mathbf{K}_{abs}$ with ongoing densification. Thus, the parameter can be determined if the hydraulic conductivities are known for two different saturated states. The ratio of the hydraulic conductivities equals the ratio of the porosities by the power of n_Φ

$$\left(\frac{\Phi^2}{\Phi^1}\right)^{n_\Phi} = \frac{k_{f,2}}{k_{f,1}} \,.$$

Since the values $k_{f,i}$ are usually measured, the porosities Φ^i have to be quantified in addition. For municipal solid waste, n_Φ lies in the range of 6 to 40. For example the parameter n_Φ is 20.8 assuming an initial porosity of 0.7 and a conductivity of 10^{-3} m/s, which is reduced to a porosity of 0.45 and a conductivity of 10^{-7} m/s.

6.3 Assessment of model verification

The performed numerical computations of laboratory tests show that the proposed constitutive model reproduces very well the observed phenomena. Although complex interactions between different components exist, the model is able to simulate lateral confined compressive test, uniaxial and triaxial compressive tests as well as tensile tests correctly. But, a lack of the analyses is the fact that the material used in the different tests is not the same. Thus, model parameters identified in one test for one sample are transferred to other samples consisting of material from other sides with different composition. Thus, optimal model validation and parameter identification are possible first if the different tests are carried out with waste coming from the same side, with the same composition and loading history. Thereby, the model parameters have to be identified on certain tests, and then the remaining tests not used for the identification procedure are simulated independently with the obtained parameter set.

7 Structural Analyses

Important possibilities to apply the developed model are presented in this chapter. Thereby, the spatial bearing mechanisms are analysed for the composite material municipal solid waste on more complex structures compared to the laboratory tests in chapter 6. Influences of the boundary conditions and the enormous importance of the mobilisation of fibrous strength are highlighted in the analyses. The time-dependent settlement behaviour is investgated in a first example. Then, stability analyses of slopes are performed for a 'dry' material numerically. The coupling of deformation and transport mechanisms is examined by one-dimensional consolidation. A last two-dimensional example emphasises the capacity of the enlarged model including the transport of the two pore fluids - leachate and landfill gas. The examples are chosen in such a way that the potentials of the developed model as well as its limitations are pointed out and that the performance of the numerical algorithms is examined in more detail.

7.1 Settlement behaviour

The prediction of time-dependent settlements is one key task in analysing landfill structures. The measured settlements on top of a landfill are one of the few indicators about the actual state inside the whole landfill body. As already discussed in section 2.2.2, municipal solid waste undergoes different characteristic stages of settlements in time. The first three stages include settlements caused mainly by the dead load of the waste itself. These effects are considered by the proposed elasto-plastic and creep models of the composite material. Settlements due to the biodegradation are not included into the approach until now. Thus, long-term prognosis of the landfill settlements is not possible so far.
The model is used for analysing the general bearing behaviour of a landfill. A 20 m high artificial landfill body is investigated for this purpose. Since numerical simulation of three-dimensional structures still requires large computational power, the analyses are restricted to two dimensions. Therefore, a strip of 1 m thickness is cutted as a characteristic cross sectional area. It is analysed assuming plane-strain conditions. Thus, no displacements occur in the y-direction of the investigated structure exhibiting an initial width of 70 m on the base and of 30 m on top . Since the two slopes are constructed un-

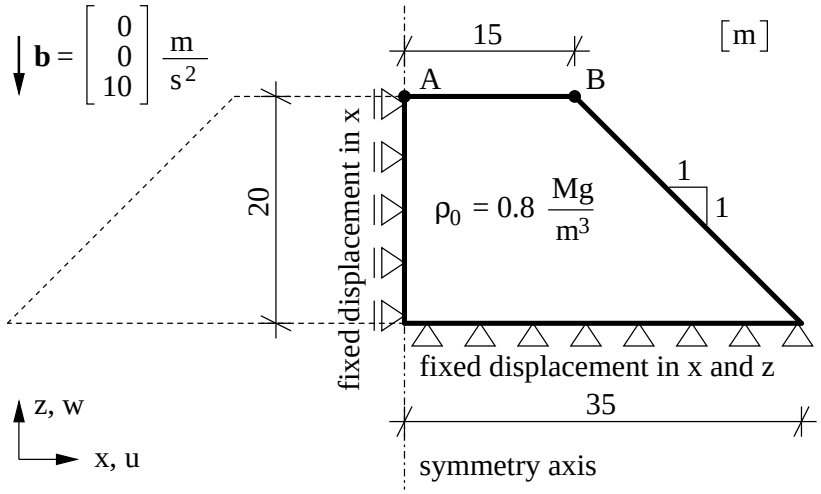

Figure 7.1: Sketch of landfill - settlement behaviour

der 45°, the symmetry is exploited in the simulation. The movements in vertical as well as in horizontal direction are inhibited on the boundary of the base totally. The density of the solid material is set to 0.8 Mg/m^3 uniformly. Thereby, the load is applied within one hour. A more realistic scenario requires additional effort in the computational code in order to simulate the dumping process in several layers in time correctly. Additional surface traction does not act on any surface. Figure 7.1 shows the geometry, boundary conditions and load graphically. The parameters are taken from the simulation of the tensile test of section 6.2.2, which are summarised in table 6.2. In contrast to the tested material, the portion of fibrous particles is reduced to n^F = 0.10 because the sample of the tensile test exhibits a very high content of papers and cardboards. Furthermore, the model parameter $c_{v,0}$ characterising the initial compactness is varied choosing values of 0.4, 0.7 and 1.0, respectively.

The structure is analysed using 20 x 20 nine-node displacement based elements with quadratic shape functions eliminating the unknowns of the centre node during the assembling. The duration of the simulations is limited to 2.5 years. An ongoing investigation is meaningless because most creep settlements are decayed during this period and the future behaviour is governed by biochemical processes in reality. Figure 7.2 shows on the left the development of the vertical displacement of two particular points for an initial value of $c_{v,0}$ = 0.7. Point 'A' is on top of the landfill in the symmetry axis, whereas point 'B' marks the top of the slope. The settlements develop in a similar way for the two points. During the loading of the first hour the vertical displacements are approximately 1.80 m and 1.50 m as it can be seen in the window in more detail. Then, the solid waste is compacted about 40 cm in the next hour. After 12 hours the total settlement is about 2.60 m and 2.10 m. Thus, a significant decrease in the compaction velocity appears within the first days. During the residual duration the displacements increase slowly and after two years a final value of 3.60 m is reached for point 'A' and

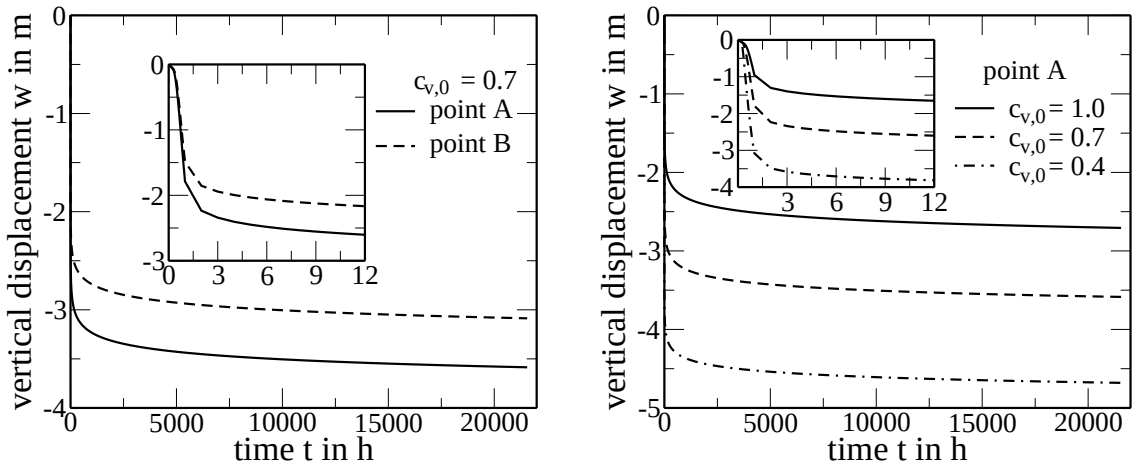

Figure 7.2: Development of settlements in time

3.10 m for point 'B'. Thus, a differential settlement of about 0.50 m occurs due to the loading conditions, which are quite different in the central part of the landfill and near the slope.

The time-settlement curves exhibit the same tendency for the two other initial densities. The more compact landfill with $c_{v,0} = 1.0$ compacts to a final value of 2.70 m only, whereas the poor compacted landfill with $c_{v,0} = 0.4$ looses 4.70 m of its initial height in the central zone. The curves are plotted in figure 7.2 on the right. The example points out that the model formulation is able to reproduce the first three stages of the municipal solid waste compressive curve correctly. The load induced settlements are about 10 to 20 % of the initial height depending on the initial density. Thus, a crucial point in the model formulation becomes apparent here. The possibility of densification as well as the initial state are characterised by the abstract model variable $a_{v,in}$. It is quite hard to relate this kinematic variable to the well-defined partial density. Especially, the definition of the initial state of compactness seems to be easier if the model is formulated using densities for analysing practical cases in future. Further, the simulation of the emplacement in layers over some years hat to be implemented in future as well as models for biodegradation of organic substances.

Due to the different loading conditions inside the landfill, it is obvious that the bottom layers have a much larger influence on the total settlement. The lowest layer of an initial height of 2.50 m contributes about 0.60 m to the settlement in the symmetry axis, whereas the top layer is moved down more or less without deforming. The spatial distribution of the deformation can be pointed out indirectly by observing the internal variable $a_{v,in}$ characterising the irreversible compaction. The development of this variable is shown for four different time points in figure 7.3. Thus, the areas at top and near the slope with low overburden pressure do not compact and remain in the initial state $a_{v,in} = -0.7$ more or less. In contrast, the zone in the central part goes into a considerably denser state. Thereby, the value $a_{v,in}$ decreases down to -1.35.

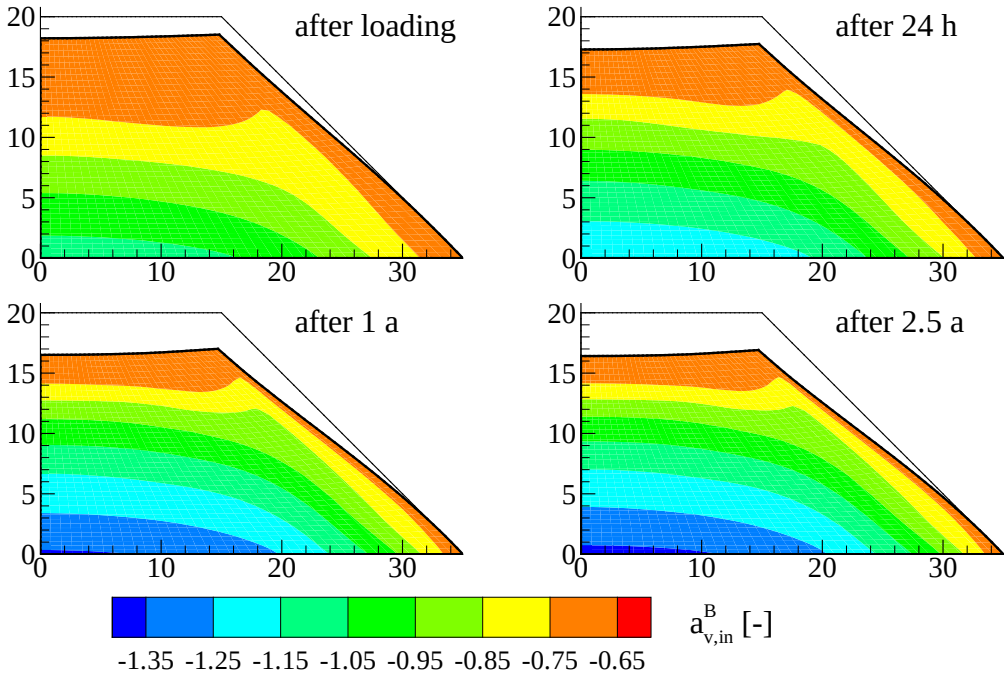

Figure 7.3: Deformed landfill with inelastic volume strain

The spatial distribution of CAUCHY stresses is shown in figure 7.4. The component T^B_{zz} alters only slightly in time. Thus, the bearing mechanism is not influenced by compaction and creep. Of course, the highest compressive stresses are in the central region on the bottom because the highest overburden load is situated there. The high stresses are responsible for the high deformation in this part of the landfill. Since the contour lines are almost horizontal in this central part, simple one-dimensional approaches work quite well for prognoses of settlements here if the environmental conditions are constant. Against it, the influence of the geometry is noticeable nearby the slope. A bowl-shaped settlement arises on top due to the different compressions and the differential settlement is about 0.50 m. Such high differences are levelled by the emplacement process under real conditions. Additional differential settlements occurring in-situ are often caused by spatial fluctuation of the composition of the dumped material, which can be incorporated into the model approach by setting different values for the model parameters and different initial conditions for each element.
Although large vertical displacements occur in time, the horizontal movements remain comparable small in this example. The point 'B' moves slightly in direction of the symmetry axis caused by the large volume reduction in the centre again. The high lateral strength of the fibrous fraction prevails a disruption of the landfill body. The component T^F_{xx} of CAUCHY stress tensor is plotted in figure 7.5. The highest stresses appear in the central region and increase in time. The changing is mainly generated by geometric effects. If the area of an arbitrarily chosen cross section is reduced due to the

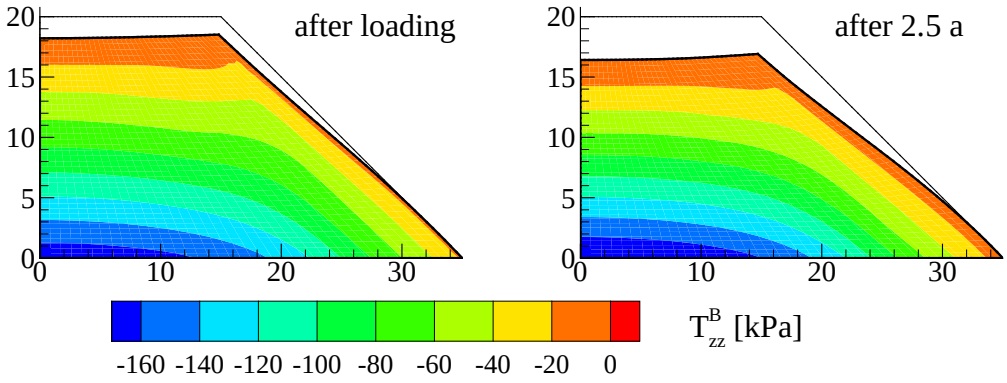

Figure 7.4: Deformed landfill with CAUCHY stresses of basic matrix

vertical compaction, the stresses have to increase in order to ensure force equilibrium. In contrast, higher values exist also near the slope after loading. But, these stresses are reduced by the movement of the slope in time. The inclination of the slope decreases, and therefore the forces required for holding back the loose zone near the surface to the landfill body are reduced, too.

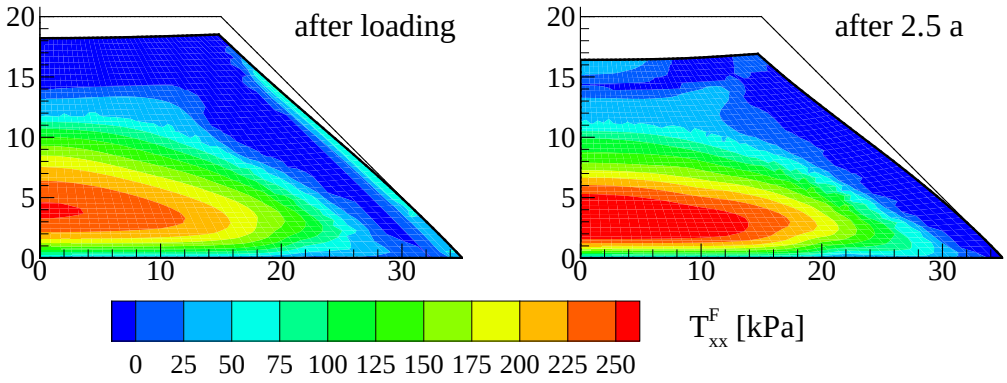

Figure 7.5: Deformed landfill with CAUCHY stresses of fibrous fraction

7.2 Numerical analysis of slope stability

Slope stability analysis is usually performed in geotechnics applying slip circle methods assuming a potential sliding surface and subdividing the volume in lamellae. The different algorithms, FELLENIUS, JANBU, BISHOP etc., distinguish in the additionally presupposed conditions in order to obtain a uniquely solvable equation system, see [1]. Kölsch enhances BISHOP's method in order to include the effects of fibrous reinforcement in municipal solid waste. In contrast, the application of numerical methods is usually limited to scientific investigation until now.

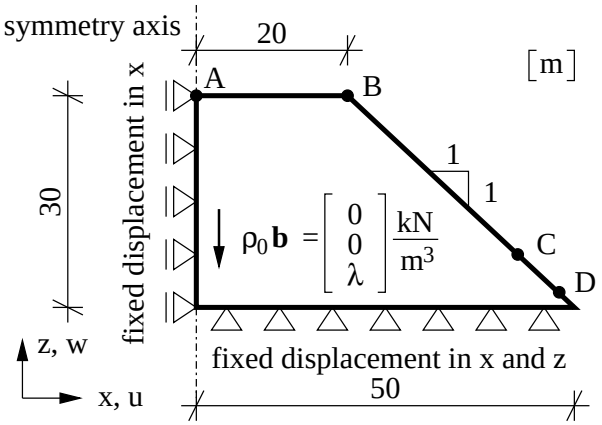

Figure 7.6: Sketch of landfill - slope stability analysis - horizontally fixed boundary

Katzenbach et al. [55] discuss possible strategies for the usage of numerical methods in stability analysis in geotechnical applications. In the following the developed constitutive model implemented into a finite element code for an analysis under plane-strain conditions is used in order to evaluate the performance of the model under typical in-situ conditions. Thereby, the landfill is concerned as 'dry' medium and the equation system (5.7) has to be solved during the computations only.
At first, the landfill illustrated in figure 7.6 is investigated in detail. The landfill has an initial height of 30 m and its slope has an inclination of 45°. Symmetry is exploited for the boundary on the left. Both vertical and horizontal displacements are fixed in the base. No additional surface tractions act on the top and on the slope. The model parameters are varied throughout the simulations. Thus, LAME's constants for the elastic region of material behaviour of the basic matrix and the model parameters of the fibrous fraction are taken from table 6.2. The time-dependent compaction is eliminated by setting parameter A of the creep model to zero. The parameter $c_{v,in}$ characterising the initial compaction is 1.0. Furthermore, different parameter set listed in table 7.1 describes the shear resistance.
The load vector is generated by uniformly distributed volume forces here. The computations are controlled by the arc-length method introducing the load factor λ. Thus, an

material	shear parameters	softening of fibres
all	$b_{\phi'} = b_{\psi} = b_{c'}$ = 1.0; $c_{\phi'} = c_{\psi} = c_{c'}$ = 3.17	
material 1	$a_{\phi'}$ = 40.0°; a_{ψ} = 20.0°; $a_{c'}$ = 20.0 kPa	without softening
material 1s	$a_{\phi'}$ = 40.0°; a_{ψ} = 20.0°; $a_{c'}$ = 20.0 kPa	with softening
material 2	$a_{\phi'}$ = 30.0°; a_{ψ} = 15.0°; $a_{c'}$ = 10.0 kPa	without softening
material 2s	$a_{\phi'}$ = 30.0°; a_{ψ} = 15.0°; $a_{c'}$ = 10.0 kPa	with softening
material 3	$a_{\phi'}$ = 45.0°; a_{ψ} = 20.0°; $a_{c'}$ = 10.0 kPa	without softening

Table 7.1: Parameter sets for slope stability analysis

additional equation has to be added to the equation system (5.7)

$$(\mathrm{d}\underline{\check{\mathbf{u}}}^s)^T \cdot \underline{\underline{\mathbf{M}}} \cdot \mathrm{d}\underline{\check{\mathbf{u}}}^s - \Delta s^2 \;=\; 0\,. \tag{7.1}$$

The equation (7.1) enforces that the vector norm of the incremental node displacements $\mathrm{d}\underline{\check{\mathbf{u}}}^s$ of an increment equals a predefined value Δs. The diagonal matrix $\underline{\underline{\mathbf{M}}}$ selects the displacement values. Usually all node displacements are considered uniformly. A more detailed description of the arc-length method can be found in the literature, e.g., [87], [92], [105].

Figure 7.7 compares the load-factor versus displacement curves for point D laying in the initial configuration 1.5 m above the bottom in the slope. The portion of fibrous material inside the landfilled waste is varied and the influence of the softening of the fibres is investigated. The basic matrix of the material 1 has a high friction angle of 35.4°and a high cohesion of 17.7 kPa. Thus, the landfill is already stable for the pure basic matrix up to a dead load of about 10 kN/m^3. The bearing capacity of the composite material under the given geometry and boundary conditions increases considerably if the reinforcement effect of the fibres is activated. The increase is disproportionately because small portions of 1 % or 2 % result in a relatively small growth of the load compared to higher contents of 5 % or 10 %. But, large deformations are required to mobilise the full strength of the material. As it is shown in figure 7.7 on the right an approach, which neglects the softening of the fibres, overestimates the bearing capacity considerably. For a fibrous content of 5 % the failure load including the softening is only 25 kN/m^3 compared to 40 kN/m^3 for the material without softening. Nevertheless, neglecting the softening of the fibres accelerates the analyses and reduces the computational time in parameter studies.

Figure 7.8 shows the development of the slope failure using the norm of the inelastic ALMANSI strains of the basic matrix $\left|\mathbf{A}^B_{in}\right|$, which is defined as

$$\left|\mathbf{A}^B_{in}\right| \;=\; \sqrt{\mathbf{A}^B_{in} : \mathbf{A}^B_{in}}\,. \tag{7.2}$$

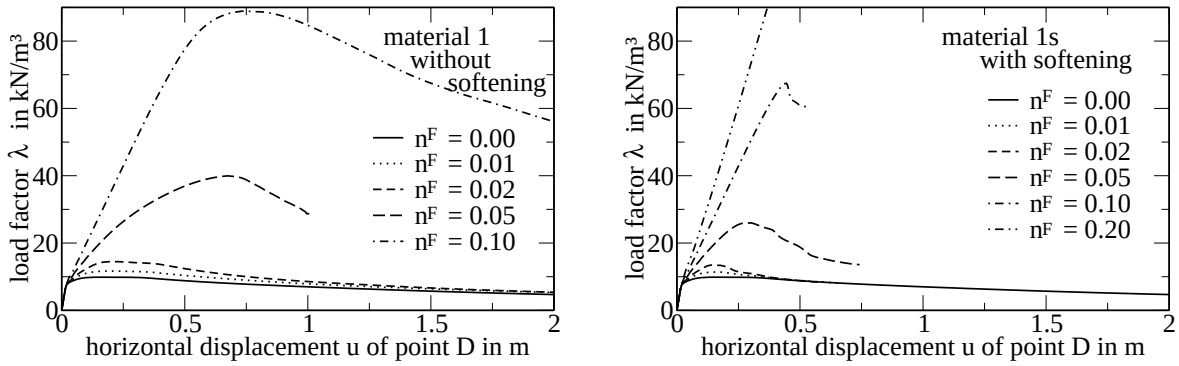

Figure 7.7: Load versus horizontal displacement of point D

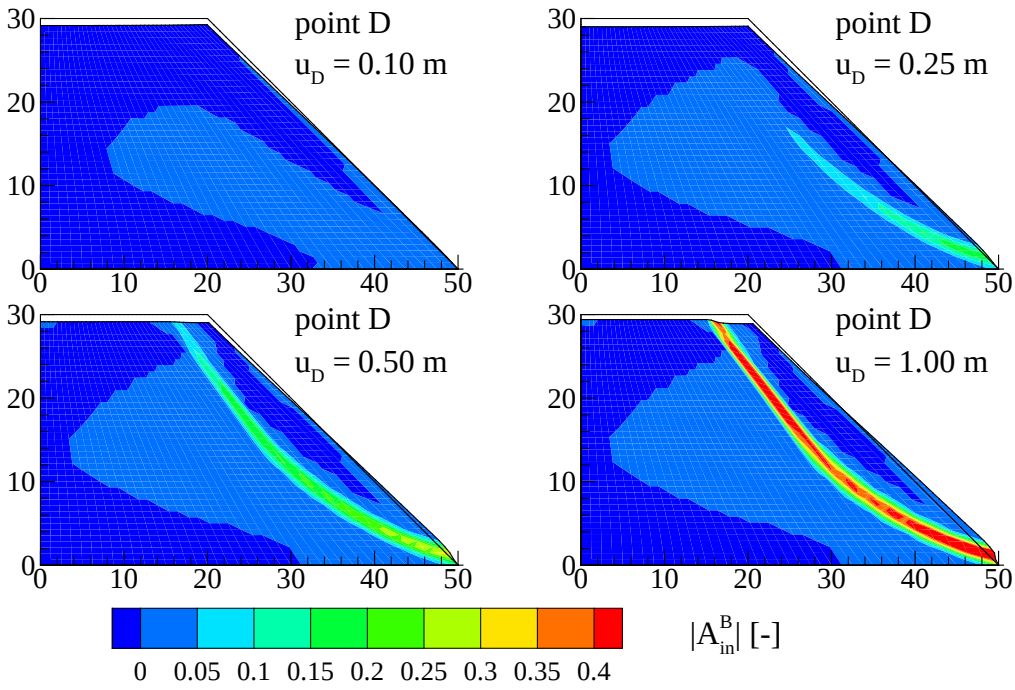

Figure 7.8: Norm of inelastic strains $|A^B_{in}|$ of basic matrix for material 1, n^F = 0.02

The norm characterises the shearing of the basic matrix. At first, the shear resistance of the granular basic matrix is exceeded nearby the toe of the slope. The waste tends to move outwards and the region, in which inelastic shearing occurs, propagates inside the landfill body. Thereby, the deformation commences to concentrate in a narrow band. Such a shear band is developing between two interpolation points of the displacement approximation. Due to the dilatant material behaviour the shear resistance of the basic matrix reduces slowly in the modelling approach and the applicable load decreases. Since the strength of the fibres depends on the loading state of the basic matrix, the stresses carried by fibres are reduced, too. The maximal load is exceeded before the shear band reaches the top of the landfill. In reality, the landfill collapses if the maximal load is exceeded. Then, inertia forces have to be added to the model formulation and the moving waste masses behave rather like a fluid than like a solid.

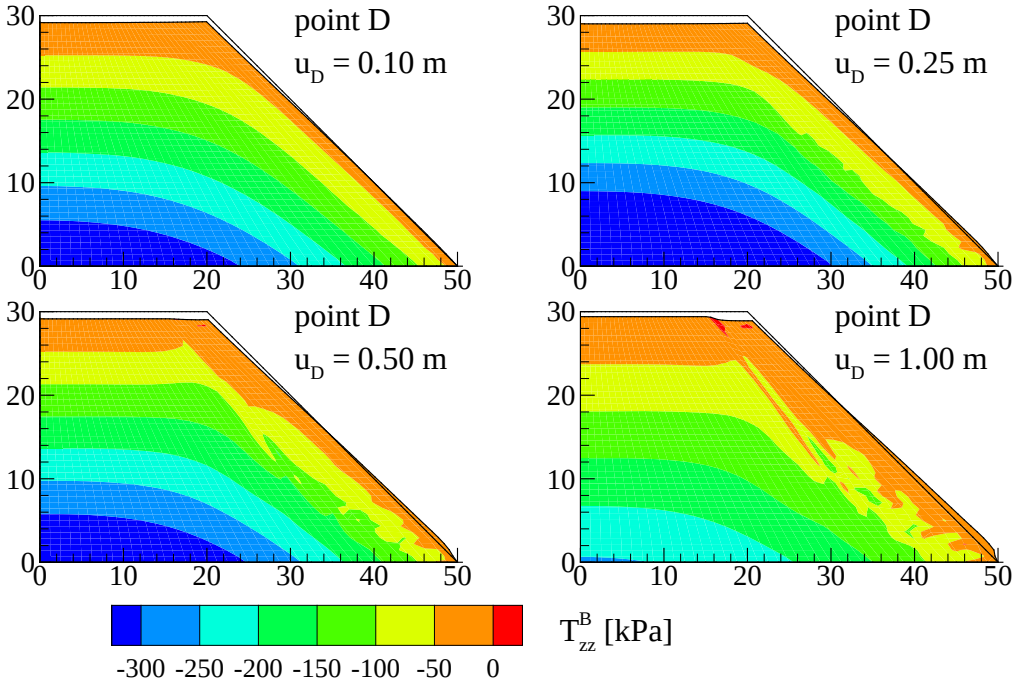

Figure 7.9: CAUCHY stress component T^B_{zz} of basic matrix for material 1, n^F = 0.02

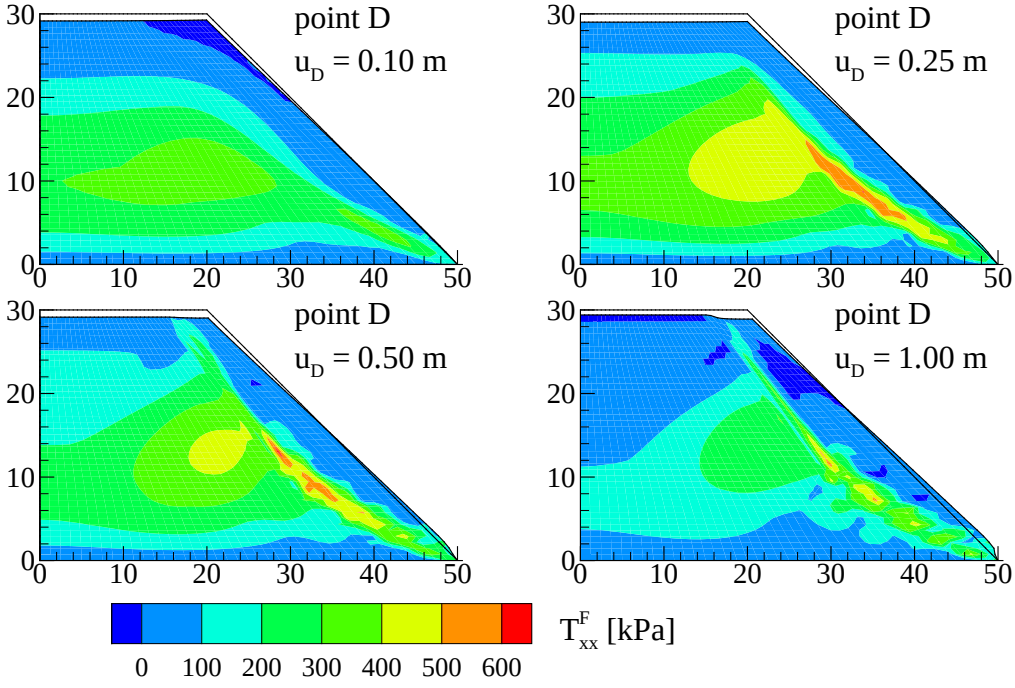

Figure 7.10: CAUCHY stress component T^F_{xx} of fibres for material 1, n^F = 0.02

The development of the vertical CAUCHY stress component T^B_{zz} is displayed in figure 7.9. At first, the spatial stress distribution exhibits the typical form of embankment structures. The highest stresses are in the central region because the vertical cover is larger there. After failure the parts not belonging to the moving waste block are unloaded in the simulation due to the arc-length control. The stress distribution does not change, but the stress level decreases. Further, oscillations of stresses occur in the zone of the shear band. A similar effect can be observed for the stresses of the fibres as displayed by the development of the horizontal CAUCHY stress component T^F_{xx} in figure 7.10. At an early stage higher stresses exist in the central part. Furthermore, the fibrous particles hold back the sliding block and the reinforcement effect is indicated by high stresses in the region of the developing shear band. The stresses increase if the deformation goes on. After exceeding the maximal load the fibres are elastically unloaded in the central part. Against it, inelastic processes continue in the shear band. Thereby, oscillations of the stresses occur as well.
Figure 7.11 compares the load-factor versus displacement curves for point C, which is situated 5.25 m above the base in the initial configuration, in dependency on different shear parameters for the basic matrix. Material 2 and 3 have a significant lower cohesion - half of the value of material 1. While the friction angle of material 3 is slightly higher than the friction angle of material 1, the value is reduced for material 2 considerably. Thus, for the landfilled waste only consisting of the basic matrix the failure load is significantly reduced by the modification of the model parameters. Especially, for material 2 the maximal load is only one third compared to material 1. The same behaviour is observable assuming a 10 % content of fibres. Thereby, the load is increased to a level of about 40 kN/m^3, but it is still lower than the bearing capacity of 90 kN/m^3 for material 1. In contrast, the failure load of material 3 is higher for the announced content of fibres. The break in the displacement curve is caused by a change of the governing failure mechanism. At first, a typical slip circle failure occurs as shown for all investigated cases in figure 7.12 using the norm $\left|A^B_{in}\right|$. Later, a zone near the toe is

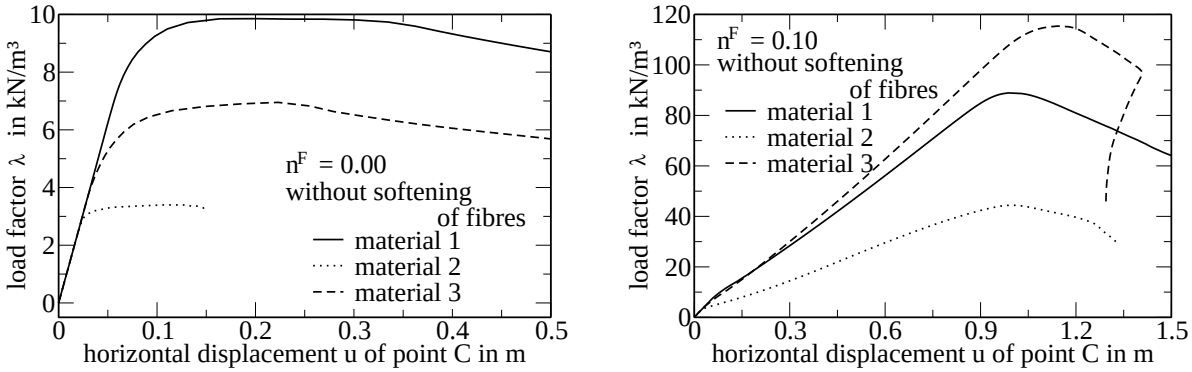

Figure 7.11: Load versus horizontal displacement of point C

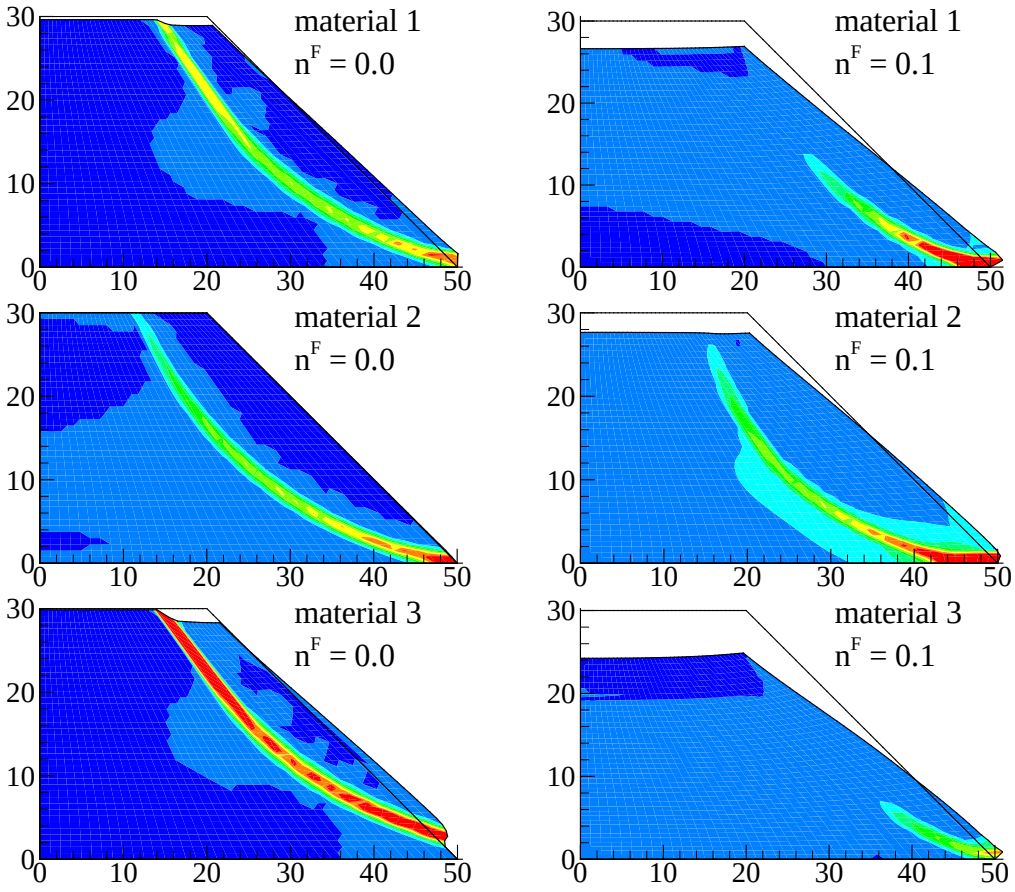

Figure 7.12: Failure modes for different shear parameter of the basic matrix

teared from the landfill body in the post-failure in addition. Point C is situated about this block for material 2 and does not move outwards after the tearing.
The spatial accuracy of the computations are checked by refinement of the finite element mesh. Thus, the number of nine-node displacement elements is increased from 20 x 20 taken for the analyses so far to 40 x 40 and 80 x 80. Figure 7.13 highlights the behaviour of the different meshes. In general, displacement based finite elements approximate the failure load from an upper bound. Thus, the failure load is overestimated slightly by the computations using the coarse mesh. Since the load-displacement curves are almost identically until a certain point, which is not far from the limit state, this point can be considered as lower bound for the critical load in the simulation. Considerable differences occur in the post-failure behaviour These differences are closely related to the constitutive model. It is a well-known fact that non-associated plastic flow as well as softening may cause spurious mesh-dependent results. Thereby, the type of the governing differential equation changes from elliptic to hyperbolic and an unique solution cannot be obtained anymore. A characteristic sign for this behaviour is the concentration of the inelastic strains generated by shearing and tearing between a row of neighbouring interpolation points of the displacement field as shown in figure 7.14.

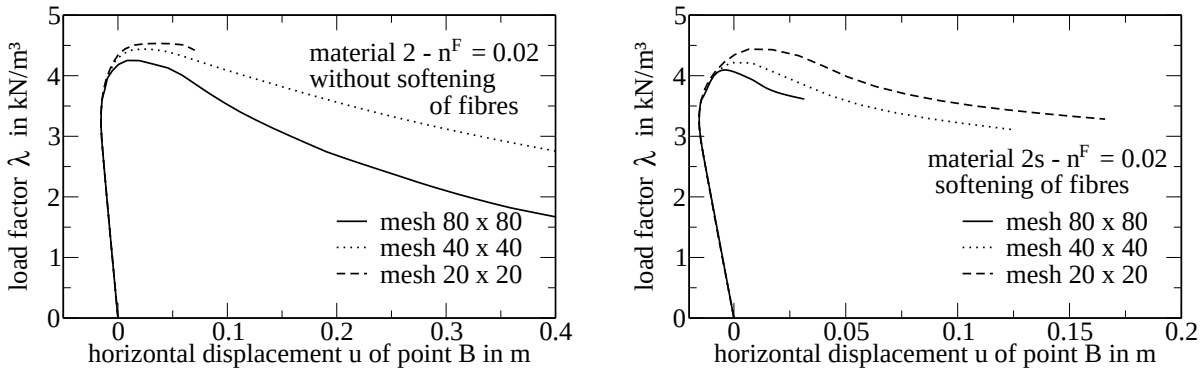

Figure 7.13: Load versus horizontal displacement of point B

The distance between two points is reduced by the mesh refinement. The occurring shear band tends to converge into a slip surface having no thickness and the dissipated work inside the shear band is going to zero in the limit. Therefore, it is obvious that the obtained results have no physical meaning anymore. Non-local constitutive models are applied in order to overcome the aforementioned problem. The development of such approaches is still object of actual research. For granular materials, nonpolar continuum formulations are already introduced successfully, e.g. by Volk [100] or Vardoulakis and Sulem [99]. Furthermore, softening or damaging of metals and concrete can be described by explicit and implicit gradient methods, e.g., Zümendorf [109], or integral methods, e.g., Bažant and Jirásek [8]. Maier [76] compares different approaches for hypoplastic models applied to granular materials. It is conjectured that the mesh dependency is also responsible for the stress oscillation.

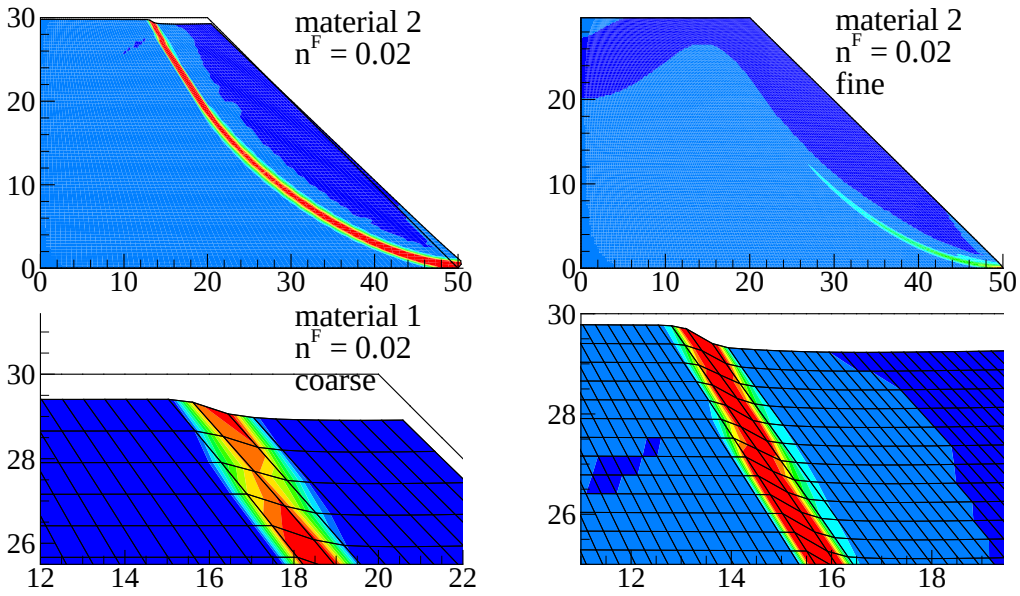

Figure 7.14: Mesh refinement

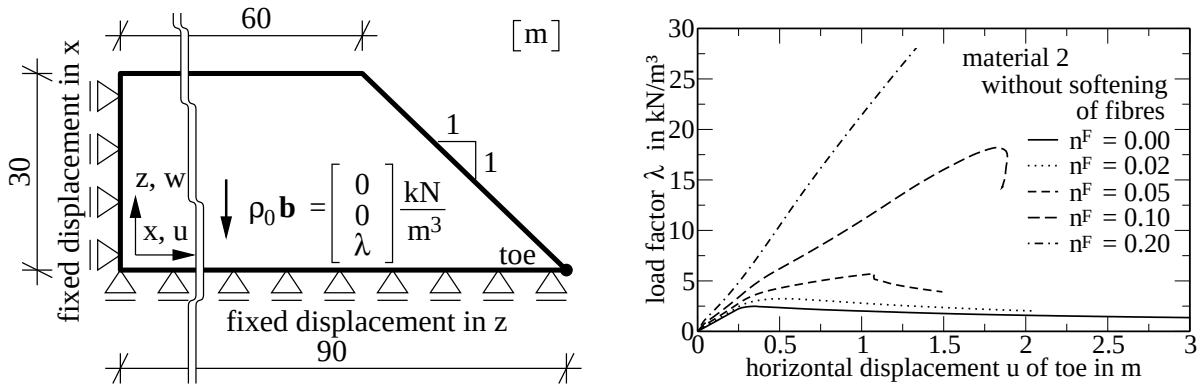

Figure 7.15: Sketch of landfill - slope stability analysis - only vertically fixed base

In general, an adaptive mesh-refinement procedure is useful in order to limit the computational effort. Since the whole domain is discretised finer in the performed computations, a lot of unnecessary elements and nodal unknowns arise in the discrete equations system describing the problem. Furthermore, the distortion of the finite elements can cause numerical trouble, which can be avoided by remeshing during the analysis, too.
A final investigation shows the influence of the boundary condition on the base. Thus, the horizontal width of the base is increased to 90 m. Symmetry conditions are assumed on the left boundary as illustrated in figure 7.15 because main focus lays on the behaviour of the slope here. The base can move free in horizontal direction, whereas the vertical displacement is fixed. The load-displacement curves of the toe are shown in figure 7.15 on the right. One detects that the failure load is much lower compared to the example with a horizontally fixed base. The maximal load predicted by the model is only 2.48 kN/m^3 for the basic matrix instead of 9.85 kN/m^3 if the base is fixed. The same behaviour is observable if a low content of fibrous material exists. For n^F = 0.02 the bearing load reduces from 14.48 kN/m^3 to 3.23 kN/m^3. Higher loads are carried only for portions of fibrous material larger than 10 %. But, the mobilisation of the full fibrous strength requires large horizontal movements. The computations are connected with numerical trouble and converge in some cases after reducing the global iteration tolerance only. The full three-dimensional plasticity model of the fibrous fraction consisting of three different yield surfaces under tension complicates the analysis. Thus, the global NEWTON-RAPHSON procedure fails if more than one GAUSSIAN point switches between an elastic and an elasto-plastic behaviour. It should be reconsidered if a viscous model for the fibres defined only in the plane can be adopted instead of the proposed anisotropic three-dimensional model.
Figure 7.16 demonstrates the activated failure mechanism for a fibrous content n^F = 0.02. A sliding joint develops 34 m away from the toe under an inclination of 58°. This value coincides well with Vardoulakis formula for the definition of the slid-

ing inclination, [55],

$$\theta = 45° + \frac{\phi' + \psi}{4} \approx 45° + \frac{35.4 + 17.7}{4} = 58.3° \,, \tag{7.3}$$

using the initial parameters of the basic matrix. The huge block situated right from the sliding joint moves outwards, whereas the residual part rests on its original place. The deformation concentrates again in a small zone defining rather a crack than a shear band. Thereby, the involved mass is much higher compared to the slope failure occurring for a fixed base. By ongoing of the movement a second sliding joint arises separating the zone near the toe from the remaining part. Thus, the middle block sinks down and pushes the toe zone away.

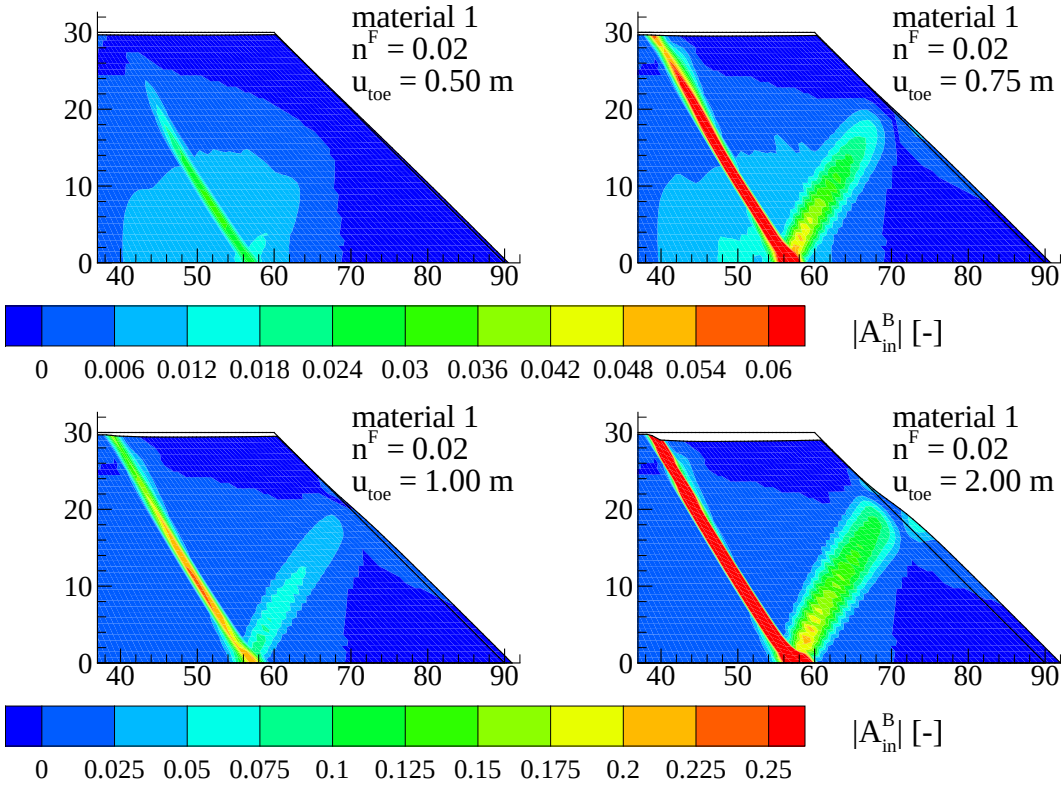

Figure 7.16: Norm of inelastic strains

The two investigated boundary conditions represent limit conditions. The upper limit is defined for a horizontally fixed base, whereas the lowest bearing capacity is obtained if the base can move free. The real boundary condition lays always between these two cases. The joints between the waste and the subsoil or the base sealing system are predefined weak points. The horizontal component of the reaction force, which exists in case of a fixed boundary, has to be transferred through this zone into the subsoil and produces additional horizontal deformations there. GDA-recommendation E-21 [25] provides remarks how this expansion forces have to be analysed for stability analysis of the base sealing system.

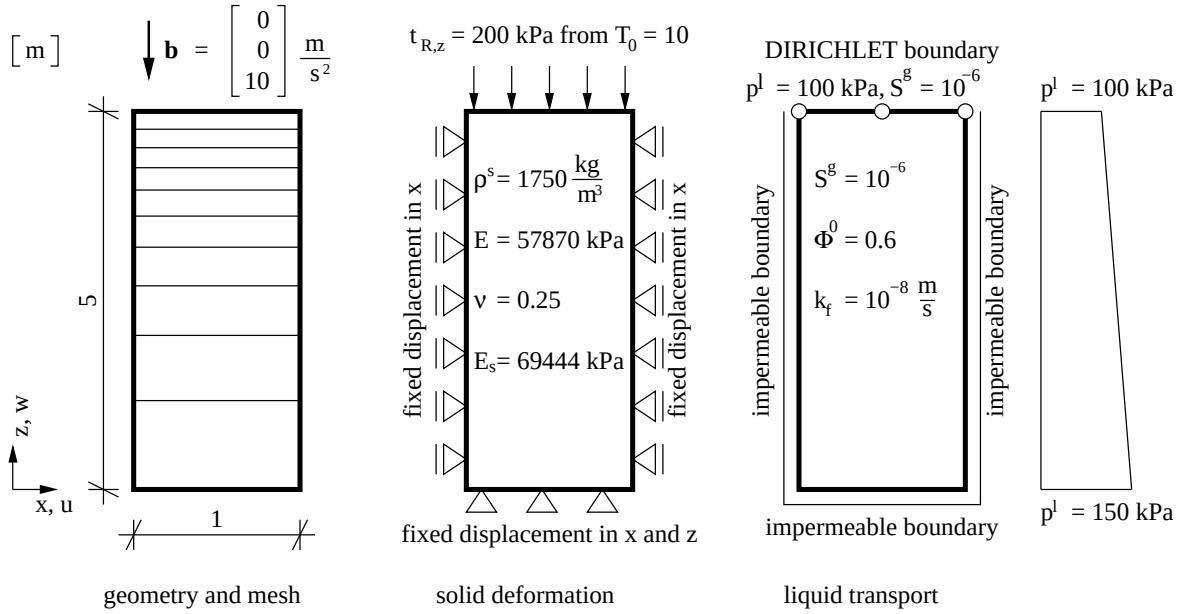

Figure 7.17: Initial and boundary conditions for one-dimensional consolidation

7.3 One-dimensional consolidation

One-dimensional consolidation is used to demonstrate major coupling effects between the deformation behaviour of the solid waste and the transport of pore liquids. Effects from creep as well as the fibrous fraction are neglected in this example to simplify the analysis. Thus, a 5 m high layer consisting on an elastic solid skeleton is loaded at time t_0 by the dead load and at time t_1 by an additional surface traction t_R. Since it exists an analytical solution for the special case of linear kinematics applying HOOKES's elasticity law, see [35], YOUNGS's modulus E and Poisson ratio ν, which are equivalent to LAME's constant λ and μ, are chosen in such way that only small deformations occur in a first computation. Therefore, differences coming from the nonlinear kinematics and the nonlinear elasticity are likewise small.
The geometry as well as initial and boundary conditions are displayed in figure 7.17 showing the used mesh created by 10 elements in addition. The horizontal displacements of the left and the right boundary are fixed. The two boundaries are of von NEUMANN type for the transport process assuming that no flow occurs in horizontal direction. The lower boundary is of DIRCHLET type for displacements u and w and of von NEUMANN type for the transport. Against it, no surface forces act on the upper boundary for the deformation analysis for the stage of the dead load, whereas a traction force is added later on. The liquid pressure as well as the gas saturation are prescribed on top of the layer allowing the outflow of liquid and gas over this boundary. The initial porosity Φ^0 is set to 0.6, the initial hydraulic conductivity to 10^{-8} m/s. The initial gas saturation S^G is set to a very low value of 10^{-6}. Thus, the gas phase has no influence on

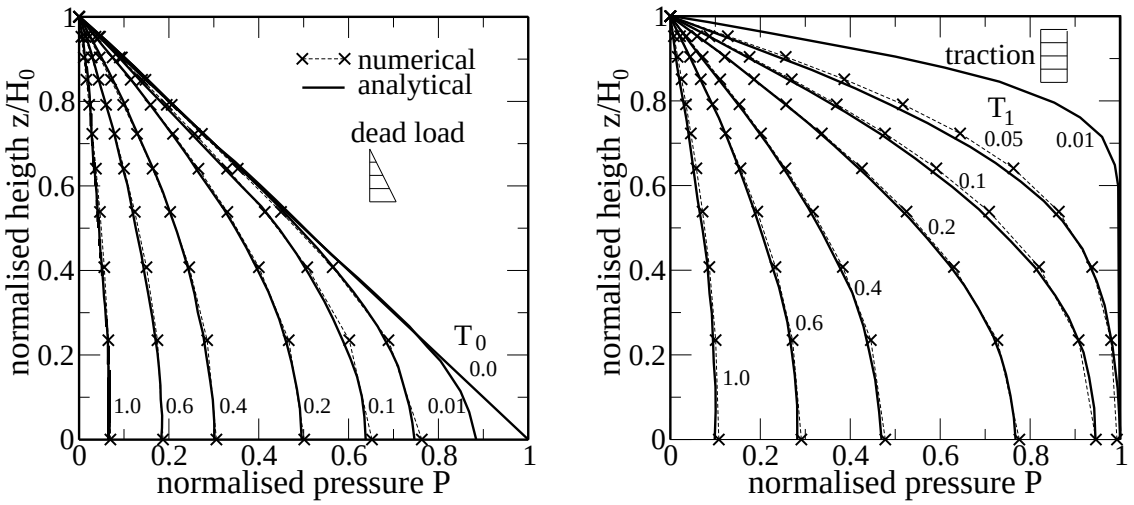

Figure 7.18: Development of liquid pressure in time

the liquid transport. The initial liquid pressure p^l is distributed linearly over the height z having atmospheric pressure on top. The physical liquid density $\tilde{\rho}$ is 1.0 Mg/m^3, the partial solid density ρ^s of the dry material is 1.75 Mg/m^3.
Introducing dimensionless time T_i and dimensionless liquid pressure P help to compare numerical and analytical solutions

$$T_i = \frac{k_{f,0}\, E_s}{\gamma^l\, H_0^2}\,(t - t_i)\,, \qquad P = \frac{p^l - p^l_{hyd}}{\Delta\, p}\,. \tag{7.4}$$

Thereby, the hydraulic conductivity $k_{f,0}$ in the initial state, the initial height H_0 and the unit weight of the pore liquid enter the first formula. The origin of time scale T_i coincides with the time point of loading. The oedometric modulus E_s is related to elastic parameters by

$$\frac{1}{E_s} = \frac{1}{E}\left(1 - \frac{2\nu^2}{1-\nu}\right)\,. \tag{7.5}$$

The dimensionless pressure measures the difference of the actual liquid pressure and the hydrostatic pressure with respect to the maximal pore excess pressure $\Delta\, p$ occurring in case of small deformations. For the dead load the initial excess pore pressure is Δp = 67.5 kPa on the bottom and it is linearly distributed over the height. Against it, in case of the addition of surface traction t_r the initial excess pore pressure is constant over the height with Δp = 200 kPa. The development of the liquid pressure is compared for the two load cases in figure 7.18 showing that analytical solution and numerical solution coincide very well. More or less no differences occur in the plotted isochrones of the normalised liquid pressure about the dimensionless height.
The total settlement on top due to the dead load is -2.43 mm and the settlement due to the surface traction -14.44 mm for the analytic solution. The numerical model delivers a

settlement of 2.428 mm for the dead load and an additional displacement of -14.35 mm for the surface load. The small differences originate from the nonlinear kinematics and the nonlinear elasticity law used in the numerical approach. The consolidation grade describes how the total settlements develop in time. It is defined by

$$U_c = \frac{w(t)}{w(t \to \infty)} \,. \tag{7.6}$$

Figure 7.19 compares on the left the consolidation grade obtained from the numerical solution with the analytical approach, which is plotted over the normalised time T. Thus, no essential differences exist and the developed model is able to reproduce the consolidation problem correctly. Figure 7.19 shows on the right the development of settlements if the stiffness decreases by the factor of 10 and 100. Then, the reduction of the pore space increases considerably resulting in higher settlements and a significant update of the geometry for the flow problem. The computations are carried out with and without changing of the permeability using equation (4.84) with n_Φ = 20. Obviously, the real time for decaying of consolidation increases, but an interesting fact arises in addition. The change of the geometry accelerates the process, which can be seen from the upper curves. But if the hydraulic conductivity is reduced drastically, the time for consolidation will be increased by a factor of 10 for the most compressible material under the given initial and boundary conditions. Since the hydraulic conductivity has a major contribution to the transport of the fluids, the correct description of the interaction of deformation and intrinsic permeability is the key factor in the analysis.

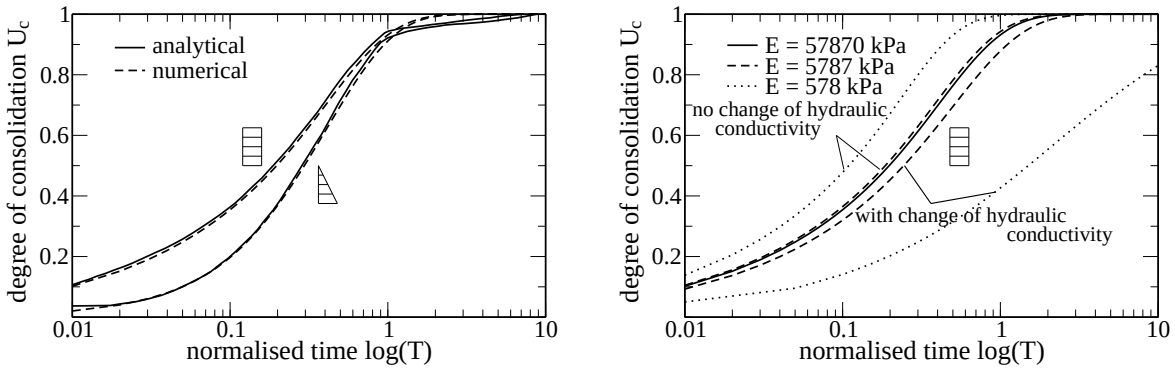

Figure 7.19: Development of settlements in time

7.4 Coupled transport and deformation analysis

Coupling effects between deformation and liquid transport are investigated under unsaturated situation in a two-dimensional example adopting the landfill analysed in section 7.1. In the initial, unloaded state a roof profile is assumed in order to avoid the creation

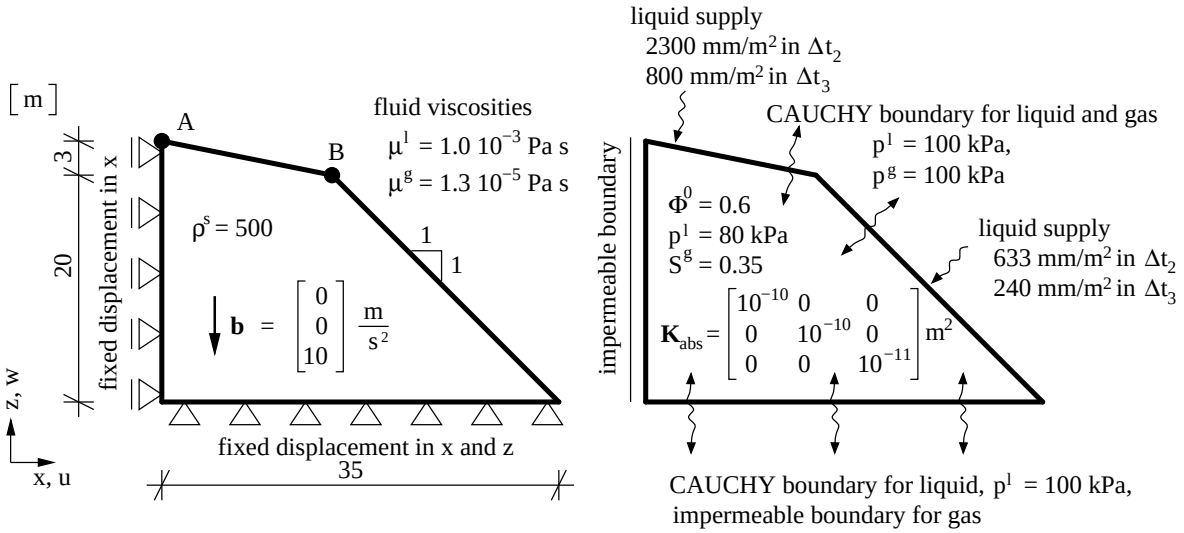

Figure 7.20: Geometry, initial and boundary conditions in coupled problem

of the bowl-shaped settlements on top. Therefore, the point 'A' laying in the symmetry axis is 3 m above point 'B' situated in the steep slope. The material parameters of the deformation model are taken from the tensile test summarised in table 6.2. The parameter $c_{v,0}$ characterising the initial compaction is set to 1.0. Figure 7.20 shows the geometrical dimensions on the left. The initial porosity Φ^0 of 0.6 is uniformly distributed in the whole domain. The likewise high intrinsic permeability of the solid skeleton is 10^{-10} m^2 in horizontal and 10^{-11} m^2 in vertical direction at the beginning. The parameter n_Φ governing the change of the intrinsic permeability during densification is set to 20. The dynamic viscosities are defined for a temperature of 293 K. It is assumed that the gas is a mixture of methane and carbon dioxide with equal gravimetric concentration. The initial gas saturation is 0.35 and the initial liquid pressure 80 kPa. The matric suction and the relative permeability are described by the BROOKS-COREY approach with parameters of table 6.4 related to a density of 0.54 Mg/m^3.

In the symmetry axis the displacements in x-direction are fixed, whereas the boundary at the bottom is unable to move in x- and z-direction. Since the content of fibrous particles is high, n^F = 0.1, it is expected that a stability problem does not occur. The boundary conditions for the transport problem are displayed in figure 7.20 on the right. The symmetry axis is a von NEUMANN boundary and no fluid mass is transferred in horizontal direction there. The boundary to the subsoil is impermeable for the gas phase, whereas liquid can flow out. The outflow is modelled by a CAUCHY boundary condition assuming a low intrinsic permeability of 10^{-16} m^2 in equation (3.61). Gas can flow in and out across the slope and the top, which is modelled by a CAUCHY boundary, too. Defining such a boundary condition ensures that the leachate can leave the landfill on the slope side, too.

Four different stages are investigated in this test example. In the first stage Δt_1 = 38 h

the landfill is loaded by the gravity force and commences to deform time-dependent due to the creep of the solid skeleton. Then, water infiltrates on top and on the slope in the second stage with Δt_2 = 3432 h. This supply is increased for a period of 8 days in the third stage Δt_3 and finally the ongoing of mechanical deformation and fluid transport is analysed in the last stage Δt_4 without adding any liquid. The amount of the precipitation is an averaged value for tropical areas in the second stage and the very high infiltration of the third stage coincides with two heavy monsoon rains occurring within few days.

Figure 7.21 shows the development of the liquid saturation in the first two stages. After two hours the full gravity force is applied. Changes in the liquid saturation are generated mainly by the spontaneously vertical deformations of the landfilled solid waste. Thereby, the pore space is reduced and the liquid saturation increases resulting in a higher mobility of the liquid, too. The creep processes lead to an ongoing of the deformation connected with a further reduction of voids and higher saturations in the central part as shown at time t = 2774 h. In addition, the phreatic surface raises to a height of about 2.5 m in the symmetry axis.

If the precipitation of the third stage commences, slight altering of the saturation is recognisable at the top at time t = 3491 h displayed in figure 7.22. The infiltrated liquid mass moves downward and reaches denser zones later on at time t = 3531 h and t = 3691 h. Thus, the saturation increases in the deeper layers. Finally, the water reaches the saturated zones in the bottom area. Then, it is stored there and leads to a phreatic raise to a height of about 5 m in the symmetry axis at time t = 3731 h. Since the mobile water leaves the region near the top and near the slope downwards, the saturation commences to decrease again in the fourth stage, in which the supply of liquid is stopped in the scenario.

Figure 7.23 compares the changes of porosity after applying the load with the situation after the heavy precipitation. Of course, the altering correlates well with the stress dis-

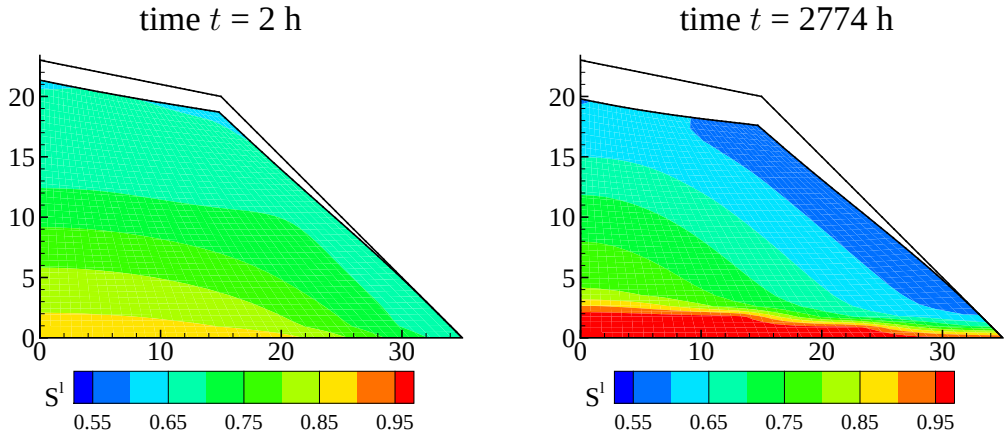

Figure 7.21: Development of liquid saturation S^l in stages Δt_1 and Δt_2

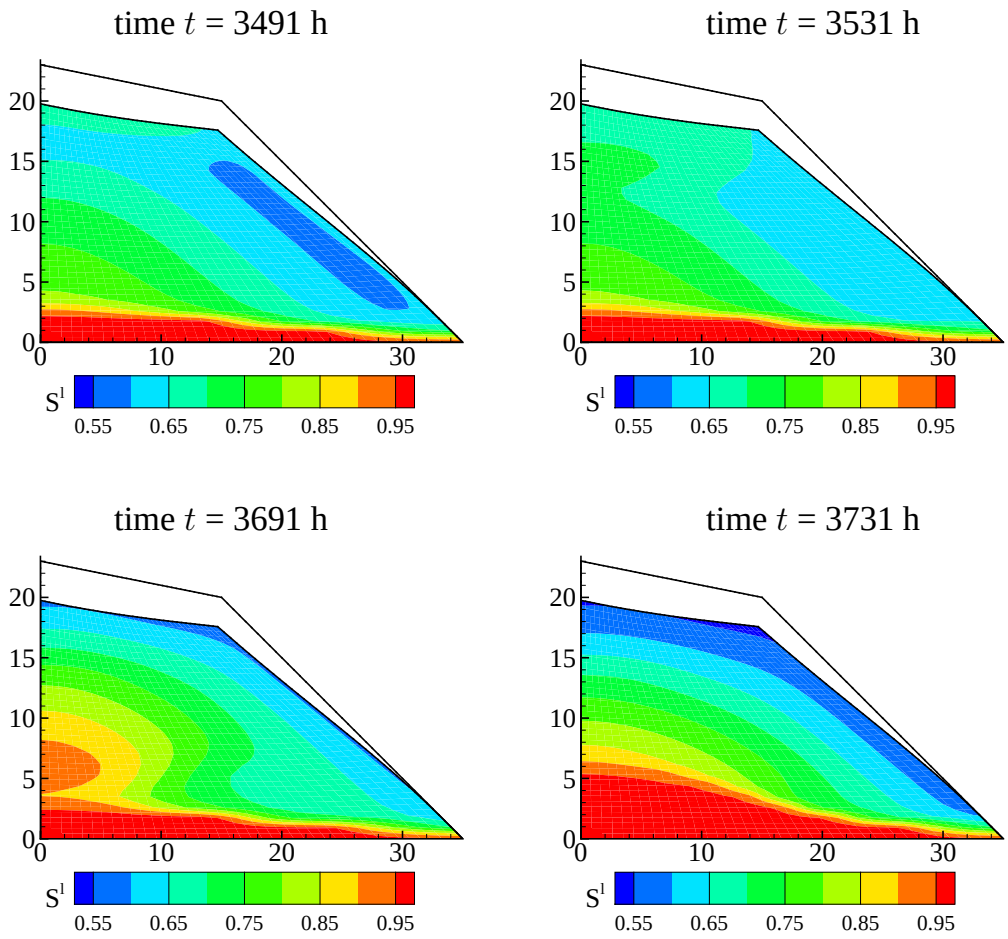

Figure 7.22: Development of liquid saturation S^l in stages Δt_3 and Δt_4

tribution and the largest reductions occur in the central part. The reduction in the zones having low overburden stresses are comparable small.

The reduction of the voids causes a significant decrease of the intrinsic permeability. The changes are compared in figure 7.24 defining the ratio $\Delta K_{abs} = \left(\Phi/\Phi^0\right)^{n_\Phi}$. Since there are no changes in the porosity in the upper layers and near the slope, there is no reduction of the intrinsic permeability. In contrast, the intrinsic permeability is reduced in the central part by a factor of ten after loading at time t = 2 h and later by a factor of 100. The development of the dry solid density ρ^s and the wet density $\rho^s + \rho^l$ follows the development of pore space and the filling state of the voids with liquid as illustrated in figure 7.25 at time time t = 3731 h. Profiles in the symmetry axis show a characteristic increase with depth.

The example shows how transport and deformation interact in general. It is well-known that moisture content influences the biodegradation processes inside landfills. If organic substances degrade in time, additional pore space is creates which partially collapses. Thus, additional deformations occur that have to be implemented into the approach straightforward in future.

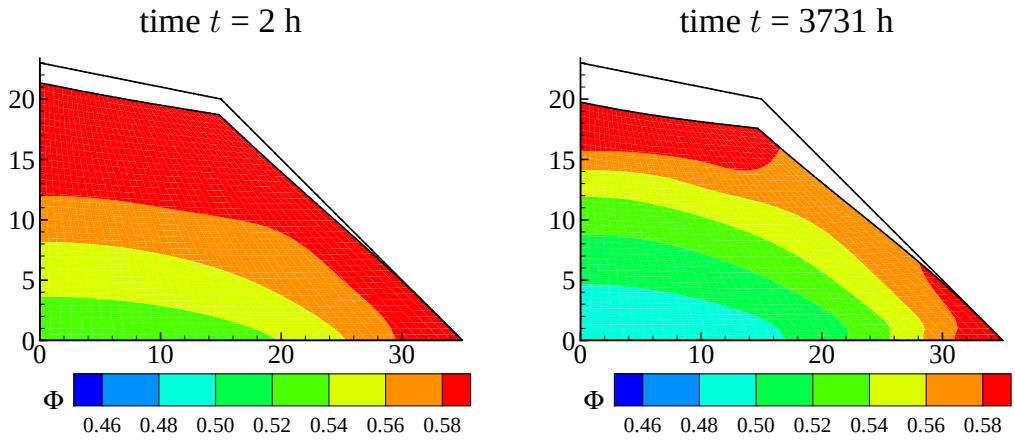

Figure 7.23: Altering of porosity Φ

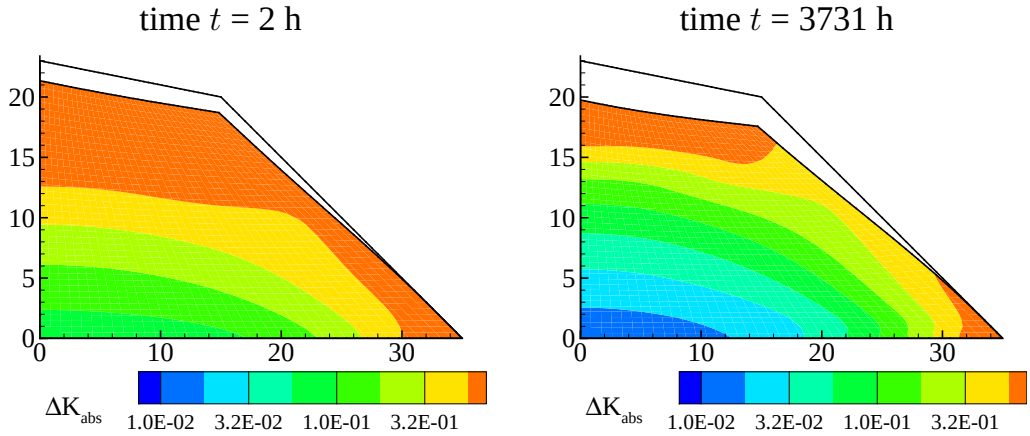

Figure 7.24: Altering of intrinsic permeability $\Delta \mathbf{K}_{abs}$

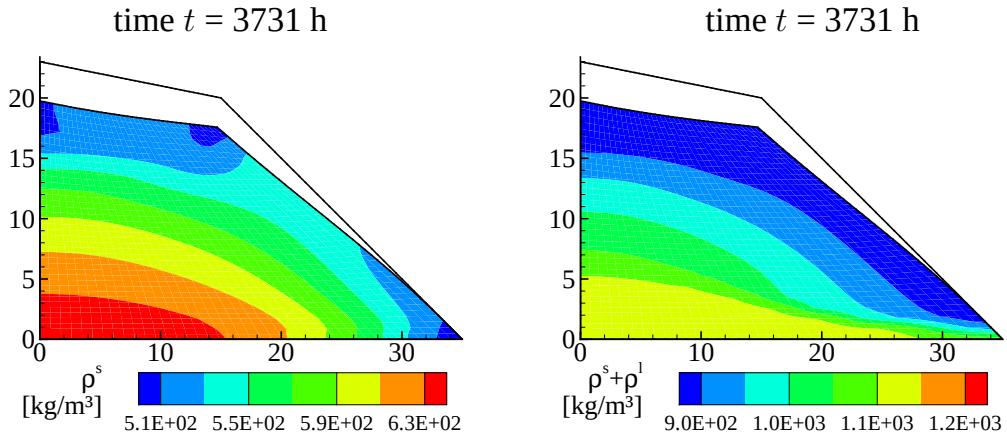

Figure 7.25: Dry and wet density of municipal solid waste

8 Summary and Outlook

Physical and biochemical processes taking place in landfills are quite complex. The landfilled waste consists of a solid skeleton exhibiting a system of large interparticle pores and crevices. But, larger single solid particles may own a micropore system, too. Municipal solid waste is very inhomogeneous and has anisotropic properties. Larger fibrous constituents influence the strength as well as the hydraulic behaviour. The pores are filled with leachate and gas. Microorganisms decompose organic matter into methane and carbon dioxide. Thus, the prediction of the long-term behaviour of landfills is quite difficult. Simple engineering approaches exist to predict the future development, but they do not take into account the underlying physical and biochemical processes. If boundary and environmental conditions change considerably, such simple models may fail completely. Therefore, more detailed models are required to understand the processes and their interactions better.

In this contribution a sophisticated model to couple the deformation behaviour of the solid waste with the fluid transport is developed using the *Theory of Porous Media* as adequate theoretical framework for the description of the multifield problem. The basic mechanical principles are presented, from which the governing model equations are derived. Appropriate initial and boundary conditions complete the mathematical formulation and enable the unique solution of the underlying partial differential equation system. Since municipal solid waste undergoes large irreversible deformations, the applied kinematics are nonlinear. The fact that the reversible part of the deformation is small simplifies the constitutive modelling of the solid waste. Experimental observations prove that the fibrous constituents increase the strength of the waste significantly. Thus, the solid waste is subdivided into two fractions in the modelling approach. The basic matrix includes particles having more granular properties, whereas fibres and sheets form the fibrous fraction. Such an approach allows the establishment of independent constitutive relations for the two solid fractions.

The shear strength of the basic matrix is formulated using a failure hypothesis similar to the MOHR-COULOMB criterion. Since the shear resistance increases if the solid waste is compacted, the shear parameters, angle of internal friction and cohesion, are no constants. Time-dependent deformations induced by gravity are captured by an anisotropic creep model. The creep rate depends on the stress level as well as on the state of compaction. The emplacement of the waste in layers as well as the compaction of the

material result in an orientation of the fibres in a horizontal plane. Transversal-isotropic elasticity models such a behaviour. Two failure mechanisms exist for the fibres. At low overburden stresses the fibres are pulled out of the surrounding basic matrix, whereas at higher stress levels the anchorage is much stronger and the fibres tear. A principle stress criterion with anisotropic hardening and softening is able to reproduce the behaviour of the fibres very well. Thereby, the tensile strength depends on the stresses of the basic matrix.
The transport processes are described by DARCY's law for unsaturated flow. Both BROOKS-COREY and van GENUCHTEN formulation are adopted to describe the matric suction and the relative permeabilities. The intrinsic permeability of the porous solid skeleton depends on its density. Thus, the reduction of the intrinsic permeability due to compaction is formulated in dependency on reduction of porosity.
The partial differential equations of the balance of the linear momentum of the mixture and the mass balances of leachate and landfill gas combined with initial and boundary conditions represent the initial-boundary value problem that describes the essential mechanical processes inside a landfill. Numerical methods are applied in order to solve the problem. The balance of linear momentum is equivalently formulated by the *Principle of Virtual Work* approximating the displacement field using the displacement based finite element-method. The box-method, a special type of the finite volume element method, transforms the two mass balances of the fluids into discrete equations. Integration in time is performed by an Euler-backward scheme. The integration of the constitutive equations of the solid fractions succeeds applying a predictor-corrector algorithm. The coupled problem is solved simultaneously.
Since many nonlinear dependencies are included into the sophisticated constitutive model, the number of parameters is likewise large. Thus, advanced genetic algorithms are applied in order to identify the model parameters on lateral confined compressive tests, uniaxial and triaxial compressive tests and tensile tests. Due to the particle size and the difficulties in carrying out such tests, the experimental data base is limited. Moreover, not all model parameters can be fitted on the same material. Nevertheless, the model is transferred to examples with field scale in structural analyses. Thus, the influence of the fibrous constituents on the bearing capacity is investigated in slope stability analyses. Landfills with a high content of fibres are stable, even though the slope is very steep. In contrast, the bearing capacity is reduced if the waste includes only a small portion of fibrous particles. The importance of the boundary conditions is highlighted by considering limit cases. Thus, if the friction between the waste and the subsoil is very low, the resistance against sliding mechanisms is much lower compared to the resistance against slip circle failure by high friction. The importance of the interactions between deformation and fluid transport is pointed out in one-dimensional consolidation. Thus, the compaction of the material causes a significant reduction of the intrinsic permeability of the solid skeleton, which is analysed in more detail for a

scenario investigation.
Modelling of strength softening changes the type of the underlying partial differential equation system. The problem becomes ill-posed if the deformations localise into a small shear band requiring additional techniques to avoid unphysical solutions. The incorporation of convenient nonlocal model formulations has to be checked in future.
A major part of the settlements is created by the biodegradation of organic matter into landfill gas and water, which runs out of the landfill. The question how much of the particle volume is added to the pore space and how much it contributes to the settlements is still unanswered. Since it is expected that the degradation of organic substances does not reduce the shear strength of the basic matrix of the solid waste considerably, the decomposition of plastics, textiles, papers and cardboards reduce the tensile strength of the composite material significantly. Whether acids appearing as intermediate products of the biodegradation attack the fibrous constituents is unknown as well as how the temperature raise due to the exothermic character of the biochemical processes influences the properties of the solid waste. Further, the ongoing of mineralisation alters the hydraulic parameter, in addition.
Modelling of the complex processes and their interactions occurring in landfills helps to better understand the major phenomena. Numerical analyses enable the investigation of extremal situations. Thus, this contribution provides the basis for the development of a fully coupled landfill model for deformation, transport and biochemical reactions in future.

Bibliography

[1] L. Abramson: *Slope stability and stabilization methods*. Wiley, New York, NY, 2002.

[2] H. Ahrens & D. Dinkler: *Finite-Element-Methoden*. Bericht Nr. 88-50, Institut für Statik, TU Braunschweig, 2005.

[3] H. Ahrens, H. Duddeck, U. Kowalsky, H. Pensky & T. Streilein: *Development and Improvement of Unified Models and Applications to Structural Analysis*. In E. Steck, R. Ritter, U. Peil & A. Ziegenbein, editors, Plasticity of Metals: Experiments, Models, Computation - Final report Collaborative research centre 319 ”Stoffgesetze für das inelastische Verhalten metallischer Werkstoffe - Entwicklung und technische Anwendung”, 1985-1996, chapter 9, pages 174–217. Wiley-VCH, Weinheim, 2001.

[4] H. Altenbach, J. Altenbach & R. Rikards: *Einführung in die Mechanik der Laminat- und Sandwichtragwerke: Modellierung und Berechnung von Balken und Platten aus Verbundwerkstoffen*. Deutscher Verlag für Grundstoffindustrie, Stuttgart, 1996. reprint.

[5] N. Apel: *Approaches to the description of anisotropic material behaviour at finite elastic and plastic deformations - theory and numerics*. PhD thesis, Institut für Mechanik, Universität Stuttgart, Bericht Nr. I-12, 2004.

[6] P. Bastian: *Numerical computation of multiphase flows in porous media*. Habilitation, Technical Faculty, Christian-Albrechts-Universität Kiel, 1999.

[7] K.-J. Bathe: *Finite-Elemente-Methoden*. Springer, Berlin, 2nd edition, 2002.

[8] Z. P. Bažant & M. Jirásek: *Nonlocal integral formulations of plasticity and damage: survey of progress*. International Journal of Engineering Mechanics, 128(11), 1119–1149, 2002.

[9] J. Bear: *Dynamics of fluids in porous media*. Dover publications, inc., 1988. reprint.

[10] R. Beaven: *The hydrogeological and geotechnical properties of household waste in relation to sustainable landfilling*. PhD thesis, Department of Civil Engineering, Queen Mary and Westfield College, 2000.

[11] J. Bluhm: *A consistent model for saturated and empty porous media*. Habilitationsschrift, Forschungsberichte FB Bauwesen, Universität-GH Essen, Heft 74, 1997.

[12] J. Bluhm: *Modelling of saturated thermo-elastic porous solids with different phase temperatures*. In W. Ehlers & J. Bluhm, editors, Porous media - Theory, Experiments and Numerical Applications, pages 87–118. Springer, Berlin, 2002.

[13] J. Bluhm & R. de Boer: *Effective stresses - a clarification*. Archive of Applied Mechanics, 66, 479–492, 1996.

[14] J. Bonet & R. Wood: *Nonlinear continuum mechanics for finite element analysis*. Cambridge University Press, 1997.

[15] R. M. Bowen: *Continuum physics*, volume 3, chapter Theory of mixtures, pages 1–127. Academic Press New York, 1976.

[16] J. Cowland, K. Tang & J. Gabey: *Density and strength properties of Hong Kong refuses*. In Proc. Sardinia 93, Fourth International Landfill Symposium S. Margherita di Pula, Cagliari, Italy, volume 2, pages 1433–1446. CISA, Environmental Sanitary Engineering Centre, 1993.

[17] J. d'Ans & E. Lax: *Taschenbuch für Chemiker und Physiker, Band 1, Physikalisch-chemische Daten*. Springer, Berlin, 4th edition, 1992.

[18] R. Davis & A. Selvadurai: *Plasticity and geomechanics*. Cambridge University Press, 2002.

[19] R. de Boer: *Vektor- und Tensorrechnung für Ingenieure*. Springer-Verlag Berlin, 1982.

[20] R. de Boer & J. Bluhm: *Phase transitions in gas- and liquid-saturated porous solids*. Transport in Porous Media, 34, 249–267, 1999.

[21] R. de Boer & A. Didwania: *Two-phase flow and the capillarity phenomenon in porous solids - a continuum thermomechanical approach*. Transport in Porous Media, 56, 137–170, 2004.

[22] R. de Boer & W. Ehlers: *Theorie der Mehrkomponentenkontinua mit Anwendung auf bodenmechanische Probleme*. Forschungsbericht aus dem Fachbereich Bauwesen der Universität-GH-Essen, Heft 40, 1986.

[23] O. del Greco & C. Oggeri: *Geotechnical parameters of sanitary waste*. In Proc. Sardinia 93, Fourth International Landfill Symposium S. Margherita di Pula, Cagliari, Italy, volume 2, pages 1421–1431. CISA, Environmental Sanitary Engineering Centre, 1993.

[24] C. Desai & H. Siriwardane: *Constitutive laws for engineering materials with emphasis on geologic materials*. Prentice-Hall. Englewood Cliffs, NJ, 1984.

[25] DGGT: *GDA-Empfehlungen Geotechnik der Deponien und Altlasten*. Ernst & Sohn, Berlin, 1997.

[26] S. Diebels: *Mikropolare Zweiphasenmodelle: Formulierung auf der Basis der Theorie Poröser Medien*. Habilitationsschrift, Institut für Mechanik, Universität Stuttgart, Bericht Nr. II-4.

[27] N. Dixon & D. Jones: *Engineering properties of municipal solid waste*. Geotextiles and Geomembranes, 23, 205–233, 2005.

[28] D. Drucker & W. Prager: *Soil mechanics and plastic analysis or limit design*. Quarterly of Applied Mathematics, 10(2), 157–165, 1952.

[29] J. Ebers-Ernst: *Modellierung des inelastischen Verformungsverhaltens von Siedlungsabfalldeponien*. PhD thesis, Bericht Nr. 2001-91, Institut für Statik, TU Braunschweig, 2001.

[30] W. Ehlers: *A single-yield surface function for geomaterials*. Archieve of applied mechanics, 65, 246–259, 1995.

[31] W. Ehlers: *Foundation of multiphasic and porous materials*. In W. Ehlers & J. Bluhm, editors, Porous media - Theory, Experiments and Numerical Applications, pages 3–86. Springer, Berlin, 2002.

[32] G. Eipper: *Theorie und Numerik finiter elastischer Deformationen in fluidgesättigten porösen Medien*. PhD thesis, Institut für Mechanik, Universität Stuttgart, Bericht Nr. II-1, 1998.

[33] J. Fassett, G. Leonardo & P. Repetto: *Geotechnical properties of municipal solid waste and their use in landfill design.* In Waste Tech '94, Landfill Technology Technical Proceedings, Charleston (USA).

[34] S. Finsterle: *Inverse Modellierung zur Bestimmung hydrogeologischer Parameter eines Zweiphasensystems*. PhD thesis, ETH, Zürich, DISS. ETHZ Nr. 9985, 1992.

[35] W. Förster: *Bodenmechanik*. B.G. Teubner, Stuttgart, 1998.

[36] E. Gartung & H. K. Neff: *Empfehlungen des Arbeitskreises "Geotechnik der Deponiebauwerke" der DGGT* . Die Bautechnik, 75(9), 610–629, 1998.

[37] E. Gartung & H. K. Neff: *Empfehlungen des Arbeitskreises "Geotechnik der Deponiebauwerke" der DGGT* . Die Bautechnik, 77(9), 615–640, 2000.

[38] N. Gawande, D. Reinhart & A. Cortázar: *Landfill msw hydraulic conductivity estimation using in situ moisture sensors*. In Proc. Sardinia 05, Tenth International Waste Management and Landfill Symposium S. Margherita di Pula, Cagliari, Italy, pages 177–178. CISA, Environmental Sanitary Engineering Centre, 2005.

[39] K.-H. Gertloff: *Setzung und Dichte im Inneren einer Hausmülldeponie*. Müll und Abfall, 3, 178–195, 1996.

[40] J. Gourc, F. Olivier, S. Thomas, L. Chatelet, P. Denecheau & M. Munoz: *Monitoring of waste settlements on five landfills: Comparison of the efficiency of different devices*. In Proc. Sardinia 01, Eighth International Waste Management and Landfill Symposium S. Margherita di Pula, Cagliari, Italy, volume III, pages 515–525. CISA, Environmental Sanitary Engineering Centre, 2001.

[41] R. Greve: *Kontinuumsmechanik - Ein Grundkurs*. Springer-Verlag Berlin, 2003.

[42] M. Grisolia & Q. Napoleoni: *Geotechnical characterization of municipal solid waste: Choice of design*. In M. Kamon, editor, Environmental Geotechnics, pages 641–646. Balkema, Rotterdam, 1996.

[43] M. Grisolia, Q. Napoleoni, P. Sirini & G. Tancredi: *Geotechnical behavior of sanitary landfill based on laboratory and in situ tests*. The journal of resource management and technology, 20(4), 197–203, 1991.

[44] J. Hanel: *Modell zur Analyse von gekoppelten Transport- und Stoffabbauprozessen in Deponien*. PhD thesis, Institut für Statik der TU Braunschweig, 2001.

[45] S. Hartmann: *Lösung von Randwertaufgaben der Elastoplastizität - Ein Finite-Elemente-Konzept für nichtlineare kinematische Verfestigung bei kleinen und finiten Verzerrungen*. PhD thesis, Bericht 1/1993, Institut für Mechanik, Universität Gesamthochschule Kassel, 1993.

[46] M. Hassanizadeh & W. Gray: *General conservation equations for multi-phase systems: 1. averaging procedure*. Advances in Water Resources, 131–144, 1979.

[47] M. Hassanizadeh & W. Gray: *General conservation equations for multi-phase systems: 2. mass, momenta, energy, and entropy equations*. Advances in Water Resources, 191–203, 1979.

[48] M. Hassanizadeh & W. Gray: *General conservation equations for multi-phase systems: 3. constitutive theory for porous media flow*. Advances in Water Resources, 25–40, 1980.

[49] P. Haupt: *Continuum mechanics and theory of materials*. Springer-Verlag Berlin, 2nd edition, 2002.

[50] P. Haupt & T. Kersten: *On the modelling of anisotropic material behaviour in viscoplasticity*. International Journal of Plasticity, 19, 1885–1915, 2003.

[51] R. Helmig: *Multiphase flow and transport processes in the subsurface*. Springer, Berlin, 1997.

[52] O. Hjelmar, H. A. van der Slot, D. Guyonnet, R. Rietra, A. Brun & D. Hall: *Development of acceptance criteria for landfilling of waste: an approach based*

on impact modelling and scenario calculations. In Proc. Sardinia 01, Eighth International Waste Management and Landfill Symposium S. Margherita di Pula, Cagliari, Italy, volume III, pages 711–721. CISA, Environmental Sanitary Engineering Centre, 2001.

[53] P. Huber: *Die TA Siedlungsabfall und ihre Bindung*. Schriften zum deutschen und europäischen Umweltrecht, Band 21. Heymanns,Köln, 2000.

[54] C. Jommi: *Remarks on the constitutive modelling of unsaturated soils*. In A. Tarantino & C. Mancuso, editors, Experimental Evidence and Theoretical Approaches in Unsaturated soils, pages 139–153. Balkema, Rotterdam, 2000.

[55] R. Katzenbach, C. Gutberlet & G. Bachmann: *Anforderungen an die Anwendung numerischer Standsicherheitsnachweise im Erd- und Grundbau*. Der Bauingenieur, 82, 199–205, 2007.

[56] E. Kavazanjian: *Mechanical properties of municipal solid waste*. In Proc. Sardinia 01, Eighth International Waste Management and Landfill Symposium S. Margherita di Pula, Cagliari, Italy, volume III, pages 415–424. CISA, Environmental Sanitary Engineering Centre, 2001.

[57] E. Kavazanjian, N. Matasovic & R. Bachus: *Large-diameter static and cyclic laboratory testing of municipal solid waste*. In Proc. Sardinia 99, Seventh International Waste Management and Landfill Symposium S. Margherita di Pula, Cagliari, Italy, volume III, pages 437–444. CISA, Environmental Sanitary Engineering Centre, 1999.

[58] E. Kavazanjian & S. Merry: *The 10 July 2000 Payatas landfill failure*. In Proc. Sardinia 05, Tenth International Waste Management and Landfill Symposium S. Margherita di Pula, Cagliari, Italy, pages 587–588. CISA, Environmental Sanitary Engineering Centre, 2005.

[59] J. Kindlein, D. Dinkler & H. Ahrens: *Numerical modelling of multiphase flow and transport processes in landfills*. Waste Manage Research, 24, 376–387, 2006.

[60] R. Kockel: *Scherfestigkeit von Mischabfall im Hinblick auf die Standsicherheit von Deponien*. PhD thesis, Schriftenreihe des Instituts für Grundbau, Ruhr-Universität Bochum, Heft 24, 1995.

[61] R. Koerner & T. Soong: *Assessment of ten landfill failures using 2-d and 3-d stability analysis procedures*. In Vienna-Terzaghi-Lecture, pages 9–47. Österreichische Geotechnik Tagung, Wien, 1999.

[62] F. Kölsch: *Der Einfluß der Faserbestandteile auf die Scherfestigkeit von Siedlungsabfall*. PhD thesis, Leichtweiß-Institut für Wasserbau, Technische Universität Braunschweig, Heft 133, 1996.

[63] F. Kölsch, K. Fricke, C. Mahler & E. Damanhuri: *Stability of landfills - the Bandung dumpsite disaster*. In Proc. Sardinia 05, Tenth International Waste Management and Landfill Symposium S. Margherita di Pula, Cagliari, Italy, pages 179–180. CISA, Environmental Sanitary Engineering Centre, 2005.

[64] U. Kowalsky: *Mikrophysiskalisch begründetes Werkstoffmodell zur Berechnung thermomechanisch beanspruchter Konstruktionen*. PhD thesis, Bericht Nr. 94-78, Institut für Statik, TU Braunschweig, 1994.

[65] P. Lade & J. Duncan: *Cubical triaxial tests on cohesionless soil*. Journal of the Soil Mechanics and Foundations Divisions, 99, 793–812, 1973.

[66] A. O. Landva & J. I. Clark: *Geotechnics of waste fill*. In A. O. Landva & G. D. Knowles, editors, Geotechnics of Waste Fills - theory and practise, ASTM STP 1070, pages 86–103. American Society for Testing and Materials, Philadelphia, 1990.

[67] U. Langer, N. Dixon, P. Gotteland & J.-P. Gourc: *Waste mechanics: investigations using synthetic msw*. In Proc. Sardinia 05, Tenth International Waste Management and Landfill Symposium S. Margherita di Pula, Cagliari, Italy, pages 351–352. CISA, Environmental Sanitary Engineering Centre, 2005.

[68] E. Lee: *Elastic-Plastic Deformation at Finite Strains*. Journal of Applied Mechanics, 36, 1–6, March 1969.

[69] E. Lee & D. Liu: *Finite-Strain Elastic-Plastic Theory with Application to Plane-Wave Analysis*. Journal of Applied Physics, 38(1), 19–27, 1967.

[70] R. Lewis & B.A.Schrefler: *The finite element method in the static and dynamic deformation and consolidation of porous media*. Wiley, Chichester, 2nd edition, 1998.

[71] C. Liu, R. Chen & K. Chen: *Unsaturated consolidation theory for the prediction of long-term municipal solid waste landfill settlement.* Waste Management & Research, 24, 80–91, 2006.

[72] N. Lu & W. Likos: *Unsaturated soil mechanics*. Wiley, Hoboken, 2004.

[73] J. Lüke: *Entwicklung und Anwendung eines Stoffgesetzes für Siedlungsabfälle*. PhD thesis, RWTH Aachen, Geotechnik in Forschung und Praxis, WBI-Print 11, Glückauf, Essen, 2002.

[74] D. Lürding: *Modellierung großer Deformatioen in orthotropen, hyperelastischen Schalenkonstruktionen*. PhD thesis, Mitteilungen aus dem Institut für Mechanik, 125, Ruhr-Universität Bochum, 2000.

[75] S. Machado, M. Carvalho & O. Vilar: *Constitutive model for municipal solid waste*. Journal of geotechnical and geoenvironmental engineering, 128(11), 940–951, 2002.

[76] T. Maier: *Comparison of non-local and polar modelling of softening in hypoplasticity*. International Journal for Numerical and analytical methods in geomechanics, 28(3), 251–268, 2004.

[77] M. Manassero, W. van Impe & A. Bouazza: *Waste disposal and containment*. In M. Kamon, editor, Environmental Geotechnics, pages 1425–1473. Balkema, Rotterdam, 1996.

[78] A. Marques, G. Filz & O. Vilar: *Composite compressibility model for municipal solid waste*. Journal of Geotechnical and Geoenvironmental Engineering, 129(4), 372–378, 2003.

[79] M.Baerns, H. Hofmann & A. Renken: *Chemische Reaktionstechnik*. Georg Thieme Verlag, Stuttgart, 1992.

[80] J. McDougall & I. Pyrah: *Modelling load, creep and biodegradation settlement in landfill*. In Proc. Sardinia 03, Ninth International Waste Management and Landfill Symposium S. Margherita di Pula, Cagliari, Italy, pages 261–262. CISA, Environmental Sanitary Engineering Centre, 2003.

[81] J. McDougall, R. Sarsby & N. Hill: *A numerical investigation of landfill hydraulics using variably saturated flow theory*. Géotechnique, 46(2), 329–341, 1996.

[82] J. McDougall & R. Silver: *Hydro-bio-mechanical modelling landfilled waste: real insights?* In Proc. Sardinia 05, Tenth International Waste Management and Landfill Symposium S. Margherita di Pula, Cagliari, Italy, pages 935–936. CISA, Environmental Sanitary Engineering Centre, 2005.

[83] C. Miehe: *A constitutive frame of elastoplasticity at large strains based on the notation of a plastic metric*. International Journal of Solids and Structures, 33, 3103–3130, 1998.

[84] K. Münnich & H.-J. Collins: *Evaluation of the water balance of municipal waste landfills*. In Proc. Sardinia 01, Eighth International Waste Management and Landfill Symposium S. Margherita di Pula, Cagliari, Italy, volume II, pages 3–10. CISA, Environmental Sanitary Engineering Centre, 2001.

[85] K. Münnich, K. Fricke, K. & J. Bauer: *Überwachung und Beurteilung von Deponien*. In U. Peil, editor, SFB 477 - Sicherstellung der Nutzungsfähigkeit von Bauwerken mit Hilfe innovativer Bauwerksüberwachung, Berichtskolloquium, pages 67–73. 2006.

[86] M. Ortiz, P. Pinsky & R. Taylor: *Operator split methods for the numerical-solution of the elastoplastic dynamic problem*. Computer Methods in Applied Mechanics and Engineering, 39(2), 137–157, 1985.

[87] H. Parisch: *Festkörper-Kontinuumsmechanik*. B.G. Teubner, Stuttgart, 2003.

[88] H. Pohlheim: *GEATbx Introductions - Evolutionary algorithms: overview, methods, operators*, 2005. `http://www.geatbx.com`.

[89] S. Reese: *Theorie und Numerik des Stabilitätsverhaltens hyperelastischer Festkörper*. PhD thesis, Institut für Mechanik, Darmstadt, 1994.

[90] E. Reuter: *Verformungsanalyse und Standsicherheitsbeurteilung für die Zentraldeponie Hannover*. In Prühs, H., editor, Geotechnische Probleme beim Bau von Abfalldeponien, 11. Nürnberger Deponieseminar, volume 69 of *Veröffentlichungen des Grundbauinstitutes der Landesgewerbeanstalt Bayern*, pages 241–269, 1995.

[91] T. Ricken & V. Ustohalova: *Modeling of thermal mass transfer in porous media with applications to the organic phase transition in landfills*. Computational Material Science, 32, 498–508, 2005.

[92] E. Riks: *The application of Newtons's method to the problem of elastic stability*. Journal of Applied Mechanics, Transactions of the ASME, 1060–1065, 1972.

[93] T. Scheelhaase, W. Bidlingmeier, A. Klümper, A. Maile & M. Rechberger: *Geotechnical behaviour of mechanically-biologically pretreated residual waste*. In Proc. Sardinia 01, Eighth International Waste Management and Landfill Symposium S. Margherita di Pula, Cagliari, Italy, volume III, pages 445–453. CISA, Environmental Sanitary Engineering Centre, 2001.

[94] J. Simo & M.Ortiz: *A unified approach to finite deformation elastoplastic analysis based on the use of hyperelastic constitutive equations*. Computer Methods in Applied Mechanics and Engineering, 49(2), 221–245, 1985.

[95] G. Stoltz & J. Gourc: *Influence of compressibility of domestic refuses on fluid conductivity*. In 2nd International Workshop on Hydro-Physico-Mechanics of Wastes, Southampton 18th-19th April, 2007.

[96] T. Streilein: *Erfassung formativer Verfestigung in viskoplastischen Stoffmodellen*. PhD thesis, Bericht Nr. 97-83, Institut für Statik, TU Braunschweig, 1997.

[97] S. Thomas, A. Aboura, J.-P. Gourc, P. Gotteland, H. Billard, T. Delineau, T. Gisbert, J. Ouvry & M. Vuillemin: *An in-situ waste mechanical experiment on a french landfill*. In Proc. Sardinia 99, Seventh International Waste Management

and Landfill Symposium S. Margherita di Pula, Cagliari, Italy, volume III, pages 445–451. CISA, Environmental Sanitary Engineering Centre, 1999.

[98] C. Truesdell: *Rational Thermodynamics - A Course of Lectures on Selected Topics*. McGraw-Hill New York, 1969.

[99] I. Vardoulakis & J. Sulem: *Bifurcation analysis in geomechanics*. Blackie Academic & Professional, London, 1995.

[100] W. Volk: *Untersuchung des Lokalisierungsverhaltens mikropolarer poröser Medien mit Hilfe der Cosserat-Theorie*. PhD thesis, Institut für Mechanik, Universität Stuttgart, Bericht Nr. II-2, 1999.

[101] P. von Wolffersdorff: *Verformungsprognosen für Stützkonstruktionen*. PhD thesis, Institut für Bodenmechanik und Felsmechanik der Universiät Fridericiana in Karlsruhe, Heft 141, 1997.

[102] K. S. Watts & J. A. Charles: *Settlement of recently placed domestic refuse landfills*. Proceedings Institution of Civil Engineers, Part 1, 88, 178–195, 1990.

[103] K. Wegener: *Zur Berechnung großer plastischer Deformationen mit einem Stoffgesetz vom Überspannungstyp*. PhD thesis, Braunschweig Series on Mechanics, no. 2-1991, TU Braunschweig, 1991.

[104] M. Wehnert, H. Neher, P. Vermeer, L. Zangl & M. Dzengel: *Analyse des Verformungsverhaltens einer Hausmülldeponie*. Die Bautechnik, 82(4), 218–226, 2005.

[105] G. Wempner: *Discrete approxiamtions related to nonlinear theories of solids*. International Journal of Solid and Structures, 7, 11581–1599, 1971.

[106] J. White: *The application of the University of Southampton landfill degradation and transport model LDAT to the HPM2 challenge dataset derived from two consolidating anaerobic reactors by Ivanova et al.* In 2nd International Workshop on Hydro-Physico-Mechanics of Wastes, Southampton 18th-19th April, 2007.

[107] A. Young: *Mathematical modelling of landfill degradation*. Journal of chemical technology and biotechnology, 46(3), 189–208, 1989.

[108] G. Ziehmann: *Setzungen von Abfalldeponien - Theorie und Laborversuche zur Kennzeichnung von Einflussgrößen*. PhD thesis, Leichtweiß-Institut für Wasserbau, Technische Universität Braunschweig, Cuvillier Verlag, Göttingen, 2002.

[109] T. Zümendorf: *Ein gradientenabhängiges Modell für Schädigung bei viskoplastischem Materialverhalten*. PhD thesis, Bericht Nr. 2006-104, Institut für Statik, TU Braunschweig, 2006.

Berichte aus dem Institut für Statik ab 1994

Nr.	94-78	U. KOWALSKY: Mikrophysikalisch begründetes Werkstoffmodell zur Berechnung thermomechanisch beanspruchter Konstruktionen (1994).
Nr.	95-79	N. OBERBECK: Instationärer Wärme-Feuchte-Schadstoff - Transport in Beton, Theorie und Berechnung (1995).
Nr.	95-80	N. MELEKA: Nonlinear Analysis of Flat Slab Floors (1995).
Nr.	97-81	H. FLOREN: Strukturanalysen unterirdischer Hohlräume im Salzgebirge mit hybriden Randelement- / Finite-Element-Methoden (1997).
Nr.	96-82	T. GARTUNG: Berechnung von Asphaltstraßen mit einem einheitlichen rheologischen Konzept einschließlich Schädigung (1996).
Nr.	97-83	T. STREILEIN: Erfassung formativer Verfestigung in viskoplastischen Stoffmodellen (1997).
Nr.	97-84	B. GUERICKE: Geomechanische Untersuchungen zur Sicherheitsanalyse von Deponien im Salzgestein (1997).
Nr.	97-85	U. GLABISCH: Stoffmodell für Grenzzustände im Salzgestein zur Berechnung von Gebirgshohlräumen (1997).
Nr.	97-86	E. ELARABI: Numerical Analysis of the Swelling Soil Effects on Structures (1997).
Nr.	98-87	I. SPOHR: Störenergie-Konzept für den elasto-plastischen Beulsicherheitsnachweis beliebig belasteter Zylinderschalen (1998).
Nr.	99-88	C.-X. HUANG: Berechnung von Temperaturspannungen und Rißbildungen infolge Hydratation in 3D-Betonkonstruktionen (1999).
Nr.	2000-89	H. PENSKY: Beschreibung von streuendem Materialverhalten und von Schädigung bei inelastischen Werkstoffen (2000).
Nr.	2000-90	A. STEFFENS: Modellierung von Karbonatisierung und Chloridbindung zur numerischen Analyse der Korrosionsgefährdung der Betonbewehrung (2000).
Nr.	2001-91	J. EBERS-ERNST: Modellierung des inelastischen Verformungsverhaltens von Siedlungsabfalldeponien (2001).
Nr.	2001-92	J. HANEL: Modell zur Analyse von gekoppelten Transport- und Stoffabbauprozessen in Deponien (2001).
Nr.	2002-93	B. WIEDEMANN: Modelle für vorgespannte Membranen mit Faltenbildung (2002).

Nr.	2002-94	R. TACKE: Feuchte- und Festigkeitsentwicklung hydratisierenden Betons – Modellierung und numerische Analyse (2002).
Nr.	2002-95	E. WALHORN: Ein simultanes Berechnungsverfahren für Fluid-Struktur-Wechselwirkungen mit finiten Raum-Zeit-Elementen (2002).
Nr.	2003-96	B. HÜBNER: Simultane Analyse von Bauwerk-Wind-Wechselwirkungen (2003).
Nr.	2003-97	J. GEISTEFELDT: Stochastische Finite-Element-Methoden mit Anwendung auf aeroelastische Tragsysteme (2003).
Nr.	2003-98	O. KNOKE: Beulwiderstände zusammengesetzter Zylinder-Kegel-Schalen (2003).
Nr.	2005-99	A. KÖLKE: Modellierung und Diskretisierung bewegter Diskontinuitäten in randgekoppelten Mehrfeldsystemen (2005).
Nr.	2006-100	D. DINKLER (HRSG.): Institut für Statik, Lehre und Forschung, 1996 - 2006 (2006).
Nr.	2006-101	A. VEHRE: Ein Reduktionsverfahren für Fluid-Struktur-Wechselwirkungen mit finiten Raum-Zeit-Elementen (2006).
Nr.	2006-102	M. LÖHR: Analyse aeroelastischer Systeme mit Spektralen Stochastischen Finite-Element-Methoden (2006).
Nr.	2006-103	L. ASCHENBRENNER: Mehrkomponenten-Modell zur Beschreibung des Deformationsverhaltens von Asphalt (2006).
Nr.	2006-104	T. ZÜMENDORF: Ein gradientenabhängiges Modell für Schädigung bei viskoplastischem Materialverhalten (2006).
Nr.	2007-105	C. LEPPERT: Mehrphasenmodell für granulare Medien zur numerischen Untersuchung des Phasenübergangs bei der Entleerung von Silos (2007).

Sonderdrucke

Phänomenologische Modelle für Werkstoffe des Bauwesens.
Hermann Ahrens zum 60. Geburtstag (1998).
Herausgeber: D. Dinkler, U. Kowalsky.

Baustatik-Baupraxis 8.
Berichte der Fachtagung am 21. und 22. März 2002 in Braunschweig.
Herausgeber: D. Dinkler.

Institut für Statik, Technische Universität Braunschweig
Beethovenstraße 51, 38106 Braunschweig, Deutschland
Telefon +49 (0)531 / 391-3667, Telefax +49 (0)531 / 391-8116
E-Mail statik@tu-bs.de, Homepage http://www.statik.tu-braunschweig.de